Physics-Informed, Data-Driven Framework for Model-Form Uncertainty Estimation and Reduction in RANS Simulations

Jian-Xun Wang

Dissertation submitted to the Faculty of the
Virginia Polytechnic Institute and State University
in partial fulfillment of the requirements for the degree of

Doctor of Philosophy
in
Aerospace Engineering

Heng Xiao, Chair
Christopher J. Roy
Lin Ma
Robert Weiss

February 22$^{\text{th}}$, 2017
Blacksburg, Virginia

Keywords: Uncertainty quantification, Data-driven, RANS, Turbulence modeling, Machine learning, Data assimilation, Model-form uncertainty, Random matrix, Maximum entropy

Copyright 2017, Jian-Xun Wang

Physics-Informed, Data-Driven Framework for Model-Form Uncertainty Estimation and Reduction in RANS Simulations

Jian-Xun Wang

ABSTRACT

Computational fluid dynamics (CFD) has been widely used to simulate turbulent flows. Although an increased availability of computational resources has enabled high-fidelity simulations (e.g. large eddy simulation and direct numerical simulation) of turbulent flows, the Reynolds-Averaged Navier-Stokes (RANS) equations based models are still the dominant tools for industrial applications. However, the predictive capability of RANS models is limited by potential inaccuracies driven by hypotheses in the Reynolds stress closure. With the ever-increasing use of RANS simulations in mission-critical applications, the estimation and reduction of model-form uncertainties in RANS models have attracted attention in the turbulence modeling community. In this work, I focus on estimating uncertainties stemming from the RANS turbulence closure and calibrating discrepancies in the modeled Reynolds stresses to improve the predictive capability of RANS models. Both on-line and off-line data are utilized to achieve this goal. The main contributions of this dissertation can be summarized as follows: First, a physics-based, data-driven Bayesian framework is developed for estimating and reducing model-form uncertainties in RANS simulations. An iterative ensemble Kalman method is employed to assimilate sparse on-line measurement data and empirical prior knowledge for a full-field inversion. The merits of incorporating prior knowledge and physical constraints in calibrating RANS model discrepancies are demonstrated and discussed. Second, a random matrix theoretic framework is proposed for estimating model-form uncertainties in RANS simulations. Maximum entropy principle is employed to identify the probability distribution that satisfies given constraints but without introducing artificial information. Objective prior perturbations of RANS-predicted Reynolds stresses in physical projections are provided based on comparisons between physics-based and random matrix theoretic approaches. Finally, a physics-informed, machine learning framework towards predictive RANS turbulence modeling is proposed. The functional forms of model discrepancies with respect to mean flow features are extracted from the off-line database of closely related flows based on machine learning algorithms. The RANS-modeled Reynolds stresses of prediction flows can be significantly improved by the trained discrepancy function, which is an important step towards the predictive turbulence modeling.

Physics-Informed, Data-Driven Framework for Model-Form Uncertainty Estimation and Reduction in RANS Simulations

Jian-Xun Wang

GENERAL AUDIENCE ABSTRACT

Turbulence modeling is a critical component in computational fluid dynamics (CFD) simulations of industrial flows. Despite the significant growth in computational resources over the past two decades, the time-resolved high-fidelity simulations (e.g., large eddy simulation and direct numerical simulation) are not feasible for engineering applications. Therefore, the small-scale turbulent velocity fluctuations have to resort to the time-averaging modeling. Reynolds-averaged Navier-Stokes (RANS) equations based turbulence models describe the averaged flow quantities for turbulent flows and are believed to be the dominant tools for industrial applications in coming decades. However, for many practical flows, the predictive accuracy of RANS models is largely limited by the model-form uncertainties stemming from the potential inaccuracies in the Reynolds stress closure. As RANS models are used in the design and safety evaluation of many mission-critical systems, such as airplanes and nuclear power plants, properly estimating and reducing these model uncertainties are of significant importance. In this work, I focus on estimating uncertainties stemming from the RANS turbulence closure and calibrating discrepancies in the modeled Reynolds stresses to improve the predictive capability of RANS models. Several data-driven approaches based on state-of-the-art data assimilation and machine learning algorithms are proposed to achieve this goal by leveraging the use of on-line and off-line high-fidelity data. Numerical simulations of several canonical flows are used to demonstrate the merits of the proposed approaches. Moreover, the proposed methods also have implications in many fields in which the governing equations are well understood, but the model uncertainties come from unresolved physical processes.

To my parents

Acknowledgments

It would not have been possible to accomplish this doctoral dissertation and my Ph.D study at Virginia Tech without the support of the people around me.

I would like to first thank my adviser, Dr. Heng Xiao, for his motivation, enthusiasm, patience, and consistent guidance throughout the course of my Ph.D. study. I learned from him various techniques for conducting excellent research. Moreover, I motived by him to pursue an academic life with a great enthusiasm. I am thankful to my committee members, Dr. Christopher J. Roy, Dr. Lin Ma, and Dr. Robert Weiss, for serving on my doctoral committee and providing me professional and academic advice.

I also want to express my thanks to my coauthor and colleague, Mr. Jin-Long Wu for his collaboration in developing the frameworks of data-driven RANS modeling error estimation and reduction. I am thankful to Dr. Robert Weiss and Mr. Hui Tang for the collaboration on inverse problem of tsunami flows. I thank my external collaborators, Dr. Julia Ling of Sandia national labs, Dr. Gialunca Iaccarino of Stanford University, Dr. Duan Lian of Missouri University of Science and Technology, and Dr. Roger G. Ghanem of University of South California for their valuable inputs and ideas.

I am also thankful to my recent and past colleagues in AOE department at Virginia Tech, especially, Mr. Shunxiang Cao, Mr. Yang Song, Mr. Howard Chuang, Mr. Xingsheng Sun, Mr. Petr Cagas, Mr. Carlos Michelen-Strofer, Mr. Rui Sun, Dr. Yue Wu, Mr. Haoting Wang, and Mr. Ning Liu. I also appreciate academic discussions with nice people outside the AOE department. For example, Dr. Taige Wang of Dept. of Mathematics always spent time with me on discussing some research problems of our common interests.

Another sincere acknowledgment is for all my friends who is always supporting me. Special thanks to Mr. Daren Chen, Mr. Yanzhi Dou, and Ms. Yiming Zhang for their support and help in both work or life. I greatly thank my girlfriend, Dr. Sisi Meng, for her everlasting supports to my academic pursuits. Finally, I give my great gratitude to my families, my Mom and Dad, for their love and supports which have always encouraging me to achieve significant accomplishments one by one. I love you all.

Contents

Chapter 1

Introduction

Computational fluid dynamics (CFD) has been widely used to simulate turbulent flows. Although the rapidly increasing availability of computational resources enables high-fidelity simulations, e.g., Large Eddy Simulation (LES) and Direct Numerical Simulation (DNS), it is not yet computationally feasible to routinely apply them for complex, industrial flows. The numerical models based on Reynolds-Averaged Navier-Stokes (RANS) equations are still the workhorse tools for turbulent simulations in engineering analysis, design, and optimizations. Despite with less computational cost, the predictions of RANS models have large uncertainties for the flows with strong pressure gradients, non-parallel shear layers, and mean flow curvature [1]. These uncertainties are mostly attributed to the phenomenological closure models of the Reynolds stress [2, 3], which are referred to as model-form uncertainties. Model-form uncertainties are the dominant source of uncertainties in RANS simulations, which largely diminish their predictive capability for practical flows. Therefore, it is of critical importance to estimate and reduce these uncertainties to make risk-informed decisions, especially in the context of applying RANS to mission-critical systems, e.g., the thermo-hydraulic system in the nuclear industry.

The main focus of this work is on the development of methodologies to estimate model-form uncertainties in RANS simulations and to reduce them based on available high-fidelity data. The uncertainties are directly introduced onto the source of the RANS model inadequacy by perturbing the RANS-modeled Reynolds stresses. Two approaches of Reynolds stress perturbation are proposed. One is based on the physics-based decomposition by using random scalar fields, and the other is based on the random matrix theory with the maximum entropy principle. The realizability has been imposed in both approaches. In the physics-based approach, the physical prior knowledge can be easily encoded. To reduce the model-form uncertainties, a Bayesian approach, i.e., iterative ensemble Kalman method, is employed. Both sparse on-line data and prior physical knowledge are assimilated to calibrate the Reynolds stress discrepancies within the Bayesian approach. Finally, the data-driven uncertainty reduction (calibration) approach is extended to apply to the flows for which on-line data are

not available.

1.1 Previous Work

1.1.1 Black-Box, Parametric Approach

Previous efforts in estimating and reducing model-form uncertainties in RANS simulations have mostly followed parametric approaches, which are based on a universal Bayesian uncertainty quantification and calibration framework proposed by Kennedy and O'Hagan [4]. In their seminal work, the uncertainties associated with the computer model are assumed to stem from two sources: model parameters and model inadequacy. Therefore, the true quantity of interest (QoI) $\tilde{u}(\mathbf{x})$ can be expressed as,

$$\tilde{u}(\mathbf{x}) = u(\mathbf{x}, \theta) + \epsilon(\mathbf{x}, \alpha), \tag{1.1}$$

where u is the modeled QoI; $\mathbf{x}$ denotes the input parameter vector; θ is the model parameter vector; $\epsilon(\mathbf{x}, \alpha)$ is the model inadequacy term, which is the difference between the mathematical model and the physical reality. This model inadequacy term is modeled as a black-box, Gaussian process (GP) and α represents its hyper-parameter vector. The model uncertainties can be estimated by perturbing the model parameters θ and model inadequacy field $\epsilon(\mathbf{x}, \alpha)$. The prior distributions of model parameters θ and hyper-parameters α of GP random field can be updated by data within the Bayesian framework. This framework has been used in many applications, and a number of sophisticated variants have been developed [5, 6, 7]. For estimating and reducing model uncertainties in RANS simulations, extensive research and development can be attributed to this black-box, parametric framework.

Some researchers tried to estimate uncertainties in RANS turbulence models by only perturbing model parameters. For example, Platteeuw et al. [8] perturbed coefficients of the k-ε model based on the collocation method, while Dunn et al. [9] performed similar perturbations by using the Latin Hypercube sampling method. The perturbed coefficients involve repeating RANS simulations, and the sensitivities of the propagated QoIs are observed. When relevant data (e.g., experimental measurements of velocity field) are available, these uncertainties can be reduced, and the mean of each parameter can be calibrated within a Bayesian framework. This is also referred to as the Data Assimilation (DA) problem. The initial perturbations of model parameters can be seen as the Monte Carlo samples of their prior distributions, which will be updated to the posteriors by assimilating available data. Sagaut and co-works [10] constructed priors of the parameters for two popular RANS models, k-ε model and k-ω SST model, through generalized Polynomial Chaos. These perturbed parameters were calibrated by minimizing the discrepancies between the propagated QoIs and corresponding data. Ray et al. [11] also conducted the Bayesian perturbation and calibration of RANS model parameters for jet-in-cross flows. However, these parametric approaches are still constrained by the functional form of turbulence models, e.g., stress-strain relationship based on Boussinesq

eddy viscosity assumption. This assumption may not be valid for many types of flows, and the uncertainties or discrepancies introduced by the assumption cannot be captured in the parametric approaches. In other words, these approaches neglect model-form discrepancies that stem from inadequacies in the hypothesized stress-strain relationship.

To consider the structural uncertainties due to potentially inaccurate assumptions in RANS turbulence models, an inadequacy term modeled as a Gaussian random field is introduced. Edeling et al. [12] employed a multiplicative inadequacy term on the QoIs and calibrated both coefficients of the k–ε model and hyper-parameters of the inadequacy term within a Bayesian framework. In addition to the model inadequacy term, some researchers [13, 14, 15] also introduced an ensemble of RANS models and considered the differences among the predictions of the multiple models. With data, the predictions of competing models are weighted based on the posterior plausibility of each model. This approach is referred to as the model-scenario averaging method. While considering the model inadequacy by introducing a Gaussian random field and an ensemble of RANS models has had some success, these physics-neutral uncertainty quantification and reduction approaches have essential limitations to fully explore the uncertainty space. First, the model inadequacy term is modeled as a black-box random field and is directly added to the model predicted QoI. As a result, the physical prior knowledge is difficult to incorporate, and the physical constraints (e.g., conservation law) cannot be guaranteed. Moreover, the generality of the calibration is largely restricted. Recently, Brynjarsdottir and O'Hagan [16] emphasized the importance of incorporating prior information, but they also highlighted the difficulties of enforcing prior information in the black-box framework. They pointed out that a simple constraint (e.g., zero-gradient boundary condition) on the model inadequacy is challenging to enforce. Realistic prior knowledge in turbulence modeling, e.g., realizability of Reynolds stress, conservation law, is generally even more complicated. Second, introducing multiple competing RANS models to estimate model-form uncertainty may not fully explore the uncertainty space, since these models are likely to share similar biases. For example, Oliver and Moser [14] analyzed a group of widely used RANS models including k–ε, k–ω, Spalart-Allmaras, shear stress transport (SST), and v^2–f models. However, these RANS models are all based on the scalar eddy viscosity assumption, and thus the corresponding predictions share similar biases. The uncertainties are significantly underestimated by only considering this ensemble of models.

1.1.2 Open-Box, Nonparametric Approaches

Recently, several research groups in the turbulence modeling community have recognized the limitations of the black-box, parametric approaches and started to embed the model inadequacy term locally into the closure models, where the source of the model-form uncertainties locates. We refer these efforts to as open-box, nonparametric approaches, which are reviewed in detailed below.

Moser and co-workers [3] explicitly pointed out that the model inadequacy of RANS equa-

tions is originated from the closure model of Reynolds stresses. That is, the RANS equations based on physical theories (e.g., conservation law) are reliable, except for the approximations made in the embedded turbulence closure for modeling unresolved physics, i.e., Reynolds stresses. Iaccarino and co-workers [17, 18] held the same insight and proposed a physics-based, non-parametric approach to estimate the model-form uncertainties in RANS simulations. In their framework, uncertainties are injected onto physically meaningful projections of the RANS-modeled Reynolds stress, i.e., its eigenvalues, eigenvectors, and turbulence kinetic energy. Since the realizability constraints of Reynolds stresses provide perturbation bound on the eigenvalues of the Reynolds stress anisotropy (in the form of the classical Lumley triangle [19] or the recently proposed barycentric triangle [20]), the perturbations are only introduced in the eigenvalues by perturbing the Reynolds stresses towards their three limiting states within the physically realizable range. Gorlé et al. [21] proposed a marker function and used it to identify regions where the RANS-predicted Reynolds stress divergence is inaccurate. Based on the marker function, the eigenvalue perturbations are only conducted to the regions where the baseline turbulence model is believed to perform poorly. This uncertainty estimation framework based on eigenvalue perturbation has been successfully applied to several engineering applications [22, 23, 24]. Most recently, Mishra et al. [25] complemented this framework by exploring envelopes of uncertainties in the eigenvectors with two more perturbations. The seminal works of Iaccarino and co-workers provide practical methods to estimate model-form uncertainties in RANS simulations from a non-parametric sense. Moreover, the framework has moderate computational overhead, since only less than five additional RANS simulations are required. However, it should be noted that this approach only serves as an empirical estimation of uncertainties and does not fully explore the entire uncertainty space. This is because the QoIs are not necessarily linear combinations of the ones propagated from the turbulence limiting states, though the true Reynolds stress is a convex linear combination of the Reynolds stresses in the limiting states.

Recently, Xiao et al. [26] proposed a Bayesian framework for quantifying and reducing model-form uncertainties in RANS simulations by assimilating limited amount of observation data and available physical prior knowledge. Compared to the enveloping estimation framework of Iaccarino et al. [17, 18, 25], where the uncertainties were estimated by perturbing the Reynolds stresses towards their three or five limiting states, the physics-based, Bayesian framework of Xiao et al. [26] modeled the discrepancies in the magnitude and eigenvalues of Reynolds stresses as Gaussian random fields. Wang et al. [27] complemented the perturbation framework by parameterizing and perturbing the eigenvectors with the Euler angle system. This physics-based framework systematically explored the uncertainty space of Reynolds stress fields. Moreover, an iterative ensemble Kalman method was employed to reduce the uncertainties by assimilating all sources of available information, including empirical prior knowledge, physical constraints, and a limited amount of observation data. Wang et al [28] discussed the merits of incorporating various types of prior knowledge in the proposed uncertainty estimation and reduction framework. Details of this framework can be found in Chapters 2 and 3. While the physics-based framework has achieved significant success and been applied to complex, three-dimensional flows [29], it is challenging to spec-

ify prior distributions over these physical variables without introducing artificial constraints. The priors play a critical role in the uncertainty propagation and Bayesian inference, particularly when the data are limited [28]. However, it is not clear if or how much artificial information is introduced into the prior distributions of each physical component specified in [26]. To address this issue, Xiao et al. [30] proposed a random matrix theoretic (RMT) approach with maximum entropy principle to estimate model-form uncertainties in RANS simulations. The RMT approach is an alternative to the physics-based approach, where the realizability of perturbed Reynolds stresses is guaranteed automatically by injecting uncertainties directly in the set of positive semidefinite matrices. More importantly, the RMT approach provides objective priors for Bayesian inferences that satisfy the given constraints without introducing artificial information. Wang et al. [27] utilized the RMT approach to assess and improve the specification of priors used in the physics-based, Bayesian framework. The details of the RMT framework are presented in Chapters 4 and 5.

The Bayesian frameworks for calibrating model discrepancies and reducing model uncertainties (including parametric [14, 10, 12, 15] and nonparametric ones [26, 28]) can only be applied to scenarios where on-line observation data (e.g., sparse velocity measurements, pressure and lift coefficients measurements) are available. However, in the design stage of engineering system where the target configuration has not been built yet, the on-line measurement data are not available. Instead, the data sets of closely related flows, e.g., flows with same geometry but at different Reynolds numbers or flows with slightly changed geometries, are usually accessible. These data sets are referred to as off-line databases. Most recently, researchers started to investigate the use of off-line data to reduce the model-form uncertainty by applying data-driven, machine learning algorithms. Dow and Wang [31] used DNS data from a plane channel flow to infer the full-field discrepancy in the turbulent viscosity modeled by the $k\omega$ model. The inferred discrepancy field is used to improve flows in channels with wavy boundaries. In a similar vein, Wu et al. [32] extended the framework of Xiao et al. [26] and showed that the full-field Reynolds stress discrepancies calibrated with sparse velocity data could be extrapolated to flows at much higher Reynolds numbers. The extrapolated discrepancy has led to significant improvement of the predicted QoIs. However, both the extrapolation approaches of Dow et al. [31] and Wu et al. [32] are largely limited for that they infer model discrepancy terms in the physical coordinates $\mathbf{x}$. As a result, the predictions can only be applied to the flows in the same geometry at the same location. Duraisamy and co-workers [33, 34] also proposed a two-step approach to reduce the RANS model discrepancies. They introduced a multiplicative discrepancy field $\beta(\mathbf{x})$ into the transport equations of turbulent quantities (e.g., ω in k–ω models) to adjust the production-dissipation balance in the model equation. In the first step, a full-field inversion of the discrepancy term $\beta(\mathbf{x})$ is performed for flows where data are available. In the second step, neural networks are employed to extract the functional form of discrepancy $\beta(\mathbf{q})$ with respect to the flow and model variables $\mathbf{q}$. This two-step framework has been tested on a few simple flow configurations [35, 34] *a priori*, further *a posteriori* tests have yet to be demonstrated. Although the learning is performed in the flow feature $\mathbf{q}$ space in [35, 34], the input feature vector was constructed with a very small number (three) of features and

the invariant properties were not fully considered. Ling et al. [36] pointed out the merits of embedding the invariant properties into machine learning process. They proposed a rich set of invariant input features and explored several machine learning models for identifying the regions where RANS assumptions are violated [37]. Most recently, they also attempted to directly learn the anisotropy tensors of Reynolds stresses by using random forests [38] and deep neural networks [39]. By comprehensively considering the physical interpretability of learning targets and the invariance properties of input features, Wang et al. [40] proposed a physics-informed machine learning (PIML) approach to use off-line data to learn the functional form of Reynolds stress discrepancy on its six physically meaningful projections with respect to a group of ten invariant mean flow features. They successfully demonstrated that the trained (calibrated) discrepancy model could be used to improve RANS-modeled Reynolds stresses in flows with slightly changed configurations. Wang et al. [41] further expanded the input feature space by using an invariant basis and demonstrated significant success in using PIML towards predictive turbulence modeling in flows with same geometries but at different Reynolds numbers. The PIML framework for reducing model uncertainties and calibrating model discrepancies based on off-line data is depicted in Chapter 6.

1.2 Contribution

The contribution of this dissertation to the turbulence modeling community can be summarized as follows:

1. A physics-based, data-driven Bayesian framework was developed for estimating and reducing model-form uncertainties in RANS simulations. This framework accounts for empirical prior knowledge and leverages the use of sparse on-line measurement data. The merits of incorporating prior knowledge and physical constraints in calibrating RANS model discrepancies were demonstrated and discussed.

2. A random matrix theoretic framework was proposed for estimating model-form uncertainties in RANS simulations. Maximum entropy principle was employed to identify the probability distribution that satisfies given constraints but without introducing artificial information. Objective prior perturbations of RANS-predicted Reynolds stresses in the physical projections were provided based on comparisons between the physics-based and random matrix theoretic perturbation approaches.

3. A physics-informed, machine learning framework towards predictive RANS turbulence modeling was proposed. The functional forms of model discrepancies with respect to mean flow features were extracted from the off-line database of closely related flows based on machine learning algorithms. The RANS-modeled Reynolds stresses of prediction flows can be significantly improved by the trained discrepancy function, which is an important step towards predictive turbulence modeling.

1.3 Outline

This dissertation is formated in the "manuscript" format ("multi-paper" format), in which each of the main chapters is in the format of a peer-reviewed journal.

The first chapter introduces the concept of model-form uncertainties in RANS simulations and the significance of estimating and reducing them for mission-critical engineering applications. A literature review of previous studies on RANS model-form uncertainty estimation and reduction is given to discuss the current state and standing issues in this area. The contents of this dissertation are summarized as follows. First, a physics-based, Bayesian framework of estimating and reducing model-form uncertainties in RANS simulations is proposed in Chapter 2, where the uncertainties are injected to the physical projections of RANS-modeled Reynolds stresses. Moreover, physical prior knowledge and sparse on-line velocity data are assimilated by using an iterative ensemble Kalman method to reduce these uncertainties. In Chapter 3, the merits of incorporating various types of prior knowledge are discussed, which suggests that the informative physical prior plays an important role in improving the performance of reducing RANS model uncertainties, and the proposed physics-based, the Bayesian framework is an effective way to encode empirical knowledge from various sources of turbulence modeling. However, challenges associated with this physic-based approach are to assess the amount of artificial information introduced into the estimated prior uncertainties and to avoid imposing unwarranted constraints. Therefore, in Chapter 4, a random matrix approach is proposed for estimating the model-form uncertainties in RANS simulations by using the maximum entropy principle to identify the probability distribution that satisfies the known constraints but without introducing artificial information. Chapter 5 compares and discusses the advantages and disadvantages of the physics-based and random matrix theoretic approaches for RANS model-form uncertainty estimation. In addition, the specification of priors in the physics-based approach is assessed and improved based on the comparison. In the proposed framework, the on-line data (i.e., data of the flow to be predicted) are required to reduce the uncertainties by a Bayesian calibration. However, for engineering design, the on-line measurement data are usually not available. Instead, off-line databases of the closely related flows (e.g., flows at different Reynolds numbers or with slightly changed geometries) can be accessed. The Reynolds stress calibration approach is extended the to scenarios where no on-line data are available by using the mean flow features as the input instead of referring to the spatial coordinates. Moreover, machine learning techniques are employed to learn the function form of discrepancy in the RANS-predicted Reynolds stress from the off-line flow data sets. Finally, the last chapter concludes the dissertation by highlighting the key findings of this work and further perspectives for future work.

1.4 Contribution to Co-Authored Papers

Five of the journal papers were prepared in collaboration with co-authors. The contributions by the author of this dissertation are listed below.

1. Chapter 2.
    - Took part in planning the paper
    - Took part in developing the theory
    - Made the numerical implementations
    - Took part in numerical simulations
    - Took part in writing the paper
2. Chapter 3.
    - Took major part in planning the paper
    - Made the numerical implementations
    - Carried out the numerical simulations
    - Wrote major part of the paper
3. Chapter 4.
    - Took part in planning the paper
    - Took part in developing the theory
    - Made the numerical implementations
    - Carried out the numerical simulations
    - Took part in writing the paper
4. Chapter 5.
    - Took major part in planning the paper
    - Made the numerical implementations
    - Carried out the numerical simulations
    - Wrote major part of the paper
5. Chapter 6.
    - Took major part in planning the paper
    - Took part in developing the theory
    - Made the numerical implementations
    - Carried out the numerical simulations
    - Wrote major part of the paper

Bibliography

[1] T. Craft, B. Launder, K. Suga, Development and application of a cubic eddy-viscosity model of turbulence, International Journal of Heat and Fluid Flow 17 (2) (1996) 108–115.

[2] S. B. Pope, Turbulent flows, Cambridge university press, 2000.

[3] T. Oliver, R. Moser, Uncertainty quantification for RANS turbulence model predictions, in: APS Division of Fluid Dynamics Meeting Abstracts, 2009.

[4] M. C. Kennedy, A. O'Hagan, Bayesian calibration of computer models, Journal of the Royal Statistical Society: Series B (Statistical Methodology) 63 (3) (2001) 425–464.

[5] D. Higdon, M. Kennedy, J. C. Cavendish, J. A. Cafeo, R. D. Ryne, Combining field data and computer simulations for calibration and prediction, SIAM Journal on Scientific Computing 26 (2) (2004) 448–466.

[6] D. Huang, T. Allen, W. Notz, R. Miller, Sequential kriging optimization using multiple-fidelity evaluations, Structural and Multidisciplinary Optimization 32 (5) (2006) 369–382.

[7] S. Conti, J. P. Gosling, J. E. Oakley, A. O'Hagan, Gaussian process emulation of dynamic computer codes, Biometrika 96 (3) (2009) 663–676.

[8] P. Platteeuw, G. Loeven, H. Bijl, Uncertainty quantification applied to the $k-\varepsilon$ model of turbulence using the probabilistic collocation method, in: AHS Adaptive Structures Conference; 10th AIAA Non-Deterministic Approaches Conference; 9th AIAA Gossamer Spacecraft Forum and the 4th AIAA Multidisciplinary Design Optimization Specialist Conference, American Institute of Aeronautics and Astronautics, 2008.

[9] M. C. Dunn, B. Shotorban, A. Frendi, Uncertainty quantification of turbulence model coefficients via Latin Hypercube Sampling method, Journal of Fluids Engineering 133 (4) (2011) 041402.

[10] L. Margheri, M. Meldi, M. Salvetti, P. Sagaut, Epistemic uncertainties in rans model free coefficients, Computers & Fluids 102 (2014) 315–335.

[11] J. Ray, S. Lefantzi, S. Arunajatesan, L. Dechant, Bayesian parameter estimation of a k-ε model for accurate jet-in-crossflow simulations, AIAA Journal (2016) 1–17.

[12] W. Edeling, P. Cinnella, R. P. Dwight, H. Bijl, Bayesian estimates of parameter variability in the k–ε turbulence model, Journal of Computational Physics 258 (2014) 73–94.

[13] S. H. Cheung, T. A. Oliver, E. E. Prudencio, S. Prudhomme, R. D. Moser, Bayesian uncertainty analysis with applications to turbulence modeling, Reliability Engineering & System Safety 96 (9) (2011) 1137–1149.

[14] T. A. Oliver, R. D. Moser, Bayesian uncertainty quantification applied to RANS turbulence models, in: Journal of Physics: Conference Series, Vol. 318, IOP Publishing, 2011, p. 042032.

[15] W. Edeling, P. Cinnella, R. P. Dwight, Predictive RANS simulations via Bayesian model-scenario averaging, Journal of Computational Physics 275 (2014) 65–91.

[16] J. Brynjarsdóttir, A. OHagan, Learning about physical parameters: The importance of model discrepancy, Inverse Problems 30 (11) (2014) 114007.

[17] M. Emory, J. Larsson, G. Iaccarino, Modeling of structural uncertainties in Reynolds-averaged Navier-Stokes closures, Physics of Fluids 25 (11) (2013) 110822.

[18] C. Gorlé, G. Iaccarino, A framework for epistemic uncertainty quantification of turbulent scalar flux models for Reynolds-averaged Navier-Stokes simulations, Physics of Fluids 25 (5) (2013) 055105.

[19] J. L. Lumley, G. R. Newman, The return to isotropy of homogeneous turbulence, Journal of Fluid Mechanics 82 (01) (1977) 161–178.

[20] S. Banerjee, R. Krahl, F. Durst, C. Zenger, Presentation of anisotropy properties of turbulence, invariants versus eigenvalue approaches, Journal of Turbulence 8 (32) (2007) 1–27.

[21] C. Gorlé, J. Larsson, M. Emory, G. Iaccarino, The deviation from parallel shear flow as an indicator of linear eddy-viscosity model inaccuracy, Physics of Fluids 26 (5) (2014) 051702.

[22] C. Gorlé, C. Garcia-Sanchez, G. Iaccarino, Quantifying inflow and rans turbulence model form uncertainties for wind engineering flows, Journal of Wind Engineering and Industrial Aerodynamics 144 (2015) 202–212.

[23] M. Emory, G. Iaccarino, G. M. Laskowski, Uncertainty quantification in turbomachinery simulations, in: ASME Turbo Expo 2016: Turbomachinery Technical Conference and Exposition, American Society of Mechanical Engineers, 2016, pp. V02CT39A028–V02CT39A028.

[24] A. A. Mishra, G. Iaccarino, K. Duraisamy, Sensitivity of flow evolution on turbulence structure, Physical Review Fluids 1 (5) (2016) 052402.

[25] A. A. Mishra, G. Iaccarino, Rans predictions for high-speed flows using enveloping models, Tech. rep., Annual Research Briefs, Center of Turbulence Research, Stanford University, Stanford, CA, USA (2016).

[26] H. Xiao, J.-L. Wu, J.-X. Wang, R. Sun, C. Roy, Quantifying and reducing model-form uncertainties in Reynolds-averaged Navier–Stokes simulations: A data-driven, physics-informed bayesian approach, Journal of Computational Physics 324 (2016) 115–136.

[27] J.-X. Wang, R. Sun, H. Xiao, Quantification of uncertainties in turbulence modeling: A comparison of physics-based and random matrix theoretic approaches, International Journal of Heat and Fluid Flow 62 (B) (2016) 577–592.

[28] J.-X. Wang, J.-L. Wu, H. Xiao, Incorporating prior knowledge for quantifying and reducing model-form uncertainty in RANS simulations, International Journal of Uncertianty Quantification 6 (2) (2016) 109–126.

[29] J. Wu, J.-X. Wang, H. Xiao, Model-form uncertainty quantification in RANS simulation of wing-body junction flow, submitted to Flow, Turbulence and Combustion. Available at https://arxiv.org/abs/1605.05962 (2016).

[30] H. Xiao, J.-X. Wang, R. G. Gahnem, A random matrix approach for quantifying model-form uncertainties in turbulence modelin, Computer Methods in Applied Mechanics and Engineering 313 (2017) 941–965.

[31] E. Dow, Q. Wang, Quantification of structural uncertainties in the k–ω turbulence model, in: 52nd AIAA/ASME/ASCE/AHS/ASC Structures, Structural Dynamics and Materials Conference, AIAA, Denver, Colorado, 2011, pp. 2011–1762.

[32] J.-L. Wu, J.-X. Wang, H. Xiao, A Bayesian calibration–prediction method for reducing model-form uncertainties with application in RANS simulations, Flow, Turbulence and Combustion (2015) 1–26.

[33] A. P. Singh, K. Duraisamy, Using field inversion to quantify functional errors in turbulence closures, Physics of Fluids 28 (2016) 045110.

[34] E. J. Parish, K. Duraisamy, A paradigm for data-driven predictive modeling using field inversion and machine learning, Journal of Computational Physics 305 (2016) 758–774.

[35] A. P. Singh, S. Medida, K. Duraisamy, Machine learning-augmented predictive modeling of turbulent separated flows over airfoils, submitted. Available at arXiv preprint arXiv:1608.03990 (2016).

[36] J. Ling, R. Jones, J. Templeton, Machine learning strategies for systems with invariance properties, Journal of Computational Physics 318 (2016) 22–35.

[37] J. Ling, J. Templeton, Evaluation of machine learning algorithms for prediction of regions of high Reynolds averaged Navier Stokes uncertainty, Physics of Fluids (1994-present) 27 (8) (2015) 085103.

[38] J. Ling, A. Ruiz, G. Lacaze, J. C. Oefelein, Uncertainty analysis and data-driven model advances for a jet-in-crossflow, Journal of Turbomachinery.

[39] J. Ling, A. Kurzawski, J. Templeton, Reynolds averaged turbulence modelling using deep neural networks with embedded invariance, Journal of Fluid Mechanics 807 (2016) 155–166.

[40] J.-X. Wang, J. Wu, H. Xiao, Using data to improve Reynolds stresses in RANS simulations: A physics-informed machine learning approach, submitted to Physical Review Fluids. Available at https://128.84.21.199/abs/1606.07987 (2016).

[41] J. X. Wang, J. L. Wu, J. Ling, G. Iaccarino, H. Xiao, Towards a complete framework of physics-informed machine learning for predictive turbulence modeling, Tech. rep., Proceedings of Summer Research Program, Center of Turbulence Research, Stanford University, Stanford, CA, USA (2016).

Chapter 2

Quantifying and Reducing Model-Form Uncertainties in Reynolds-Averaged Navier–Stokes Simulations: A Data-Driven, Physics-Informed Bayesian Approach

(Published on *Journal of Computational Physics*, 324, 115-136, 2016.)

H. Xiao, J.-L. Wu, J.-X. Wang, R. Sun, C. J. Roy
Department of Aerospace and Ocean Engineering, Virgina Tech, Blacksburg, VA, 24061, USA

Abstract

Despite their well-known limitations, Reynolds-Averaged Navier-Stokes (RANS) models are still the workhorse tools for turbulent flow simulations in today's engineering analysis, design and optimization. While the predictive capability of RANS models depends on many factors, for many practical flows the turbulence models are by far the largest source of uncertainty. As RANS models are used in the design and safety evaluation of many mission-critical systems such as airplanes and nuclear power plants, quantifying their model-form uncertainties has significant implications in enabling risk-informed decision-making. In this work we develop an data-driven, physics-informed Bayesian framework for quantifying model-form uncertainties in RANS simulations. Uncertainties are introduced directly to the Reynolds stresses and are represented with compact parameterization accounting for empirical prior knowledge and physical constraints (e.g., realizability, smoothness, and symmetry). An iterative ensemble Kalman method is used to assimilate the prior knowledge and observation data

in a Bayesian framework, and to propagate them to posterior distributions of velocities and other Quantities of Interest (QoIs). We use two representative cases, the flow over periodic hills and the flow in a square duct, to evaluate the performance of the proposed framework. Both cases are challenging for standard RANS turbulence models. Simulation results suggest that, even with very sparse observations, the obtained posterior mean velocities and other QoIs have significantly better agreement with the benchmark data compared to the baseline results. At most locations the posterior distribution adequately captures the true model error within the developed model form uncertainty bounds. The framework is a major improvement over existing black-box, physics-neutral methods for model-form uncertainty quantification, where prior knowledge and details of the models are not exploited. This approach has potential implications in many fields in which the governing equations are well understood but the model uncertainty comes from unresolved physical processes.

2.1 Introduction

2.1.1 Model-Form Uncertainties in RANS-Based Turbulence Modeling

In Computational Fluid Dynamics (CFD), the Reynolds-Averaged Navier-Stokes (RANS) solvers are still the workhorse tool for turbulent flow simulations in today's engineering analysis, design and optimization, despite their well-known limitations, e.g., poor performance in flows with separation, mean pressure gradient, and mean flow curvature [1]. This is due to the fact that high-fidelity models such as Large Eddy Simulation (LES) and Direct Numerical Simulation (DNS) are still prohibitively expensive for engineering systems of practical interests. Moreover, in engineering design and optimization, many simulations must be performed with short turn-around times, which precludes the use of these high fidelity models.

The RANS equations employ a time- or ensemble-averaging process to eliminate temporal dependency for stationary turbulence. The averaging leads to an unclosed correlation tensor, the Reynolds stress, which needs to be modeled [1, 2]. Turbulence modeling is a primary source of uncertainty in the CFD simulations of turbulent flows. Hundreds of RANS turbulence models have been proposed so far. Each has better performance in certain cases yet none is convincingly superior to others in general. This is due to the fact that the empirical closure models cannot accurately model the regime-dependent, physics-rich phenomena of turbulent flows. Predictions obtained with any of these models have uncertainties that are difficult to quantify. The model-form uncertainties in RANS simulations originating from the turbulence models are the main focus of this work.

2.1.2 Model-Form Uncertainty Quantification: Existing Approaches

A traditional approach for estimating RANS modeling uncertainties involves repeating the simulations by perturbing the coefficients used in the turbulence models, or by using several different turbulence models [3] (e.g., k–ε, k–ω, and eddy-viscosity transport models [1]) and observe the sensitivity of the Quantities of Interests (QoIs). However, different models are often based on similar approximations, and they are likely to share similar biases [4]. Consequently, this *ad hoc* model ensemble approach tends to underestimate of the uncertainty in the model. In turbulence modeling, the Boussinesq assumption states that the Reynolds stress tensor is aligned with and proportional to the local traceless mean strain rate tensor. This assumption is shared by all linear eddy-viscosity models that are commonly used in engineering practice, including the k–ε, k–ω, and eddy-viscosity transport models.

In their seminal work, Kennedy and O'Hagan [5] developed a Bayesian calibration approach that includes a model discrepancy term to account for Model-Form Uncertainty (MFU). In this approach the MFU is quantified by parameterizing the difference between the *outputs* of the computational model and experimental observations as a stationary Gaussian process whose hyperparameters can be inferred from data [5]. This framework has been used in many applications, and a number of sophisticated variants have been developed, e.g., by introducing non-stationary Gaussian processes to model the discrepancy [6], using multiplicative discrepancy term [7], or using high-fidelity models and field measurements to provide observation data [8, 9, 7]. While this approach has had some success, the physics-neutral approach treats the entire numerical model as a black box and does not exploit the prior information that often exists about the nature of the MFU in a given model. Moreover, this framework addresses MFU only in terms of the QoIs, whereas the modeling errors in RANS simulation arise specifically from the modeled Reynolds stress term. Recent work of Brynjarsdottir and O'Hagan [10] emphasized the importance of incorporating prior information, but they also highlighted the difficulties of enforcing prior information in this black-box framework. Even a simple constraint such as zero-gradient boundary condition on the discrepancy is challenging to enforce as shown in [10]. Realistic prior knowledge in engineering practice is generally even more complicated.

Recently, several prominent groups in the CFD community (e.g., Moser and co-workers [11, 12, 13], Iaccarino and co-workers [14, 15, 16, 17, 18], and Dow and Wang [19]) have recognized the limitations of the black-box approach and attempted to open the box by injecting the uncertainties locally into the closure models (i.e., not on the model output directly). Research from these groups is reviewed in detailed below. These approaches have some similarities to earlier work of Berliner et al. [20, 21] in the context of geophysical fluid dynamics, where uncertainties were introduced to the discretized coefficients of the governing geostrophic equations.

Moser and co-workers [11, 12, 13] are the first to explicitly point out and utilize the "composite nature" of the RANS equations. That is, the equations are based on reliable theories describing conservation of mass, momentum, and energy, but contain approximate embedded

models to account for the unresolved or unknown physics, i.e., the Reynolds stress terms. Based on this insight, they introduced a Reynolds stress discrepancy tensor $\boldsymbol{\epsilon}$, which is added to the modeled Reynolds stress ($\tilde{\boldsymbol{\tau}}^{rans}$) in the RANS equations to account for the uncertainty due to the modeling of $\tilde{\boldsymbol{\tau}}^{rans}$. Stochastic differential equations forced by Wiener processes are formulated for the discrepancy $\boldsymbol{\epsilon}$. These equations are structurally similar to but simpler than the Reynolds stress transport equations commonly used in turbulence modeling [e.g., 22, 1]. Applications to plane channel flows (where only the plane shear component of the Reynolds stress tensor is important) at various Reynolds numbers have shown promising results, while extensions to general three-dimensional flows are underway (Moser and Oliver, personal communication).

Iaccarino and co-workers [14, 15, 16, 17, 18] proposed a framework to estimate the model-form uncertainty in RANS modeling by perturbing the Reynolds stress projections towards their limiting states within the physically realizable range. Empirical indicator functions are used to ensure the spatial smoothness (i.e., spatial correlation) of the perturbations in the physical domain, and to inject uncertainties only to the regions where the baseline turbulence model is believed to perform poorly. The novelty of their framework is that both physical realizability and spatial correlations are accounted for, which are two pieces of critical prior information in turbulence modeling. Another advantage of their framework is the moderate computational overhead, since only a few limiting states of the Reynolds stresses are computed. On the other hand, it should be noted that the obtained scattering of the states can only serve as an empirical estimation of the uncertainties, and are not guaranteed to cover the truth. While the true Reynolds stress is a convex linear combination of the Reynolds stresses in the limiting states, the true velocities or other QoIs are not necessarily linear combinations of their respective limiting states.

Dow and Wang [19] quantified model-form uncertainties in the k–ω model by finding the eddy viscosity field that minimizes the misfit in the computed velocity field compared to the DNS data. While their approach has some similarities with that of Iaccarino et al., the most notable difference is that uncertainties are injected to the eddy viscosity and not to the Reynolds stresses directly. Another key difference is that they used DNS data, while Iaccarino et al. did not and instead focused only on forward propagation of uncertainties in the Reynolds stress.

Duraisamy et al. [23, 24, 25], on the other hand, introduced uncertainties as full-field multiplicative discrepancy term β in the production term of the transport equations of turbulent quantities (e.g., $\tilde{\nu}_t$ in the SA model and ω in the k–ω models). Full-field DNS data or sparse data from experimental measurements were used to calibrate and infer uncertainties in this term. It is expected that the inferred discrepancy field can provide valuable insights to the development of turbulence models. They also suggested the possibility of extrapolating the learned discrepancy fields to similar flows via machine learning techniques.

In summary, the CFD community has recognized the advantages of open-box approaches for quantifying model-form uncertainties in RANS simulations, and promising results have been

obtained. However, much work is still needed.

2.1.3 Objective and Novelty of the Present Work

In this work, we focus on a scenario where a limited amount of data (usually from measurements at a few locations) is available. This is often the case when CFD is used in practical applications in conjunction with experimental data to provide predictions. Examples include prediction of flows in a wind farm and atmospheric pollutant dispersion in a city [14]. Built on existing insights and experiences in the literature, the objective of this work is to develop a rigorous, open-box, physics-informed framework for quantifying model-form uncertainties in RANS simulations. Compared to the pioneering framework of Iaccarino et al. [14, 15, 16, 17, 18] where the model-form uncertainty in RANS simulations was estimated by perturbing the Reynolds stresses towards their three limiting states, the novelty of our approach is that an ensemble-based Bayesian inference method is used to incorporate all sources of available information, including empirical prior knowledge, physical constraints (e.g., realizability, smoothness, and symmetric), and available observation data.

This work aims to quantify and reduce the model form uncertainty by utilizing both state-of-the-art statistical inference techniques and domain knowledge in turbulence modeling. As a first step, we focus on an idealized scenario where model-form uncertainty is the dominant source of uncertainty, and the coupling with other uncertainties, e.g., model input uncertainty and numerical uncertainty, is not considered.

The proposed framework has been evaluated on two canonical flows, the flow over periodic hills and the flow in a square duct, in the present work. Further application to a more complicated, three dimensional flow of critical relevance to aerospace engineering, i.e., the flow over a wing–body junction, has also been explored and presented in a separate work [26]. While the authors believe that the present contribution is novel and represents an advancement over the state of the art, we expect significant challenges that need to be addressed before the proposed approach can be extended to industrial flows, e.g., the flows past an aircraft or in a gas turbine.

The rest of the paper is organized as follows. The model-form uncertainty quantification framework is introduced in Section 2, and numerical implementation details are given in Section 3. Numerical results for two application cases, the flow over periodic hills and the flow in a square duct, are presented in Section 4 to assess the merits and limitations of the developed framework. The success, limitations, practical significance, and possible extensions of the proposed method are further discussed in Section 5. Finally, Section 6 concludes the paper.

2.2 Proposed Framework

2.2.1 Prior Knowledge in RANS Modeling

An important feature of the proposed framework is the explicit, straightforward representation of prior knowledge in a Bayesian inference framework. As such, we summarize the prior knowledge in RANS-based turbulent flow simulations below, some of which has been reviewed in Section 6.1:

1. *Composite model:* The uncertainties in the modeled Reynolds stresses are the main source uncertainties in the RANS model predictions [11].
2. *Physical realizability:* The true Reynolds stress at any point in the domain resides in a subspace of a six-dimensional space [27, 17].
3. *Spatial smoothness:* The Reynolds stress field usually has smooth spatial distributions except across certain discontinuous features (e.g., shocks and abrupt changes of geometry).
4. *Problem-specific prior knowledge:* There are some well-known scenarios where eddy viscosity models are expected to perform poorly as enumerated above, e.g., flow separation, mean flow curvature. Taking the flow over periodic hills as shown in Fig. 5.2 for example, the flood contour indicates typical prior knowledge of the relative magnitude of the Reynolds stress discrepancies in each region, i.e., the regions with recirculation, non-parallel free-shear flow, and the strong mean flow curvature have larger discrepancies.

2.2.2 Representations of Prior Knowledge in the Modeling Framework

In light of the prior knowledge presented above and based on the existing methods in the literature [11, 17, 19], we make the following modeling choices to represent the prior knowledge.

Composite Model

The true Reynolds stress $\boldsymbol{\tau}$ is modeled as a random field of symmetric tensors with $\tilde{\boldsymbol{\tau}}^{rans}$ as its deterministic mean field, where $\tilde{\boldsymbol{\tau}}^{rans}$ is the Reynolds stress field given in the baseline RANS simulation whose model-form uncertainty is to be quantified.[1]

[1] We use $\tilde{}$ to emphasize the fact that $\tilde{\boldsymbol{\tau}}^{rans}$ is a deterministic field, which is in contrast to the random field $\boldsymbol{\tau}$.

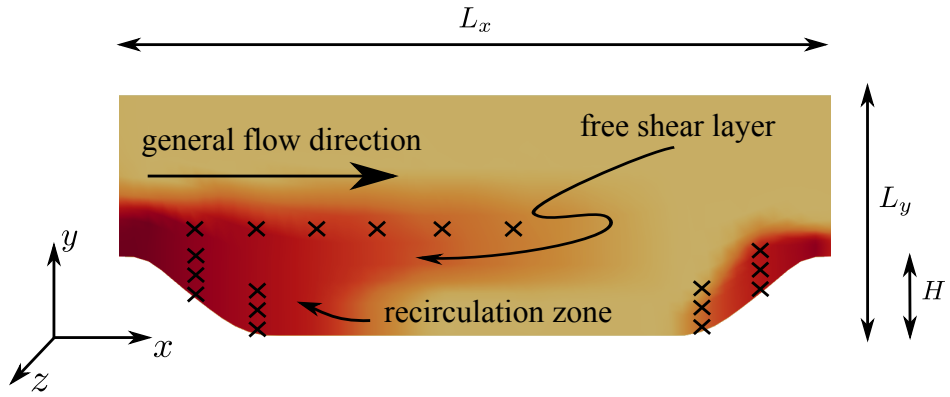

Figure 2.1: Domain shape for the flow over periodic hills. The x-, y- and z-coordinates are aligned with streamwise, wall-normal and spanwise directions, respectively. All dimensions are normalized with H with $L_x/H = 9$, $L_y/H = 3.036$. The contour shows the variance field $\sigma(x)$, where darker color represents the larger variance. The locations where velocities are observed are indicated as crosses ($\times$).

Physical Realizability of Reynolds Stresses

To ensure physical realizability of its realizations, the value of the Reynolds stress field $\boldsymbol{\tau}$ at any given location x is projected onto a space with six physically meaningful dimensions via the following eigen-decomposition [17, 14]:

$$\boldsymbol{\tau} = 2k\left(\frac{1}{3}\mathbf{I} + \mathbf{a}\right) = 2k\left(\frac{1}{3}\mathbf{I} + \mathbf{V}\Lambda\mathbf{V}^T\right) \tag{2.1}$$

where k is the turbulent kinetic energy, $\mathbf{I}$ is the second order unit tensor, $\mathbf{a}$ is the anisotropy tensor, $\mathbf{V} = [\mathbf{v}_1, \mathbf{v}_2, \mathbf{v}_3]$, and $\Lambda = \mathrm{diag}[\lambda_1, \lambda_2, \lambda_3]$ are its orthonormal eigenvectors and eigenvalues, respectively, with $\lambda_1 + \lambda_2 + \lambda_3 = 0$. This decomposition transforms the Reynolds stress to a space represented by six variables with clear physical interpretations: magnitude (represented by the turbulent kinetic energy k, which must be non-negative), shape (represented by two scalars λ_1, λ_2), and orientation (represented by three mutually orthonormal vectors[2] $\mathbf{v}_1$, $\mathbf{v}_2$, and $\mathbf{v}_3$) of the Reynolds stress tensor [28, 14]. Further, λ_1, λ_2, and λ_3 are transformed to the Barycentric coordinates (C_1, C_2, C_3), with $C_1 + C_2 + C_3 = 1$, and subsequently to the natural coordinates (ξ, η). With the mapping from Barycentric coordinates to natural coordinates (see Fig. 6.1), the physically realizable turbulent stresses enclosed in the Barycentric triangle (panel a) are transformed to a square (panel b), i.e., $\{(\xi, \eta) \,|\, \xi \in [-1, 1], \eta \in [-1, 1]\}$, which is more convenient for parameterization. Details of the mapping are presented in 2.A. In summary, we transform the Reynolds stress tensor to six physical dimensions denoted as $(k, \xi, \eta, \mathbf{v}_1, \mathbf{v}_2, \mathbf{v}_3)$. All mappings involved are linear and invertible except for a trivial singular point in $(C_1, C_2, C_3) \mapsto (\xi, \eta)$.

[2]They can be considered as the three orthogonal axes of an ellipsoid, and thus the three vectors have three degrees of freedom in total, i.e., its orientation in three-dimensional space.

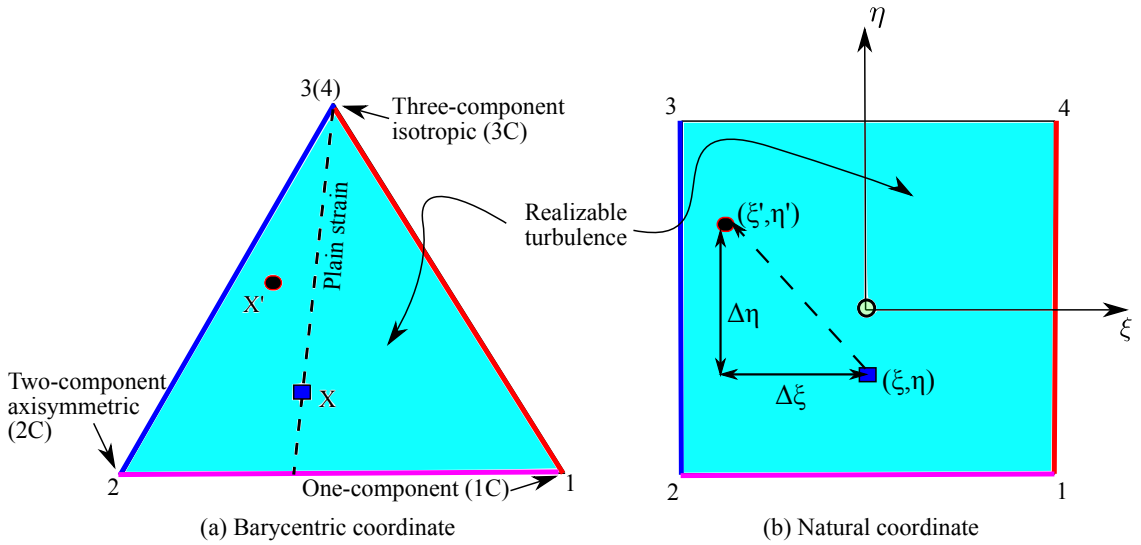

(a) Barycentric coordinate (b) Natural coordinate

Figure 2.2: Mapping between Barycentric coordinates and natural coordinates, transforming the Barycentric triangle that encloses all physically realizable states [28, 16] to a square via standard finite element shape functions (detailed in 2.A). Corresponding edges in the two coordinates are indicated with matching colors. The singular point 3(4) in the Barycentric coordinate, which maps to the edge 3–4 in the natural coordinate, does not pose any practical difficulties.

After the mapping of Reynolds stress $\tilde{\boldsymbol{\tau}}^{rans}$ to the physically meaningful dimensions, i.e., k, ξ, η, uncertainties are injected to the projected space on these variables. This is achieved by modeling the corresponding truths $k(x)$, $\xi(x)$, and $\eta(x)$ as random fields with $\tilde{k}^{rans}(x)$, $\tilde{\xi}^{rans}(x)$, and $\tilde{\eta}^{rans}(x)$ as priors. Specifically,

$$\log k(x) = \log \tilde{k}^{rans}(x) + \delta^k(x) \tag{2.2a}$$

$$\xi(x) = \tilde{\xi}^{rans}(x) + \delta^\xi(x) \tag{2.2b}$$

$$\eta(x) = \tilde{\eta}^{rans}(x) + \delta^\eta(x) \tag{2.2c}$$

where the spatial coordinate x is the index of the random fields. Note that the logarithmic discrepancy of the turbulent kinetic energy k is modeled in Eq. (6.5d) to ensure the non-negativity of k.

The realizability in this framework is ensured by bounding the perturbed anisotropy (η, ξ) within the square $[-1, 1] \times [-1, 1]$ in the ξ–η plane as shown in Fig. 2b. Any perturbed state outside this range will be bounded to the edge of the square, which is admittedly an ad hoc modeling choice. As a result, the prior may become non-Gaussian and the perturbation sample may deviate from zero-mean if a large number of perturbations are bounded. However, note that for a Gaussian prior the percentage of out-of-bound points can be estimated, and thus the variance of the perturbation can be controlled straightforwardly given an allowable ratio of out-of-bound points. This is one of the advantages of mapping the Barycentric tri-

angle to the square before introducing perturbation as opposed to directly perturbing the baseline within the Barycentric triangle.

The bounding scheme for ensuring realizability can distort the distribution of the sampled Reynolds stresses from the specified prior. Specifically, when the baseline Reynolds stresses are located near the realizability boundaries, e.g., the top vertex of the Barycentric triangle for points near walls, the bounding can cause the sample distribution to become truncated Gaussian. However, note that the tail truncation and the associated probability mass concentration near the boundaries are caused by the bounding procedure to ensure realizability, regardless of whether Barycentric coordinates or natural coordinates are used. This issue is further investigated in two follow-on studies [29, 30], where we proposed a random matrix approach which directly samples a maximum entropy distribution defined on the set of positive semidefinite matrices, and the artificial probability mass concentration described above is avoided. However, note that the approximate Bayesian inference method (i.e., the ensemble Kalman method) used in this work is not sensitive to the prior. From a practical point of view, the prior can be alternatively interpreted as an "initial guess" used in optimization [e.g., 24].

Perturbing the orientations of the modeled Reynolds stress tensor can potentially cause instability in the RANS momentum equation. Consistent with the work of Iaccarino et al., we focus on the magnitude (k) and the shape (λ_1 and λ_2, or equivalently the natural coordinates ξ and η) of the Reynolds stress tensor $\boldsymbol{\tau}$, and do not introduce uncertainties into the orientations $(\mathbf{v}_1, \mathbf{v}_2, \mathbf{v}_3)$. Consequently, the assumed uncertainty space of Reynolds stresses may not contain the truth because the true Reynolds stresses are likely to have different orientations from those of the RANS predictions. The implications of this fact will be further discussed in Section 2.4.1.

Spatial Smoothness of Reynolds Stress Distribution

To ensure spatial smoothness and to reduce the dimension of the uncertainty space, the random fields to be inferred, i.e., δ^k, δ^ξ, and δ^η, are projected to a deterministic functional basis set $\{\phi_i(x)\}$. That is,

$$\delta^k(x, \theta^k) = \sum_{i=1}^{\infty} \omega_i^k|_{\theta^k}\ \phi_i(x) \tag{2.3a}$$

$$\delta^\xi(x, \theta^\xi) = \sum_{i=1}^{\infty} \omega_i^\xi|_{\theta^\xi}\ \phi_i(x) \tag{2.3b}$$

$$\delta^\eta(x, \theta^\eta) = \sum_{i=1}^{\infty} \omega_i^\eta|_{\theta^\eta}\ \phi_i(x) \tag{2.3c}$$

where the coefficients of the i^{th} mode ω_i^k, ω_i^ξ, and ω_i^η are random variables[3] depending on the realized outcome of θ^k, θ^ξ, and θ^η, respectively, and $\phi_i(x)$ are deterministic spatial basis functions. An orthogonal basis set is chosen in this work as will be detailed below, but the orthogonality is not mandatory.

Remarks: The mapping in Section 2.2.2 involves linear transformation of the Reynolds stress at a given point to physical variables, which ensures the physical realizability of the Reynolds stresses in the prior. The orthogonal projection in Section 2.2.2 aims to represent the spatial distribution function on a basis set in a compact manner, which ensures spatial smoothness and reduces the uncertainty dimensions of $\boldsymbol{\tau}(x)$.

Representation of Problem-Specific Prior Knowledge

Finally, problem-specific knowledge is encoded in the choice of basis set $\{\phi_i\}$. Here we will use the flow over periodic hills as example to illustrate the representation of the problem-specific prior knowledge.

We model the prior of the discrepancies δ^k, δ^ξ and δ^η as zero-mean Gaussian random fields (also known as Gaussian processes) $\mathcal{GP}(0, K)$, where

$$K(x, x') = \sigma(x)\sigma(x') \exp\left(-\frac{|x - x'|^2}{l^2}\right) \tag{2.4}$$

is the kernel indicating the covariance at two locations x and x'. The variance $\sigma(x)$ is a spatially varying field specified (see the flood contour in Fig. 5.2) to reflect the prior knowledge that large discrepancies in modeled Reynolds stress are expected in certain regions. The correlation length scale l can be specified based on the local turbulence length scale, but is taken as constant in this work for simplicity.

The orthogonal basis functions $\phi_i(x)$ in Eq. (5.5) take the form $\phi_i(x) = \sqrt{\hat{\lambda}_i}\hat{\phi}_i(x)$, where $\hat{\lambda}_i$ and $\hat{\phi}_i(x)$ are eigenvalues and eigenfunctions, respectively, of the kernel K in Eq. (5.4) computed from the Fredholm integral equation [31]:

$$\int K(x, x')\hat{\phi}(x')\, dx' = \hat{\lambda}\hat{\phi}(x)\,. \tag{2.5}$$

With this choice of basis set the expansions in Eq. (5.5) for the fields δ^k, δ^ξ and δ^η become Karhunen–Loeve (KL) expansions [31], such that ω_i^k, ω_i^ξ, and ω_i^η are uncorrelated random variables with zero means and unit variances.

[3]Throughout the manuscript, subscripts denote indices, and superscripts indicate explanation of the variable. For example, ω_i^k is the coefficient for the i^{th} mode in the expansion of the discrepancy field δ^k for the turbulent kinetic energy k. Tensors are denotes in bold (e.g., $\boldsymbol{\tau}$) and not with index notation.

Remarks The Gaussian process and KL expansions are intentionally presented in this Section to emphasize the fact that they are our specific choices for this problem and prior knowledge only. The optimal choice of basis set depends on the specific characteristics (e.g., smoothness, compactness of support) of the prior. Other functional basis sets, including wavelets [32] or radial basis functions [33], will be explored in future work.

2.2.3 Inverse Modeling Based on an Iterative Ensemble Kalman Method

After the transformations above, the Reynolds stress random field $\boldsymbol{\tau}(x)$ is parameterized by the coefficients ω_i^k, ω_i^ξ, and ω_i^η in Eq. (5.5), which are truncated to m modes and written in a stacked vector form as follows[4]:

$$\boldsymbol{\omega} \equiv [\omega_1^k,\, \omega_1^\xi,\, \omega_1^\eta,\, \omega_2^k,\, \omega_2^\xi,\, \omega_2^\eta,\, \cdots,\, \omega_m^k,\, \omega_m^\xi,\, \omega_m^\eta] \tag{2.6}$$

We employ an *iterative, ensemble-based* Bayesian inference method [34] to combine the prior knowledge as represented above and the available data to infer the distribution of $\boldsymbol{\omega}$. This method is closely related to ensemble filtering methods (e.g., ensemble Kalman filtering), which are a class of standard data assimilation techniques commonly used in numerical weather forecasting [35]. An overview of the ensemble Kalman method based inverse modeling procedure is presented in Fig. 2.3. In the iterative ensemble method, the state of the system $\mathbf{x}$ is defined to include both the physical variables (i.e., velocity field $\mathbf{u}$) and the unknown coefficients $\boldsymbol{\omega}$, i.e., $\mathbf{x} \equiv [\mathbf{u}, \boldsymbol{\omega}]^T$. This is called "state augmentation" [34]. One starts with an ensemble of states $\{\mathbf{x}_j\}_{j=1}^N$ drawn from their prior distributions. During each iteration, all samples in the ensemble are updated to incorporate the observations through the following procedure:

1. reconstruction of Reynolds stresses from the coefficients $\boldsymbol{\omega}$,
2. computation of velocity fields from the given Reynolds stress fields by solving the RANS equations (implemented as forward model tauFoam, detailed in Section 4.3.5), and
3. a Kalman filtering procedure to assimilate the velocity observation data to the computed states, leading to an updated ensemble.

The updating procedure is repeated until the ensemble is statistically converged. The convergence is achieved when the two-norm of the misfit between the predictions and the observations falls below the noises level of the observations [34]. The converged ensemble is

[4]It is trivial for each variable to have a different number of modes, but this possibility is omitted here to simplify notation.

considered a sample-based representation of the posterior distribution of the system state, from which the mean, variance, and higher moments can be computed. The algorithm of the inversion scheme is presented in 2.B, and further details can be found in [34].

The noises added to the observations represent a combination of measurement errors and process errors [36]. The former is likely to be negligible for DNS data. However, the latter can be significant and is used to account for the fact that the observed system and the system described in the numerical model can have different dynamics. From a Bayesian perspective, adding the process noise allows the likelihood and the prior distribution to have overlap in their supports and thus be able to reconcile with each other in the inference procedure. As long as the chosen noise level σ_{obs} is larger than a threshold (1% of truth in this work), the inferred posterior means are not sensitive to this parameter. See further discussion in [e.g., 34].

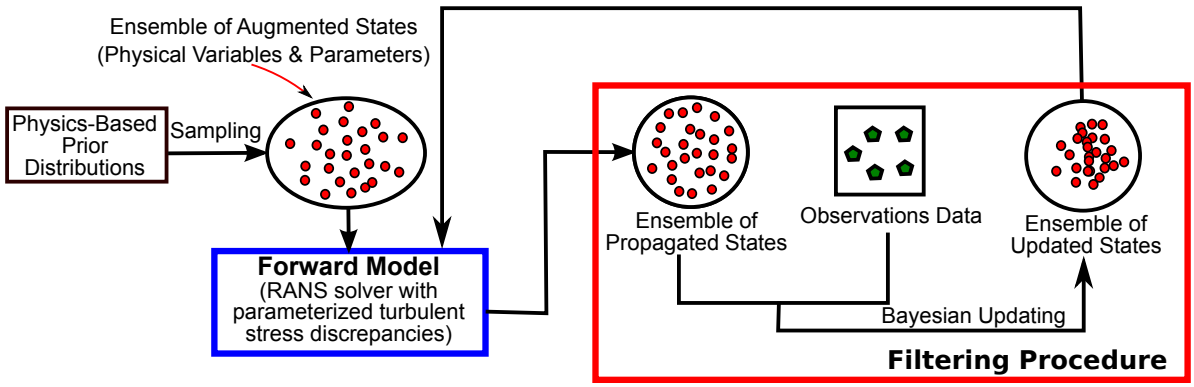

Figure 2.3: Inference of coefficients in the parameterized model discrepancies (e.g., discrepancies in RANS modeled Reynolds stresses) using an iterative ensemble Kalman inversion method. This approach combines prior knowledge of a given problem and available data to quantify and reduce model-form uncertainty.

An important property of the iterative ensemble Kalman method is that the posterior ensembles and its mean all lie in the linear space $\mathcal{A}$ spanned by the prior ensemble $\{\mathbf{x}_j\}_{j=1}^{N}$. In essence, this scheme attempts to search the space $\mathcal{A}$ to find the optimal solution that minimizes the misfit between the posterior mean and the observations, accounting for the uncertainties in both [34]. As with many inverse problems, this problem is intrinsically ill-posed. Specifically, because of the sparseness of the observation (the scenario of concern in our work), the amount of data is usually not sufficient to constrain the uncertainties in the states, which include the model discrepancies as components. The forward model essentially provides the regularization of the ill-posedness with its physical representation of the system dynamics.

The ensemble Kalman-based uncertainty quantification scheme used here is an approximate Bayesian method, and is computationally cheaper than the exact Bayesian scheme based on Markov Chain Monte Carlo sampling. It is not expected to give posterior distributions with

comparable accuracy to those obtained from exact Bayesian schemes [37]. This limitation will be further discussed in Section 4.5.

2.2.4 Summary of the Algorithm in the Proposed Framework

In summary, the overall algorithm of the proposed framework for quantifying and reducing uncertainties in a RANS simulation is presented as follows.

1. Perform the baseline RANS simulation to obtain the velocity $\tilde{\boldsymbol{u}}^{rans}(x)$ and Reynolds stress $\tilde{\boldsymbol{\tau}}^{rans}(x)$.
2. Perform the transformation $\tilde{\boldsymbol{\tau}}^{rans} \mapsto (\tilde{k}^{rans}, \tilde{\xi}^{rans}, \tilde{\eta}^{rans})$.
3. Compute KL expansion to obtain basis set $\{\phi_i(x)\}_{i=1}^m$, where m is the number of modes retained.
4. Generate initial prior ensemble of coefficient vectors $\{\boldsymbol{\omega}_j\}_{j=1}^N$, where N is the ensemble size.
5. Use iterative scheme shown in Fig. 2.3 to obtain the posterior ensemble of the state distribution. Specifically, in each iteration do the following:
   (a) Recover the discrepancy fields δ^k, δ^ξ, and δ^η from the coefficient $\{\boldsymbol{\omega}_j\}_{j=1}^N$ in the current state and the basis functions via Eq. (5.5), and obtain realizations of k, ξ, and η from Eq. (5.10) for each sample in the ensemble.
   (b) Obtain Reynolds stress ensembles $\{\boldsymbol{\tau}_j\}_{j=1}^N$ via mapping $(k, \xi, \eta) \mapsto \boldsymbol{\tau}$.
   (c) For each sample in the ensemble $\{\boldsymbol{\tau}_j\}_{j=1}^N$, solve the RANS equations for velocity field $\boldsymbol{u}_j$ with given Reynolds stress field $\boldsymbol{\tau}_j$.
   (d) Compare the ensemble mean with velocity observations, and use the Kalman filtering procedure to correct the augmented system state ensemble $\{\mathbf{x}_j\}_{j=1}^N$, where $\mathbf{x}_j = [\mathbf{u}_j, \boldsymbol{\omega}_j]^T$. The updated coefficient vector ensemble $\boldsymbol{\omega}_j$ is thus obtained as part of the system state ensemble.
   (e) Stop if statistical convergence of the ensemble as defined in Section 2.2.3 is achieved.

2.3 Implementation and Numerical Methods

The uncertainty quantification framework including the mapping of Reynolds stresses and the iterative ensemble Kalman method is implemented in Python, which interfaces with RANS models and the KL expansion procedures to form the complete framework. The package

UQTk developed by Sandia National Laboratories is used to perform the KL expansions [38]. Two types of RANS solvers are used in this framework, a conventional baseline RANS solver `simpleFoam` and a forward RANS solver `tauFoam` which computes velocity field with a given Reynolds stress field. Both solvers are described as below.

The baseline simulation uses a built-in RANS solver `simpleFoam` in OpenFOAM for incompressible, steady-state turbulent flow simulations. OpenFOAM (for "Open source Field Operation And Manipulation") is an open-source, general-purpose CFD platform based on finite-volume discretization. The platform consists of a wide range of solvers and post-processing utilities. The SIMPLE (Semi-Implicit Method for Pressure Linked Equations) algorithm [39] is used to solve the coupled momentum and pressure equations. Collocated grids are used, and the Rhie and Chow interpolation is used to prevent the pressure–velocity decoupling [40]. Second-order spatial discretization schemes are used to solve the equations on an unstructured, body-fitting mesh. Given the specification of the flow including initial conditions (to start the iteration), boundary conditions, geometry, and the choice of turbulence model, the `simpleFoam` solver computes the velocity field along with Reynolds stresses by solving the RANS equations as well as the equations for the turbulence quantities (e.g., turbulent kinetic energy k and the rate of dissipation ε for k–ε models). We choose the Launder–Sharma low Reynolds number k–ε model [41] in the baseline simulations. Accordingly, the meshes are refined wall-normal direction near the wall to resolve the boundary layer. This is to avoid the complexity of using wall-functions, which is in consistent with the work of Emory et al. [17]. As can be seen in the overall algorithm presented in Section 2.2.4, for each uncertainty quantification case the baseline simulation is performed only once.

The forward RANS model `tauFoam` is invoked repeatedly in the Bayesian inference procedure. This solver is adopted from and similar to `simpleFoam` except that it computes the velocity directly with a *given Reynolds stress field*. There is no need to specify a turbulence model and or to solve the equations for turbulence quantities, since the Reynolds stress is given. Moreover, as the forward RANS simulations are initialized with the converged baseline solutions, the number of iterations needed to achieve convergence is much smaller than that in the baseline simulation. As a result, the computational cost for each call of the forward RANS model `tauFoam` is much lower than that of the conventional RANS solver `simpleFoam`. In the simulations presented below, the forward RANS simulations need only 10% of the computational cost as that of the baseline simulation to achieve the same residual.

2.4 Numerical Simulations

Two canonical flows, the flow in a channel with periodic constrictions (periodic hills) and the fully developed turbulent flow in a square duct, are chosen to evaluate the performance of the proposed framework. The periodic hill flow features a recirculation zone formed by a forced separation, a strong mean flow curvature due to the domain geometry, and a shear layer that is not aligned with the overall flow direction. All these features are known to pose

challenges for turbulence modeling. The square duct flow is characterized by a secondary flow pattern in the plane perpendicular to the main flow. The in-plane secondary flow is driven by the imbalance in the normal components of the Reynolds stress tensor, which cannot be captured by models with isotropic eddy viscosity turbulent models including most of the widely used models such as k–ε, k–ω, and eddy viscosity transport models. The two challenging cases are chosen to demonstrate the capability of the proposed framework in quantifying and reducing uncertainties in the RANS model predictions by incorporating sparse observations.

2.4.1 Flow over Periodic Hills

Case Setup

The periodic hill flow is widely used in the CFD community to evaluate the performance of turbulence models due to the availability of experimental and numerical benchmark data [42]. The geometry of the computational domain and the coordinate system are shown in Fig. 5.2. The Reynolds number based on the crest height H and the bulk flow velocity U_b at the crest is $Re_b = 2800$. Periodic boundary conditions are applied in the streamwise (x) direction, and non-slip boundary conditions are applied at the walls. The mean flow is two-dimensional, and thus the spanwise (z) direction is not considered for the RANS simulations.

The mesh and computational parameters used in the uncertainty quantification procedure are presented in Table 3.2. Despite the coarse meshes, the walls are adequately resolved in both cases as required by the Lauder–Sharma turbulence model [41]. The distance between the center of the first cell and the wall is smaller than 1 in most regions for periodic hill case and 0.7 for the square duct case. Parameters of the meshes for both cases are shown in Table 3.2.

The uncertainties in ξ, η, k are all considered, and thus δ^ξ, δ^η and δ^k are all random fields. This choice is based on our prior knowledge that both the Reynolds stress anisotropy (indicated by the shape $\boldsymbol{\tau}$, or equivalently, ξ and η) and turbulent kinetic energy k predicted by the RANS model are biased, and both are important for the accurate prediction of the flow behavior. The length scale parameter l is chosen according to the approximate length scale of the flow, which can be obtained either from our physical understanding of the flow or, if that is not available, from the baseline RANS simulation. Velocity observations are generated by adding Gaussian random noises with standard deviation σ_{obs} to the truth from DNS data. Specifically, the observations used in each iteration are independent realizations from a Gaussian distribution whose mean is the truth and standard deviation σ_{obs} is 10% of the true mean value. The noises at different locations are uncorrelated. The observation points are arranged so that they are closer in regions where the spatial changes of the flow are more rapid (the recirculation zone leeward of the hill and the reattached flow region windward of the hill), and are further apart in the free shear region downstream of the hill

crest. This arrangement of observations is expected in actual experiments. The ensemble usually converges in approximately 10 iterations. For all cases presented in this work, 60 samples are used in the ensemble. We have performed detailed sensitivity studies on the ensemble size, and it was found that the inferred velocities and QoIs do not vary if more than 30 samples are used. This finding is consistent with earlier studies when EnKF was used in data assimilations in applications such as weather forecasting [43]. The computational cost of the proposed procedure is further discussed in Section 2.5.1.

The non-stationary Gaussian process models for δ^ξ, δ^η and δ^k share the same variance field $\sigma(x)$, which are shown as flood contour in Fig. 5.2. Design of the variance field is strictly based on physical prior knowledge as described in Section 2.2.2, and does not take the DNS data into account, since the complete field of the true Reynolds stresses are rarely known in practical applications. Specifically, the variance fields of the priors as shown in Figs. 5.2 and 6.3 are constructed by superimposing a constant background value σ_0 and a spatially varying field $\sigma_{local}(x)$, i.e., $\sigma(x) = \sigma_0 + \sigma_{local}(x)$. For the periodic hill case, the background σ_0 is set to be 0.2. To obtain the field $\sigma_{local}(x)$, we specify that $\sigma_{local} = 0.5$ at the following locations, where RANS predictions are considered less reliable: (1) the hill crest, (2) the center of the recirculation region, (3) the windward side of the hill, and (4) the free-shear layer downstream the crest. Interpolations based on radial basis functions with exponential kernels are used to obtain $\sigma_{local}(x)$ at other locations. As such, its value decays to zero far away from the locations specified above. The length scale of the basis functions is estimated based on the characteristic length of the mean flows, which is chosen as the hill height H.

The first sixteen modes obtained from the KL expansion are used to reconstruct the discrepancy field. The number of modes retained is chosen such that the reconstructed field has at least 80% of the total variance of the original random field. A rule of thumb is that a coverage ratio of 80% is adequate for a faithful representation. Increasing the number of modes increases the difficulty of the inference and may lead to deteriorated results for a given amount of observation data.

Parameter sensitivity analysis has been conducted to ensure that reasonable variations of the computational parameters above do not lead to significantly different results or conclusions. In particular, we have shown in a follow-on study [44] that even in the complete absence of prior knowledge (i.e., a constant variance field $\sigma(x)$), the inferred velocities are still significantly improved, albeit slightly less so than that with an informative prior. Specifically, in the region near the upper wall, much more uncertainties are presented in the posterior ensemble when a non-informative, constant variance field is used.

Results

The first six modes of the KL expansion are presented in Fig. 2.4 along with two typical realizations. This is to illustrate the uncertainty space of the Reynolds stress discrepancy field (or more precisely its projections δ^ξ, δ^η and δ^k) . All the modes have been shifted and

Table 2.1: Mesh and computational parameters used in the flow over periodic hills and the flow in a square duct.

cases	**periodic hill**	**square duct**
mesh ($n_x \times n_y$)	50×30	30×30
domain size ($L_x \times L_y \times L_z$)	$9H \times 3.306H \times 0.1H$	$0.4D \times 0.5D \times 0.5D$
$\Delta x \times \Delta y \times \Delta z$ in y^+	$35 \times [2, 65] \times 850$	$24 \times [1.4, 30] \times [1.4, 30]$
first grid point in y^+	~ 1, below $2y^+$ in most region	0.7
number of samples N	60	
fields with uncertainty	ξ, η, k	ξ, η
number of modes m per field	16	8
length scale[(a)]	H	0.1D
number of observation	18	25[(b)]
std. dev. observation noise (σ_{obs})	10% of truth	

(a) Normalized by hill crest height H and domain size h for the periodic hill case and square duct case, respectively.
(b) Only 13 points of velocity data are supplied effectively due to the diagonal symmetry.

normalized to the range $[0, 1]$. It can be seen that in all the models and the realizations the variations mostly concentrate in the three pre-specified regions (recirculation zone, free shear region, and the reattached flow windward of the hill), and the upper part of the channel has rather small variations. This is consistent with our physical prior knowledge specified through the variance field design.

Accurate predictions of the recirculation and the reattachment of the flow are of the most interest in the flow over periodic hills. Therefore, we identify three quantifies of interest for this case: (1) the velocity field, in particular the velocities in the recirculation zone and reattached flow region windward of the hill, (2) the distribution of shear stresses τ_w on the bottom wall, and (3) the reattachment point x_{attach}. Other quantities that are important in engineering design and analysis (e.g., friction drag, form drag, size of separation bubble) are closely related to the three QoIs above.

The prior and posterior ensembles of the velocities are presented in Fig. 2.5 with comparison to the DNS benchmark results. The geometry of the domain is also shown to facilitate visualization. From Fig. 2.5a it can be seen that the prior mean velocity profiles are very close to those from the baseline RANS simulation, with only minor differences at a few locations (e.g., near the bottom wall at $x/H = 4$, 5, and 6). This is not surprising, since the Reynolds stresses prior ensemble use the RANS modeled Reynolds stress $\tilde{\boldsymbol{\tau}}^{rans}$ as the mean. In other words, the ensemble is obtained by introducing perturbations to the $\tilde{\boldsymbol{\tau}}^{rans}$. Therefore, the similarity between the velocity profiles in the baseline simulation and those of the prior ensemble indicates that the mapping from Reynolds stress to velocity is approximately linear with respect to the perturbations introduced to the prior Reynolds stresses ensemble. Clearly,

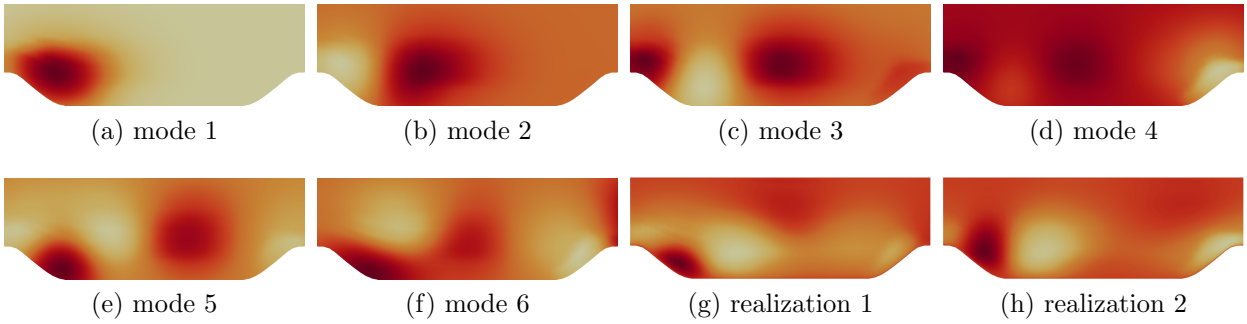

(a) mode 1 (b) mode 2 (c) mode 3 (d) mode 4

(e) mode 5 (f) mode 6 (g) realization 1 (h) realization 2

Figure 2.4: Illutstration of KL expansion modes of the periodic hill case. All the modes have been shifted and scaled into the range between 0 (lightest) and 1 (darkest) to facilitate presentation, and the legend is thus omitted. Panels (a) to (f) represent modes 1 to 6, respectively. Lower modes are more important. Panels (g) and (h) show the turbulent kinetic energy associated with two typical realizations of the Reynolds stress discrepancy fields.

both the baseline velocities and the prior mean velocities deviate significantly from the benchmark results, particularly in the recirculation region (leeward of the hill). From Fig. 2.5 it can be seen that the posterior ensemble mean of the velocities along all the lines are significantly improved compared to the baseline results.

The remaining differences between the obtained posterior mean and the benchmark data can be attributed to two sources: (1) the sparseness of the observation data, and (2) the inadequacy of the proposed inference model, specifically, the posterior mean Reynolds stress does not reside in the space $\mathcal{A}$ spanned by the prior ensemble. However, note that obtaining the correct Reynolds stresses is a sufficient but not necessary condition to infer the correct velocities. For example, if the divergence of the true Reynolds stresses resides in the space spanned by the prior ensemble, the true mean velocity can still be obtained. This is not surprising since it is the divergence of the Reynolds stress tensor field that appears as source term in the RANS momentum equation. To illustrate this point, it is particularly interesting to investigate the scenario when large amounts of data are available, since any remaining discrepancies should then be explained solely by the inadequacy of the inference processes. We performed an experiment where all the benchmark velocities along ten sampled lines at $x/H = 0, 0.5, 1, 2, \cdots, 8$ were used as observations. In this scenario the posterior mean velocities agree with the benchmark data very well, even in the regions between the sample lines, where no data are available. However, significant discrepancies still remain between the inferred posterior mean of the Reynolds stresses and the benchmark. We argue that the inability to obtain the correct Reynolds stress field is *not an intrinsic limitation* of the proposed method. Rather, it can be explained by the non-unique mapping between Reynolds stress and velocities as described by the RANS equations. That is, two distinctly different Reynolds stress fields can lead to identical or very similar velocity fields, because the divergence of the Reynolds stress appears in the RANS equation as pointed out above. The

non-unique mapping is further discussed in Section 2.5.3. However, when we assume that some sparse measurements of Reynolds stresses are available, which admittedly are difficult to obtain in practical experiments, the inferred Reynolds stresses did improve significantly. The results are omitted here for brevity.

In order to obtain the true Reynolds stresses, the posterior mean Reynolds stress must reside in the space $\mathcal{A}$ spanned by the prior ensemble, but in practical inferences there is no guarantee this will be the case. There are two reasons for this. First, uncertainties are only introduced to the magnitude (k) and shape (ξ and η) of the baseline Reynolds stresses, and not to the orientations ($\mathbf{v}_1$, $\mathbf{v}_2$, and $\mathbf{v}_3$). Second, a limited number of modes are retained in the KL expansion, which correspond to very smooth fields of Reynolds stress discrepancies. Therefore, if we think of the true Reynolds stress as residing in a high-dimensional space, in the current framework we assume that the truth is reasonably close to the baseline prediction $\tilde{\boldsymbol{\tau}}^{rans}$, and thus we only search the vicinity of $\tilde{\boldsymbol{\tau}}^{rans}$ for realizable candidates. This is justified by the confidence that the chosen baseline RANS model is rather capable, usually backed by previous experiences accumulated by the community on the model of concern.

Finally, we emphasize that if the true Reynolds stresses do reside in the space spanned by the prior ensemble, the posterior mean velocity and the Reynolds stresses would indeed coincide with the truths. This scenario could occur if the baseline Reynolds stress $\tilde{\boldsymbol{\tau}}^{rans}$ only differs from the true Reynolds stress in magnitude k and shape ξ and η, and the discrepancy is smooth enough to be represented by the chosen number of modes. However, both scenarios are rather unlikely in any nontrivial cases. For verification purposes we have designed a case of flow over periodic hills with synthetic data (as opposed to DNS data) that satisfies the requirements above, and have confirmed that the obtained posterior mean velocity indeed exactly agrees with the truth in this case, and that the true Reynolds stress can also be obtained. The results are detailed in a separate work [44].

This claim that the prior has small influence to the prior is apparently contradictory to the Bayesian inference theory, which states that the posterior is proportional to the product of the prior and the likelihood informed by the observation data. However, in the ensemble Kalman method used in this work, the observation data are imposed on the prior iteratively (albeit with different noises in each iteration). As a result, the influence of the prior on the posterior diminishes as the posterior proceeds to statistical convergence. From a practical perspective, the iterative ensemble Kalman method can also be interpreted as an optimization procedure (e.g., that used by Parish et al. [24]), with the prior corresponding to the initial guess. This interpretation, as an alternative to the Bayesian interpretation, has been advocated in the literature [34, 45].

Figure 2.6 shows the 95% credible intervals estimated from the data in the prior and posterior velocity ensembles. That is, at each point, 95% of the samples fall within the shaded region (light/pink shaded for the prior and dark/blue shaded for the posterior). Note that the credible intervals shown here are point estimations and do not contain information on the spatial correlations of the velocity profiles. It can be seen from Fig. 2.6 that the 95%

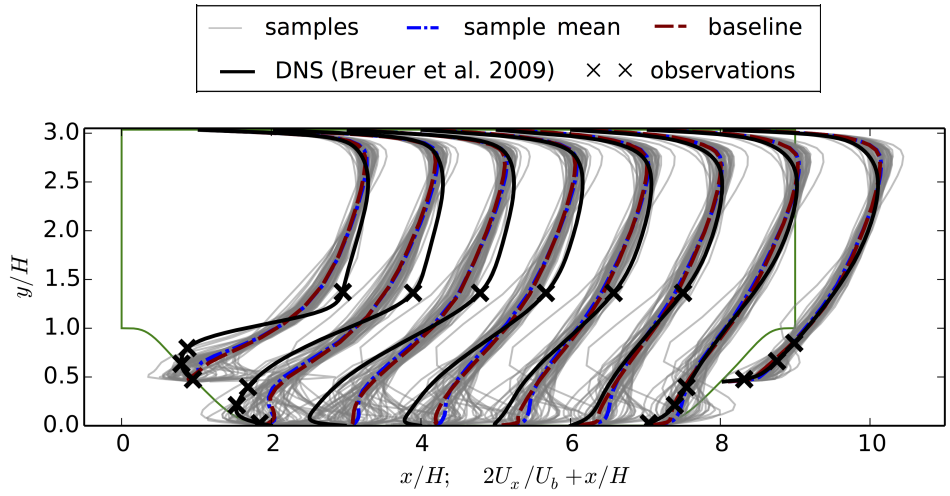

(a) Prior velocities ensemble

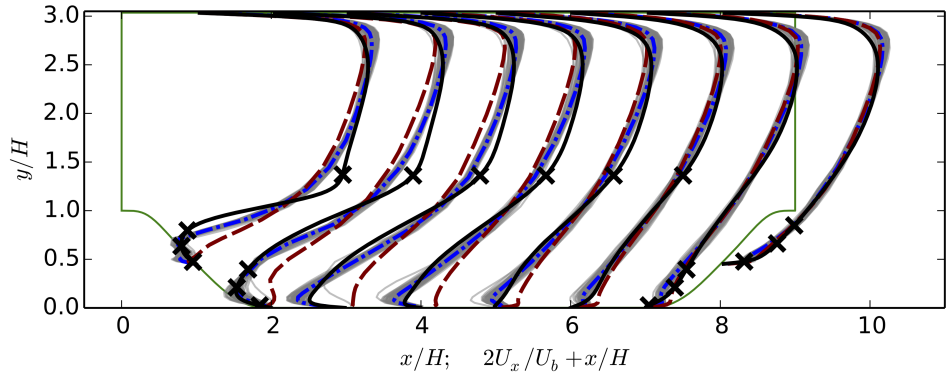

(b) Posterior velocities ensemble

Figure 2.5: The prior and posterior ensembles of velocity profile for the flow over periodic hill at eight locations $x/H = 1, \cdots, 8$ compared with benchmark data and baseline results. The locations where velocities are observed are indicated with crosses ($\times$).

credible interval in the posterior is significantly narrowed compared to that in the prior, which suggests that the model form uncertainty is reduced by incorporating the velocity observation data. Such a reduction of uncertainty is more visible in the recirculation zone, where more observation data are available. In contrast, the prior uncertainty near the upper wall largely remains, which is due to the lack of observation data in this region.

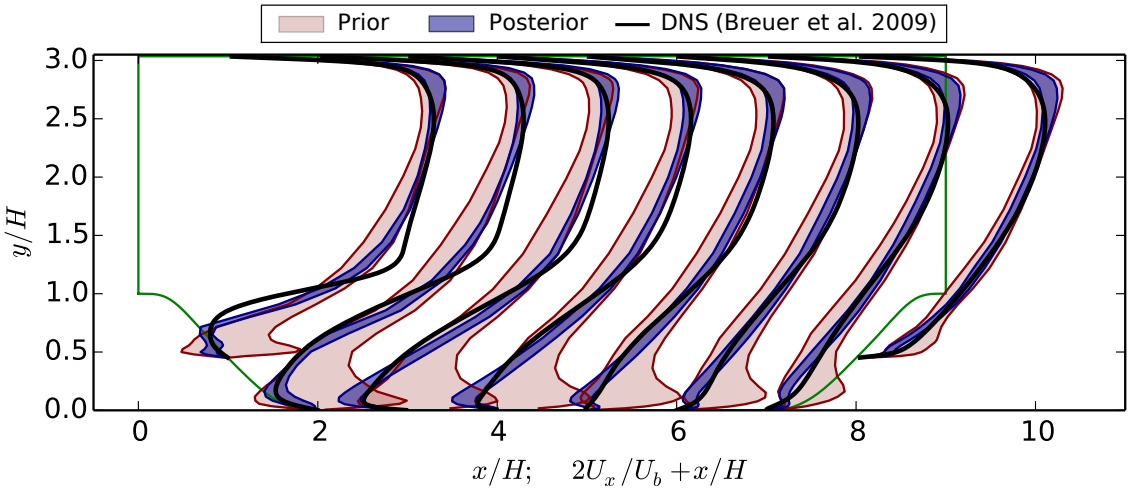

Figure 2.6: The 95% credible intervals of the prior (light/pink shaded region) and posterior (dark/blue shaded region) ensembles of velocity profiles for the flow over periodic hills.

The other two QoIs, bottom wall shear stress τ_w and the reattachment point x_{attach}, are shown in Fig. 2.7. Similar to the velocity profiles in Fig. 2.5, both prior and posterior ensembles are presented and compared with benchmark data and baseline results. It can be seen from Fig. 2.7a that the prior ensemble means of both τ_w and x_{attach} deviate from the benchmark DNS data significantly. In particular, the baseline RANS simulation predicts a much smaller recirculation zone than the truth. Figure 2.7b shows that in most of the region (between $x/H = 1$ and $x/H = 8$) the posterior ensemble mean has better agreement with the DNS data than the baseline results. In fact, in this region, all samples in the posterior ensemble have better agreement with the benchmark than the baseline results in terms of both wall shear stress and reattachment point. This improvement demonstrates the merits of the current framework. Incorporating observation data and physical prior knowledge indeed leads to improved predictions of both QoIs.

It is noted that in the immediate vicinity of the hill crest, i.e., near $x/H = 0.5$ and $x/H = 8.5$, the posterior ensemble is similar to or even slightly deteriorated compared to the baseline in terms of agreement with DNS data. The reason is that in this region the flow has rapid spatial variations. Specifically, there is a separation between $0 < x/H < 1$, and a large mean flow curvature with strong pressure gradient between $8 < x/H < 9$. Consequently, the length scales of the coherent structures in this region are small, and thus the correlations between this part of the flow and other regions are weak. On the other hand, no velocity observations are available in this region. Here we point out an important fact that the Bayesian

inference based on ensemble Kalman method primarily relies on the *correlation* between the predicted system state variables at different locations to make corrections. Specifically, the observations only bring information to the states at the locations correlated to the observed states. Hence, poor prediction is expected for a region that has neither observations within it nor statistically significant correlations with the regions that have observations. The role of correlation in the current framework is further discussed in Section 2.5.2.

The prior and posterior distributions of the reattachment point represented by samples are shown in Fig. 2.7 (bottom panels). It can be seen that the bias in the prior distribution as compared to the DNS data is large, while in the posterior distribution the bias is significantly corrected. Moreover, the prior sample scattering is wide, indicating large uncertainties. In contrast, the posterior distribution is significantly narrowed, which indicates increased confidence in the prediction by incorporating velocity observations into the Bayesian inference.

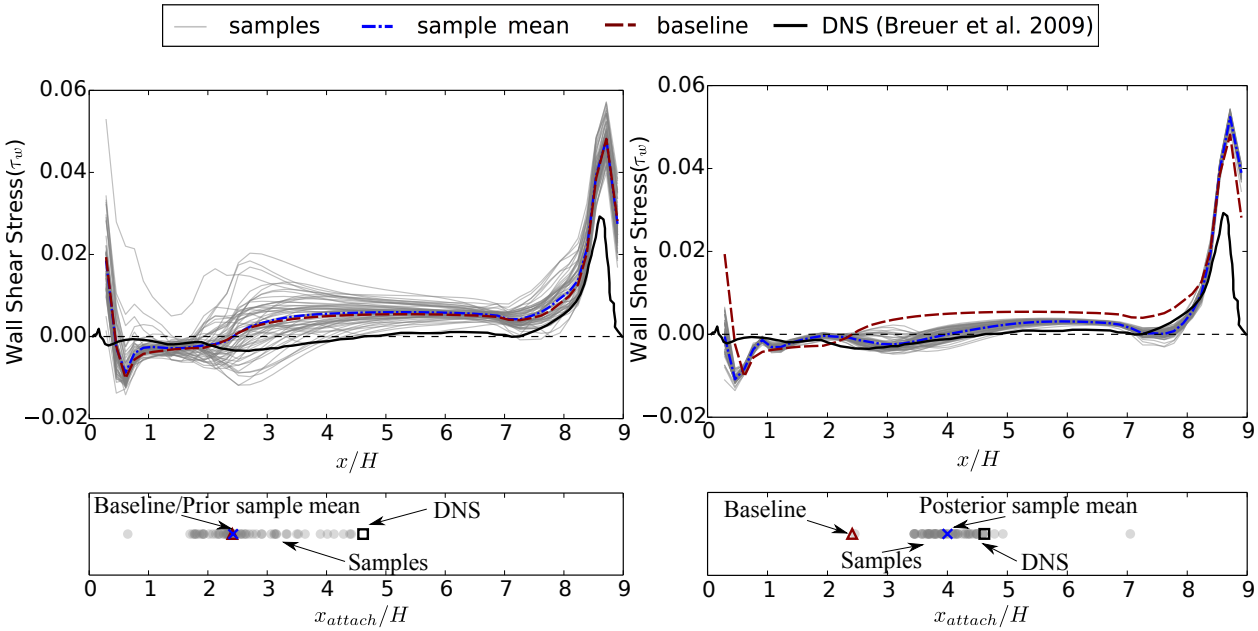

(a) Prior ensemble (b) Posterior ensemble

Figure 2.7: (a) Prior ensemble and (b) posterior ensemble of the bottom wall shear stress τ_w (*top panels*) and reattachment point x_{attach} (*bottom panels*) for the flow over periodic hills. The region with negative shear stress τ_w indicates the extent of recirculation zone on the bottom wall. The reattachment point is the downstream end of the recirculation zone, which can be determined by the location at which the wall shear stress changes from negative to positive. Note that certain samples in the ensemble have two recirculation zones that are very close to each other. In these cases the reattachment point of the downstream one is taken.

The comparison of 95% credible interval obtained from the prior and posterior ensemble of wall shear stresses are presented in Figure 2.8. Similar reduction of model-form uncertainty

as shown in Fig. 2.6 is observed here. Compared to that in the prior, the 95% credible interval in the posterior has a much smaller uncertainty and a better coverage of the benchmark data in the region between $x/H = 1$ and 5. This is because there are more observations available in the vicinity. Admittedly, in some regions, e.g., between $0 < x/H < 1$ and $8 < x/H < 9$, the posterior credible interval does not improve or even deteriorate compared to the prior, which is due to the lack of observation data and the relatively small length scale in these regions as discussed above. It is noted that in some regions the 95% credit intervals, e.g., in Figs. 2.6 and 2.8, failed to cover the truth, which indicates that the current method should still be used with caution when making high-consequence decisions. The iterative ensemble Kalman method tends to underestimate uncertainties in the posterior distributions, a difficulty shared by many other maximum likelihood estimators as well [46].

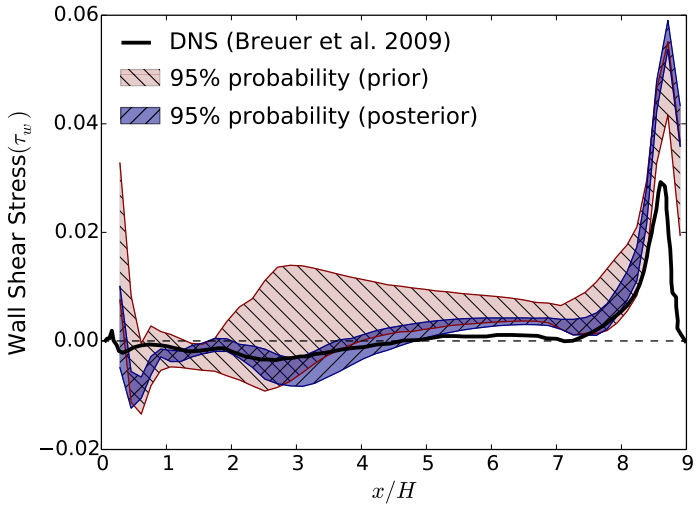

Figure 2.8: The 95% credible intervals of the prior (light/pink shaded region) and posterior (dark/blue shaded region) ensembles of bottom wall shear stress for the flow over periodic hills.

Figure 2.9 shows that the bias in the turbulent kinetic energy (TKE) from baseline RANS prediction has been partly corrected, especially for the upstream region. It is possible that the production of TKE due to the instability in the free-shear region after the separation is the driving factor. Consequently, the improved prediction of TKE in this region leads to the corrections for the velocities and other QoIs in the entire field. However, note that the posterior mean of TKE is not necessarily better than the baseline results at all locations. The TKE levels immediately downstream of the hill crest have been increased, but at the downstream locations the posterior mean are not significantly better than the baseline. In the process of minimizing misfit with the observations, some compromises are inevitably made, with some regions such as the upstream experiencing more corrections than other regions such as the downstream region. A possible explanation is that the TKE in the free-shear region has stronger correlations with the velocities at the observed locations. However, it is also possible that the TKE does not necessarily need to be improved to provide better

velocity field due to the non-unique mapping from Reynolds stress field to velocity field, as has been discussed above. More detailed discussion can be found in Section 2.5.3.

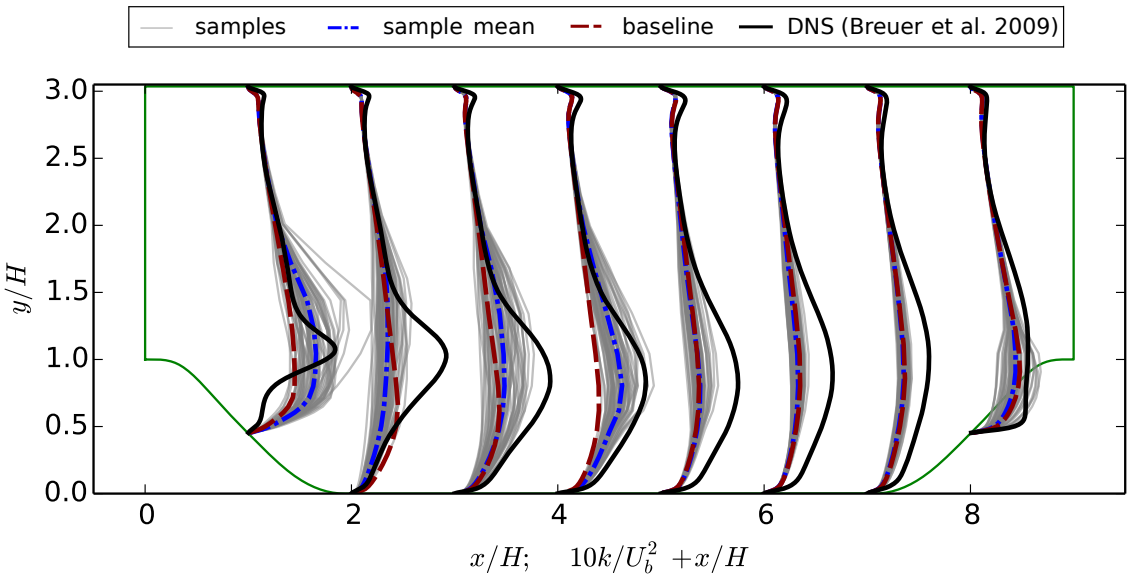

Figure 2.9: Posterior ensemble of the turbulent kinetic energy k with its mean compared to the baseline results and the benchmark DNS data. The prior ensemble is omitted for k, since its mean is the same as the baseline prediction.

2.4.2 Fully Developed Turbulent Flow in a Square Duct

Case Setup

The fully developed turbulent flow in a square duct is a widely known case for which many turbulence models fail to predict the secondary flow induced by the Reynolds stresses. The geometry of the case is shown in Fig. 6.3. The Reynolds number based on the edge length D of the square and the bulk velocity U_b is $Re_b = 10320$. All lengths presented below are normalized by the height h of the computational domain, which is half of D. Extensive benchmark data from DNS are available in the literature [47, 48].

Standard computational setup as used in the literature is adopted in this work. Only one quadrant of the physical domain is simulated considering the symmetry of the flow with respect to the centerlines along y- and z-axes as indicated in Fig. 6.3. We emphasize here that our study is concerned with the mean flow, since the objective is to quantify the uncertainties in RANS simulations. The instantaneous flows are beyond the scope of our discussions, and they do not have the symmetries mentioned here. Non-slip boundary conditions are imposed at the walls and symmetry boundary conditions (zero in-plane velocities) are applied on the symmetry planes. Theoretically, one can further reduce the computational domain size to

1/8 of the physical domain by utilizing the symmetry with respect to the square diagonal. However, this symmetry is not exploited, as it would be difficult to impose proper boundary conditions on the diagonal. The symmetry in the baseline RANS simulation results is implied by the diagonal symmetry of the geometry and boundary conditions. When conducting forward RANS simulations with given Reynolds stress fields, caution must be exercised to ensure that the perturbations introduced to $\tilde{\boldsymbol{\tau}}^{rans}$ have diagonal symmetry, which will be discussed later. Otherwise, the posterior velocities may be asymmetric with respective to the diagonal.

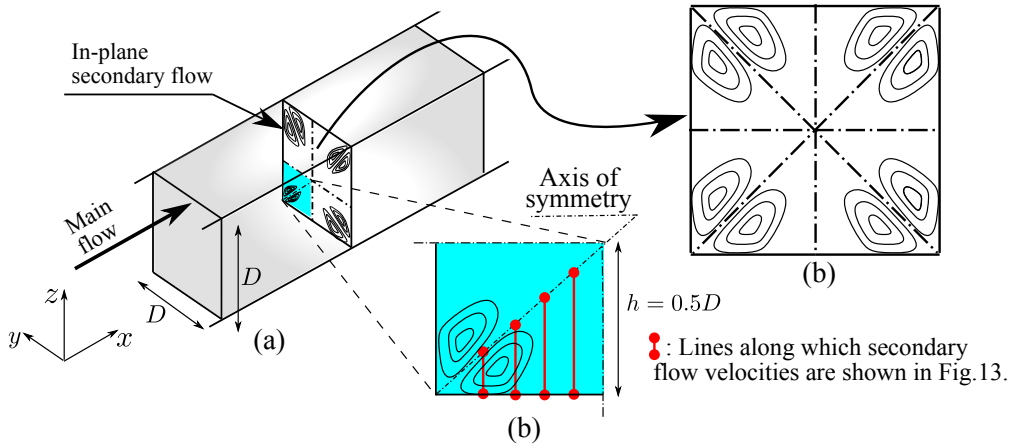

Figure 2.10: (a) Schematic for the fully developed turbulent flow in a square duct. The x axis is aligned with the streamwise direction. Secondary flows exist in the y–z plane, which are schematically represented with contours. (b) Symmetry of the (mean) flow with respect to the centerlines in y- and z-directions and along the diagonals. (c) The computational domain covers only a quarter of the physical domain due to the centerline symmetry. The cross-sections along which QoIs (e.g., velocities and Reynolds stress imbalance) are compared to benchmark data are also indicated.

The mesh and computational parameters for this case are shown in Table 3.2. Choice of parameters can be motivated similarly as in the periodic hill case. A notable difference is that only uncertainties in the shape of the Reynolds stress (i.e., ξ and η) are considered in the square duct flow case. The QoI for this flow is the in-plane flow velocities, which are primarily driven by the normal stress imbalance $\tau_{yy} - \tau_{zz}$, a quantity that is associated with the shape of $\boldsymbol{\tau}$. The design of the variance field σ is based on the same principle as in the periodic hill flow. Specifically, we chose $\sigma_0 = 0.2$ throughout the field and $\sigma_{local} = 0.5$ at the lower left corner. The length scale of the radial basis kernel is chosen as 0.1D based on the estimation of length scale of secondary flow (see Table 3.2). It is known that RANS models have more difficulties in predicting the flow near the corner, which justifies the large value of $\sigma(x)$ near the corner and the gradual decrease away from the corner as well as towards the diagonal. Moreover, the variance field is chosen to be symmetric along the diagonal of the y–z plane in consideration of the flow symmetry.

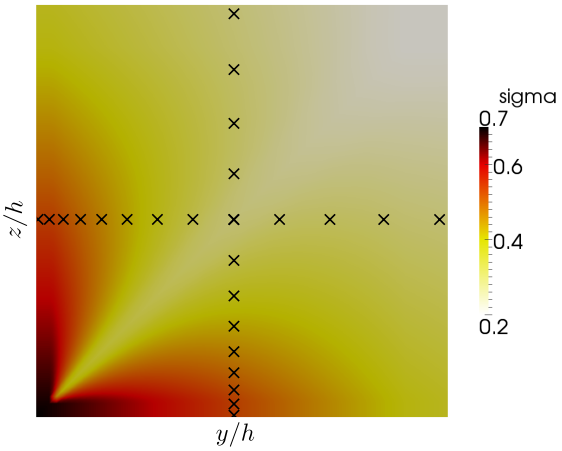

Figure 2.11: Contour of the variance field $\sigma(x)$ and locations of the observations for the square duct flow case. Larger variances are allowed near the corner due to the difficulties RANS models have in predicting the secondary flow in this region. The variance field is chosen to be symmetric along the diagonal of the y–z plane in consideration of the flow symmetry.

Results

The first six modes of KL expansion are shown in Fig. 2.12 along with two typical realizations. All the modes have been shifted and normalized into the range $[0, 1]$. Only the diagonally symmetric modes are retained to guarantee the symmetry of the Reynolds stress along the diagonal, which leads to the symmetry of the posterior velocities. The observations are obtained from the DNS data [47] by adding Gaussian random noises as in the periodic hill flow. Velocities are observed at 25 points as shown in Fig 6.3, half of which are distributed along the line $y/h = 0.5$ and the other half along $z/h = 0.5$. Note that half of the information from the observations is redundant due to the diagonal symmetry of the flow.

The ability of a numerical model to predict the secondary flow in y–z plane is of most interest for the flow in square duct. Therefore, the in-plane velocity field is identified as the QoI for this case. The in-plane flow velocity (U_y) on the four cross-sections as indicated in Fig. 6.3 are presented to facilitate quantitative comparison with the baseline and benchmark results. The velocity profiles U_z in the z direction have similar characteristics as U_y (but are not identical) and are thus omitted. The prior and posterior ensembles of the velocity profiles for U_y are shown in Fig. 2.13. Only the velocity profiles in the region below the diagonal are presented due to the diagonal symmetry. It can be seen from Fig. 2.13 that the baseline RANS simulation predicts uniformly zero in-plane velocities as expected. Around the baseline prediction, the prior ensembles are scattered due to the perturbation of δ_ξ and δ_η. The large range of scattering indicates that the secondary flow is sensitive to the anisotropy

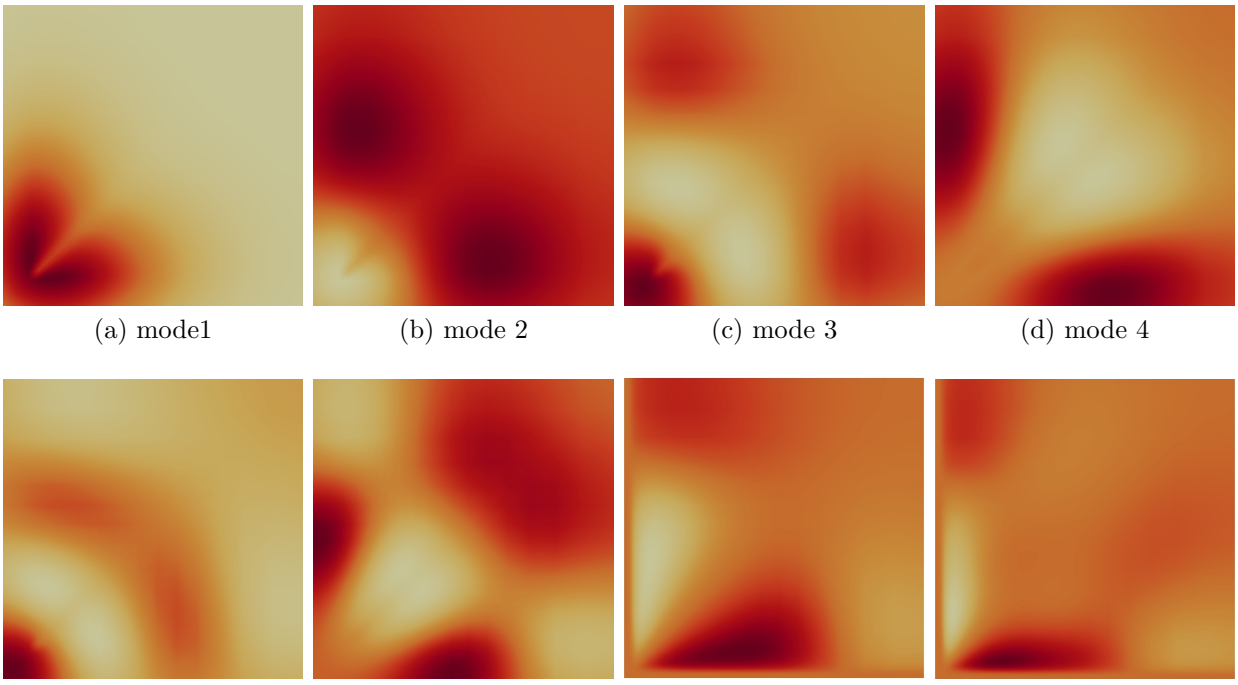

(a) mode1 (b) mode 2 (c) mode 3 (d) mode 4

(e) mode 5 (f) mode 6 (g) realization 1 (h) realization 2

Figure 2.12: Illustration of KL expansion modes for the square duct flow case. All presented modes have been shifted and scaled into a range of 0 (lightest) to 1 (darkest) to facilitate presentation, and the legend is thus omitted. Panels (a) to (f) denote modes 1 to 6, respectively, with lower modes being more important. Only the modes with diagonal symmetry are retained to guarantee the symmetry of perturbed Reynolds stresses field. Panels (g) and (h) show the magnitude of Reynolds stress imbalance $|\tau_{yy} - \tau_{zz}|$ associated with two typical realizations of the discrepancy fields.

of Reynolds stresses tensor, which has been reported in previous studies [18, 47]. Compared to the prior ensemble mean and the baseline RANS prediction, the posterior ensemble mean of the velocities are significantly improved along all four cross sections, as shown by good agreements with the benchmark data. The scattering has been significantly reduced as well, while still covering the truth adequately in most regions. The remaining differences and the regions where the ensemble fails to cover the truth can be explained similarly as in the periodic hill case. Similar to that in the periodic hill case,

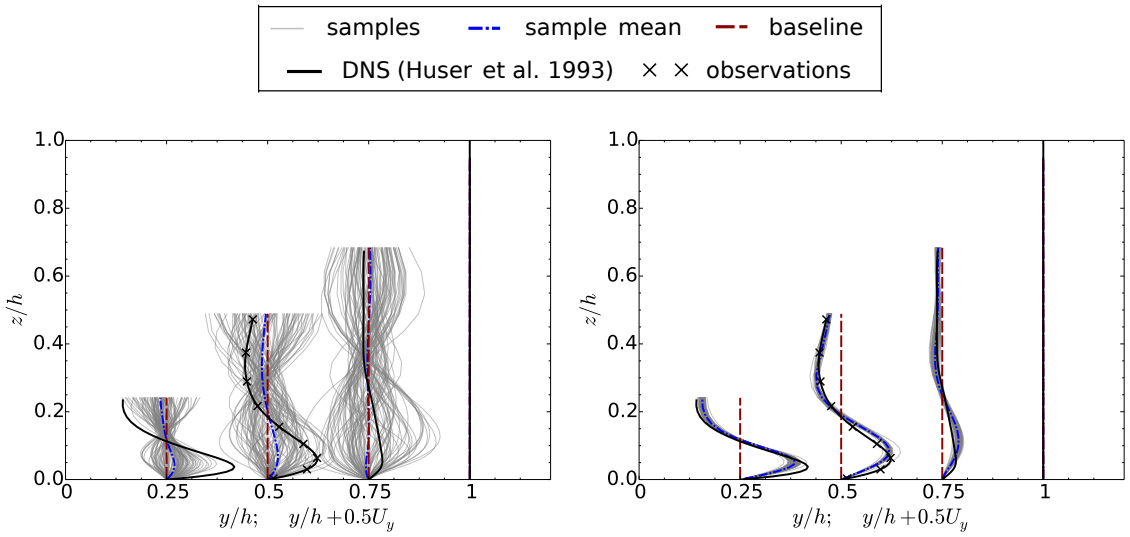

(a) Prior ensemble (b) Posterior ensemble

Figure 2.13: (a) Prior velocity ensemble and (b) posterior velocity ensemble at four spanwise locations $y/h = 0.25, 0.5, 0.75$ and 1 with comparison to baseline and benchmark results. The velocity U_z in the z direction have similar characteristics and are thus omitted. The velocity profiles in the prior ensemble are scaled by a factor of 0.3 for clarity.

Figure 2.14 shows a comparison of the posterior ensemble mean field of the in-plane flow velocity and the benchmark data. They are presented as vector plots to show the overall features of secondary flow and particularly the vortex structure. The length and direction of an arrow indicate the magnitude and direction, respectively, of the in-plane flow velocity at that location. The plots are arranged such that a perfect agreement between the two would show as exact symmetry of the two panels along the center line. The vector plot of the velocity field from the baseline RANS prediction is omitted since it is uniformly zero. It can be seen that the posterior ensemble mean demonstrates a very good agreement with the benchmark data in most aspects, i.e., the direction and the intensity of secondary flow at most locations as well as the center of vortex structure. Only minor differences between the two can be identified. For example, the posterior mean velocity has a slightly smaller gradient of velocity magnitude compared to the benchmark results near the symmetry line. The agreement clearly demonstrates the merits of the current framework, particularly considering the fact that most of the commonly used turbulence models are not capable of

predicting the in-plane flow. Specifically, all isotropic eddy viscosity models completely miss the secondary flow, which is explained by the negligible $\partial U_y/\partial y$ and $\partial U_z/\partial z$ terms and the Boussinesq assumption that Reynolds stress is proportional to local strain rate of the mean flow. Even advanced models (e.g., Reynolds stress transport models) tend to underestimate the flow intensity [49]. Admittedly, velocity observations at some locations are used in this method, but the amount of data used in the inference is rather small compared to the total degrees of freedom of the Reynolds stress field.

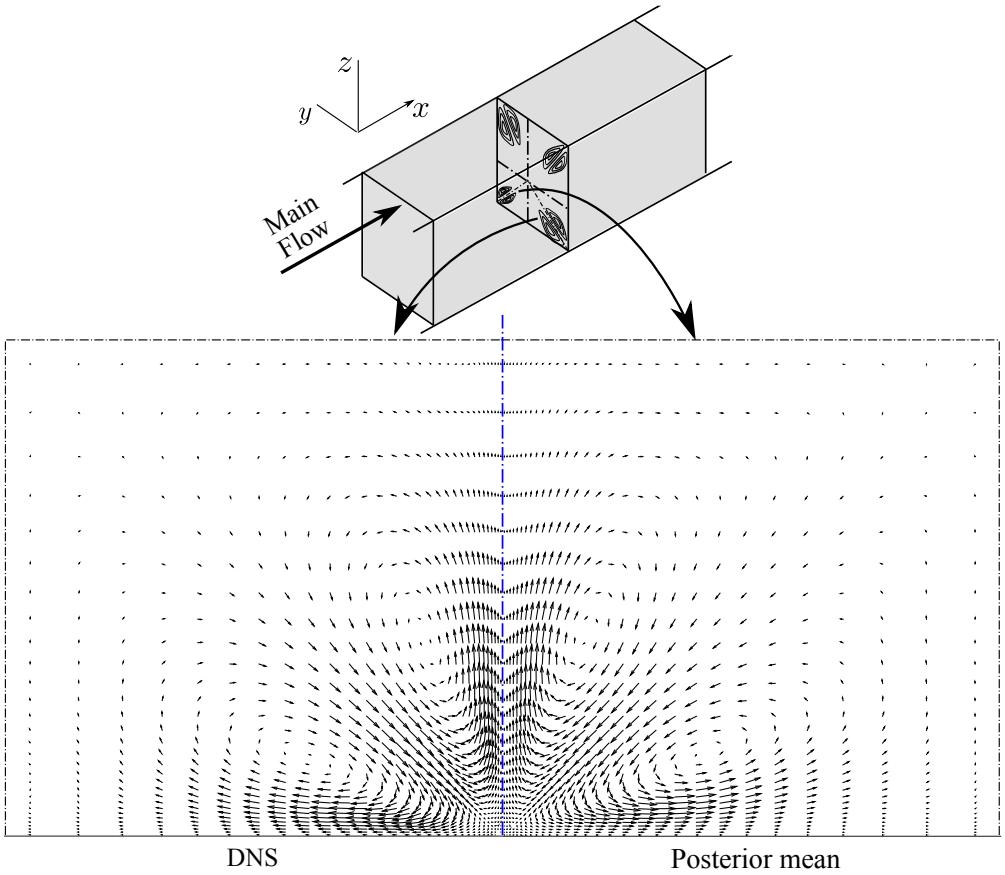

Figure 2.14: Comparison of the velocity field in a square duct between the posterior mean and benchmark DNS data.The length and direction of an arrow indicate the magnitude and direction, respectively, of the in-plane flow velocity. The plots are arranged such that a perfect agreement between the two would show as exact symmetry of the two panels along the vertical center line. The vector field from the baseline RANS prediction is omitted since it is uniformly zero.

As mentioned above, the normal stress imbalance $\tau_{yy} - \tau_{zz}$ is the main driving force of the secondary flow. Therefore, the prior and posterior ensembles of the imbalance at five locations, $y/h = 0.25, 0.5, 0.6, 0.75$, and 1, are presented in Fig. 2.15. It can be seen that the baseline RANS prediction of $\tau_{yy} - \tau_{zz}$ is zero. Compared to the baseline RANS prediction, the posterior normal stress imbalance shows a significant improvement in regions close to

the observations ($y/h = 0.5$), although differences still exist, especially in the regions far away from the observations (e.g., at $y/h = 1$). It is consistent with the argument made in Section 2.2.2 that the correlation decreases with distance, and that the quality of correction heavily depends on correlations. Note that the inferred stress imbalances at $y/h = 0.75$ agree with the benchmark much better than do those at $y/h = 0.25$, although they have approximately the same distances from the observations, which are distributed along $y/h = 0.5$. This can be explained by the fact that the length scale of the flow decreases towards the corner (e.g., near $y/h = 0.25$) due to the constriction of the duct walls, and thus the correlation decreases much faster in this region than near the symmetry line.

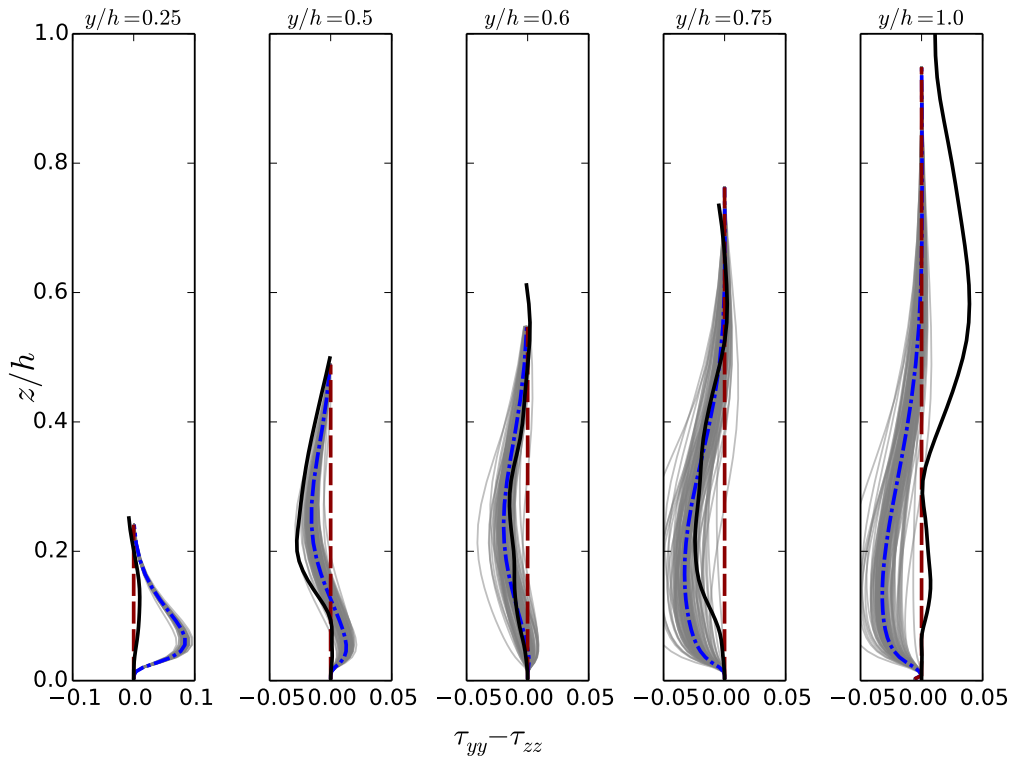

Figure 2.15: Comparison of the normal stresses imbalance at five locations $y/h = 0.25, 0.5, 0.6, 0.75$ and 1.0. A larger horizontal axis range is used in the panel for $y/h = 0.25$ due the large range of values $\tau_{yy} - \tau_{zz}$ at this location.

2.5 Discussion

2.5.1 Computational Cost of the Model-Form Uncertainty Quantification

As mentioned in Sections 4.3.5. The ensemble Kalman method uses 60 samples (see Table 3.2) and needs approximately 10 iterations to achieve statistical convergence. Therefore, each uncertainty quantification case involves 600 evaluations of the forward RANS model `tauFoam`. Since each forward RANS evaluation is only 10% as expensive as a baseline RANS simulation (see Section 4.3.5), the total computational cost of the uncertainty quantification procedure is 60 times as that of the baseline simulation. However, note that the propagation of samples can be done in parallel, i.e., in each iteration the 60 forward RANS simulations were run simultaneously on 60 CPU cores. As a result, the wall time of the uncertainty quantification procedure is approximately the same as that of the baseline simulation, assuming the latter is run on a single core. Finally, the computational costs associated with the projection of Reynolds stresses, the KL expansion, and the Kalman filtering are all neglected in the analysis above. This is justified because the computational cost of the uncertainty quantification is indeed dominated by the forward model evaluations.

2.5.2 The Role of Correlation in Current Framework

It has been pointed out that the relatively poor inference performance is expected in the vicinity of the crest, which is due to the lack of observations in the region and statistically significant correlations with the regions that have observations. The concept of correlation plays an important role in the current inference framework and warrants further discussions.

In three-dimensional complex flows more measurement data may be needed to obtain results of similar quality as presented here. In particular, when the flow consists of a number of distinct regions that are weakly correlated, a design of experiment study is needed to ensure all regions of interest have measurements data if possible. However, note that the correlation within the flow field can be studied a priori solely based on an ensemble of RANS simulations before any measurements are performed. Based on the study of correlations, the measurements can subsequently be optimized. Therefore, such simulation-informed experimental design is feasible in practice. We have performed such a correlation study in a more complex flow, the flow over a wing-body junction, and the detailed results are presented in ref. [26].

It is essential to choose proper correlation length scales based on that of the mean flow, which is part of the physics-based prior knowledge. While an overly small length scale would fail to make corrections to the regions without observation, an overly large length scale would lead to spurious corrections. The correlation structure (e.g., of the velocities) in a flow field is very complex and difficult to visualize due to the high dimensionality of the state. However, we

can illustrate the idea by considering the streamlines of the mean flow. Intuitively, velocities at two points on the same streamline should have a relatively high correlation. Consequently, observing the velocity at one point can inform us about velocities at other points on the same streamline. Two points in different coherent structures or regions as mentioned above, e.g., one point in the recirculation zone and another in the shear zone, are likely to be on different streamlines. This explains why points within the same region have higher correlations than the correlations among different regions. That also justifies the arrangement of observation points shown in Fig. 5.2 with observations scattered in all three regions of interest. This explanation of correlation structure is of course a highly simplified picture. In reality, fluid flows are highly complex, coupled dynamic systems. Velocities at different points can be correlated due to continuity requirements and pressure. It is well known that the pressure is described by an elliptic equation (for incompressible flows), which has whole-domain coupling characteristics.

2.5.3 Success and Limitation of the Current Framework

The overall idea of the proposed method is to improve flow field and QoI predictions and to quantify the uncertainties therein by combining all sources of available information, including observation data, physical prior knowledge, and RANS model predictions. A Bayesian framework based on an iterative ensemble Kalman method is used for the uncertainty quantification. Numerical simulation results have demonstrated the feasibility of the framework. In particular, even with velocity observations at very few locations, the posterior velocities are significantly improved compared to the baseline results.

One may also expect that the uncertainties in the modeled Reynolds stresses can be quantified and reduced. Indeed, the posterior ensemble obtained from the Bayesian inference process also has information on the Reynolds stresses. However, our experience suggests that the posterior mean of an arbitrarily chosen component or projection of the Reynolds stresses is not significantly more accurate than those of the baseline prediction.

This apparent contradiction can be explained from two perspectives: the high dimensionality of the Reynolds stress field and the mapping $\boldsymbol{\tau} \mapsto \mathbf{u}$ from Reynolds stresses to mean velocities. The most straightforward reason as mentioned in Section 2.2.3 is that the Reynolds stress discrepancy is a tensor field in a high-dimensional uncertainty space, and thus the amount of velocity data is not sufficient to constrain its uncertainties, even when other prior information is considered. Moreover, the RANS equations describe a many-to-one mapping from Reynolds stresses to mean velocities, and thus the mapping $\boldsymbol{\tau} \mapsto \mathbf{u}$ is not invertible (i.e., a given velocity field may correspond to many possible Reynolds stress fields). This is evident from the fact that the divergence of the Reynolds stress tensor, rather than the Reynolds stress itself, appears in the RANS equation. Although difficult to prove rigorously, we postulate that even Reynolds stress fields that have different divergences can map to very similar velocity fields. One can loosely think of the velocity field as being driven by a

projection of the Reynolds stress on a *low-dimensional manifold*. The specific form of the projection depends on the physics of individual flow. Taking the flow in a square duct for example, it has been demonstrated by analytical derivations [50, 47, 18] that the secondary flow is primarily generated by the normal stress imbalance field $\tau_{yy} - \tau_{zz}$, or more precisely, its cross spatial derivative $\frac{\partial^2}{\partial y \partial z}(\tau_{yy} - \tau_{zz})$. The imbalance scalar can be obtained from the Reynolds stress tensor through linear mapping described by a rank deficient matrix. Since only velocity observation data are used in the Bayesian inference in this work, one can only reasonably expect to infer the projection (i.e., the imbalance), but not the full Reynolds stress field. This can be partly explained by the fact that the projection has a lower dimension, but more importantly, the projection is an observable variable from a control-theoretic perspective. This has been demonstrated in Fig. 2.15. The mapping between Reynolds stresses and velocity as describe by the RANS equations are extremely complex due to the their nonlinearity. This complexity and its implications to the current framework will be further investigated.

Another limitation of the current framework lies in the iterative ensemble method used for the uncertainty quantification, which is a computationally affordable method for approximate Bayesian inference. The posterior distribution obtained with this method may deviate from the true distribution. This compromise is made in this work in consideration of the high computational costs of RANS models (e.g., hours to days for realistic flow simulations), which makes more accurate sampling methods such as those based on the Markov Chain Monte-Carlo method prohibitively expensive. The accuracy of the ensemble-based method will be assessed in future work by comparing current results with those obtained with MCMC, possibly by utilizing recently developed dimension-reduction methods (e.g., active subspace methods [51], likelihood informed dimension-reduction [52]) and sampling techniques (e.g., delayed rejection adaptive metropolis [53]), or by building surrogate models to facilitate the MCMC sampling.

2.5.4 What If There Are No Observation Data Available?

In light of the limitations of the framework as described above, two legitimate follow-up questions can be raised. That is, given that the full Reynolds stress discrepancy field cannot be inferred accurately from the velocity observations, (1) what would the value of the framework be in engineering practice and (2) how can this framework can be used in scenarios with no observation data.

Regarding the first question, sparse observation data are often available for engineering systems that are in operation. For example, real-time monitoring sensors are often installed in wind farms, nuclear power plants, and many other important facilities and devices. For these cases, the current framework can provide a powerful method for combining information from the numerical models (often greatly simplified due to stringent positive lead-time requirement in predictions), observation data, and physical prior knowledge.

In scenarios where there are no observation data available as posed in the second question, the current framework can be used in two ways. First, with the absence of observation data the inference procedure essentially degenerates to forward uncertainty propagation, i.e., propagating the uncertainties in the form of physical prior knowledge on Reynolds stresses to uncertainties in QoIs (e.g., velocity, wall shear stresses, and reattachment point). This is somewhat similar to but more comprehensive than the framework of Iaccarino and coworkers [14, 15, 16, 17, 18], since the prior in our work covers an uncertainty space rather than only a few limit states. Second, when observation data are available in a geometrically similar case but perhaps at a lower Reynolds number (e.g., the downscaled model in a laboratory experiment), the model uncertainties can first be quantified and reduced with the data available on the scaled model. After the calibration, the posterior Reynolds stress uncertainty distribution is extrapolated to the case of concern (e.g., the flow in a geometrically similar prototype at a higher Reynolds number) to make predictions. Dow and Wang [19] used a similar calibration–prediction procedure to predict flows in channels of different geometries by using Gaussian processes describing the eddy viscosity discrepancy. Similar ideas have been suggested and advocated by Duraisamy et al. [23, 24]. In all cases the calibration–prediction procedure relies upon a crucial assumption that the calibration case and the prediction case share physically similar characteristics, despite the differences in specific flow conditions (e.g., Reynolds number or geometry). The feasibility of the calibration–prediction method based on the current framework has been preliminarily explored by Wu et al. [54], which showed promising results when the calibrated Reynolds stress discrepancies are used to predict flows in the same geometry but at a Reynolds number one order of magnitude higher. Prediction of flows in a different geometry, on the other hand, has achieved less successes. However, extreme caution must be exercised and expert opinions must be consulted when using such an extrapolation method as presented in [54], since even a slight change of Reynolds number can lead to significant changes of flow characteristics. Ultimately, the use of this assumption has to be the judgment of the user, which is clearly undesirable. An improved, more intelligent framework should be sought for. It seems that modern machine learning methods have the potential of alleviating users of such burdens, which is a topic of current research [23].

2.6 Conclusion

In this work we propose an open-box, physics-informed, Bayesian framework for quantifying and reducing model-form uncertainties in RANS simulations. Uncertainties are introduced directly to the Reynolds stresses and are represented with compact parameterization accounting for empirical prior knowledge and physical constraints (e.g., realizability, smoothness, and symmetry). An iterative ensemble Kalman method is used to incorporate the prior knowledge with available observation data in a Bayesian framework and propagate the uncertainties to posterior distributions of the Reynolds stresses and other QoIs. Two test cases, the flow over periodic hills and the flow in a square duct, have been used to demonstrate the feasibility and to evaluate the performance of the proposed framework. Simulation results

suggest that even with sparse observations, the obtained posterior mean velocities have significantly better agreement with the benchmark data compared to the baseline results. The methodology provides a general framework for combining information from physical prior knowledge, observation data, and low-fidelity numerical models (including RANS models and beyond) that are frequently used in engineering practice.

A notable limitation is that the full Reynolds stress field inferred from this method is not accurate. This is attributed to the high dimension of the Reynolds stress uncertainty space, the sparseness of the velocity observation data, and the nonlinear, possibly even non-unique, mapping between the Reynolds stresses and velocities as described by the RANS equations. However, we argue that the inferred Reynolds stresses are still valuable despite this limitation, and that they can be extrapolated to cases with similar physical characteristics. Another limitation of the current framework lies in the iterative ensemble method used for the uncertainty quantification, which is computationally less intensive but less accurate than exact Bayesian inference based on Markov Chain Monte-Carlo sampling. The impact of the approximate Bayesian inference method will be investigated in future studies.

Acknowledgment

We thank the anonymous reviewers for their comments, which helped in improving the quality and clarity of the manuscript. We gratefully acknowledge partial funding of graduate research assistantships for JLW, JXW, and RS from the Institute for Critical Technology and Applied Science (ICTAS, Grant number 175258).

Bibliography

[1] D. C. Wilcox, Turbulence modeling for CFD, 3rd Edition, DCW Industries, 2006.

[2] S. B. Pope, Turbulent Flows, Cambridge University Press, Cambridge, 2000.

[3] C. J. Roy, W. L. Oberkampf, A comprehensive framework for verification, validation, and uncertainty quantification in scientific computing, Computer Methods in Applied Mechanics and Engineering 200 (25) (2011) 2131–2144.

[4] A. Saltelli, P. Stano, P. B. Stark, W. Becker, Climate models as economic guides: Scientific challenge or quixotic quest?, Issues in Science and Technology 31 (3).

[5] M. C. Kennedy, A. O'Hagan, Bayesian calibration of computer models, Journal of the Royal Statistical Society: Series B (Statistical Methodology) 63 (3) (2001) 425–464.

[6] Y. Xiong, W. Chen, D. Apley, X. Ding, A non-stationary covariance-based kriging method for metamodelling in engineering design, International Journal for Numerical Methods in Engineering 71 (6) (2007) 733–756.

[7] D. Huang, T. Allen, W. Notz, R. Miller, Sequential kriging optimization using multiple-fidelity evaluations, Structural and Multidisciplinary Optimization 32 (5) (2006) 369–382.

[8] S. Conti, J. P. Gosling, J. E. Oakley, A. O'Hagan, Gaussian process emulation of dynamic computer codes, Biometrika 96 (3) (2009) 663–676.

[9] D. Higdon, M. Kennedy, J. C. Cavendish, J. A. Cafeo, R. D. Ryne, Combining field data and computer simulations for calibration and prediction, SIAM Journal on Scientific Computing 26 (2) (2004) 448–466.

[10] J. Brynjarsdóttir, A. O'Hagan, Learning about physical parameters: The importance of model discrepancy., Inverse Problems 30 (2014) 114007.

[11] T. Oliver, R. Moser, Uncertainty quantification for RANS turbulence model predictions, in: APS Division of Fluid Dynamics Meeting Abstracts, Vol. 1, 2009.

[12] T. A. Oliver, R. D. Moser, Bayesian uncertainty quantification applied to RANS turbulence models, in: Journal of Physics: Conference Series, Vol. 318, IOP Publishing, 2011, p. 042032.

[13] S. H. Cheung, T. A. Oliver, E. E. Prudencio, S. Prudhomme, R. D. Moser, Bayesian uncertainty analysis with applications to turbulence modeling, Reliability Engineering & System Safety 96 (9) (2011) 1137–1149.

[14] C. Gorlé, G. Iaccarino, A framework for epistemic uncertainty quantification of turbulent scalar flux models for Reynolds-averaged Navier-Stokes simulations, Physics of Fluids 25 (5) (2013) 055105.

[15] C. Gorlé, J. Larsson, M. Emory, G. Iaccarino, The deviation from parallel shear flow as an indicator of linear eddy-viscosity model inaccuracy, Physics of Fluids 26 (5) (2014) 051702.

[16] M. Emory, J. Larsson, G. Iaccarino, Modeling of structural uncertainties in Reynolds-averaged Navier-Stokes closures, Physics of Fluids 25 (11) (2013) 110822.

[17] M. Emory, R. Pecnik, G. Iaccarino, Modeling structural uncertainties in Reynolds-averaged computations of shock/boundary layer interactions, AIAA paper 479 (2011) 1–16.

[18] M. A. Emory, Estimating model-form uncertainty in Reynolds-averaged Navier–Stokes closures, Ph.D. thesis, Stanford University (2014).

[19] E. Dow, Q. Wang, Quantification of structural uncertainties in the k–ω turbulence model, in: 52nd AIAA/ASME/ASCE/AHS/ASC Structures, Structural Dynamics and Materials Conference, AIAA, Denver, Colorado, 2011, AIAA Paper, 2011-1762.

[20] C. K. Wikle, R. F. Milliff, D. Nychka, L. M. Berliner, Spatiotemporal hierarchical bayesian modeling tropical ocean surface winds, Journal of the American Statistical Association 96 (454) (2001) 382–397.

[21] L. M. Berliner, Physical-statistical modeling in geophysics, Journal of Geophysical Research: Atmospheres 108 (D24).

[22] B. Launder, G. Reece, W. Rodi, Progress in development of a Reynolds-stress turbulence closure, Journal of Fluid Mechanics 68 (1975) 537–566.

[23] B. Tracey, K. Duraisamy, J. J. Alonso, A machine learning strategy to assist turbulence model development, AIAA Paper 1287 (2015) 2015.

[24] E. J. Parish, K. Duraisamy, A paradigm for data-driven predictive modeling using field inversion and machine learning, Journal of Computational Physics 305 (2016) 758–774.

[25] A. P. Singh, K. Duraisamy, Using field inversion to quantify functional errors in turbulence closures, Physics of Fluids 28 (2016) 045110.

[26] J.-L. Wu, J.-X. Wang, H. Xiao, Quantifying model form uncertainty in rans simulation of wing–body junction flow, available at: arXiv:1605.05962 (2016).

[27] H. Tennekes, J. L. Lumley, A first course in turbulence, MIT press, 1972.

[28] S. Banerjee, R. Krahl, F. Durst, C. Zenger, Presentation of anisotropy properties of turbulence, invariants versus eigenvalue approaches, Journal of Turbulence 8 (32) (2007) 1–27.

[29] H. Xiao, J.-X. Wang, R. G. Ghanem, A random matrix approach for quantifying model-form uncertainties in turbulence modeling, submitted. Available at http://arxiv.org/abs/1603.09656 (2016).

[30] J.-X. Wang, R. Sun, H. Xiao, Quantification of uncertainties in turbulence modeling: A comparison of physics-based and random matrix theoretic approaches, submitted. Available at http://arxiv.org/abs/1603.05549 (2016).

[31] O. P. Le Maître, O. M. Knio, Spectral methods for uncertainty quantification: with applications to computational fluid dynamics, Springer, 2010.

[32] I. Daubechies, Orthonormal bases of compactly supported wavelets, Communications on pure and applied mathematics 41 (7) (1988) 909–996.

[33] M. D. Buhmann, Radial basis functions: theory and implementations, Cambridge university press, 2003.

[34] M. A. Iglesias, K. J. Law, A. M. Stuart, Ensemble Kalman methods for inverse problems, Inverse Problems 29 (4) (2013) 045001.

[35] G. Evensen, Data assimilation: the ensemble Kalman filter, Springer, 2009.

[36] B. Dennis, J. M. Ponciano, S. R. Lele, M. L. Taper, D. F. Staples, Estimating density dependence, process noise, and observation error, Ecological Monographs 76 (3) (2006) 323–341.

[37] K. Law, A. Stuart, Evaluating data assimilation algorithms, Monthly Weather Review 140 (2012) 3757–3782.

[38] B. Debusschere, K. Sargsyan, C. Safta, UQTk User Manual, Sandia National Laboratories, Albuquerque, NM 87185 and Livermore, CA 94550, version 2.1 Edition (June 2014).

[39] S. V. Patankar, D. B. Spalding, A calculation procedure for heat, mass and momentum transfer in three-dimensional parabolic flows, International Journal of Heat and Mass Transfer 15 (10) (1972) 1787–1806.

[40] C. M. Rhie, W. L. Chow, A numerical study of the turbulent flow past an isolated airfoil with trailing edge separation, AIAA 21 (11) (1983) 1525–1532.

[41] B. E. Launder, B. I. Sharma, Application of the energy dissipation model of turbulence to the calculation of flow near a spinning disc, Letter of Heat Mass Transfer, 1 (1974) 131–138.

[42] M. Breuer, N. Peller, C. Rapp, M. Manhart, Flow over periodic hills–numerical and experimental study in a wide range of Reynolds numbers, Computers & Fluids 38 (2) (2009) 433–457.

[43] P. Houtekamer, H. L. Mitchell, X. Deng, Model error representation in an operational ensemble Kalman filter, Monthly Weather Review 137 (7) (2009) 2126–2143.

[44] J.-X. Wang, J.-L. Wu, H. Xiao, Incorporating prior knowledge for quantifying and reducing model-form uncertainty in RANS simulations, submitted. Available at http://arxiv.org/abs/1512.01750 (2015).

[45] C. Schillings, A. M. Stuart, Analysis of the ensemble Kalman filter for inverse problems, submitted. Available at http://arxiv.org/abs/1602.02020 (2016).

[46] S. P. Neuman, Maximum likelihood Bayesian averaging of uncertain model predictions, Stochastic Environmental Research and Risk Assessment 17 (5) (2003) 291–305.

[47] A. Huser, S. Biringen, Direct numerical simulation of turbulent flow in a square duct, Journal of Fluid Mechanics 257 (1993) 65–95.

[48] AGARD, A selection of test cases for the validation of large-eddy simulations of turbulent flows, Tech. Rep. 345, AGARD Advisory Report (1998).

[49] A. Demuren, W. Rodi, Calculation of turbulence-driven secondary motion in non-circular ducts, Journal of Fluid Mechanics 140 (1984) 189–222.

[50] H. Perkins, The formation of streamwise vorticity in turbulent flow, Journal of Fluid Mechanics 44 (04) (1970) 721–740.

[51] P. G. Constantine, E. Dow, Q. Wang, Active subspace methods in theory and practice: Applications to kriging surfaces, SIAM Journal on Scientific Computing 36 (4) (2014) A1500–A1524.

[52] T. Cui, J. Martin, Y. M. Marzouk, A. Solonen, A. Spantini, Likelihood-informed dimension reduction for nonlinear inverse problems, Inverse Problems 30 (11) (2014) 114015.

[53] H. Haario, M. Laine, A. Mira, E. Saksman, DRAM: efficient adaptive MCMC, Statistics and Computing 16 (4) (2006) 339–354.

[54] J.-L. Wu, J.-X. Wang, H. Xiao, A Bayesian calibration-prediction method for reducing model-form uncertainties with application in RANS simulations, Flow, Turbulence and Combustion.

[55] C. Hua, An inverse transformation for quadrilateral isoparametric elements: analysis and application, Finite elements in analysis and design 7 (2) (1990) 159–166.

Appendix

2.A Mapping from Barycentric Coordinates to Natural Coordinates

Following the work of Iaccarino et al., we introduce uncertainties (also referred to as perturbations) to the Reynolds stresses by perturbing its magnitude (the turbulent kinetic energy k) and the shape (the eigenvalues λ_1 and λ_2 of the anisotropy tensor) as shown in Eq. (6.2). The eigenvalues can be linearly transformed to the Barycentric coordinate (C_1, C_2, C_3) as

follows [28, 17]:

$$C_1 = \lambda_1 - \lambda_2 \tag{2.7a}$$
$$C_2 = 2(\lambda_2 - \lambda_3) \tag{2.7b}$$
$$C_3 = 3\lambda_3 + 1 \tag{2.7c}$$

where C_1, C_2, and C_3 indicate the portion of areas of the three sub-triangles in the Barycentric triangle, and thus they sum to 1. Placing the triangle in a Cartesian coordinate $\mathbf{x}^b \equiv (y^b, y^b)$, the location of any point within the triangle is a convex combination of those of the three vertices, i.e.,

$$\mathbf{x}^b = \mathbf{x}^b_{1c} C_1 + \mathbf{x}^b_{2c} C_2 + \mathbf{x}^b_{3c} C_3 \tag{2.8}$$

where $\mathbf{x}^b_{1c}$, $\mathbf{x}^b_{2c}$, and $\mathbf{x}^b_{3c}$ are the coordinates of the three vertices of the triangle (see Fig. 6.1). The superscript b is used to distinguish it from the coordinate system for the fluid flow problems.

While Emory[17] perturbed the Reynolds stress towards the three limiting states (the vertices of the triangle), we need to parameterize and explore the entire triangle. To facilitate parameterization with minimum artificial capping of Reynolds stresses falling outside the realizable range, we further transform the Cartesian coordinate (x^b, y^b) to the natural coordinate (ξ, η) by using the standard finite element shape functions:

$$x^b = x(\xi, \eta) = \sum_{i=1}^{4} N_i(\xi, \eta) x^b_i \tag{2.9a}$$
$$y^b = y(\xi, \eta) = \sum_{i=1}^{4} N_i(\xi, \eta) y^b_i \tag{2.9b}$$

where (x^b_i, y^b_i) are the coordinates of four vertices, and N_1, N_2, N_3, and N_4 are shape functions defined as

$$N_1(\xi, \eta) = \frac{(1-\xi)(1-\eta)}{4}$$
$$N_2(\xi, \eta) = \frac{(1+\xi)(1-\eta)}{4}$$
$$N_3(\xi, \eta) = \frac{(1+\xi)(1+\eta)}{4}$$
$$N_4(\xi, \eta) = \frac{(1-\xi)(1+\eta)}{4}.$$

The mapping from the natural coordinate (ξ, η) to the physical coordinate (x^b, y^b) as shown in Eq. (2.9) is routinely used in finite element methods. However, the inverse mapping, i.e., computing the natural coordinate (ξ, η) for a given physical coordinate (x^b, y^b), is nontrivial and uncommon due to the difficulty of solving the bilinear equation system Eq. (2.9). In this work we use the analytical results from [55] to obtain this mapping.

In summary, the Reynolds stresses field $\tilde{\boldsymbol{\tau}}^{rans}$ computed from the baseline RANS simulation are mapped to the physical interpretable variables $\tilde{k}^{rans}, \tilde{\xi}^{rans}, \tilde{\eta}^{rans}$ via the following sequence:

$$\tilde{\boldsymbol{\tau}} \xrightarrow{(6.2)} (\tilde{k}, \tilde{\lambda}_1, \tilde{\lambda}_2) \xrightarrow{(6.3)} (\tilde{k}, \tilde{C}_1, \tilde{C}_2) \xrightarrow{(2.8)} (\tilde{k}, \tilde{x}^b, \tilde{y}^b) \xrightarrow{\text{inv. of (2.9)}} (\tilde{k}, \tilde{\xi}, \tilde{\eta})$$

where unperturbed quantities $\mathbf{v}_1^{rans}$, $\mathbf{v}_2^{rans}$, and $\mathbf{v}_3^{rans}$, dependent variables λ_3 and C_3, and superscript *rans* are omitted for simplicity of notation. Equations describing the mappings are indicated above the corresponding arrow. Equation (6.2) indicates eigen-decomposition and reconstruction. After the sequence of mapping, uncertainties are introduced into these transformed quantities by modeling the truth of k, ξ, η as random fields with their respective baseline results as priors (see Eq. (5.10)). They are subsequently used to obtain Reynolds stresses via the inverse of mapping sequence as above:

$$(k, \xi, \eta) \xrightarrow{(2.9)} (k, x^b, y^b) \xrightarrow{\text{inv. of (2.8)}} (k, C_1, C_2) \xrightarrow{\text{inv. of (6.3)}} (k, \lambda_1, \lambda_2) \xrightarrow{(6.2)} \boldsymbol{\tau}$$

2.B Iterative Ensemble Kalman Method for Inverse Modeling

The algorithm of the iterative ensemble Kalman method for inverse modeling is summarized below. See [34] for details.

Given velocity prediction from the baseline RANS simulation $\mathbf{u}^{rans}$ and observations with error covariance matrix R, the following steps are performed:

1. **(Sampling step)** Generate initial ensemble $\{\mathbf{x}_j\}_{j=1}^N$ of size N, where the augmented system state is:
$$\mathbf{x}_j = [\mathbf{u}^{rans}, \boldsymbol{\omega}]_j$$
2. **(Prediction step)**
   (a) Propagate the state from current state n to the next iteration level $n+1$ with the forward model `tauFoam`, indicated as $\mathcal{F}$,
   $$\hat{\mathbf{x}}_j^{(n+1)} = \mathcal{F}[\mathbf{x}_j^{(n)}]$$
   This step involves reconstructing Reynolds stress fields for each sample and computing the velocities from the RANS equations.

(b) Estimate the mean $\bar{\mathbf{x}}$ and covariance $P^{(n+1)}$ of the ensemble as:

$$\bar{\mathbf{x}}^{(n+1)} = \frac{1}{N}\sum_{j=1}^{N}\hat{\mathbf{x}}_j^{(n+1)}$$

$$P^{(n+1)} = \frac{1}{N-1}\sum_{j=1}^{N}\left(\hat{\mathbf{x}}_j\hat{\mathbf{x}}_j^T - \bar{\mathbf{x}}\bar{\mathbf{x}}^T\right)^{(n+1)}$$

3. **(Analysis step)**

(a) Compute the Kalman gain matrix as:

$$K^{(n+1)} = P^{(n+1)}H^T(HP^{(n+1)}H^T + R)^{-1}$$

(b) Update each sample in the predicted ensemble as follows:

$$\mathbf{x}_j^{(n+1)} = \hat{\mathbf{x}}_j^{(n+1)} + K(\mathbf{y} - H\hat{\mathbf{x}}_j^{(n+1)})$$

The vector $\mathbf{y}$ represents observation and H is the observation matrix, which maps state space to the observation space.

4. Repeat the prediction and analysis steps until the ensemble is statistically converged.

Chapter 3

Incorporating Prior Knowledge for Quantifying and Reducing Model-Form Uncertainty in RANS Simulations

(Published on *International Journal of Uncertainty Quantification*, 6 (2): 109-126, 2016.)

J.-X. Wang, J.-L. Wu, H. Xiao
Department of Aerospace and Ocean Engineering, Virgina Tech, Blacksburg, VA, 24061, USA

Abstract

Simulations based on Reynolds-Averaged Navier–Stokes (RANS) models have been used to support high-consequence decisions related to turbulent flows. Apart from the deterministic model predictions, the decision makers are often equally concerned about the prediction confidence. Among the uncertainties in RANS simulations, the model-form uncertainty is an important or even a dominant source. Therefore, quantifying and reducing the model-form uncertainties in RANS simulations are of critical importance to make risk-informed decisions. Researchers in statistics communities have made efforts on this issue by considering numerical models as black boxes. However, this physics-neutral approach is not a most efficient use of data, and is not practical for most engineering problems. Recently, we proposed an open-box, Bayesian framework for quantifying and reducing model-form uncertainties in RANS simulations based on observation data and physics-prior knowledge. It can incorporate the information from the vast body of existing empirical knowledge with mathematical rigor, which enables a more efficient usage of data. In this work, we examine the merits of incorporating various types of prior knowledge in the uncertainties quantification and re-

duction in RANS simulations. The result demonstrates that informative physics-based prior plays an important role in improving the reduction of model-form uncertainties, particularly when the observation data are limited. Moreover, it suggests that the proposed Bayesian framework is an effective way to incorporate empirical knowledge from various sources of turbulence modeling.

3.1 Introduction

In recent years, Computational Fluid Dynamics (CFD) models based on Reynolds-Averaged Navier–Stokes (RANS) equations have been used to support high-consequence decisions related to turbulent flows. For example, RANS simulations have been used to support the development of the emergency evacuation plans in scenarios of pollutant releases in cities [1]. In the nuclear energy industry, government regulators and plant operators have explored the feasibility of using RANS models to model the thermo-hydraulic systems in nuclear power plants to support safety assessments and licensing [2, 3]. In these contexts, quantifying and reducing uncertainties in the RANS simulations is of critical importance for the stake-holders to make risk-informed decisions.

Although the uncertainties in RANS simulations may also occur due to uncertain inputs and parameters, meshes, and numerical methods, the uncertainties that are attributed to the inadequacy and intrinsic assumptions in the physical model of turbulence, referred to as model-form uncertainties, are most challenging to quantify in RANS simulations. Oliver et al. [4] was the first to propose a "composite model theory" in the context of RANS modeling, where the model-form uncertainties are localized to the Reynolds stress tensors. Dow and Wang [5] introduced uncertainties in the turbulent eddy viscosity to estimate the structural uncertainties in the k–ω model [6]. On the other hand, Iaccarino and co-workers [7, 8, 9, 10, 11] introduced uncertainties directly to the Reynolds stress, and estimated the RANS modeling uncertainties by perturbing the predicted Reynolds stress in a physically realizable range.

Recently, Xiao et al. [12] proposed a Bayesian framework for quantifying and reducing uncertainties in RANS simulations by incorporating velocity observation data and physics-based prior knowledge. A key element in this framework is the inference of Reynolds stress discrepancy field from sparse velocity observations. Therefore, it can be considered a Bayesian calibration framework. This is in contrast to Oliver et al. [4] and Iaccarino and co-workers [7], who focused solely on the forward propagation of uncertainties in Reynolds stresses to velocity and other Quantities of Interests (QoIs). On the other hand, the physics-neutral Bayesian framework of Kennedy and O'Hagan [13] treats numerical models as black boxes and does not allow straightforward representation of the prior knowledge [14]. In addition, the available data are usually too sparse in engineering application to drive such physics-neutral approach, which poses a practical hurdle for its acceptance in engineering communities. Compared to the Bayesian model calibration framework of Kennedy and O'Hagan, a notable feature of

the method of Xiao et al. [12] is that it incorporates physics-based prior knowledge, which can effectively augment the information provided by the limited amount of data. Sources of prior knowledge range from constraints that can be expressed with mathematical rigor (e.g., physical realizability of Reynolds stress tensor) to imprecise, subjective beliefs that are not amenable to mathematical representation (e.g., empirical knowledge accumulated in the turbulence modeling from decades of applications of RANS simulations).

The target application scenario of the framework proposed in [12] is the prediction of complex turbulent flows with a limited amount of observation data. The framework enables predictions with quantified uncertainties by combining numerical model simulations and observation data (e.g., real-time measurements from sensors in a nuclear power plant or data from air quality monitoring stations in a city). As in other Bayesian inference frameworks, the posterior distributions of the predicted QoIs depend on both prior information and data. Since the amount of data is limited in the application scenario, the effects of prior knowledge are expected to be particularly important. The objective of this work is to examine the role of incorporating prior knowledge in quantifying and reducing uncertainties in RANS simulations. Meanwhile, we will demonstrate that physics-based prior knowledge can be expressed and incorporated properly within the proposed framework [12].

In the context of RANS modeling, following types of prior knowledge are considered:

1. the assumption that Reynolds stress is the dominant source of uncertainty in RANS equations,
2. physical realizability constraints on Reynolds stress tensors,
3. the symmetry (if any) of the flow of concern,
4. smooth spatial distribution of the Reynolds stresses,
5. overall understanding on the coherent structures of the flow,
6. subjective belief on the discrepancies of predicted Reynolds stress tensors (or more precisely their projections, including the magnitude, shape, and orientation) in different flow regions.

Items 1–2 are strict constraints resulting from the assumption of the modeling and the physical realizability, which can be guaranteed straightforwardly in the uncertainty quantification framework [7]. In contrast, items 3–6 involve analysts' physical understanding and subjective judgment of the flow. The strict constraints are built into the framework of Xiao et al.[12], while proper means are provided for the analyst to specify subjective priors of various precisions. In this study, we show that the inference uncertainties (in Reynolds stresses and other QoIs) are significantly reduced by using realistic, informative priors compared to using non-informative priors. We also show that using more informative priors can lead to similar

inference uncertainty reduction compared to that obtained by incorporating additional observation data. Both comparisons demonstrate that the empirical knowledge accumulated in the turbulence modeling community can be effectively used for quantifying and reducing RANS model uncertainties. Although the importance of prior knowledge is demonstrated specifically in the context of RANS modeling of turbulent flows, it is expected that the conclusions can be extended to other complex physical systems as well.

The remaining of the paper is organized as follows. In Section 2 the framework introduced in [12] is summarized with emphasis on the utilization and representation of prior knowledge. Numerical simulations based on the flow in a channel with periodic constrictions are presented in Section 3 to highlight the importance of informative prior knowledge. In Section 4 we further discuss the mapping of Reynolds stress and mean velocities to show the success and limitation of the framework. Finally, Section 5 concludes the paper.

3.2 Uncertainty Quantification Framework and Representation of Prior Knowledge

Table 3.1: Representation of physics-based prior knowledge in the open-box uncertainty quantification and reduction framework for RANS modeling proposed in [12]

	Prior knowledge	Representation in the framework [12]	Demonstrated in cases
1	Reynolds stress is a dominant uncertainty source in RANS equations	modeling of Reynolds stress as a random field (built into framework)	–
2	physical realizability of Reynolds stresses	parameterization of physical variables, e.g., magnitude and shape of Reynolds stresses (built into framework)	–
3	symmetry of the flow	use of symmetric basis functions in parameterization	–
4	Reynolds stresses have smooth spatial distribution	use of smooth basis functions in parameterization	S1/S2
5	relative discrepancies of Reynolds stresses in different regions	proper choice of spatially varying variance fields $\sigma(\mathbf{x})$ and length scale field $l(\mathbf{x})$ in constructing of a non-stationary Gaussian kernel	D1
6	overall knowledge of the flow	proper design of observation locations (experimental design)	D2

The framework for quantifying and reducing model-form uncertainties in RANS simulations as proposed by Xiao et al. [12] is summarized below, emphasizing the prior knowledge in RANS simulations and their representation in the framework. The prior knowledge that is incorporated in the framework is presented in Table 3.1.

It is a consensus in the turbulence modeling community that discrepancy in the modeled Reynolds stress field is the main source of model-form uncertainties in the RANS equations [15]. Consequently, uncertainties are injected to the Reynolds stress field by perturbing the RANS-modeled Reynolds stress (see Prior 1 in Table 3.1). More precisely, the true Reynolds stress $\boldsymbol{\tau}(\mathbf{x})$ is modeled as a random field with the spatial coordinate $\mathbf{x}$ as index and the RANS-predicted Reynolds stress $\tilde{\boldsymbol{\tau}}^{rans}(\mathbf{x})$ as prior mean. The Reynolds stress at any location is a symmetric tensor. Note that an arbitrary perturbation can lead to a tensor that does not correspond to any physically possible states. Therefore, perturbations are introduced within the realizable states of Reynolds stress based on the physical meaningful projections of the Reynolds stress tensor and not on its individual components. This is to ensure that all realizations of the random field $\boldsymbol{\tau}(\mathbf{x})$ are physically possible (see Prior 2 in Table 3.1). Specifically, the Reynolds stress tensor is transformed to physically interpretable variables as follows:

$$\boldsymbol{\tau} = 2k\left(\frac{1}{3}\mathbf{I} + \mathbf{a}\right) = 2k\left(\frac{1}{3}\mathbf{I} + \mathbf{V}\Lambda\mathbf{V}^T\right) \tag{3.1}$$

where k is the turbulent kinetic energy, which indicates the magnitude of $\boldsymbol{\tau}$; $\mathbf{I}$ is the second order identity tensor; $\mathbf{a}$ is the anisotropy tensor; $\mathbf{V} = [\mathbf{v}_1, \mathbf{v}_2, \mathbf{v}_3]$ and $\Lambda = \mathrm{diag}[\lambda_1, \lambda_2, \lambda_3]$ with $\lambda_1 + \lambda_2 + \lambda_3 = 0$ are the orthonormal eigenvectors and eigenvalues of $\mathbf{a}$, respectively, indicating the shape and orientation of $\boldsymbol{\tau}$. The eigenvalues λ_1, λ_2, and λ_3 are mapped to a Barycentric coordinate (C_1, C_2, C_3) with $C_1 + C_2 + C_3 = 1$. Consequently, all physically realizable states are enclosed in the Barycentric triangle shown in Fig. 6.1a. To facilitate the parameterization, the Barycentric coordinate is further transformed to the natural coordinate (ξ, η), with the triangle mapped to a square as shown in Fig. 6.1b. Finally, uncertainties are introduced to the mapped quantities k, ξ, and η by adding discrepancy terms to the corresponding RANS predictions, i.e.,

$$\log k(\mathbf{x}) = \log \tilde{k}^{rans}(\mathbf{x}) + \delta^k(\mathbf{x}) \tag{3.2a}$$

$$\xi(\mathbf{x}) = \tilde{\xi}^{rans}(\mathbf{x}) + \delta^\xi(\mathbf{x}) \tag{3.2b}$$

$$\eta(\mathbf{x}) = \tilde{\eta}^{rans}(\mathbf{x}) + \delta^\eta(\mathbf{x}) \tag{3.2c}$$

Uncertainties are not introduced into the orientation $(\mathbf{v}_1, \mathbf{v}_2, \mathbf{v}_3)$ of the Reynolds stress. This is because the perturbations of angles may result in a reconstructed Reynolds stress that has the momentum flux from the low momentum cell to the high momentum cell, which has the similar effect as a reverse diffusion term. This effect may lead to unphysical solutions.

The smooth spatial distribution of the Reynolds stress is another constraint. The smoothness is guaranteed by constructing the Reynolds stress discrepancy fields δ^k, δ^ξ, and δ^η (denoted as

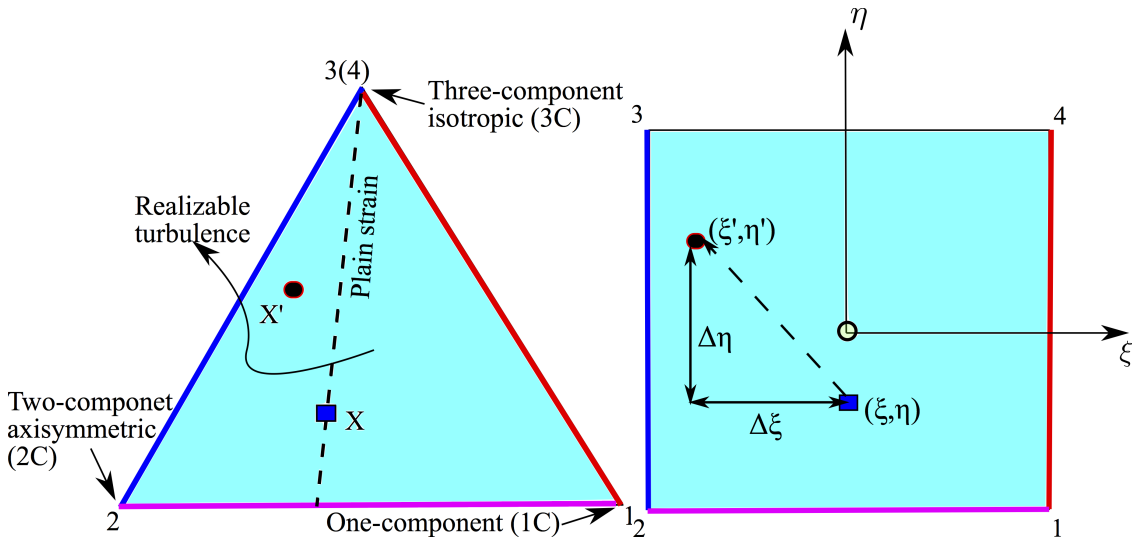

(a) Barycentric coordinate (b) natural coordinate

Figure 3.1: Mapping between the Barycentric coordinate to the natural coordinate, transforming the Barycentric triangle enclosing all physically realizable states [16, 10] to a square via standard finite element shape functions. Corresponding edges in the two coordinates are indicated with matching colors.

δ generically below) with smooth basis functions (see Priors 3 and 4 in Table 3.1). Specifically, the prior distributions of the discrepancies are chosen as non-stationary zero-mean Gaussian random fields $\mathcal{GP}(0, K)$ (also known as Gaussian processes), where

$$K(\mathbf{x}, \mathbf{x}') = \sigma(\mathbf{x})\sigma(\mathbf{x}') \exp\left(-\frac{|\mathbf{x} - \mathbf{x}'|^2}{l^2}\right) \tag{3.3}$$

is the kernel indicating the covariance at two locations $\mathbf{x}$ and $\mathbf{x}'$. The variance $\sigma(\mathbf{x})$ can be specified as a spatially varying field (see the contour in Fig. 5.2 for example) to reflect the prior knowledge on relative discrepancies of modeled Reynolds stress in different flow regions (see Prior 5 in Table 3.1). The correlation length scale l can be specified based on the local turbulence length scale, but is taken as a constant in this work for simplicity.

The basis set is chosen as the eigenfunctions of the kernel K computed from the Fredholm integral [17]. This choice of basis function leads to the Karhunen–Loeve (KL) expansion of the random field. That is, the discrepancy fields δ can be represented as follows [12]:

$$\delta(\mathbf{x}, \theta) = \sum_{i=1}^{\infty} \omega_i|_\theta \, \phi_i(\mathbf{x}), \tag{3.4}$$

where $\phi_i(\mathbf{x})$ are deterministic spatial basis functions, and the coefficients ω_i (denoting $\omega_{k,i}$, $\omega_{\xi,i}$, $\omega_{\eta,i}$) are random variables depending on the realization outcome of θ. The prior dis-

tributions for these coefficients are independent standard Gaussian ones. In practice the infinite series is truncated to m terms, with m depending on the smoothness of the kernel K.

With the decomposition above, the Reynolds stress field is modeled as the random fields with RANS modeled Reynolds stress as prior mean and the discrepancies parameterized by the coefficients $\omega_{k,i}$, $\omega_{\xi,i}$, $\omega_{\eta,i}$ with $i = 1, 2, \cdots, m$. The uncertainty distributions of the coefficients are then inferred by using an iterative ensemble Kalman method, which is an approximate Bayesian inference method widely used for data assimilation in geoscience communities [18]. In this method the prior distribution of Reynolds stresses (as parameterized by the coefficients) is first represented by samples drawn from the prior distribution. The collection of samples, referred to as prior ensemble, is propagated to velocities by using a forward RANS solver `tauFoam`, which computes velocities from a given Reynolds stress field. This forward RANS solver is developed based on a conventional steady-state RANS solver in OpenFOAM by replacing the turbulence modeling component (i.e., solution of the transport equations for turbulence quantities) with a supplied Reynolds stress field. With the predicted ensemble of the forward RANS solver, the Kalman filtering procedure is used to incorporate velocity observation data to the prediction, yielding a corrected ensemble. The procedure is repeated until statistical convergence is achieved. The converged posterior ensemble is a sample-based representation of the uncertainty distribution of the Reynolds stresses and other quantities of interests given the observation data. For the scenarios as mentioned above, the amount of data used in the inference procedure is limited. Therefore, proper arrangement of observation locations (i.e., experimental design) is important. The prior knowledge on the overall feature of the flow can be incorporated as a guidance to conduct the experimental design, which leads to a more effective use of data. (see Prior 6 in Table 3.1).

3.3 Numerical Simulations

3.3.1 Problem Setup

The flow over periodic hills at Reynolds number $Re_b = 2800$ is studied to demonstrate the merits of incorporating physics-based prior knowledge in quantifying and reducing the model-form uncertainties in RANS simulations. Direct numerical simulation (DNS) data [19] are adopted as the benchmark for comparison. The computational domain is shown in Fig. 5.2, where all dimensions are normalized with the crest height H. The Reynolds number Re_b is based on the height H and bulk velocity U_b at the crest.

In addition to the DNS benchmark data, synthetic benchmark data are also utilized in this study, which is created from the RANS model with a specified Reynolds stresses perturbation. The reason of using synthetic truth is that we can control the dimensions of the uncertainty space and thus are able to explore its effects upon the result. Moreover, the coefficients vector $\boldsymbol{\omega}$ is known from the synthetic truth, which can be used to verify the proposed inversion

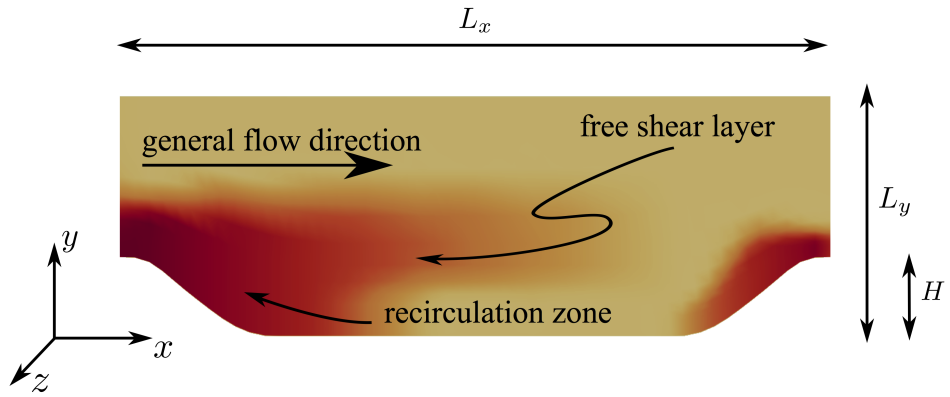

Figure 3.2: Domain shape for the flow in the channel with periodic hills. The x-, y- and z-coordinates are aligned with the streamwise, wall-normal, and spanwise directions, respectively. All dimensions are normalized by H with $L_x/H = 9$ and $L_y/H = 3.036$. The contour shows the variance field $\sigma(\mathbf{x})$, where darker color represents larger variance.

scheme. To generate the synthetic truth, we use the standard RANS simulation outputs as baseline and perturb the Reynolds stress field with specified δ^ξ, δ^η, and δ^k. For simplicity, we only perturb the η with δ^η constructed from two KL modes with coefficients $\hat{\boldsymbol{\omega}}_\eta = [\hat{\omega}_{\eta,1}, \hat{\omega}_{\eta,2}]$, where $\hat{\omega}_{\eta,1} = 1.5$, $\hat{\omega}_{\eta,2} = 1.0$, and $\hat{\cdot}$ denotes synthetic truth. Notice that the fundamental difference between the synthetic truth and DNS benchmark is whether the uncertainty space spanned by the prior ensemble covers the true Reynolds stresses. For synthetic truth, the prior can cover the truth since we know where it resides. However, the uncertainty space does not necessarily cover the true Reynolds stresses that generate DNS velocity benchmark. This is because the orientations of the Reynolds stresses are not perturbed and that the KL modes are truncated.

The observation data are obtained by sparsely observing the velocity fields of the truth. Independent and identically distributed Gaussian random noises with standard deviation σ_{obs} are added to represent the observation errors. The observations generated from synthetic truth are referred to as "synthetic observation", while those observed from DNS data are denoted as "DNS observation". In the following, four cases are studied to investigate the effects of incorporating the prior knowledge into the framework. In Sec. 3.3.2, two cases S1 and S2 are studied, where synthetic observation data are adopted to explore the effects of prior knowledge on the dimension of uncertainty space. We span a less informative searching space (i.e., prior uncertainty space with a high dimension) in case S1, while we span a more informative searching space (i.e., prior uncertainty space with a low dimension) in case S2. Note that the prior uncertainty spaces cover the synthetic truth in both cases. In Sec. 3.3.3, two cases D1 and D2 with DNS observations are studied to investigate the merits of physics-based prior of the variance field $\sigma(\mathbf{x})$ (see Prior 5 in Table 3.1). The cases D1 and D2 are performed with the same parameters and setup except for different variance fields. In case D2, the empirical knowledge on the $\sigma(\mathbf{x})$ fields, shown in Fig. 5.2, are incorporated

into the framework, which is in contrast to a uniform $\sigma(\mathbf{x})$ field in the case D1. In addition, two scenarios of case D2 with different arrangements of the observation locations are investigated to demonstrate the merits of physics-based knowledge on experimental design in Sec. 3.3.4 (also see Prior 6 in Table 3.1). The mesh and computational parameters used in the uncertainty quantification and reduction procedure are summarized in Table 3.2. The uncertainties in Reynolds stress anisotropy (ξ and η) and amplitude (k) are all considered in cases D1 and D2. The correlation length scale l is chosen based on the length scale of the flow, which can be determined from the physical understanding of the flow. In synthetic cases, the length scale l is larger to achieve a lower dimensional uncertainty searching space. For each case, a prior ensemble of 60 samples is employed.

Table 3.2: Mesh and computational parameters used in the flow over periodic hills.

cases	S1	S2	D1	D2
fields with uncertainty	ξ, η, k	η	ξ, η, k	
number of modes	18	2	48	
correlation length scale l/H[(a)]	5		1	
number of observations	16		18	
variance field $\sigma(\mathbf{x})$	Non-informative ($\sigma(\mathbf{x})$ = constant)			Informative[(b)]
σ_{obs} of observation noises	10% of truth			
RANS mesh ($n_x \times n_y$)	50×30			
number of samples N	60			

(a) see Eq. 5.4, the length scale is normalized by hill crest heigth H.
(b) $\sigma(\mathbf{x})$ as shown in Fig. 5.2

3.3.2 Prior Knowledge on Dimensionality of Uncertainty Space

Under most circumstances, the exact dimension of the uncertainty space where the truth resides is unknown. In order to cover the truth, we commonly span the uncertainty space with a higher dimension. In case S1, the inversion is conducted in the uncertainties space expanded in both the shape and amplitude of $\boldsymbol{\tau}$ (i.e., ξ, η and k) with six KL modes for each field. Therefore, the uncertainty space has a higher dimension (18 modes) than that of the exact space where the synthetic truth resides (2 modes). The prior ensemble of Reynolds stress perturbed in this uncertainty space is obtained, whose component τ_{xy} is shown in Fig. 3.3a. It can be seen that the sample mean of τ_{xy} nearly coincides with the baseline results, and the region of ensemble covers the truth. This evidence indicates that the ensemble is sufficient to represent the prior distribution. It also can be seen that the prior sample mean is biased compared with the truth. By performing the model evaluations based on the samples of the prior Reynolds stresses, the prior velocity ensemble is obtained. Figure 3.4a presents the prior ensemble of velocities U_x, which is scattered due to the large

uncertainties in prior $\boldsymbol{\tau}$ ensemble.

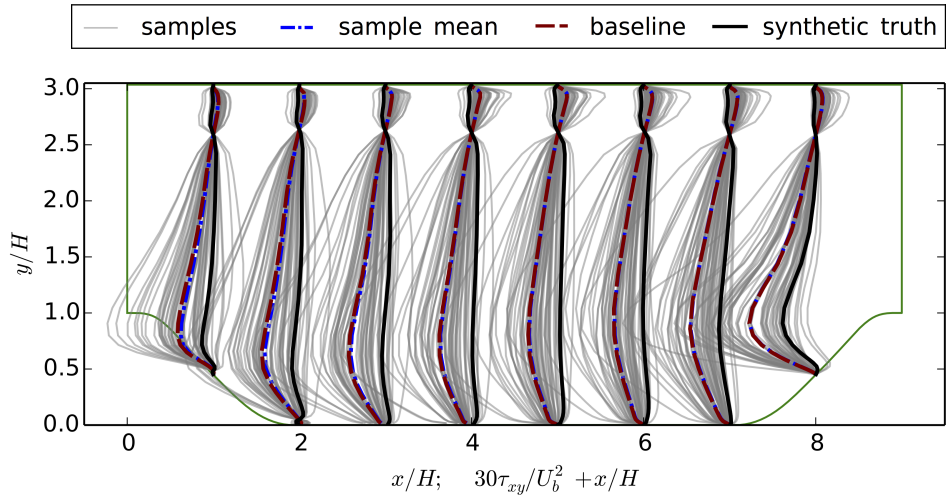

(a) Prior Reynolds stress ensemble

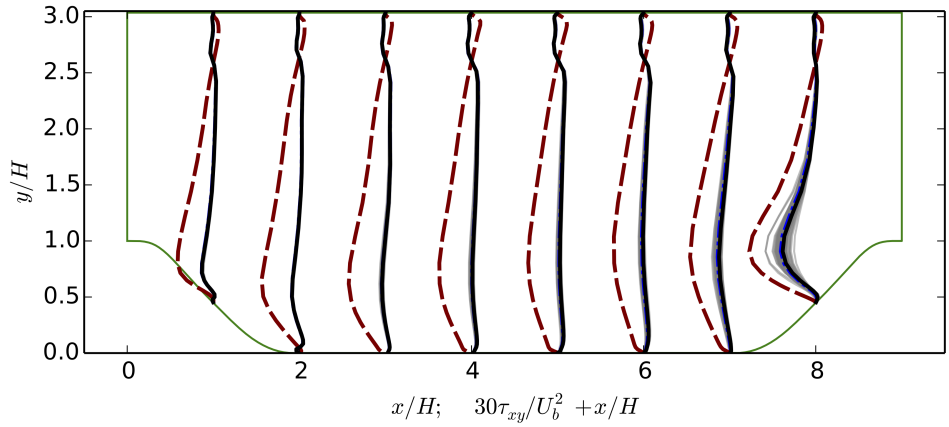

(b) Posterior Reynolds stress ensemble

Figure 3.3: The Prior and posterior ensembles of τ_{xy} profiles of case S1, in which the synthetic truth is used and the searching space is larger than the uncertainty space where the truth resides. The ensemble profiles are shown at eight locations $x/H = 1, \cdots, 8$, compared with synthetic truth and baseline results. In panel (b), the samples and sample mean overlap with the synthetic truth in most of the locations.

Synthetic observations of velocities at 16 locations along the line of $x/H = 2$ (shown in Fig. 3.4) are used for inference. Figure 3.3b shows the posterior τ_{xy} ensemble. We can see that its scattering is significantly reduced and all samples converge to the synthetic truth. However, some uncertainties still exist in the posterior Reynolds stress τ_{xy} and are slightly larger in the regions further away from the observed locations. This indicates that the corrections on the prior ensemble become less effective, because when the observed and unobserved locations have a larger distance, the spatial correlations between the two are

weak.

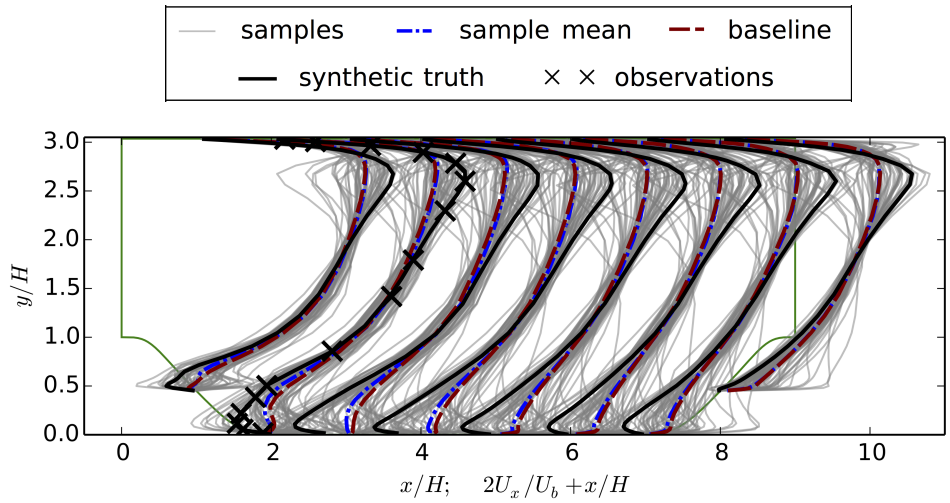

(a) Prior velocities ensemble

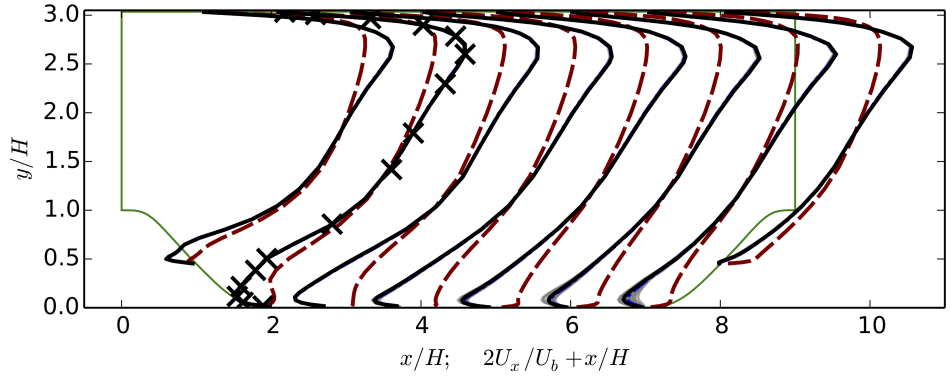

(b) Posterior velocities ensemble

Figure 3.4: The Prior and posterior ensembles of velocity profiles of case S1. The locations where velocities are observed are indicated with $\times$. The ensemble profiles are shown at eight locations $x/H = 1, \cdots, 8$, compared with synthetic truth and baseline results. In panel (b), all the posterior samples are collapsed to the synthetic truth, and the corresponding lines are overlapped.

Figure 3.4b shows the posterior velocity U_x profiles, which collapse to the truth. Although uncertainties still exist in the posterior Reynolds stresses (e.g., at $x/H = 8$ in Fig. 3.3), the velocities obtained based on these Reynolds stress samples are less scattered. The reason is likely to be that the mapping from Reynolds stress to velocity is not unique, and different Reynolds stress fields may map to the similar velocity fields. This issue will be further discussed in Sec. 3.4

The uncertainty reduction process in the proposed framework is the inversion of the modes coefficients $\boldsymbol{\omega}$ for the Reynolds stresses discrepancy $\delta\boldsymbol{\tau}$. Since the posterior velocity has a

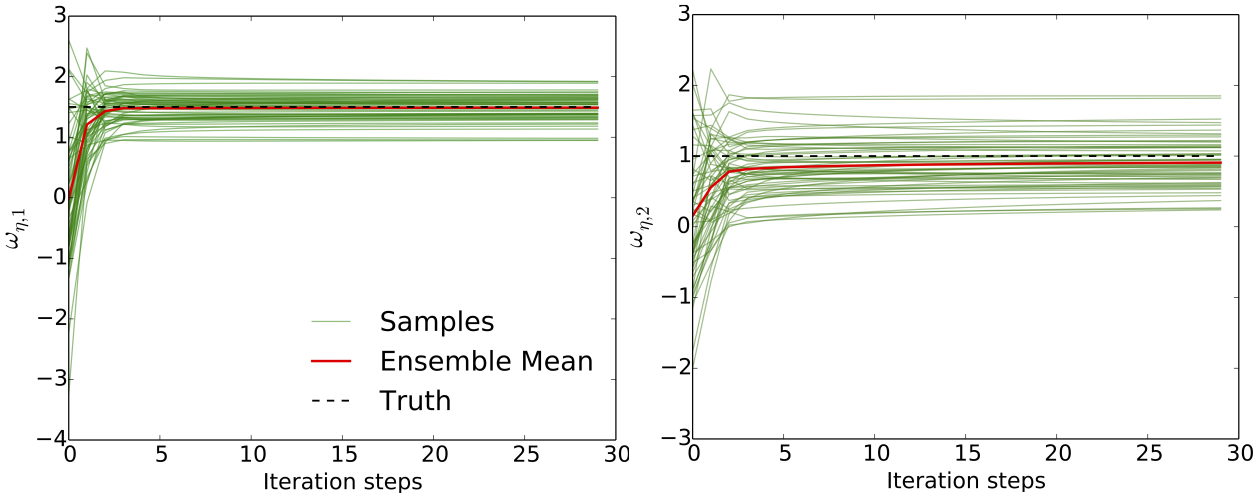

(a) Ensemble of ω for the 1$^{\text{st}}$ mode of δ^{η}

(b) Ensemble of ω for the 2$^{\text{nd}}$ mode of δ^{η}

Figure 3.5: Convergence histories of unknown parameters $\omega_{\eta,1}$ and $\omega_{\eta,2}$, which are the coefficients for the 1^{st} and 2^{nd} modes of δ^{η}, respectively, for case S1. The true coefficients for this synthetic case are indicated by the dashed lines.

good agreement with its truth, it is anticipated that the posterior of $\boldsymbol{\omega}$ should also converge to the truth. This anticipation can be verified in the synthetic cases S1 and S2 where the true values of coefficients ($\hat{\omega}_{\eta,1} = 1.5$ and $\hat{\omega}_{\eta,1} = 1.0$) are known. The convergence history of coefficients ensembles ($\omega_{\eta,1}$ and $\omega_{\eta,2}$) is presented in Fig. 3.5. It shows that most samples in the $\omega_{\eta,1}$ and $\omega_{\eta,2}$ ensembles are initially scattered from -2 to 2, due to the fact that they are drawn from the standard normal distribution $\mathcal{N}(0,1)$. The initial mean values of $\omega_{\eta,1}$ and $\omega_{\eta,2}$ are both zero, which are biased compared to their respective truths. Nonetheless, the ensemble mean values converge to the truths within only a few iterations, and the scattering of the samples are slightly reduced for both coefficients. The convergence of the inferred coefficients results in the successful correction of the velocity field with reduced uncertainties. By comparing Figs. 3.5a and 3.5b, we find that the converged $\omega_{\eta,2}$ ensemble has a slightly larger variance than that of the $\omega_{\eta,1}$ ensemble, which means that the posterior uncertainty of $\omega_{\eta,2}$ is slightly larger. This is because the KL modes used to construct the random fields are not equally weighted. The higher modes are less important than the lower modes. Therefore, the coefficients for the higher modes are less sensitive to observations in the inversion process.

In case S1, uncertainties still exist in the posterior coefficients of KL modes and thus in the posterior Reynolds stresses ensembles. This is because the prior ensemble is sampled in an uncertainty space with a higher dimension than that the truth resides in. This situation is typical in practical scenarios, since the truth is unknown for most non-trivial problems. Therefore, the inversion is started from a larger searching space to ensure the coverage of the truth. However, if the dimension of uncertainty space can be reduced based on prior

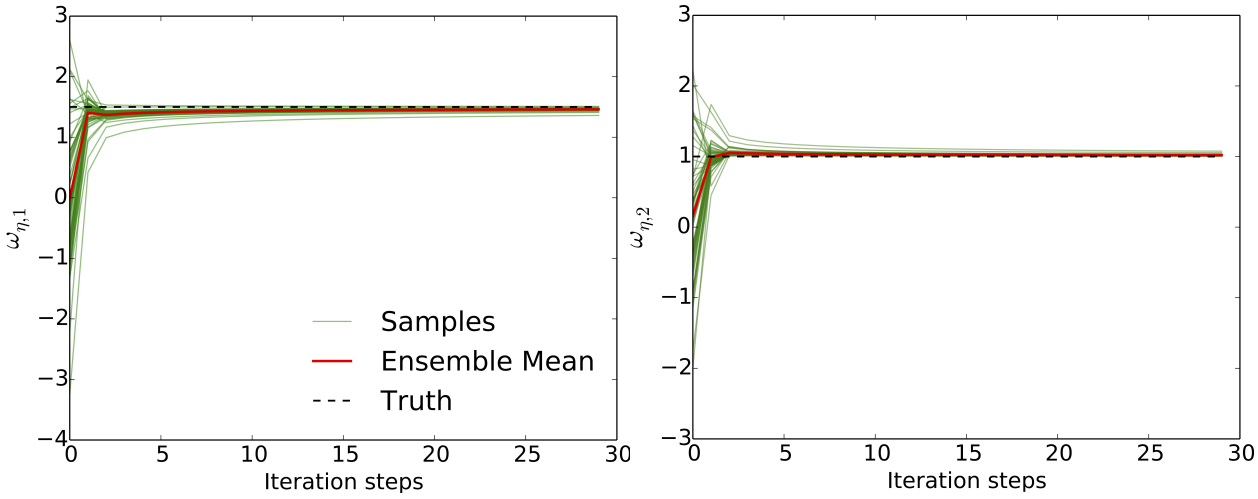

(a) Ensemble of ω for the 1st mode of δ^{η} (b) Ensemble of ω for the 2nd mode of δ^{η}

Figure 3.6: Convergence histories of unknown parameters $\omega_{\eta,1}$ and $\omega_{\eta,2}$ for case S2. The searching space in this synthetic case is smaller than that of case S1. The synthetic truths are indicated by the dashed lines.

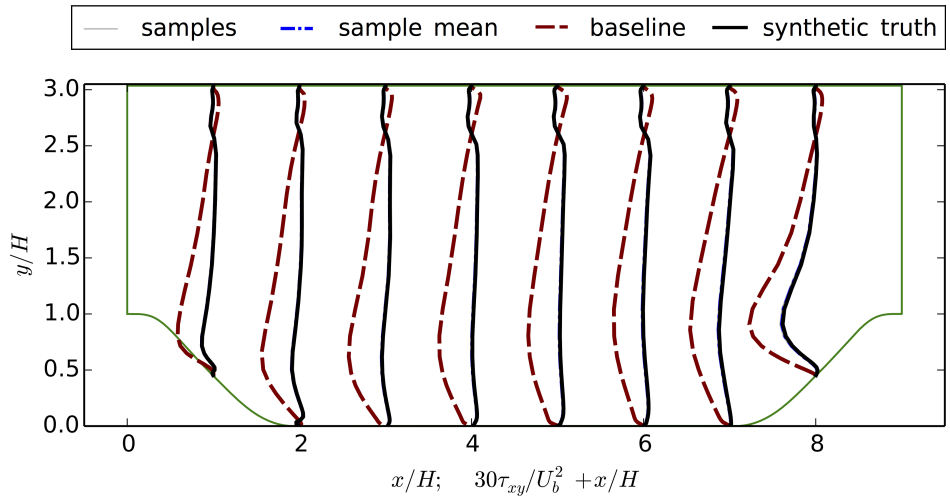

Figure 3.7: The posterior ensembles of τ_{xy} profiles of case S2, in which the synthetic truth is used and the searching space is the same as the uncertainty space where truth resides. The ensemble profiles are shown at eight locations $x/H = 1, \cdots, 8$, compared with synthetic truth and baseline results. The prior ensemble is the same as that of case S1 and is omitted for simplicity. All of the samples are collapsed to the truth, and thus the corresponding lines of samples and sample mean overlap with the synthetic truth.

knowledge, the uncertainties of the inversion results can be further reduced. We demonstrate this statement with case S2, in which the inversion is performed in a low-dimensional uncertainty space where the synthetic truth resides. In order to search this low-dimensional space, the prior ensemble is generated in the space spanned by two KL modes of the $\eta(\mathbf{x})$ field. All other computational parameters are the same as those in case S1. Figure 3.6 shows the convergence of the coefficients for the first and second modes of η. The coefficients $\omega_{\eta,1}$ and $\omega_{\eta,2}$ ensembles almost exactly converge to the synthetic truths, which is in contrast to Fig. 3.5. In addition, comparison of Fig. 3.7 and Fig. 3.3b shows that the uncertainties in the posterior Reynolds stress component τ_{xy} are reduced. The posterior uncertainties are larger in the case where the searching space has higher dimension, especially in the regions far away from the observed location, e.g., along the line at $x/H = 8$. With the same amount of observation data, the inference uncertainties are reduced by narrowing down the dimension of searching space. The reason is that higher dimensional uncertainty space means more degrees of freedom that need to be inferred, which may lead to an ill-posed problem and pose a challenge for the inversion.

3.3.3 Prior Knowledge on Variance Field $\sigma(\mathbf{x})$

The spatial field of the perturbation variance $\sigma(\mathbf{x})$ for ξ, η and k reflects analyst's prior belief on the uncertainty range at each location. If the knowledge on it is not available a priori, we can choose a non-informative prior with a uniform variance field $\sigma(\mathbf{x})$. However, for most flow problems, we usually have some empirical knowledge. For example, in the case of flow over periodic hills, there are some regions where RANS models are known to give poor predictions, e.g., regions with recirculation, non-parallel free-shear flow, and the strong mean flow curvature. The variance field $\sigma(\mathbf{x})$ shown in Fig. 5.2 is designed to reflect this empirical knowledge. It can be seen that in the free-shear layer and recirculation zone, larger perturbations of Reynolds stresses are allowed, while the baseline RANS Reynolds stresses in other regions are assumed to be relatively reliable.

The prior of velocity profiles obtained based on non-informative and informative variance fields are shown in Figs. 3.8a and 3.8b, respectively. It can be seen that the velocity samples are appreciably scattered in the entire domain if uniform $\sigma(\mathbf{x})$ is employed. Such a large scattering is attributed to the lack of physical prior knowledge. In contrast, the scattering of the prior velocity profiles is constrained by incorporating the physical knowledge on the variance field. This is shown in Fig. 3.8b. Therefore, the prior with uniform $\sigma(\mathbf{x})$ field has an uncertainty space with spatially equal variance, while the uncertainties are reduced in the regions where RANS predictions are more accurate based on the informative $\sigma(\mathbf{x})$ field. The merits of incorporating empirical knowledge can be clearly demonstrated by comparing the posterior velocity profiles of cases D1 and D2, which are shown in Figs. 3.9a and 3.9b, respectively. Compared to the prior velocity profiles, both posterior results are improved since all of the velocities samples converge to the DNS benchmark, and their scattering is largely reduced. This indicates that the proposed framework improves the model predictions

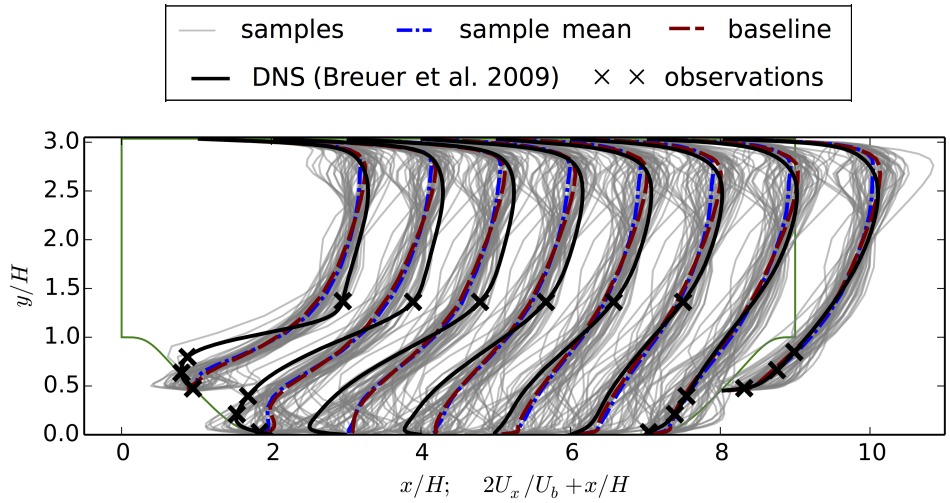

(a) U_x with non-informative $\sigma(\mathbf{x})$

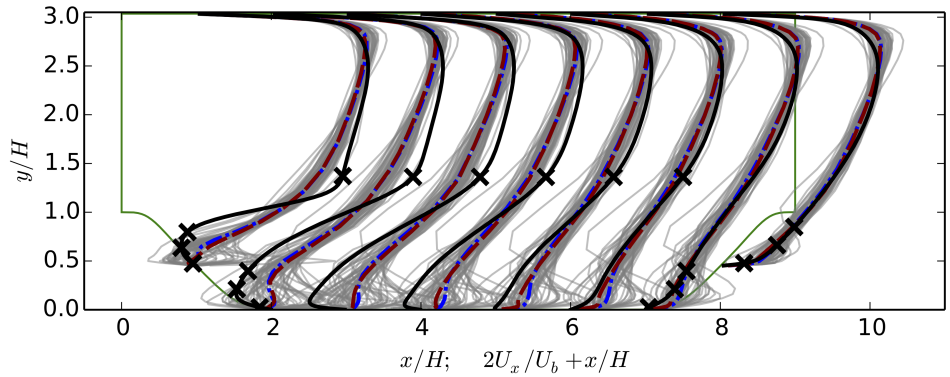

(b) U_x with informative $\sigma(\mathbf{x})$

Figure 3.8: The prior ensembles of velocity U_x profiles of case D1 and case D2, in which the observations are from DNS benchmark. (a) The variance field $\sigma(\mathbf{x})$ of case D1 is spatially uniform ($\sigma(\mathbf{x}) = 0.7$), (b) The variance field $\sigma(\mathbf{x})$ of case D2 is informative ($\sigma_{min} = 0.2$, $\sigma_{max} = 0.7$). The ensemble profiles are shown at eight locations $x/H = 1, \cdots, 8$, compared with the baseline results and DNS benchmark. The locations where velocities are observed are indicated with $\times$.

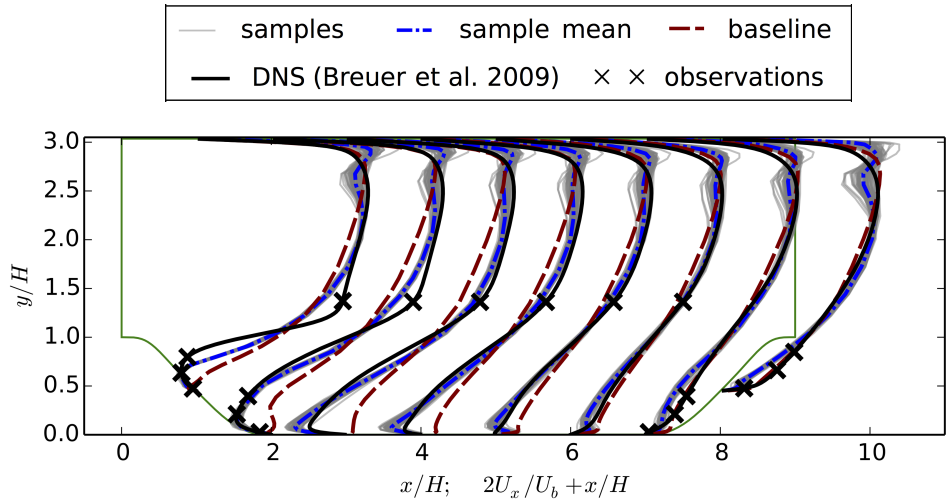

(a) U_x with non-informative $\sigma(\mathbf{x})$

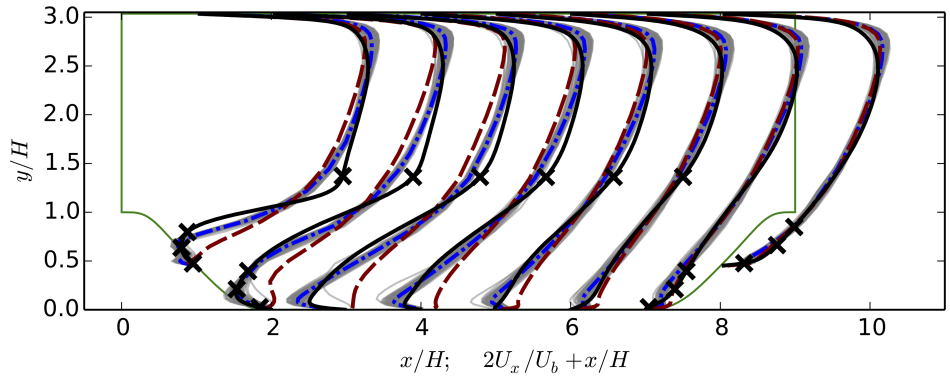

(b) U_x with informative $\sigma(\mathbf{x})$

Figure 3.9: The posterior ensembles of velocity U_x profiles of case D1 and case D2, in which the observations are from DNS benchmark. (a) The variance field $\sigma(\mathbf{x})$ of case D1 is spatially uniform ($\sigma(\mathbf{x}) = 0.7$), (b) The variance field $\sigma(\mathbf{x})$ of case D2 is informative ($\sigma_{min} = 0.2$, $\sigma_{max} = 0.7$). The ensemble profiles are shown at eight locations $x/H = 1, \cdots, 8$, compared with the baseline results and DNS benchmark. The locations where velocities are observed are indicated with $\times$.

(especially in the recirculation regions) even with a non-informative variance field, i.e., a constant $\sigma(\mathbf{x})$. However, in Fig. 3.9a, the scattering of posterior velocity samples obtained with the uniform $\sigma(\mathbf{x})$ field is still larger than that with informative $\sigma(\mathbf{x})$ field in case S2 (shown in Fig. 3.9b). Especially near the top of the domain, the uncertainty in velocity ensemble is even larger and the sample mean velocity is slightly distorted compared to the truth and is unphysical. The reason is that the $\sigma(\mathbf{x})$ field introduces relatively large perturbation in this region, where no observation is available nearby to constrain the uncertainties in the posterior ensemble. In contrast, the results obtained with an informative prior shown in Fig. 3.9b has a much better agreement with the truth in the region near the upper wall. It shows that the posterior distribution can be improved by adopting an informative variance field with prior knowledge, as it reduces unnecessary perturbations.

Figures 3.10a and 3.10b show the posteriors of the other two QoIs, wall shear stress τ_w and reattachment point x_{attach}, for cases D1 and D2, respectively. We can see that both τ_w and x_{attach} obtained from baseline RANS simulation deviate from the DNS benchmark significantly. The RANS predicted recirculation region is much smaller than the truth. The posterior means of reattachment point x_{attach} of both cases D1 and D2 have better agreements with the truth. However, the posterior distribution of x_{attach} obtained with the non-informative $\sigma(\mathbf{x})$ is overconfident with a bias, which can be clearly seen in the comparison of probability density functions (PDF) as shown in Fig. 3.10c. The x_{attach} distribution barely covers the truth and the mean is biased. Specifically, it can be seen in Fig. 3.10a that τ_w is overcorrected from $x/H = 2.5$ to $x/H = 4$ and undercorrected from $x/H = 4.5$ to $x/H = 7.5$. Significant improvement is achieved when an informative $\sigma(\mathbf{x})$ is adopted, which is shown in Figs. 3.10b and 3.10d. We can see that in most part of the region (between $x/H = 1$ and 8), the posterior ensemble has a better agreement with the benchmark. Moreover, the posterior PDF is wider than that of case D2 and well covers the truth, indicating that the overconfidence existed in Fig. 3.10c is reduced. All of these results demonstrate the merits of incorporating empirical knowledge into the $\sigma(\mathbf{x})$ field. It is noted that in the vicinity of the hill crest (i.e., near $x/H = 0.5$ and $x/H = 8.5$), the posterior ensembles of both cases show less improvement. This is because the flow in the region with rapid spatial variations has a relative small length scale and thus a weak correlation with the flow in other regions. Consequently, the corrections are not effective due to the weak correlations between this region and the regions with observations.

3.3.4 Prior Knowledge on Experimental Design

In addition to the amount of observation data, the arrangement of observed locations is also a crucial factor, as it affects the inversion results of model discrepancy and corresponding corrections to the predicted flow field. Since the model discrepancies vary location by location, the observed information is weighted. Designing the layout of the measuring points to achieve a more effective use of observation data is referred to as "experimental design". In this section we will demonstrate that prior knowledge will also improve the experimen-

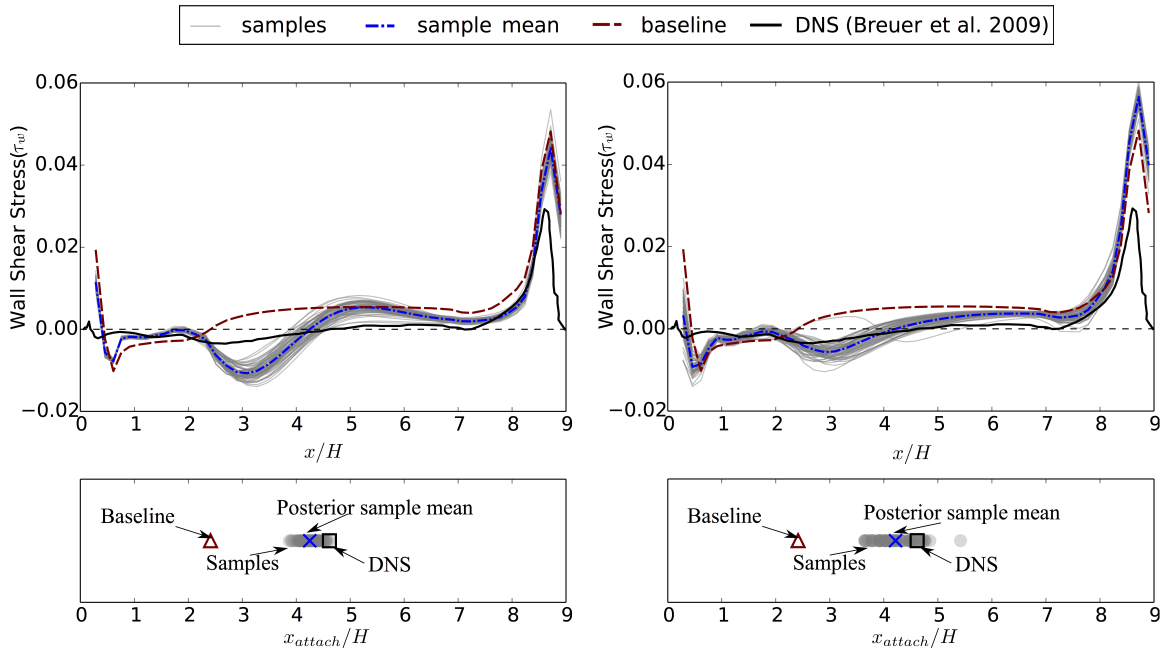

(a) Wall shear stress of case D1

(b) Wall shear stress of case D2

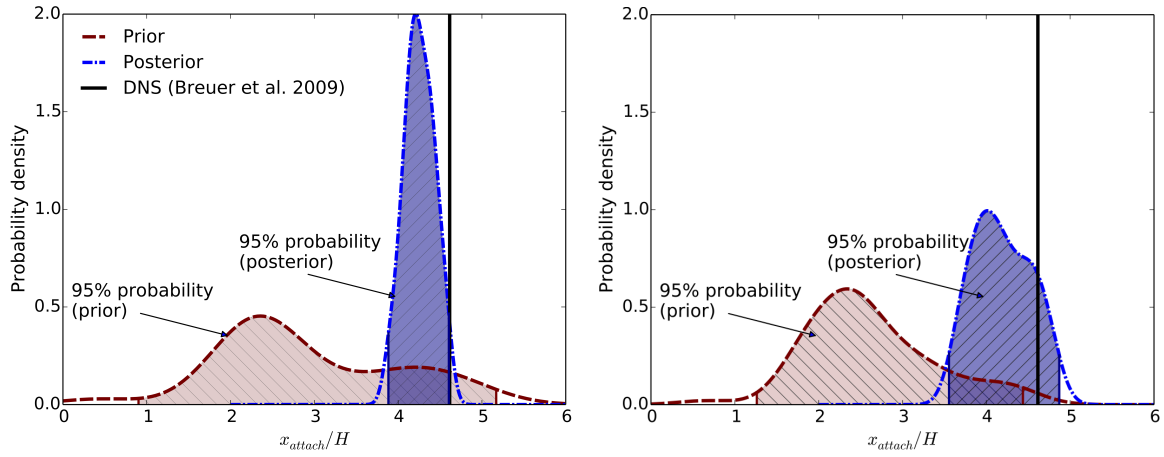

(c) Reattachment point of case D1

(d) Reattachment point of case D2

Figure 3.10: The posterior wall shear stress and reattachment point obtained with uniform, non-informative σ field (case D1) and from informative σ field (case D2). The change of wall shear stress from negative to positive indicates the end of the recirculation zone. (a) Wall shear stress of case D1; (b) Wall shear stress of case D2; (c) Reattachment point of case D1; (d) Reattachment point of case D2.

tal design for quantifying and reducing the model-form uncertainties. Two principles for experimental design should be mentioned in the proposed framework. First, the observations should be placed in the regions where the RANS predictions are relatively unreliable (e.g., the recirculation area). Second, more observations should be allocated to the regions where the length scale of flow is small. This is because the inference and correction of model discrepancies in the unobserved regions are based on their correlations with the observed locations. To demonstrate the effects of prior knowledge in the experimental design, another scenario of case D2 with a different arrangement of observations is investigated. Instead of placing the observations with informative prior based on two principles mentioned above, we uniformly arrange the same number of observations used in the case D2 in the entire flow field, which are shown in Fig. 3.11a.

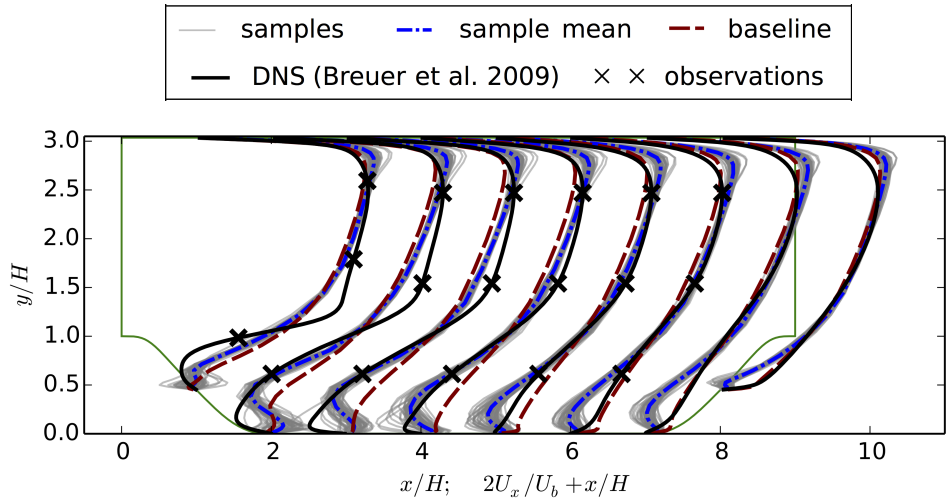

(a) U_x with non-informative experimental design

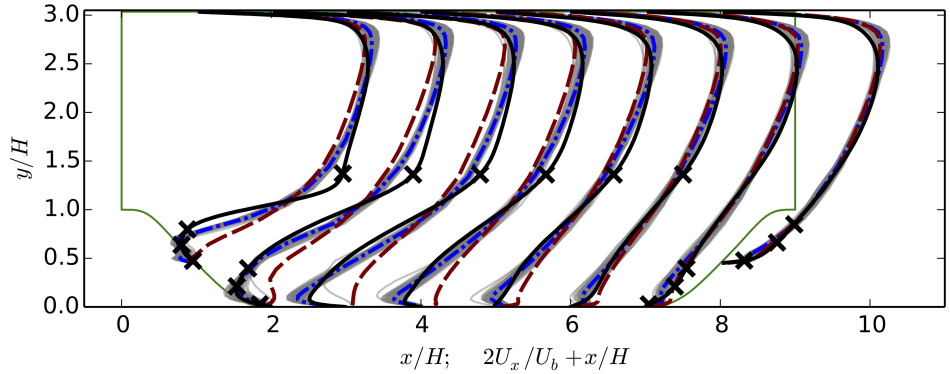

(b) U_x with informative experimental design

Figure 3.11: The posterior velocity U_x profiles of case D2. (a) The observations are uniformly arranged across the domain; (b) The observations are arranged based on the prior knowledge of the flow. The total numbers of observations in (a) and (b) are the same.

The posterior velocity profiles of case D2 with non-informative and informative experimental

designs are compared in Figs. 3.11a and 3.11b, respectively. Figure 3.11a shows that the bias in the recirculation zone is only partially corrected with a uniform layout of observations. The reverse flow near the wall ($y/H < 0.5$) is still poorly predicted, since no observation is available in the nearby region. Moreover, overcorrection can be seen in the downstream ($x/H > 5$), where the baseline RANS prediction is relatively accurate. The reason is that the length scale of flow in the near wall region is small, while no observation is placed in the windward side of hills ($x/H = 7$ to 8). Consequently, the spatial correlation is not strong enough to correct the profiles and constrain the uncertainties by incorporating the information from the observations.

3.4 Discussion

3.4.1 Effect of Observation Data Versus Effect of Empirical Prior Knowledge

In Bayesian frameworks, uncertainties in the posterior distribution can be reduced by incorporating observation data. This statement can be confirmed by exploring another scenario of case S1 in which the velocities at additional 16 points at $x/H = 7$ are observed. Figure 3.12 shows the inferred posterior ensemble of Reynolds stress component τ_{xy} with more observation data. By comparing Figs. 3.3b and 3.12, we can see that the scattering of the samples is significantly reduced with more observation data, especially near the regions where the additional observation points are introduced. Therefore, incorporating more observation data improves the inferred quantities (i.e., Reynolds stress) and reduces the corresponding uncertainties.

However, for most engineering problems the amount of data is limited and is insufficient to drive a physics-neutral, data-based statistical frameworks proposed in the statistical community. On the other hand, empirical knowledge is available for many practical applications thanks to the accumulated experiences in the engineering community. We claim that an important advantage of the proposed framework is to provide a rigorous Bayesian approach incorporating various sources of empirical knowledge. The incorporated empirical knowledge complements the inadequate observation data and thus further reduces the model-form uncertainties in RANS simulations.

3.4.2 Non-Uniqueness of Mapping from Inferred Quantities to Observed Quantities

An essential component of the proposed model-form uncertainty quantification and reduction framework is the inversion of discrepancies in the Reynolds stress tensor. However, the

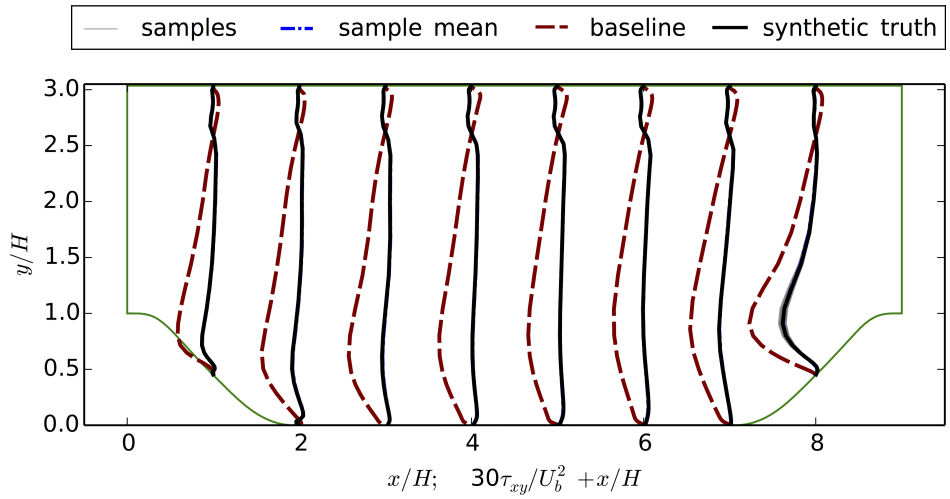

Figure 3.12: The posterior ensembles of τ_{xy} profiles of case S1 with more velocity observations (32 compared to 16 in the original case S1). The ensemble profiles are shown at eight locations $x/H = 1, \cdots, 8$, compared with synthetic truth and baseline results. All of the samples are collapsed to the truth, and thus the corresponding lines of samples and sample mean overlap with the synthetic truth.

inferred quantities (i.e., discrepancy in the Reynolds stress field) do not uniquely map to the corresponding observed quantities (i.e., velocities). This is due to the ill-possedness of the problem. That is, the mapping from velocity field to Reynolds stress field has multiple solutions. Such ill-possedness is common in many inversion problems [20].

The non-unique mapping can be demonstrated by the case S1. As shown in Fig. 3.4, the posterior velocity profiles converge to the truth and the uncertainties (i.e., scattering of velocity samples) are nearly eliminated based on the synthetic observation data. However, the inferred ensemble of modes coefficients for Reynolds stress discrepancy are still scattered (shown in Fig. 3.5). This evidence implies that the Reynolds stress fields are still scattered, even though the corresponding velocity fields are almost the same. The scattering of Reynolds stress fields also can be seen clearly in posterior ensemble of τ_{xx}, shown in Fig. 3.13. The scattering range of posterior τ_{xx} ensemble is large in the entire domain, which indicates the velocities are not sensitive to τ_{xx} in this problem. Nonetheless, based on the concept of "goal-oriented uncertainty quantification" [21], the merits of proposed framework can be justified depending on the quantities of interest (QoI). If QoI is the velocity field or wall shear stress, the predicted results are significantly improved through the framework. On the other hand, if the Reynolds stress is the QoI, more prior knowledge or observation data are needed to constrain the problem of ill-posedness. It has been shown in case S1 that the true Reynolds stress can also be inferred exactly, so long as sufficient data and prior knowledge are given.

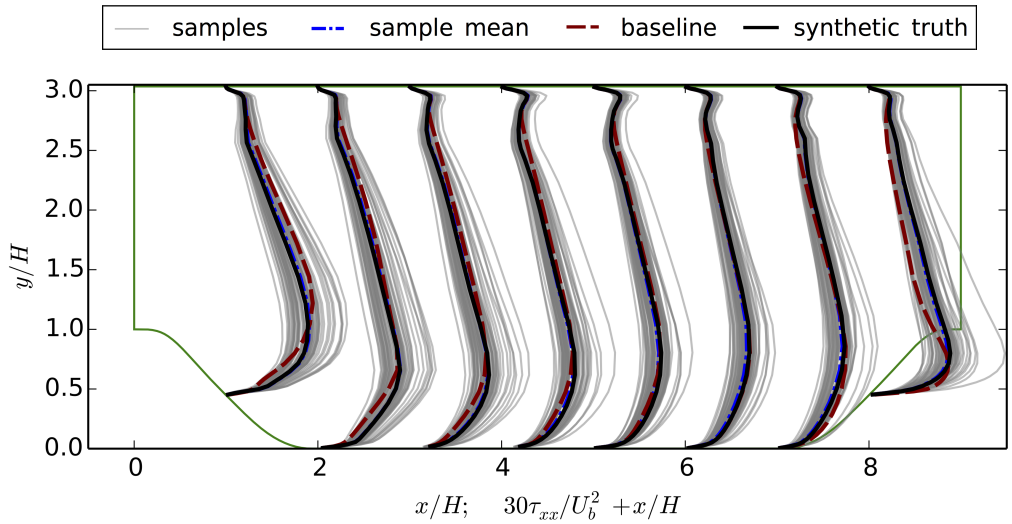

Figure 3.13: The posterior ensembles of τ_{xx} profiles of case S1. The ensemble profiles are shown at eight locations $x/H = 1, \cdots, 8$ of case S1, compared with synthetic truth and baseline results.

3.5 Conclusion

In this paper, we discussed the merits of incorporating various prior knowledge into the proposed Bayesian framework for model-form uncertainty quantification and reduction in RANS simulations. The prior knowledge considered in the framework includes the smoothness and realizability of Reynolds stress tensor field, overall understanding on the coherent structures of the flow, and the empirical experiences of RANS modeling. We examined the merits of incorporating the prior knowledge on the dimension of uncertainty space, spatial field of variance and experimental design by using four test cases. The simulation results demonstrate that the posterior QoI predictions can be significantly improved by incorporating physical prior knowledge into the Bayesian inference. Incorporating the prior information enables a more efficient usage of limited observation data. Meanwhile, the study also suggests that the proposed framework provides a relatively rigorous way to express and incorporate the existing empirical knowledge on RANS modeling. Based on the proposed framework, the empirical knowledge accumulated in decades of engineering practices can be used to improve the quantification and reduction of model-form uncertainties in RANS simulations.

Bibliography

[1] Nasstrom, J. S., Sugiyama, G., Baskett, R., Larsen, S., and Bradley, M., The national atmospheric release advisory center (NARAC) modeling and decision support system for radiological and nuclear emergency preparedness and response, *Livermore, CA: Lawrence Livermore National Laboratory Report UCRL-JRNL-211678*, 2005.

[2] Bieder, U., Calvin, C., and Mutelle, H., Detailed thermal hydraulic analysis of induced break severe accidents using the massively parallel CFD code Trio-U/PRICELES, In *Supercomputing in Nuclear Applications*, Paris, 2003.

[3] Scheuerer, M., Heitsch, M., Menter, F., Egorov, Y., Toth, I., Bestion, D., Pigny, S., Paillere, H., Martin, A., Boucker, M., and others, , Evaluation of computational fluid dynamic methods for reactor safety analysis (ECORA), *Nuclear Engineering and Design*, 235(2-4):359–368, 2005.

[4] Oliver, T. and Moser, R., Uncertainty quantification for RANS turbulence model predictions, In *APS Division of Fluid Dynamics Meeting Abstracts*, Vol. 1, 2009.

[5] Dow, E. and Wang, Q., Quantification of structural uncertainties in the k–ω turbulence model, In *52nd AIAA/ASME/ASCE/AHS/ASC Structures, Structural Dynamics and Materials Conference*, Denver, Colorado, 4-7 April 2011 2011. AIAA. AIAA Paper, 2011-1762.

[6] Wilcox, D. C., *Turbulence modeling for CFD*, DCW Industries, 3 edition, 2006.

[7] Emory, M., Pecnik, R., and Iaccarino, G., Modeling structural uncertainties in Reynolds-averaged computations of shock/boundary layer interactions, *AIAA paper*, 479:1–16, 2011.

[8] Gorlé, C. and Iaccarino, G., A framework for epistemic uncertainty quantification of turbulent scalar flux models for Reynolds-averaged Navier-Stokes simulations, *Physics of Fluids*, 25(5):055105, 2013.

[9] Gorlé, C., Larsson, J., Emory, M., and Iaccarino, G., The deviation from parallel shear flow as an indicator of linear eddy-viscosity model inaccuracy, *Physics of Fluids*, 26(5):051702, 2014.

[10] Emory, M., Larsson, J., and Iaccarino, G., Modeling of structural uncertainties in Reynolds-averaged Navier-Stokes closures, *Physics of Fluids*, 25(11):110822, 2013.

[11] Emory, M. A., Estimating model-form uncertainty in Reynolds-averaged Navier–Stokes closures, PhD thesis, Stanford University, 2014.

[12] Xiao, H., Wu, J.-L., Wang, J.-X., Sun, R., and Roy, C. J. Quantifying and reducing model-form uncertainties in Reynolds-averaged Navier-Stokes simulations: An open-box, physics-based, Bayesian approach. Submitted. Available at http://arxiv.org/abs/1508.06315, 2015.

[13] Kennedy, M. C. and O'Hagan, A., Bayesian calibration of computer models, *Journal of the Royal Statistical Society: Series B (Statistical Methodology)*, 63(3):425–464, 2001.

[14] Brynjarsdóttir, J. and O'Hagan, A., Learning about physical parameters: The importance of model discrepancy, *Inverse Problems*, 30:114007, 2014.

[15] Oliver, T. A. and Moser, R. D., Bayesian uncertainty quantification applied to RANS turbulence models, In *Journal of Physics: Conference Series*, Vol. 318, p. 042032. IOP Publishing, 2011.

[16] Banerjee, S., Krahl, R., Durst, F., and Zenger, C., Presentation of anisotropy properties of turbulence, invariants versus eigenvalue approaches, *Journal of Turbulence*, 8(32):1–27, 2007.

[17] Le Maître, O. P. and Knio, O. M., *Spectral methods for uncertainty quantification: with applications to computational fluid dynamics*, Springer, 2010.

[18] Evensen, G., *Data assimilation: the ensemble Kalman filter*, Springer, 2009.

[19] Breuer, M., Peller, N., Rapp, C., and Manhart, M., Flow over periodic hills: Numerical and experimental study in a wide range of reynolds numbers, *Computers & Fluids*, 38(2):433–457, 2009.

[20] O'Sullivan, F., A statistical perspective on ill-posed inverse problems, *Statistical science*, pp. 502–518, 1986.

[21] Duraisamy, K. and Chandrashekar, P., Goal-oriented uncertainty propagation using stochastic adjoints, *Computers & Fluids*, 66:10–20, 2012.

Chapter 4

A Random Matrix Approach for Quantifying Model-Form Uncertainties in Turbulence Modeling

(Published on *Computer Methods in Applied Mechanics and Engineering*, 313, 941-965, 2017.)

H. Xiao[a], J.-X. Wang[a], Roger G. Ghanem[b]

[a] Department of Aerospace and Ocean Engineering, Virgina Tech, Blacksburg, VA, 24061, USA

[b] Department of Aerospace and Mechanical Engineering, University of Southern California, Los Angeles, CA 90089, USA

Abstract

With the ever-increasing use of Reynolds-Averaged Navier–Stokes (RANS) simulations in mission-critical applications, the quantification of model-form uncertainty in RANS models has attracted attention in the turbulence modeling community. Recently, a physics-based nonparametric approach for quantifying model-form uncertainty in RANS simulations has been proposed, where Reynolds stresses are projected to physically meaningful dimensions and perturbations are introduced only in the physically realizable limits (Xiao et al., 2016. Quantifying and reducing model-form uncertainties in Reynolds-averaged Navier–Stokes simulations: A data-driven, physics-informed Bayesian approach. Journal of Computational Physics. 324, pp. 115-136). However, a challenge associated with this approach is to assess the amount of information introduced in the prior distribution and to avoid imposing unwarranted constraints. In this work we propose a random matrix approach for quantifying model-form uncertainties in RANS simulations with the realizability of the Reynolds stress guaranteed, which is achieved by construction from the Cholesky factorization of the normalized Reynolds stress tensor. Furthermore, the maximum entropy principle is used to

identify the probability distribution that satisfies the constraints from available information but without introducing artificial constraints. We demonstrate that the proposed approach is able to ensure the realizability of the Reynolds stress, albeit in a different manner from the physics-based approach. Monte Carlo sampling of the obtained probability distribution is achieved by using polynomial chaos expansion to map independent Gaussian random fields to the Reynolds stress random field with the marginal distributions and correlation structures as specified. Numerical simulations on a typical flow with separation have shown physically reasonable results, which verify the proposed approach. Therefore, the proposed method is a promising alternative to the physics-based approach for model-form uncertainty quantification of RANS simulations. The method explored in this work is general and can be extended to other complex physical systems in applied mechanics and engineering.

Notations

We summarize the convention of notations below because of the large number of symbols used in this paper. The general conventions are as follows:

1. Upper case letters with brackets (e.g., $[R]$) indicate matrices or tensors; lower case letters with arrows (e.g., $\vec{v}$) indicate vectors; undecorated letters in either upper or lower cases indicate scalars. An exception is the spatial coordinate, which is denoted as x for simplicity but is in fact a 3×1 vector. Tensors (matrices) and vectors are also indicated with index notations, e.g., R_{ij} and v_i with $i, j = 1, 2, 3$. In this paper, i and j are used with tensor indices while α and β are used as general indexes, e.g., for the modes of Kahunen–Loeve expansion or for the terms in the polynomial chaos expansion.

2. Bold letters (e.g., $[\mathbf{R}]$) indicate random variables (including scalars, vectors, and matrices), the non-bold letters (e.g., $[R]$) indicate the corresponding realizations, and underlined letters (e.g., $[\underline{R}]$) indicate the mean.

3. Symbols $\mathbb{M}_d^s$, M_d^+, and $\mathbb{M}_d^{+0}$ indicate the sets of symmetric, symmetric positive definite, and symmetric positive semi-definite matrices, respectively, of dimension $d \times d$ with the following relation: $M_d^+ \subset \mathbb{M}_d^{+0} \subset \mathbb{M}_d^s$.

This work deals with Reynolds stresses, which are rank two tensors. Therefore, it is implied throughout the paper that all random or deterministic matrices have sizes 3×3 with real entries unless noted otherwise.

4.1 Introduction

Numerical models based on Reynolds-Averaged Navier–Stokes (RANS) equations are the dominant tool for the prediction of turbulent flows in industrial and natural processes. For many flows the predictions from RANS simulations have large uncertainties, which are mostly attributed to the phenomenological closure models for the Reynolds stresses [22, 1]. Previous efforts in quantifying and reducing model uncertainties in RANS simulation have mostly followed parametric approaches, e.g., by perturbing, tuning, or inferring the model parameters in these closure models [2]. Recently, researchers in the turbulence modeling community have recognized the limitations of the parametric approach and started exploring nonparametric approaches where uncertainties are directly injected into the Reynolds stresses [1, 3, 4, 5, 6].

In their pioneering work, Iaccarino and co-workers [3, 4] projected the Reynolds stress onto the six physically meaningful dimensions (its magnitude, shape, and orientation) and perturbed the Reynolds stresses towards the limiting states in the physically realizable range. Xiao et al. [6] utilized the six physical dimensions as the basis to parameterize the Reynolds stress uncertainty space, and the physical-based parameterization is further used for systematic exploration of the space and for Bayesian inferences to incorporate observation data. However, although the physics-based parameterization allows for a full representation of the uncertainty space, two limitations need to be addressed. First, the realizability constraints on Reynolds stresses provide guidance only on the shape of the Reynolds stress (in the form of the classical Lumley triangle [7] or the recently proposed Barycentric triangle [8]). In comparison, much weaker constraints can be imposed on the magnitude and the orientation, except for the constraint that the magnitude (i.e., turbulent kinetic energy) must be positive. For this reason and partly due to stability considerations, previous works on injecting uncertainty to the physical projections of the Reynolds stress have focused on the shape and magnitude [3, 6, 5], and they did not introduce uncertainties to the orientations. Second, in the context of Bayesian inference of Reynolds stress uncertainties as pursued by Xiao and co-workers [6, 9, 10], it is not straightforward to specify a prior distribution on the physical variables. Xiao et al. [6] specified Gaussian priors for the Reynolds stress discrepancy in terms of the tensor shape parameters and the logarithmic of the magnitude. In principle the same prior can be specified for the orientation angles. However, it is not clear how much information is introduced into the prior with this choice of probability distributions (i.e., log-normal distribution for the magnitude and standard normal for others). Moreover, in lack of physical insight, it is not clear how large the variance for each physical variable should be compared to each other. Although the prior plays a minor role in the Ensemble Kalman filtering based inference with a moderate amount of data as studied in Xiao et al. [6], it can be of critical importance for pure uncertainty propagation as pursued by Iaccarino and co-workers [3, 4, 5] and for Bayesian inferences with small amounts of data. In particular, it is critical that no artificial constraints are introduced with overly confident prior distributions.

The entropy measure of information has been proposed more than half a century ago [11]. Since then, the maximum entropy principle has been extensively used as the guideline to

specify prior probability distributions for Bayesian inferences [12]. The principle states that out of all possible distributions that satisfy the constraints from available information, the probability distribution that has the maximum entropy is a good prior distribution. Since entropy is a measure of randomness, the maximum entropy distribution is the most non-committal and most random in the dimensions in which no information is available. Consequently, it introduces the least amount of information in addition to the specified constraints. While the maximum entropy principle has been used extensively in many disciplines such as communications [13] and image processing [14], the use of maximum entropy principle in conjunction with random matrix theory for quantifying model-form uncertainties in physical systems is only a recent development. Soize [15] was the first to derive the maximum entropy probability distribution of a symmetric positive definite random matrix with a specified mean field. Applications to structural vibration problems were demonstrated, where the mass, stiffness, and damping matrices of the real system were described as random matrices with the corresponding matrices in the reduced model as their means. In these applications, the dimension d of the matrices corresponds to the degrees of freedom in the finite element discretization of the structural system, and thus d is usually very large (e.g., of the order of $O(10^5)$ or more; refer to the numerical example in [16]). The framework was further extended to nonlinear structural dynamics problems and to other applications (e.g., composite materials [17], porous media[18]) and to problems with more complicated constraints, (e.g., on the variance of eigenvalues [19, 18], as well lower and upper bounds on the matrices [17]). See refs. [16, 20] for comprehensive reviews of the recent development. When the framework was used in the constitutive modeling of composite materials or to describe the permeability tensor of porous media, the random matrices have a dimension of 3×3.

Since Reynolds stresses are symmetric positive definite tensors, it seems natural to use random matrix approach to describe the Reynolds stresses for the quantification of RANS modeling uncertainties. However, the authors are not aware of any existing work in the literature that applied the random matrix theory in quantifying model-form uncertainties in RANS simulations. While many of the theories developed by Soize and co-workers can be applied here straightforwardly, an important characteristic of the RANS modeling application is that the Reynolds stresses are described by a field of 3×3 random matrices with spatial correlations. In contrast, the matrices in previously investigated applications either involve only a few individual large matrices (e.g., the mass, stiffness, and damping matrices in structural dynamics applications [15]) or a large number of random matrices without spatial correlation structure (e.g., the effective constitutive matrices in the meso-scale modeling of composite materials [17]). A notable exception is the recent work of Guilleminot et al. [18], where the permeability tensor is modeled as a random matrix field with a specified correlation structure. Note that most of the theories in the framework of Soize [15, 16, 20] were developed for random matrices of arbitrary yet finite dimensions, and thus they should be equally applicable for all the above-mentioned applications, where the dimension d ranges from 3 to $O(10^5)$. In this work we do not utilize the results pertaining to the asymptotic behaviors of the theories for $d \to \infty$.

In the present contribution, we use an approach based on the random matrix theory and the maximum entropy principle to quantify model-form uncertainties in RANS modeling. The objectives of this work are two-fold. First, the proposed framework for quantifying model form uncertainties in RANS simulations provides an alternative to the physics-based approach investigated by Iaccarino and co-workers [3, 4, 5] and Xiao and co-workers [6, 10]. The advantages and disadvantages of both approaches can thus be contrasted and compared (see Wang et al. [21]). Despite the better mathematical rigorousness in seeking maximum entropy distribution for the random matrix in the current approach, it is possible that the physics-based approach may still be preferred by RANS simulations practitioners for both uncertainty quantification and Bayesian inferences. This is because of its convenience in incorporating physical prior knowledge [9]. As such, another objective and motivation for this work is to provide basis for gauging the departure of the priors used in the physics-based approach from the maximum entropy condition. By comparing the prior distributions of the obtained Reynolds stress from both approaches, the current framework can reveal the amount of information introduced in the physics-based prior distribution, and thus provide guidance for the choice of priors in the physics-based approach. Detailed results from such a comparison are presented in a companion paper [21].

The rest of the paper is organized as follows. Section 2 introduces the realizability of Reynolds stresses in details and argues that the current framework of modeling Reynolds stress as positive semidefinite tensors can guarantee realizability in the same way as in the previously proposed physics-based approaches [6]. Section 3 introduces the random matrix framework for model-form uncertainty in RANS simulation and discusses its implementations. Section 4 uses the flow over periodic hills as an example application to demonstrate the performance of the proposed method. The probability measure of the obtained distribution on the limiting states is discussed in Section 5. Finally, Section 6 concludes the paper.

4.2 Realizability of Reynolds Stresses: Physical vs. Mathematical Perspectives

4.2.1 The Origin and History of Realizability Constraints

The Navier–Stokes equations for incompressible flows with constant density can be written as follows:

$$\frac{\partial v_i}{\partial t} + \frac{\partial \left(v_i v_j\right)}{\partial x_j} = -\frac{1}{\rho}\frac{\partial p}{\partial x_i} + \nu \frac{\partial^2 v_i}{\partial x_j \partial x_j} \tag{4.1a}$$

$$\text{and} \quad \frac{\partial v_i}{\partial x_i} = 0 \tag{4.1b}$$

where v_i and p are instantaneous velocity and pressure, respectively; t and x_i are time and space coordinates, respectively; ν is the kinematic viscosity; ρ is the fluid density. Solving the

Navier–Stokes equations with proper numerical methods and mesh resolution as is done in Direct Numerical Simulations (DNS) would yield the flow field $v_i(x,t)$ and $p(x,t)$ at any time and location. However, this is prohibitively expensive computationally due to the wide range of spatial and temporal scales, particularly for practical turbulent flows. Therefore, the mean flow field is solved in place of the instantaneous field. For that purpose, the instantaneous velocity can be considered a random variable, whose mean is obtained by using Reynolds ensemble averaging. As such, we use a bold symbol $\mathbf{v}_i$ to indicate the instantaneous velocity hereafter.

First, the instantaneous velocity $\mathbf{v}_i$ is decomposed into the mean quantity $\underline{v}_i$ and its fluctuation $\mathbf{v}'_i$. That is, $\mathbf{v}_i = \underline{v}_i + \mathbf{v}'_i$, and the pressure is also decomposed to mean pressure $\underline{p}$ and pressure fluctuation $\mathbf{p}'$. Substituting the decompositions into the Navier Stokes equation and taking the mean lead to the RANS equations [22]:

$$\frac{\partial \underline{v}_i}{\partial t} + \frac{\partial \left(\underline{v}_i \underline{v}_j\right)}{\partial x_j} = -\frac{1}{\rho}\frac{\partial \underline{p}}{\partial x_i} + \nu \frac{\partial^2 \underline{v}_i}{\partial x_j \partial x_j} - \frac{\partial \langle \mathbf{v}'_i \mathbf{v}'_j \rangle}{\partial x_j} \tag{4.2a}$$

$$\text{and} \quad \frac{\partial \underline{v}_i}{\partial x_i} = 0 \tag{4.2b}$$

where the covariance $\langle \mathbf{v}'_i \mathbf{v}'_j \rangle$ of the velocity fluctuations is referred to as (the negative of) Reynolds stress and is denoted as R_{ij} for simplicity, but the covariance nature of this term has profound implications. Specifically, a Reynolds stress tensor must be symmetric positive semi-definite, i.e., $R_{ij} \in \mathbb{M}_3^{+0}$, where $\mathbb{M}_3^{+0}$ is the set of symmetric positive semidefinite matrices. In fact, the Reynolds stresses are mostly positive definite (i.e., all eigenvalues are positive), i.e., $R_{ij} \in \mathbb{M}_3^{+}$, and zero eigenvalues occur only in extreme cases, e.g., on the wall boundaries or in turbulence-free regions, where velocity fluctuations for one or more components are zero. For practical purposes it is not essential to distinguish between $\mathbb{M}_3^{+}$ and $\mathbb{M}_3^{+0}$ when quantifying model form uncertainties in RANS simulations.

For a tensor to be a valid Reynolds stress tensor, or equivalently, to be physically realizable, there must exist a velocity that has this covariance. The physical realizability of Reynolds stresses and the associated second-order closure models were a topic of intensive research in the early years of turbulence model development. Early works of Schumann [23], Lumley [24], and Pope [25], among others, have led to a class of realizable second-order closure models [26]. Since these models solve an evolution equation for the Reynolds stresses, these models guarantee the realizability by imposing certain constraints on the rate of change $[\dot{R}]$ of the Reynolds stress, i.e., the constraint that its principle stress components (e.g., eigenvalues) do not further decrease when at zero [25]. The well-known Lumley triangle [7] provided a map for all realizable turbulence by projecting the Reynolds stress to a plane. Specifically, the following decomposition is performed on the Reynolds stress:

$$[R] = 2k\left(\frac{1}{3}[I] + [A]\right) = 2k\left(\frac{1}{3}[I] + [E][\Lambda][E]^T\right) \tag{4.3}$$

where k is the turbulent kinetic energy which indicates the magnitude of $[R]$; $[I]$ is the second order identity tensor; $[A]$ is the anisotropy tensor; $[E] = [\vec{e}_1, \vec{e}_2, \vec{e}_3]$ and $[\Lambda] = \text{diag}[\tilde{\lambda}_1, \tilde{\lambda}_2, \tilde{\lambda}_3]$

where $\tilde{\lambda}_1 + \tilde{\lambda}_2 + \tilde{\lambda}_3 = 0$ are the orthonormal eigenvectors and the corresponding eigenvalues of $[A]$, respectively, indicating the shape and orientation of $[R]$. The Lumley triangle is thus defined on a plane with the second and third invariants (II and III) of the anisotropy tensor as coordinates. The invariants are $\text{II} = (\text{tr}[A])^2 - \text{tr}([A]^2)$ and $\text{III} = \det[A]$, where $\text{tr}(\cdot)$ and $\det(\cdot)$ denote trace and determinant, respectively.

4.2.2 Realizability in Physics-Based Model-Form Uncertainty Quantification

The past two decades have not seen significant literature on the realizability of turbulence models, partly because the research on RANS model development has been stagnant altogether. However, recently the pioneering research of Iaccarino and co-workers [3, 4, 30] on the quantification of model form uncertainties in RANS simulations has revived the interests on Reynolds stresses realizability. Specifically, they performed the decomposition as shown in Eq. (6.2) and mapped the eigenvalues $\tilde{\lambda}_1$, $\tilde{\lambda}_2$, and $\tilde{\lambda}_3$ to Barycentric coordinates (C_1, C_2, C_3) as follows:

$$C_1 = \tilde{\lambda}_1 - \tilde{\lambda}_2 \tag{4.4a}$$

$$C_2 = 2(\tilde{\lambda}_2 - \tilde{\lambda}_3) \tag{4.4b}$$

$$C_3 = 3\tilde{\lambda}_3 + 1 \ . \tag{4.4c}$$

As illustrated in Fig. 6.1a, the Barycentric coordinates (C_1, C_2, C_3) of a point indicate portion of areas of the three sub-triangles formed by the point and the edge labeled as C_1, C_2, and C_3, respectively, in the Barycentric triangle. For example, the ratio between the shaded sub-triangle and the entire triangle is C_3. A point located on the top vertex corresponds to $C_3 = 1$ while a point located on the bottom edge (labeled C_3 in Fig. 6.1a) has $C_3 = 0$. Therefore, each coordinate ranges from 0 to 1, and they sum to 1 for any point, i.e., $C_1 + C_2 + C_3 = 1$. The three edges labeled C_1, C_2 and C_3 are opposite to the vertices representing one-component, two-component, and three-component limits of realizable turbulence states. The Barycentric coordinates have clear physical interpretation in that they indicate the componentality (i.e., dimensionality) of the turbulence. For example, the upper corner in Fig. 6.1a, which corresponds to $C_3 = 1$ or equivalently a Barycentric coordinate of $(0, 0, 1)$, indicates isotropic, fully three-dimensional turbulence. Detailed physical interpretation of the vertices and edges are shown in Fig. 6.1a. The Barycentric triangle is similar to the Lumley triangle in that it also encloses all realizable turbulence states. Emory et al. [3] estimated the uncertainties in RANS simulations by perturbing the Reynolds stress towards the three limiting states, i.e., the vertices of the Barycentric triangle. This is illustrated in Fig. 6.1b as squares. Based on their work, Xiao et al. [6] further mapped the Barycentric coordinates to natural coordinates, on which the equilateral triangle is mapped to a unit square. They parameterized the uncertainty space on the natural coordinates and systematically explored the uncertainty space. The samples as obtained in Xiao et al. [6] are illustrated in Fig. 6.1b, which are in contrast to the three perturbed states of Emory et al. [3].

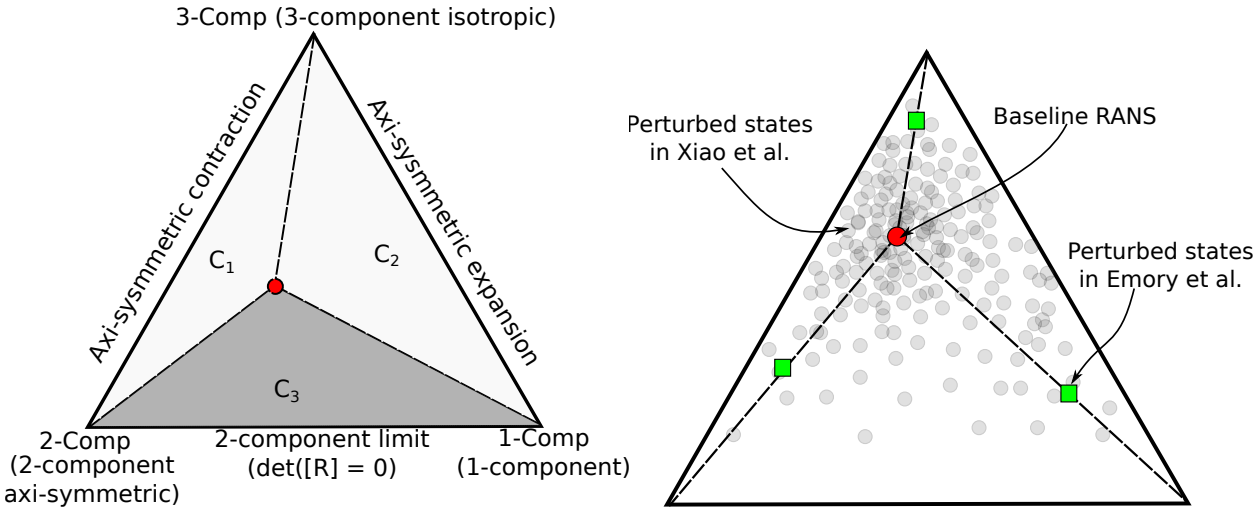

(a) (b)

Figure 4.1: (a) Barycentric triangle as a way of delineating realizable turbulence, its definition and physical interpretation. Elements in the set $\mathbb{M}_d^{+0}$ of positive semidefinite matrices maps to the interior and edges of the triangle, while the set $\mathbb{M}_d^{+0} \setminus \mathbb{M}_d^{+}$ of singular matrices maps (whose element have zero determinants) maps to the bottom edge. (b) Model-form uncertainty quantification through perturbation of Reynolds stresses within the physically realizabile limit enclosed by the Barycentric triangle. The different schemes of Emory et al. [3] and Xiao et al. [6] are shown.

While both Emory et al. [3] and Xiao et al. [6] injected uncertainties only to the magnitude and shape of the Reynolds stress tensor, it is theoretically possible to perturb the orientation as well. This work is not directly concerned with the physics-based approach for uncertainty quantification, but the physics-based parameterization will facilitate interpretations of the samples obtained with the random matrix approach. To this end, a parameterization scheme for the eigenvectors $E = [\vec{e}_1, \vec{e}_2, \vec{e}_3]$ is needed. The three mutually orthogonal, unit-length vectors can be considered a rigid body and thus its orientation has three degrees of freedom, although they have nine elements in total. We use the Euler angle with the z-x'-z'' convention to describe the orientation of the Reynolds stress anisotropy tensor following the method in rigid body dynamics [31]. That is, if a local coordinate system x–y–z spanned by the three eigenvectors of $[R]$ was initially aligned with the global coordinate system (X–Y–Z), the current configuration could be obtained by the following three consecutive intrinsic rotations about the axes of the local coordinate system: (1) a rotation about the z axis by angle φ_1, (2) a rotation about the x axis by φ_2, and (3) another rotation about its z axis by φ_3. Note that the local coordinate axes may change orientations after each rotation.

In summary, the Reynolds stress can be represented with six independent variables with clear physical interpretations. The turbulent kinetic energy k represents its magnitude; the Barycentric coordinates C_1, C_2, C_3, of which only two are independent, indicate its shape; the Euler angles φ_1, φ_2 and φ_3 represent its orientation. Realizability can be guaranteed by injecting uncertainties in these physical variables, a fact that has been exploited in the physics-based approach for RANS model-form uncertainty quantification investigated in earlier works.

4.2.3 Mathematical and Physical Interpretations of Realizability

The physics-based approach based on Barycentric triangle as explored by Emory et al.[3] and Xiao et al. [6] certainly has clear advantages. However, it is not the only way to guarantee realizability. Here we claim that an alternative method to guarantee the Reynolds stress realizability in the context of RANS model-form uncertainty quantification is to model $[R]$ as a random matrix defined on the set $\mathbb{M}_3^{+0}$ of positive semidefinite matrices. In other words, we can directly draw $[R]$ from the set $\mathbb{M}_3^{+0}$, and all obtained samples are guaranteed to be realizable Reynolds stresses. To support this claim, we utilize a theorem on the equivalence between the set of positive semidefinite matrices and the set of co-variance matrices (see e.g., [32]).

Theorem 1. *A covariance matrix $[R]$ must be positive semidefinite; conversely, every symmetric positive semi-definite matrix $[R]$ is a covariance matrix.*

The proof for the first part is straightforward and is thus omitted. The proof for the second part is of critical importance to the theme of our work, and thus it is reproduced below.

Proof. We construct a vector $\vec{\mathbf{v}} = [R]^{1/2}\,\vec{\mathbf{b}}$ with $[R]^{1/2}$ being the symmetric square root of $[R]$, and $\vec{\mathbf{b}}$ has a covariance of identity matrix, i.e., $\mathrm{Cov}\{\vec{\mathbf{b}}, \vec{\mathbf{b}}\} = [I]$. It can be seen that

$$\mathrm{Cov}\{R^{1/2}\vec{\mathbf{b}}, R^{1/2}\vec{\mathbf{b}}\} = [R]^{1/2}\ \mathrm{Cov}\{\vec{\mathbf{b}}, \vec{\mathbf{b}}\}\ [R]^{1/2} = [R]. \tag{4.5}$$

Therefore, for any positive semidefinite matrix $[R]$, there is a real-valued velocity vector $\vec{\mathbf{v}}$ whose covariance is $[R]$. This completes the proof. □

Recalling the definition and origin of the Reynolds stress realizability described in Section 4.2.1, it can be seen that the matrix $[R]$ is also a realizable Reynolds stress. Therefore, it is concluded that the mathematical constraint that $[R]$ must belong to the set $\mathbb{M}_3^{+0}$ can equally guarantee the realizability of the obtained Reynolds stresses, albeit in a different manner from the physics-based approach. The latter utilized the constraint that the projection of Reynolds stresses must reside in the Barycentric triangle to ensure the Reynolds stress realizability.

We conclude this section with the following three *equivalent* statements on the realizability constraints of the Reynolds stresses:

1. a Reynolds stress must reside within or on the edge of the Lumley triangle or Barycentric triangle after the corresponding transformations [8];
2. a Reynolds stress tensor must be positive semidefinite; and
3. a Reynolds stress tensor must be the covariance matrix of a real-valued vector, i.e., a velocity vector.

The equivalence between realizability and the invariants mapping within Lumley triangle was established by Lumley and Neuman [7] and stated in ref. [22] (pp. 394); the equivalence between the positive semidefinite requirement on the Reynolds stress and the realizability conditions was proved by Schumann [23]. The relation among three statements above is a pivotal element for anchoring the present contribution to the existing literature of turbulence modeling [23, 7, 3]. However, note that the proposed random matrix approach for quantifying RANS model-form uncertainty is fundamentally different from the physics-based approach developed in ref. [6]. The most important difference lies in the fact that in the physics-based approach the user specifies the probability distribution on the physical variables, while in the random matrix approach the maximum entropy principle provides the basis for computing the distribution of the matrices.

4.3 Random Matrix Approach and Its Implementation

4.3.1 Probability Model for Reynolds Stress Tensors

Based on the discussions above on the nature of Reynolds stresses, we build a probabilistic model for the Reynolds stress tensors. The development below mostly follows the works of Soize, Ghanem, and co-workers [e.g., 15, 17].

Using $\mathbb{M}_d^s$ to denote the set of all symmetric matrices, the measure of matrix $[R] \in \mathbb{M}_d^s$ is given as [16]:

$$d[R] = 2^{d(d-1)/4} \prod_{1 \le i \le j \le d} dR_{ij} \tag{4.6}$$

where $\prod$ indicates product, R_{ij} are individual elements of matrix $[R]$, and dR_{ij} is the Lebesgue measure on the set $\mathbb{R}$ of real numbers. Since Reynolds stresses are rank two tensors, $d = 3$ is implied.

The objective is to define a probability measure $p_{[\mathbf{R}]} : \mathbb{M}_d^{+0} \mapsto \mathbb{R}^+$ on the symmetric matrices set that maps a symmetric, positive semidefinite, second-order random matrix $[\mathbf{R}]$ to a positive number. While such a measure is not unique, in this work we seek a Probability Density Function (PDF) that has the maximum entropy. Specifically, if P_{ad} is the set of all PDFs mapping from $\mathbb{M}_d^{+0}$ to $\mathbb{R}^+$, then the maximum entropy principle states that the most non-committal PDF is the one such that (1) all available constraints are satisfied, and (2) no any other artificial constraints are introduced [18]. That is,

$$p_{[\mathbf{R}]} = \arg \max_{p \in P_{ad}} S(p) \tag{4.7}$$

where the entropy $S(p)$ of the PDF p is defined as [15]:

$$S(p) = -\int_{\mathbb{M}_d^{+0}} p([R]) \ln p([R]) d[R] \tag{4.8}$$

where ln denotes the natural logarithm.

In the context of RANS-based turbulence modeling, the following constraints should be satisfied by the PDF of Reynolds stress tensors:

1. All realizations $[R]$ of the Reynolds stress $[\mathbf{R}]$ must be physically realizable. This constraint is automatically satisfied by defining $[\mathbf{R}]$ on the set $\mathbb{M}_d^{+0}$, i.e., $[\mathbf{R}] \in \mathbb{M}_d^{+0}$.

2. Normalization condition for the PDF:

$$\int_{\mathbb{M}_d^{+0}} p_{[\mathbf{R}]}([R]) d[R] = 1, \tag{4.9}$$

   which is self-evident.

3. We assume that a best estimation $[\underline{R}]$ of the true Reynolds stress $[\mathbf{R}]$ is available at any location in the field. The estimation can be obtained in advance by performing a baseline RANS simulation or by incorporating observation data and incorporating prior corrections to the baseline RANS-predicted Reynolds stresses. Without further information, it is reasonable to take the estimation $[\underline{R}]$ so-obtained as the mean of the true Reynolds stress $[\mathbf{R}]$, with the latter being modeled as a random variable. This constraint is expressed as:

$$\mathbb{E}\{[\mathbf{R}]\} = [\underline{R}]. \tag{4.10}$$

The theories on the maximum distribution of random matrices developed in the earlier works of Soize and co-workers focused primarily on positive definite matrices, but the Reynolds stress tensors of concern in the present application are positive semidefinite only. Although we have claimed that the difference has no practical consequences, we shall still carefully reconcile the differences before utilizing the theories of Soize [15]. In order to obtain a maximum entropy distribution for a positive definite matrix that satisfies the normalization and mean constraints similar to those outlined above, Soize [15] took a two-step approach. Specifically, he first obtained the PDF for a *normalized, positive definite* random matrix $[\mathbf{G}]$ whose mean is the identity matrix $[I]$, i.e., $\mathbb{E}\{[\mathbf{G}]\} = [I]$. The probability distribution for $[\mathbf{G}]$ must also satisfy the maximum entropy condition and the normalization condition in Eq. (4.9) above. Once such a matrix $[G]$ is obtained, a matrix that satisfies the condition $\mathbb{E}\{[\mathbf{R}]\} = [\underline{R}]$ can be constructed as follows:

$$[\mathbf{R}] = [\underline{L}_R]^T[\mathbf{G}][\underline{L}_R], \tag{4.11}$$

where $[\underline{L}_R]$ is an upper triangular matrix with non-negative diagonal entries obtained from the following factorization of the specified mean $[\underline{R}]$, i.e.,

$$[\underline{R}] = [\underline{L}_R]^T[\underline{L}_R]. \tag{4.12}$$

In the present development, we consider the following two scenarios: (1) When $[R] \in \mathbb{M}_d^+$ is positive definite, the decomposition above is the well-known Cholesky factorization, and the decomposition is unique. Its numerical implementations are available in many standard numerical toolboxes (e.g., Matlab and the numpy library of Python). (2) When $[R] \in \mathbb{M}_d^{+0} \setminus \mathbb{M}_d^+$ is in the subset of singular positive semidefinite matrices, where $\setminus$ indicates set subtraction, it can be proved that the decomposition in the form above still exits with L having non-negative diagonal entries, although the decomposition is no longer unique. Moreover, Cholesky factorization routines for such matrices are still numerically stable if complete pivoting is performed [33]. In practice, we can make it slightly positive definite by adding a small element to the diagonal entries and thus still use the conventional Cholesky factorization routines.

With the reconciliation above, hereafter we only need to focus on probability distribution of the normalized positive definite matrix $[\mathbf{G}]$ and can thus directly use the results in the earlier

works of [16]. By using the classical optimization techniques based on Lagrange multipliers, the probability density function of the random matrix $[\mathbf{G}]$ is obtained as follows [16]:

$$p_{[\mathbf{G}]}([G]) = \mathbb{1}_{\mathbb{M}_d^+}([G]) \times C_{\mathrm{G}} \times \det[G]\,(d+1)(1-\delta^2)/(2\delta^2) \times \exp\left(-\frac{d+1}{2\delta^2}\,\mathrm{tr}[G]\right), \quad (4.13)$$

where $\mathbb{1}_{\mathbb{M}_d^+}([G])$ is an indicator function, i.e., it is one if $[G] \in \mathbb{M}_d^+$ and zero otherwise. The positive constant C_{G} is:

$$C_{\mathrm{G}} = \frac{(2\pi)^{-d(d-1)/4}\left(\frac{d+1}{2\delta^2}\right)^{d(d+1)(2\delta^2)^{-1}}}{\prod_{j=1}^{d}\Gamma\left(\frac{d+1}{2\delta^2}+\frac{1-j}{2}\right)} \quad (4.14)$$

where $\Gamma(z)$ is gamma function defined by $\Gamma(z) = \int_0^\infty t^{z-1}e^{-t}dt$. The dispersion parameter δ indicates the uncertainty in the random matrix and is defined as:

$$\delta = \left[\frac{1}{d}\mathbb{E}\{\|[G]-[I]\|_F^2\}\right]^{\frac{1}{2}} \quad (4.15)$$

where $\|\cdot\|_F$ is Frobenius norm, i.e., $\|G\|_F = \sqrt{\mathrm{tr}([G]^T[G])}$. It can be seen that δ is analogous to the variance of a scalar random variable normalized by its mean. It has been shown [15] that

$$0 < \delta < \sqrt{\frac{d+1}{d+5}}, \quad (4.16)$$

which reduces to $0 < \delta < \sqrt{2}/2$ for $d = 3$. This constraint is related to the positive definiteness of matrix $[\mathbf{G}]$.

The individual elements in the random matrix $[\mathbf{G}]$ are correlated and the same can thus be said of the random matrix $[\mathbf{R}]$. This correlation needs to be accounted for when generating Monte Carlo samples, which can be achieved in a similar manner as in sampling from random processes (e.g., Gaussian processes). The sampling method is detailed below.

4.3.2 Monte Carlo Sampling of Reynolds Stresses at One Point

Soize [15] outlined a Monte Carlo method to sample the probability distribution for random matrix $[\mathbf{R}]$ for a given dispersion parameter δ and mean $[\underline{R}]$. To proceed with the sampling, the random matrix with identity mean is first represented by its Chelosky factorization:

$$[\mathbf{G}] = [\mathbf{L}]^T[\mathbf{L}], \quad (4.17)$$

where random matrix $[\mathbf{L}]$ are upper triangular matrices with independent elements. In the procedure, each element $\mathbf{L}_{ij}$ in matrix $[\mathbf{L}]$ is sampled independently with the algorithms below (see Section 5.1 in ref. [34]):

1. The off-diagonal elements $\mathbf{L}_{ij}$ with $i < j$ are obtained from

$$\mathbf{L}_{ij} = \sigma_d \, \mathbf{w}_{ij}, \tag{4.18}$$

in which $\sigma_d = \delta \times (d+1)^{-1/2}$, and $\mathbf{w}_{ij}$ (i.e., $\mathbf{w}_{12}$, $\mathbf{w}_{13}$, and $\mathbf{w}_{23}$) are independent Gaussian random variables with zero mean and unit variance.

2. The diagonal elements are generated as follows:

$$\mathbf{L}_{ii} = \sigma_d \sqrt{2\mathbf{u}_i} \quad \text{with} \;\; i = 1, 2, 3 \tag{4.19}$$

where $\mathbf{u}_i$ is a positive valued gamma random variable with the following probability density function:

$$p(u) = \mathbb{1}_{\mathbb{R}^+}(u) \, \frac{u^{\frac{d+1}{2\delta^2} + \frac{1-i}{2} - 1} \exp(-u)}{\Gamma\left(\frac{d+1}{2\delta^2} + \frac{1-i}{2}\right)} \tag{4.20}$$

That is, the i^{th} diagonal term $\mathbf{u}_i$ conforms to gamma distribution with shape parameter $k = (d+1)/(2\delta^2) + (1-i)/2$ and scale parameter 1.

3. After obtaining the elements as above, a realization $[L]$ of the random matrix $[\mathbf{L}]$ can be assembled. Subsequently, realizations $[G]$ and $[R]$ for matrices $[\mathbf{G}]$ and $[\mathbf{R}]$, respectively, can be obtained from $[\mathbf{G}] = [\mathbf{L}]^T[\mathbf{L}]$ and $[\mathbf{R}] = [\underline{L}_R]^T[\mathbf{G}][\underline{L}_R]$ as in Eqs. (5.8) and (5.6).

4.3.3 Random Matrix Field Model for Reynolds Stresses

The probability model and the Monte Carlo sampling algorithm described in Sections 4.3.1 and 4.3.2 above is concerned with the Reynolds stress tensor at a single point. An important challenge in the present application is to represent and model the correlation of Reynolds stress at different spatial locations. This feature distinguishes the present contribution from previous applications of random matrix in composite materials models [17] and structural dynamics [20].

In this work we assume that the off-diagonal terms and the square roots of the diagonal terms have the same spatial correlation structures. Gaussian kernel is among the most common choice in the literature, but other kernels such as periodic (e.g., sinusoidal) kernels [18] or exponential kernels [35] have been used as well. The choice of kernel is reflected in the smoothness of the realizations of the random tensor field $\mathbf{L}$. With the Gaussian kernel used in this work, the correlation between two random variables at two spatial locations x and x' can be written as:

$$\rho_L\{\mathbf{L}_{ij}(x), \mathbf{L}_{ij}(x')\} \equiv \frac{\mathrm{Cov}\{\mathbf{L}_{ij}(x), \mathbf{L}_{ij}(x')\}}{\sigma_{ij}(x)\sigma_{ij}(x')} = \exp\left[-\frac{|x-x'|^2}{l^2}\right] \quad \text{for} \quad i < j \tag{4.21a}$$

$$\rho_L\{\mathbf{L}^2_{ii}(x), \mathbf{L}^2_{ii}(x')\} \equiv \frac{\mathrm{Cov}\{\mathbf{L}^2_{ii}(x), \mathbf{L}^2_{ii}(x')\}}{\sigma_{ii}(x)\sigma_{ii}(x')} = \exp\left[-\frac{|x-x'|^2}{l^2}\right] \quad x, x' \in \Omega \tag{4.21b}$$

where Ω is the spatial domain of the flow field. Note that repeated indices *do not* imply summation. $\sigma_{ij}^2(x)$ and $\sigma_{ii}^2(x)$ are the variances of the marginal distributions for the off-diagonal elements $\mathbf{L}_{ij}(x)$ and the square of the diagonal elements $\mathbf{L}_{ii}^2(x)$, respectively. That is, $\text{var}\{\mathbf{L}_{ij}(x)\} = \sigma_{ij}^2(x)$ and $\text{var}\{\mathbf{L}_{ii}^2(x)\} = \sigma_{ii}^2(x)$, the expression of which will be given in Eqs. (4.24) and (4.28), respectively. ρ_L is the correlation kernel, $|\cdot|$ is the Euclidean norm of vectors, and l is the correlation length scale of the stochastic process. We emphasize that the correlations above are between *the same element at different locations* x and x', and that the random variables $\mathbf{L}_{11}$, $\mathbf{L}_{22}$, $\mathbf{L}_{33}$, $\mathbf{L}_{12}$, $\mathbf{L}_{13}$, and $\mathbf{L}_{23}$, which are different elements of the matrix $[\mathbf{L}]$, are independent of each other as pointed out above.

With the correlation model defined in Eq. (4.21) for the elements of matrix $[\mathbf{L}]$, the random variables used to generate L_{ij} in Eqs. (5.9) and (5.11) can be generalized to random fields. First, it is straightforward to generalize the Gaussian random variable $\mathbf{w}_{ij}$ to a Gaussian random field (also referred to as Gaussian process),

$$\mathbf{L}_{ij}(x) = \sigma_d(x)\mathbf{w}_{ij}(x), \tag{4.22}$$

where $\mathbf{L}_{ij}(x)$ and $\mathbf{w}_{ij}(x)$ are random fields indexed by the spatial coordinate x, and

$$\sigma_d(x) = \delta(x)\,(d+1)^{-1/2} \tag{4.23}$$

is a spatially varying field specifying the standard deviation of the marginal distribution of $L_{ij}(x)$ at location x. Simple algebra shows that if we choose $\mathbf{w}_{ij}(x) \sim \mathcal{GP}(0, K)$ as the Gaussian process with covariance kernel $K(x, x') = \exp\left[-(|x - x'|^2)/l^2\right]$ as in Eq. (4.21), then

$$\sigma_{ij}(x) = \sigma_d(x) = \frac{\delta(x)}{\sqrt{d+1}}, \quad \text{or equivalently} \quad \sigma_{ij}^2(x) = \frac{\delta^2(x)}{d+1}. \tag{4.24}$$

The Gaussian processes $\mathbf{w}_{ij}(x)$ can be expressed by using the Karhunen–Loeve (KL) expansion, which can be written as follows when truncated to N_{KL} terms:

$$\mathbf{w}_{ij}(x) = \sum_{\alpha=1}^{N_{\text{KL}}} \sqrt{\lambda_\alpha}\,\phi_\alpha(x)\,\boldsymbol{\omega}_\alpha \tag{4.25}$$

where $\boldsymbol{\omega}_\alpha \sim \mathbf{N}(0, 1)$ with $\alpha = 1, \cdots, N_{\text{KL}}$ being the standard Gaussian random variables; λ_α and $\phi_\alpha(x)$ are the eigenvalue and the corresponding eigenfunction for the α^{th} mode obtained by solving the Fredholm integral equation [36]:

$$\int_\Omega \rho(x, x')\phi(x')\,dx' = \lambda\phi(x)\,, \tag{4.26}$$

where Ω is the spatial domain of the flow as defined above.

Remarks on using nonstationary and anisotropic kernels to reflect the structure of the flow field. Non-stationarity and anisotropy in the Gaussian process $\mathbf{w}(x)$ can be achieved by using spatially varying and/or anisotropic length scale $l(x)$, which depends on the characteristics

of the mean flow. For example, for a nonstationary Gaussian process, the length scale l in Eq. (4.21) can be written as $l = \sqrt{l(x)l(x')}$ following ref. [37]. As such, the physical structure of the flow field is encoded in the Karhunen–Loeve basis functions. It is also desirable to specify different variances $\sigma_{ij}(x)$ at different locations. For example, in regions with flow separation and pressure gradient, the Boussinesq assumptions are violated and thus most RANS models have poor performances. Consequently, the variance $\sigma_{ij}(x)$ should be larger in these regions, which can be achieved by specifying the dispersion parameter $\delta(x)$ to depend on the location x.

The sampling algorithm for the random variables of the diagonal terms in Eq. (5.11) can be similarly generalized to random fields as follows:

$$\mathbf{L}_{ii}(x) = \sigma_d(x)\sqrt{2\,\mathbf{u}_i(x)}, \tag{4.27}$$

where $\sigma_d(x)$ is defined the same as above. Recall the facts that $\mathbf{u}_i(x)$ has a gamma distribution with shape parameter $k = (d+1)/(2\delta^2) + (1-i)/2$ and that $\mathrm{Var}\{\mathbf{u}_i\} = k$. Substituting Eq. (4.23) into Eq. (4.27) and using the two facts above, after some algebra one can show that

$$\sigma_{ii}^2 \equiv \mathrm{Var}\{\mathbf{L}_{ii}^2\} = 4\sigma_d^4\,\mathrm{Var}\{\mathbf{u}_i\} = \frac{2\delta^2}{d+1} + \frac{2\delta^4}{(d+1)^2} \times (1-i) \quad \text{for} \quad i = 1, 2, 3, \tag{4.28}$$

where $d = 3$, and the spatial dependence of all other variables are omitted for notational brevity. However, since $\mathbf{u}_i(x)$ are random fields with gamma marginal distributions, they are not straightforward to synthesize. Although the KL expansion above can still be used to represent the random field $\mathbf{u}_i(x)$, the corresponding coefficients obtained from the expansion are neither independent nor Gaussian. To overcome this difficulty, we follow the procedure in ref. [35] and express the gamma random variables $\mathbf{u}_i$ at any location x with polynomial chaos expansion:

$$\begin{aligned} \mathbf{u}(x) &= \sum_{\beta=0}^{N_p} U_\beta(x)\Psi_\beta(\mathbf{w}(x)) \\ &= U_0 + U_1\mathbf{w}(x) + U_2(\mathbf{w}^2(x) - 1) + U_3(\mathbf{w}^3(x) - 3\mathbf{w}(x)) \\ &\quad + U_4(\mathbf{w}^4(x) - 6\mathbf{w}^2(x) + 3) + \cdots \end{aligned} \tag{4.29}$$

where N_p is the order of polynomial expansion; for a given x, $\Psi_\beta(\mathbf{w}(x))$ are the Hermite polynomials in standard Gaussian random variable $\mathbf{w}(x)$, with the first four terms explicitly written as above; U_β are the coefficients for the β^{th} polynomial, for which the spatial index x has been omitted for brevity. The coefficients can be obtained from orthogonality conditions with respect to the Gaussian measure [38]:

$$U_\beta = \frac{\langle \mathbf{u}\Psi_\beta \rangle}{\langle \Psi_\beta^2 \rangle} = \frac{1}{\langle \Psi_\beta^2 \rangle} \int_{-\infty}^{\infty} F_{\mathbf{u}}^{-1}[F_{\mathbf{w}}(w)]\ \Psi_\beta(w)\ p_{\mathbf{w}}(w) dw \tag{4.30}$$

where $\langle \mathbf{\Psi}_\beta^2 \rangle$ is the variance of the β^{th} order polynomial of standard Gaussian random variable; $F_{\mathbf{w}}(\mathbf{w})$ and $p_{\mathbf{w}}(\mathbf{w})$ are the Cumulative Distribution Function (CDF) and PDF, respectively, of the standard Gaussian variable; $F_{\mathbf{u}}$ and $F_{\mathbf{u}}^{-1}$ are the CDF and its inverse, respectively, of random variable $\mathbf{u}$. As indicated previously, Eq. (5.13) is evaluated for each x with $\mathbf{w}(x)$ being a standard Gaussian variable.

Sakamoto and Ghanem [35] derived the relation between spatial correlation of the non-Gaussian field $\mathbf{u}(x)$, i.e., $\rho_u\{\mathbf{u}(x), \mathbf{u}(x')\}$ and the correlation $\rho_w\{\mathbf{w}(x), \mathbf{w}(x')\}$ of the Gaussian random field $\mathbf{w}(x)$ used in its polynomial chaos representation. This is achieved by substituting Eq. (4.29) into the definition of covariance. They further showed that the following approximation yields very good accuracy:

$$\rho_u\{\mathbf{u}(x), \mathbf{u}(x')\} \approx \rho_w\{\mathbf{w}(x), \mathbf{w}(x')\}\,, \tag{4.31}$$

which indeed has been verified in our work by using the generated samples. This approximation is what we shall use in the present work. Therefore, given the correlation structure of field $\mathbf{u}_i$, an approximation of the kernel $\rho_w\{\mathbf{w}(x), \mathbf{w}(x')\}$ is obtained, which can be used in the KL expansion to find the eigenmodes and further synthesize the Gaussian random fields $\mathbf{w}_{ii}$. Finally, the non-Gaussian random field $\mathbf{u}_i(x)$ can be obtained by reconstructing from the polynomial chaos based on Eq. (4.29) at each location $x \in \Omega$.

4.3.4 Monte Carlo Sampling of Reynolds Stress Fields

Based on the development above, the algorithm of Monte Carlo sampling of Reynolds stress field can be performed as follows:

1. Draw independent samples ω_α from the standard Gaussian distribution $\mathbf{N}(0, 1)$ with $\alpha = 1, \cdots, N_{\text{KL}}$.

2. Use the KL expansion in Eq. (4.25) to reconstruct a Gaussian random field $w(x)$ with λ_α and $\phi_\alpha(x)$ obtained from solving Eq. (4.26).

3. Repeat steps 1–2 above six times to obtain six independent realizations of Gaussian random fields $w_{12}(x)$, $w_{13}(x)$, $w_{23}(x)$, $w_{11}(x)$, $w_{22}(x)$, and $w_{33}(x)$. The first three will be used to synthesize the off-diagonal elements $L_{12}(x)$, $L_{13}(x)$, and $L_{23}(x)$, respectively, and the last three for the diagonal elements $L_{11}(x)$, $L_{22}(x)$, and $L_{33}(x)$, respectively.

   Remark on the choice of KL modes for the representation of the six Gaussian random fields. In this work the same KL modes ϕ_α and eigenvalues λ_α are used for generating all six realizations $w(x)$ of Gaussian random fields above. This is a modeling choice made for simplicity and also for the lack of prior knowledge that can be straightforwardly represented in the current framework. However, in cases where it is desirable to use a different number N_{KL} of modes or even a different kernel $K(x, x')$ for each field, it can be achieved in a straightforward manner as well.

4. Synthesize off-diagonal elements based on Eq. (4.22).

5. Reconstruct the random fields $\mathbf{u}_1(x)$, $\mathbf{u}_2(x)$, and $\mathbf{u}_3(x)$ based on the polynomial chaos expansion in Eq. (4.29) and further obtain the fields $\mathbf{L}_{11}(x)$, $\mathbf{L}_{22}(x)$, and $\mathbf{L}_{33}(x)$ based on Eq. (4.27).

4.3.5 Considerations in Numerical Implementation

For clarity we outline the complete algorithm of sampling of Reynolds stress fields and the propagation to velocities and other Quantities of Interest (QoIs) in 4.A. Remarks are made below on computational considerations in implementing the proposed algorithm.

In the expansions described in Sections 4.3.2 and 4.3.3, the Cholesky factorization of the Reynolds stress, the polynomial chaos expansion of the marginal distribution of the gamma random variable $\mathbf{u}_i$, and the KL expansion of the Gaussian random field all need to be performed on a mesh. Theoretically, they all can be performed on the RANS simulation mesh. However, this choice would lead to unnecessarily high computational costs. The RANS mesh is designed to resolve the flow field features. Usually it is refined in the near-wall region to resolve the boundary layer. On the other hand, the mesh for the KL expansion only needs to resolve the length scale of the correlation, i.e., the field $l(x)$. Finally, the mesh used for the polynomial chaos expansion needs to resolve the variation of the dispersion parameter $\delta(x)$ field. If the dispersion is constant throughout the domain, one polynomial chaos expansion is sufficient. Therefore, the three expansions and the corresponding reconstructions below are performed on separate meshes, which are referred to as RANS mesh, PCE mesh, and KL mesh, respectively. Interpolations are needed when performing operations on fields based on different meshes. For example, in Eq. (4.29) where the gamma field is reconstructed from the coefficients $U_\beta(x)$ and the Hermite polynomials in the Gaussian random field $\mathbf{w}(x)$, the coefficients are based on the PCE mesh while the Gaussian random field is based on the KL mesh. An interpolation of the coefficients $U_\beta(x)$ from the PCE mesh to the KL mesh is thus needed. The obtained gamma fields $\mathbf{u}_i$, the diagonal terms $\mathbf{L}_{ii}(x)$, and the matrix $\mathbf{G}(x)$ are thus based on the KL mesh as well. Similarly, therefore, when the Reynolds stress is reconstructed from $[\mathbf{R}] = [\underline{L}_R]^T[\mathbf{G}][\underline{L}_R]$, the matrix $[\mathbf{G}]$ is first interpolated from the KL mesh to the RANS mesh, so that the obtained Reynolds stress realization $[R]$ can be used in the RANS simulation.

An intrinsic assumption of the framework is that the Reynolds stress provided by the baseline model is the best estimate and thus must be realizable. In cases where the baseline Reynolds stresses are non-realizable, one needs to first bring them to the realizable domain (e.g., by bringing the points outside the Barycentric triangle to the closest point on the edge). However, the choice of such a correction scheme is not unique, and any such scheme is inevitably *ad hoc*.

4.4 Numerical Results

In this section we use the flow over periodic hills at Reynolds number $Re = 2800$ to demonstrate the proposed model-form uncertainty quantification scheme for RANS simulations. The computational domain is shown in Fig. 5.2, where all dimensions are normalized with the crest height H. The Reynolds number Re is based on the crest height H and bulk velocity U_b at the crest. Periodic boundary conditions are applied at the boundaries in the streamwise (x) direction while non-slip boundary conditions are imposed at the walls. The spanwise direction is not considered since the mean flow is two-dimensional. Benchmark data from direct numerical simulations are used to compare with the sampled Reynolds stresses and the velocities obtained by propagating the Reynolds stresses through the RANS solver.

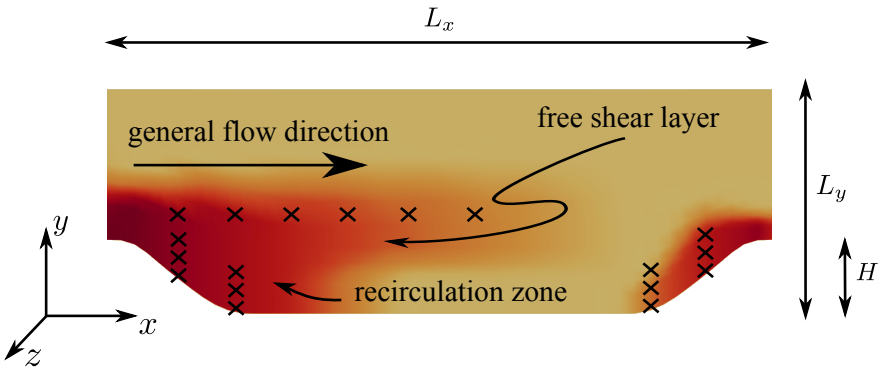

Figure 4.2: Domain shape for the flow in the channel with periodic hills. The x-, y- and z-coordinates are aligned with the streamwise, wall-normal, and spanwise directions, respectively. All dimensions are normalized by H with $L_x/H = 9$ and $L_y/H = 3.036$. The contour shows the dispersion parameter $\delta(x)$, where darker color denotes larger variance. Two typical points A and B are annotated in the figure.

4.4.1 Cases Setup

The dispersion parameter is a critical free parameter in the uncertainty quantification scheme. The specification of δ is constrained by requirement $0 < \delta < \sqrt{2}/2$ obtained from Eq. (6.5) and guided by the subjective belief of the user on the uncertainty in the Reynolds stresses, i.e., larger δ indicates larger uncertainties. We investigate three cases with different choices of dispersion parameters: (1) a small dispersion parameter $\delta = 0.2$, (2) a large dispersion parameter $\delta = 0.6$, and (3) a spatially varying $\delta(x)$ field as specified by the color (or grey scale) contour shown Fig. 5.2. A spatially varying $\delta(x)$ allows the user to encode empirical knowledge about the turbulence model and/or the flow of concern into the prior distribution of Reynolds stresses. For example, in the flow over periodic hills studied here, the underlying Boussinesq assumption is violated in the regions with recirculation, non-parallel free-shear, or strong mean flow curvature (see annotations in Fig. 5.2). Consequently, these regions

are particularly problematic for eddy viscosity models (including the k–ε model used in this work). Hence, relatively large dispersion parameters are specified in these regions compared to other regions to reflect the lack of confidence on the model. This is similar to the practice of specifying spatially varying variance fields when injecting uncertainties to the physics-based quantities (magnitude and shape of the Reynolds stress) in Xiao et al. [6]. On the other hand, it is also possible to use maximum likelihood estimation to obtain a dispersion parameter $\delta(x)$ field if some measurement data of Reynolds stresses are available, but this approach is not explored in the present work.

For Cases 1 and 2 with constant dispersion parameters in the domain, the marginal distribution of random matrix $[\mathbf{G}]$ is the same at all locations. Therefore, the polynomial chaos expansion needs to be performed only once. That is, the expansion coefficients U_β in Eq. (5.13) is spatially uniform. Hence, a PCE mesh is not needed. For Case 3 with a spatially varying $\delta(x)$, a coarse PCE mesh of 15×10 cells is used. In all three cases, the marginal distribution of the diagonal terms are only weakly non-Gaussian, and thus a third order polynomial expansion is found to be sufficient. In the KL expansion, we used 30 modes, allowing 90% of the variance to be captured. Since the RANS mesh is rather small with only 3000 cells, the KL expansion is performed on the same mesh. In the correlation kernel we used an anisotropic yet spatially uniform length scale ($l_x/H = 2$ and $l_y/H = 1$) to reflect the anisotropy of the flow. They are chosen based on the approximate length scale of the mean flow. The effects of using spatially varying correlation length scales are similar to those of using non-stationary dispersion parameter field. We use 1000 samples to adequately represent the prior distribution of the Reynolds stresses. To limit the computational cost of the RANS simulations, only 100 of the 1000 samples are randomly selected to propagate to the velocities. The computational parameters discussed above are summarized in Table 5.1.

Table 4.1: Mesh and computational parameters used in the flow over periodic hills.

Parameters	**Case 1**	**Case 2**	**Case 3**
dispersion parameter $\delta(x)$	0.2	0.6	0.16–0.65[(a)]
nature of $\delta(x)$	uniform	uniform	nonuniform
PCE mesh	–	–	15×10
order of polynomial expansion (N_p)	3		
KL mesh	50×30		
RANS mesh	50×30		
number of KL modes N_{KL}	30		
correlation length scales[(b)]	$l_x/H = 2$, $l_y/H = 1$		
number of Reynolds stress samples	1000		
number of velocity propagation samples	100		

(a) Spatial contour of $\delta(x)$ is shown in Fig. 5.2.
(b) See Eq. (4.25)

4.4.2 Results and Interpretations

As discussed above, 1000 samples of Reynolds stress random field $[\mathbf{R}](x)$ are drawn by using the algorithm described in Section 4.3.4. An additional challenge is the visualization, validation, and interpretation of the sampled Reynolds stress fields, because in general it is not straightforward to interpret the state of the turbulence from their individual components. To facilitate physical interpretation, in all three cases we map the sampled Reynolds stresses to the six independent physical dimensions with the scheme described in Section 4.2.2, i.e., the magnitude k of Reynolds stress tensor, its shape (expressed in Barycentric coordinates C_1, C_2, and C_3), and the Euler angles (φ_1, φ_2, and φ_3) of its eigenvectors. The scattering of the samples in the Barycentric triangle can be obtained from their Barycentric coordinates, and the probability density functions for all the quantities can be estimated from the samples with a given kernel.

The samples obtained in Case 1 (with $\delta = 0.2$) and Case 2 (with $\delta = 0.6$) are first analyzed by visualizing the scatter plots in the Barycentric triangle, the associated probability density contours, and the marginal distributions of the physical variables (e.g., C_3, k, and φ_3) for two typical points: (1) point A located at $x/H = 2.0$ and $y/H = 0.5$ and (2) point B located at $x/H = 2.0$ and $y/H = 0.01$. Point A is a generic point in the recirculation region, and point B is a near-wall point with two-dimensional turbulence representing limiting states. The locations of the two points in the domain are indicated in Fig. 5.2 and in the insets of Figs. 5.3 and 5.5.

The scatter plots for the Reynolds stress samples at point A are shown in Figs. 5.3a and 5.3b for Cases 1 and 2, respectively. Since this is a generic point, the Reynolds stress state predicted in the baseline simulation is projected to the interior of the Barycentric triangle. While the true state given by the DNS simulation is also located in the interior of the triangle, it is to the upper right of the baseline results. Note that the points located on the edges and vertices correspond to limiting states as illustrated in Fig. 6.1a. In both cases the samples are scattered around the baseline state, suggesting that perturbations introduced in the set $\mathbb{M}_d^{+0}$ about the baseline are still scattered around the corresponding baseline results in the Barycentric triangle. However, the two cases exhibit two notable differences. First, the scattering in Case 2 is much larger than that in Case 1, which is a direct consequence of the larger dispersion parameter ($\delta = 0.6$) compared to that in Case 1 ($\delta = 0.2$). Second, the sample mean deviates significantly from the baseline in Case 2 while they agree quite well in Case 1. This is an interesting observation. Recall that the probability distribution in Eq. (4.7) is derived under the constraint $\mathbb{E}\{[\mathbf{R}]\} = [\underline{R}]$ given in Eq. (4.10), which implies that the mean of the sample Reynolds stresses should be the baseline prediction assuming the number of samples is large enough. We have verified that the constraint is indeed satisfied and that the sampling error is negligible with the chosen sample number 1000. Therefore, we can see that the mean is not preserved during the projection from the Reynolds stress space to the Barycentric coordinates. However, note that the mapping from the Reynolds stress to the Barycentric coordinates is linear [8] as can be seen from Eqs. (6.2) and (6.3). Hence, it

can be inferred that the deviation of the sample mean from the baseline on the Barycentric map is entirely due to the realizability constraint, i.e., the capping of the samples that fall outside the realizability range. The constraint manifests itself as the edge boundaries of the Barycentric triangle. When the perturbation is small relative to the distance of the baseline state to the boundaries, as is the situation in Case 1, the perturbation does not "feel" the constraints. Consequently, the sample mean and the baseline result are approximately the same. In contrast, when the perturbation is large compared to the distance between the baseline and one of the boundaries, the constraint comes into play, leading to appreciable deviations between the sample mean and the baseline. This is better illustrated with the probability density contours in Figs. 5.3c and 5.3d for Cases 1 and 2, respectively. The contours in Fig. 5.3c are approximately elliptic, showing little influence from the boundaries. On the other hand, the contours in Figs. 5.3d clearly follow the three edges at the boundary and displays a triangular shape overall. Since no samples fall outside the Barycentric triangle as can be seen from the scatter plots in both cases, the observation also verified the claim that the random matrix based approach proposed in this work is capable of ensuring Reynolds stress realizability.

To further examine the probability distribution of the Reynolds stress samples, in Fig. 4.4 we present the discrepancies ΔC_3, $\Delta\varphi_3$, $\Delta \ln k$ between the sampled and the baseline Reynolds stress for point A. Perturbations on the other physical quantities (e.g., the other Barycentric coordinates ΔC_1 and ΔC_2) have similar characteristics to ΔC_3 presented here and thus are omitted for brevity. Similarly, perturbations $\Delta\varphi_1$ and $\Delta\varphi_2$ for the Euler angles φ_1 and φ_2 are omitted as well. Xiao et al. [6] introduced uncertainties to the predicted Reynolds stresses by modeling the discrepancies in shape and magnitude of the Reynolds stress as Gaussian random fields. It is illustrative to compare the discrepancies above (which are obtained from samples directly drawn in $\mathbb{M}_d^{+0}$) to the corresponding Gaussian distributions having the same mean and variance as those of the samples. The comparison is performed in Fig. 4.4, where the PDFs of the Gaussian distributions obtained in this way are presented along with those estimated from samples. It can be seen that in Case 1 the distributions for all three discrepancy quantities ΔC_3, $\Delta\varphi_3$, $\Delta \ln k$ are rather close to the corresponding Gaussian distributions. In contrast, the corresponding distributions in Case 2 deviate significantly from the Gaussian distributions. It is also noted that the sample mean (denoted in vertical dashed lines; same hereafter) of ΔC_3 deviate slightly from zero in Case 1 but significantly from zero in Case 2, which is consistent with the earlier observations from Figs. 5.3a and 5.3b. However, the sample means for $\Delta\varphi_3$ and $\Delta \ln k$ are zero for both Case 1 and Case 2, despite the fact that the sample distribution are non-Gaussian for Case 2. This can be explained by the fact that there are no physical constraints on $\ln k$ or φ (except for the range $[-\pi, \pi]$ specified in the definition). This is in contrast to C_3, which is bounded in $[0, 1]$. Notably, Figs. 4.4e and 4.4f seem to suggest that k (which is the turbulent kinetic energy defined as $\frac{1}{2}\operatorname{tr}([R])$) approximately follows a log-normal distribution. This could be related to the term with exponential of $-\operatorname{tr}[G]$ in Eq. (4.13). Soize [15] also gave the joint distribution of the random eigenvalues of $[\mathbf{R}]$ (see Eq. (64) therein), which theoretically can be marginalized to yield the analytical distribution of k. The analytical expression is, however, extremely

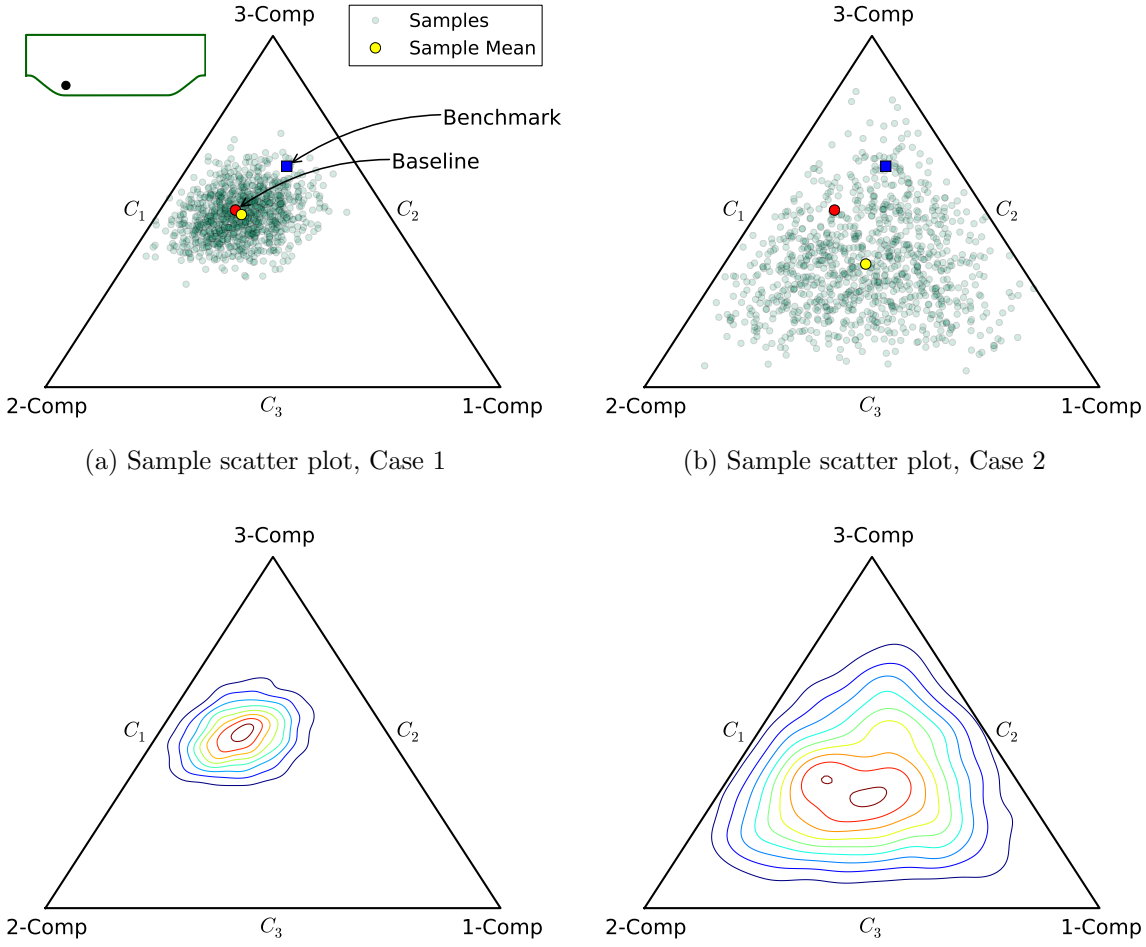

(a) Sample scatter plot, Case 1

(b) Sample scatter plot, Case 2

(c) Probability density contour, Case 1

(d) Probability density contour, Case 2

Figure 4.3: Scatter plots (panels a and b) and probability density contours (panels c and d) of the Reynolds stress samples projected to the Barycentric coordinates for point A ($x/H = 2.0, y/H = 0.5$) located in the recirculation region. Case 1 ($\delta = 0.2$) and Case 2 ($\delta = 0.6$) are compared.

complicated and is not pursued in the present work.

It is also of interest to see the probability distribution of the Reynolds stress at a near-wall location with limiting-state turbulence. Therefore, similar to Figs. 5.3 and 4.4, the scatter plots and distribution of physical variable are presented in Figs. 5.5 and 4.6, respectively, for point B located very close to the bottom wall (at $x/H = 2.0$ and $y/H = 0.01$). The true Reynolds stress at this point is two dimensional, and thus it is located right on the bottom edge of the Barycentric triangle ($C_3 = 0$) as indicated in Figs. 5.5a and 5.5b. Recall that C_3 indicates the degree of isotropy (three-dimensionality) of the turbulence. Hence, $C_3 = 0$ indicates that the turbulence is far from isotropic (in fact, it is two-dimensional), which is because the blocking of the wall suppressed almost all fluctuations in wall-normal direction. A standard eddy viscosity model, on the contrary, would predict a nearly isotropic turbulence state with $C_3 = 1$, located near the top vertex of the Barycentric triangle (indicated as dark/red filled circles). The scatter plots corresponding to Cases 1 and 2 are shown in Figs. 5.5a and 5.5b, and the corresponding probability density contours are presented in Figs. 5.5c and 5.5d. It can be seen that the sample distributions are influenced by the constraints in both cases, since the baseline state is located right next to the boundaries. Moreover, the difference between the sample mean and the baseline are large in both cases, which is also attributed to the constraints as discussed above. The distributions of ΔC_3, $\Delta\varphi_3$, and $\Delta \ln k$ are presented in Fig. 4.6. For both Cases 1 and 2, the sample distributions of ΔC_3 and $\Delta\varphi_3$ deviate significantly from Gaussian, while the distribution of k is still quite close to log-normal.

The analysis above focused on the marginal distributions of the Reynolds stresses at two representative locations with a generic and a limiting turbulence state. Since the Reynolds stress is modeled as a random matrix field, we present the turbulent shear stress R_{12} and the turbulent kinetic energy k in Figs. 4.7 and 4.8, respectively. These two quantities are the most relevant for the flow over period hills investigated here. The samples at eight streamwise locations $x/H = 1, 2, \cdots, 8$ along with the benchmark (DNS) and the baseline results. The geometry of the physical domain is also plotted to facilitate visualization. The sample mean profiles coincide with the baselines in most regions for all cases, and thus they are omitted to avoid cluttering. This is in contrast to the deviation of the sample means from the baseline results in the Barycentric triangle as observed in Figs. 5.3 and 5.5 for the same cases.

It can be seen that the turbulent shear stress R_{12} in the baseline and benchmark (DNS) results agree quite well with each other in the upper channel ($y/H = 2$ to 3) but deviate dramatically in the free-shear and recirculation regions. In the case with a small dispersion parameter $\delta = 0.2$, Fig. 4.7a shows that the uncertainty range as represented by the R_{12} samples is not able to cover the DNS results in regions where large discrepancies exist between the baseline and benchmark. This indicates that the prior may be overly confident, which may lead to difficulties in Bayesian inferences. With a large dispersion parameter $\delta = 0.6$ in Case 2, the scattering range of R_{12} increases and mostly covers the benchmark in the entire domain (Fig. 4.7b). However, the complex spatial pattern in the recirculation zone

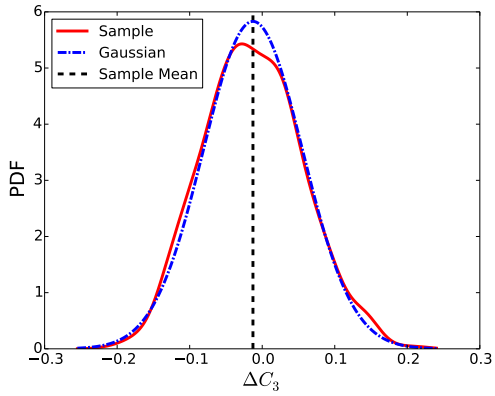

(a) Distribution of ΔC_3, Case 1

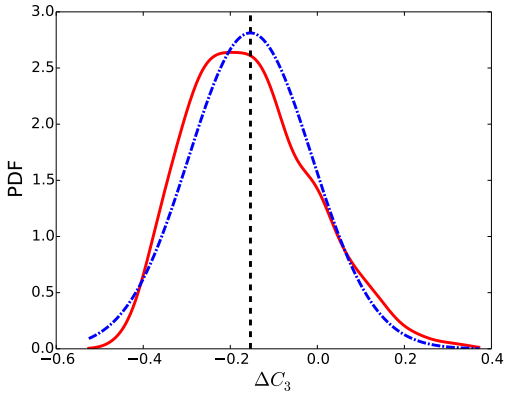

(b) Distribution of ΔC_3 for Case 2

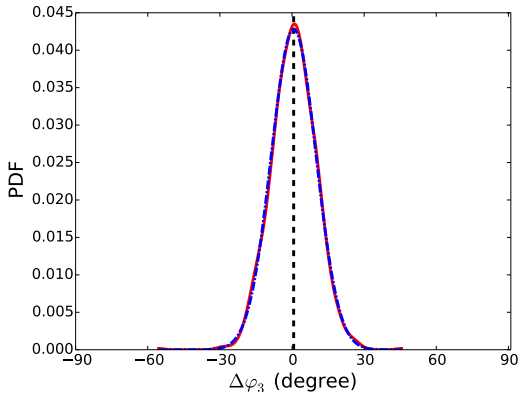

(c) Distribution of $\Delta\varphi_3$ for Case 1

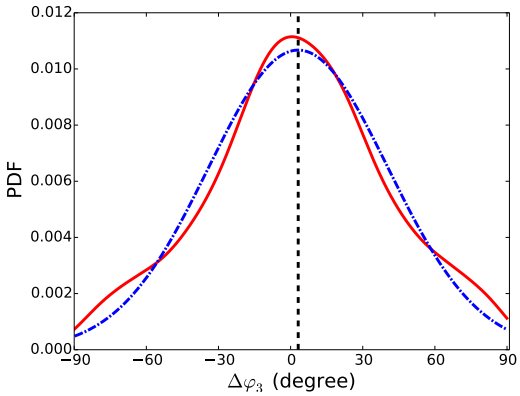

(d) Distribution of $\Delta\varphi_3$ for Case 2

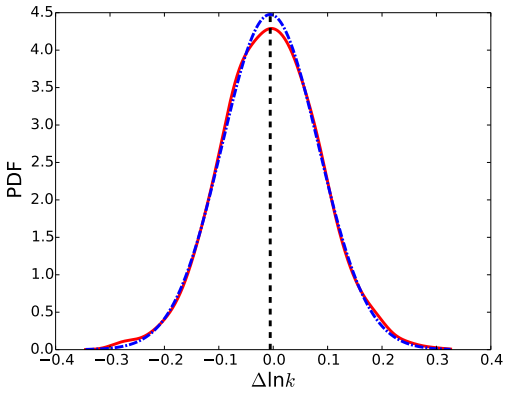

(e) Distribution $\Delta \ln k$ for Case 1

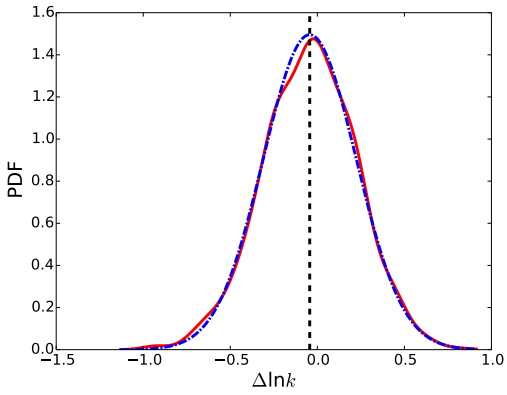

(f) Distribution $\Delta \ln k$ for Case 2

Figure 4.4: Distributions of the perturbations (ΔC_3, $\Delta\varphi_3$, and $\Delta \ln k$) in the physical variables for point A ($x/H = 2.0, y/H = 0.5$) located in the recirculation region. The distributions for Case 1 ($\delta = 0.2$) and Case 2 ($\delta = 0.6$) are compared.

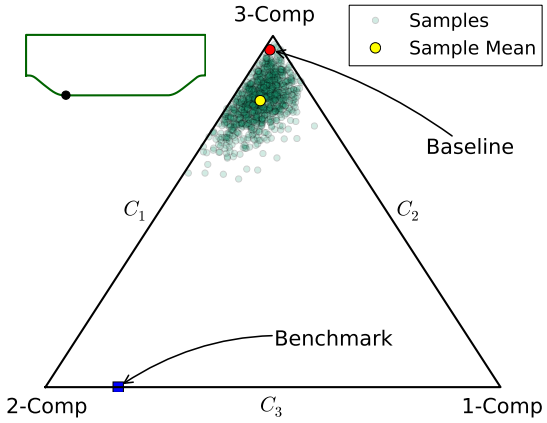

(a) Scatter plot of samples

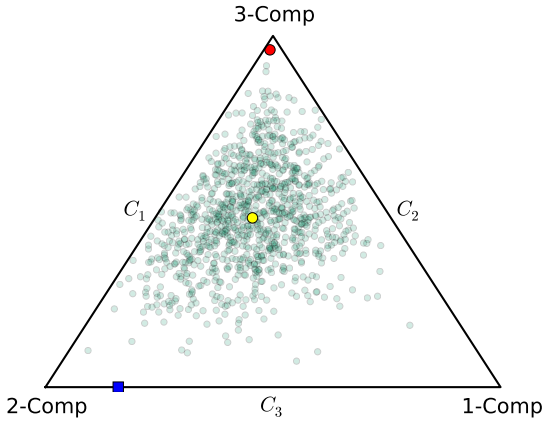

(b) Scatter plot of samples

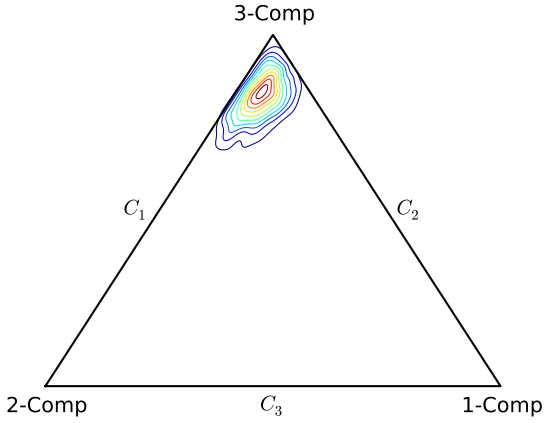

(c) Contour plot of samples

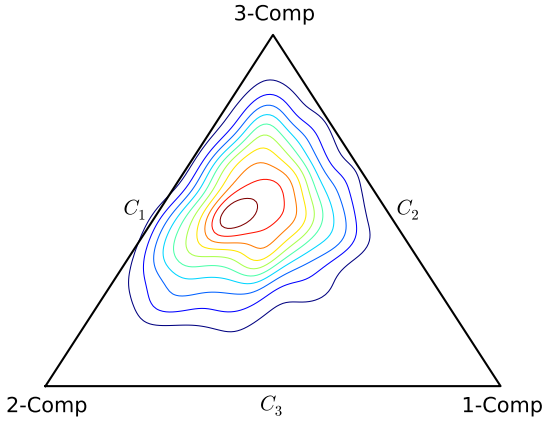

(d) Contour plot of samples

Figure 4.5: Scatter plots (panels a and b) and probability density contours (panels c and d) of the Reynolds stress samples projected to the Barycentric coordinates for point B ($x/H = 2.0, y/H = 0.01$) located in the recirculation region. Case 1 ($\delta = 0.2$) and Case 2 ($\delta = 0.6$) are compared.

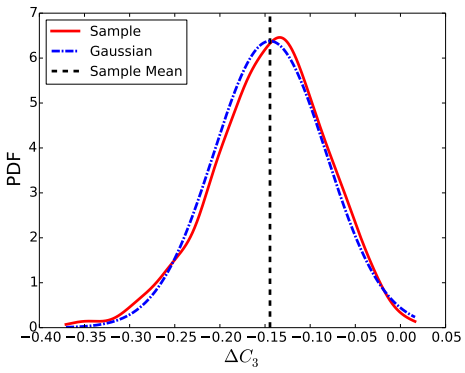

(a) PDF of ΔC_3, Case 1

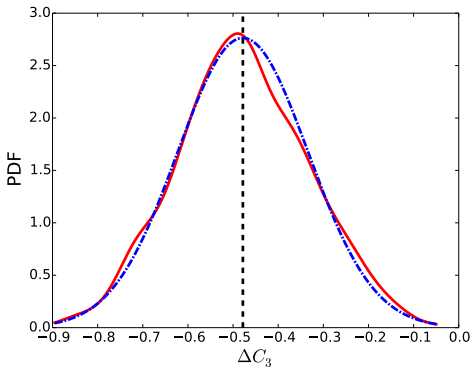

(b) PDF of ΔC_3, Case 2

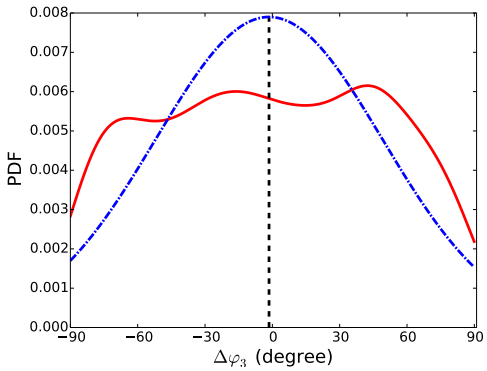

(c) PDF of $\Delta\varphi_3$, Case 1

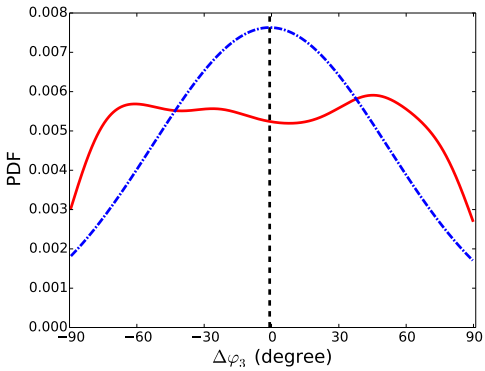

(d) PDF of $\Delta\varphi_3$, Case 2

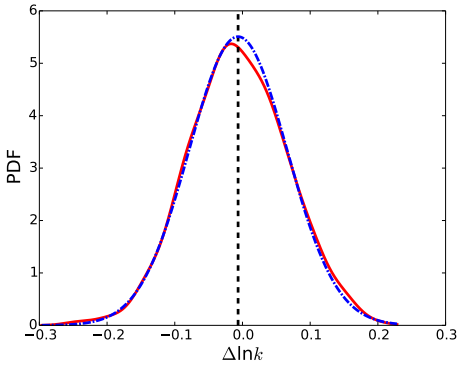

(e) PDF $\Delta \ln k$, Case 1

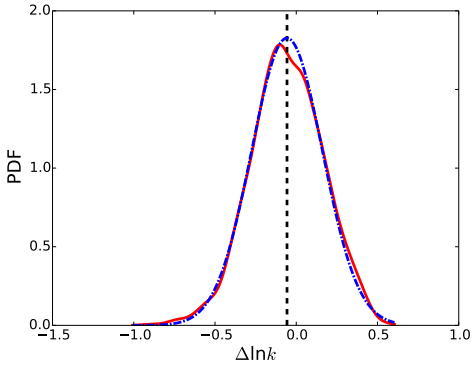

(f) PDF $\Delta \ln k$, Case 2

Figure 4.6: Probability density functions (PDF) of the perturbations (ΔC_3, $\Delta\varphi_3$, and $\Delta \ln k$) in the physical variables for point B ($x/H = 2.0, y/H = 0.01$) located in the near-wall region. The PDFs for Case 1 ($\delta = 0.2$) and Case 2 ($\delta = 0.6$) are compared.

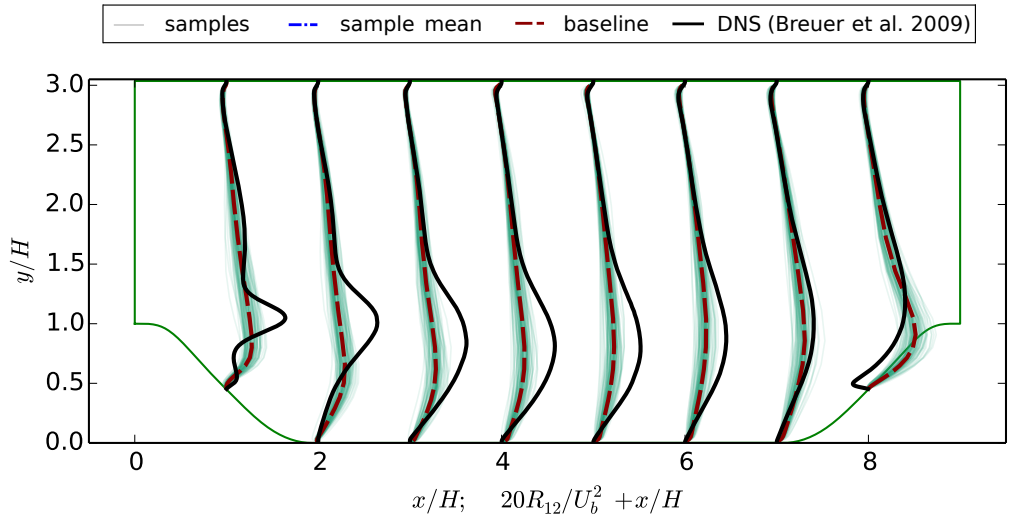

(a) Samples of R_{12} profiles, Case 1

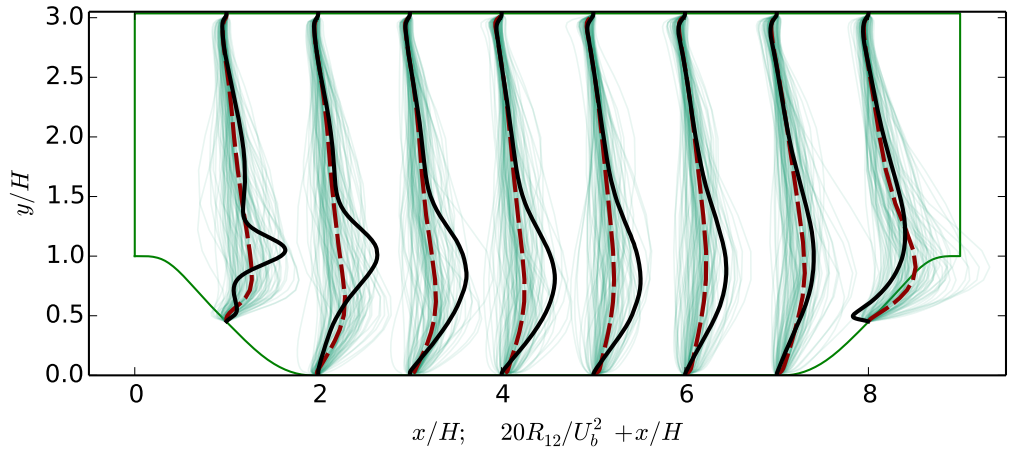

(b) Samples of R_{12} profiles, Case 2

Figure 4.7: Comparison of sampled Reynolds stress component R_{12} for Case 1 and Case 2. The profiles are shown at eight streamwise locations $x/H = 1, \cdots, 8$, compared to the baseline results and the benchmark (DNS) results obtained by direct numerical simulations [39].

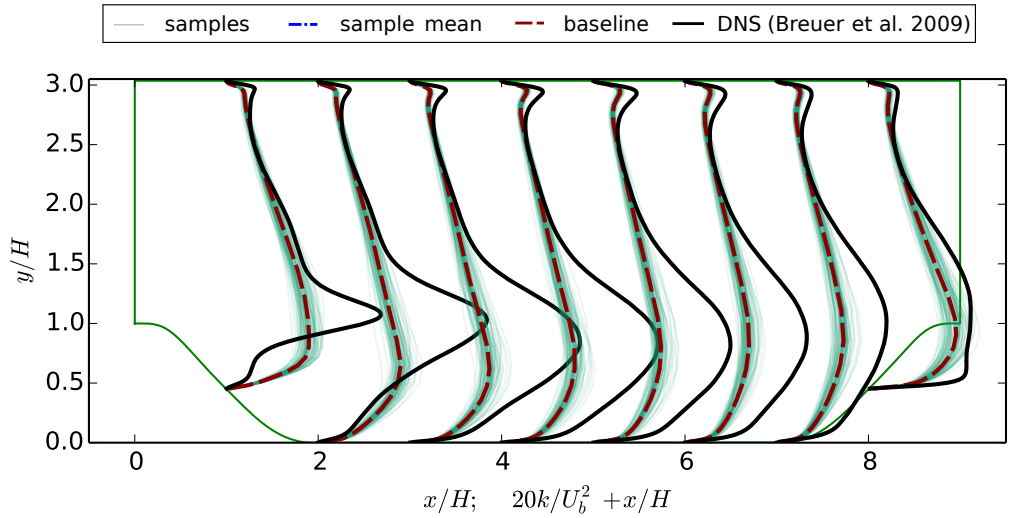

(a) Samples of k profiles, Case 1

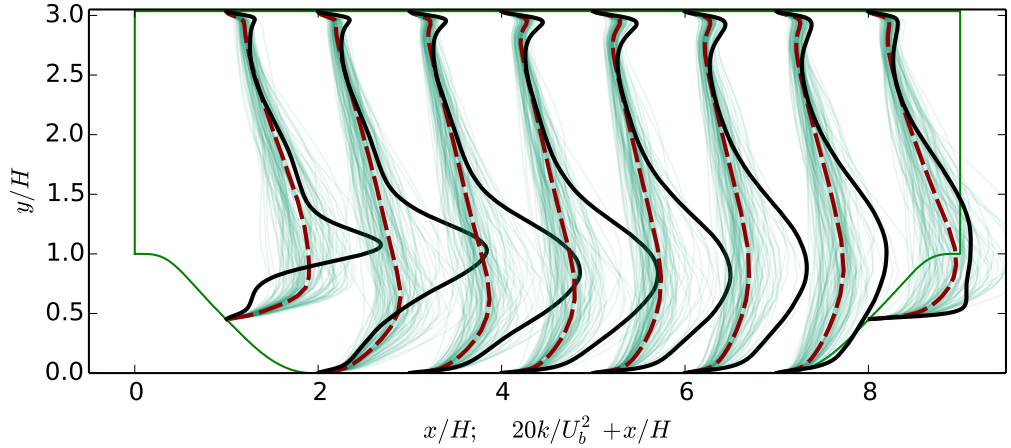

(b) Samples of k profiles, Case 2

Figure 4.8: Comparison of sampled turbulence kinetic energy k profiles for Case 1 and Case 2. The profiles are shown at eight streamwise locations $x/H = 1, \cdots, 8$, compared to the baseline results and the benchmark (DNS) results obtained by direct numerical simulations [39].

may not be fully captured by the ensemble, which is due to the large spatial variations of length scales. This is because the correlation structure and corresponding hyperparameters are still modeling choice in the proposed approach. Therefore, there is no guarantee that the ensemble would fully cover the truth. Moreover, since the dispersion parameter is spatially uniform, it also has large scattering in the upper channel, where in fact the discrepancies between baseline and DNS results are rather small. Similar patterns are also observed in the turbulent kinetic energy k profiles, which are shown in Figs. 4.8a and 4.8b for Cases 1 and 2, respectively. However, a notable difference is that the range of samples is not able to cover the DNS results even in Case 2 with a large discrepancy parameter. This is because the turbulent kinetic energy k is significantly underestimated in the baseline turbulence model, which is a known deficiency of the k–ε turbulence model when applied to this flow. The deficiency stems from the fact that the shear stresses and consequently the modeled turbulent kinetic energy production are weaker than the physical counterparts [40].

In light of the comparison between the samples and the benchmark above, it can be seen that using a spatial uniform dispersion parameter δ leads to scattering larger than necessary in the upper channel, but with insufficient scattering in regions that are indeed problematic for the baseline model (e.g., the free shear and recirculation regions). It is known from experiences in turbulence modeling that standard turbulence models have difficulties in these regions. Therefore, using a nonuniform, informative dispersion field $\delta(x)$ as shown in Fig. 5.2 can be justified as presented in Section 4.4.1 above. The samples of R_{12} and k are presented in Fig. 4.9. In both cases the scattering of the samples are larger in the free-shear and recirculation regions and are smaller in the upper channel, which is more consistent with the actual discrepancies between the baseline and the DNS results. A minor exception is that the turbulent kinetic energy near the upper wall is underpredicted by the baseline model but this is not reflected in the sample scatter. This is attributed to the fact that this feature is not reflected in the prior knowledge in the dispersion parameter $\delta(x)$ field.

Overall speaking, all sample profiles of the Reynolds stress component R_{12} and the turbulent kinetic energy k shown in Figs. 4.7–4.9 are physically reasonable. These samples are qualitatively similar to those obtained with the physics-based approach by directly perturbing the physical variables C_1, C_2, and $\ln k$ around the baseline results [6].

Remarks on the near-wall asymptotic behavior of sampled Reynolds stresses. It can be seen from Figs. 4.7–4.9 that the sampled turbulent shear stress R_{12} and turbulent kinetic energy k all approach zero towards the wall. In fact, other components of $[R]$ (not shown here) also exhibit similar and physically correct asymptotic behaviors. The correct "zero-approaching" behavior of the sampled Reynolds stresses is inherited from the baseline Reynolds stress $[\underline{R}]$. Recalling the decomposition $\underline{R} = [\underline{L}][\underline{L}^T]$, the Reynolds stress is constructed as follows:

$$[\mathbf{R}] = [\underline{L}][\mathbf{G}][\underline{L}^T]. \tag{4.32}$$

As the wall is approached, $[\underline{R}] \to [0]$ and thus $[\underline{L}] \to [0]$, where $[0]$ denotes rank two tensors with all zero elements. Consequently, although a realization $[G]$ of normalized random matrix

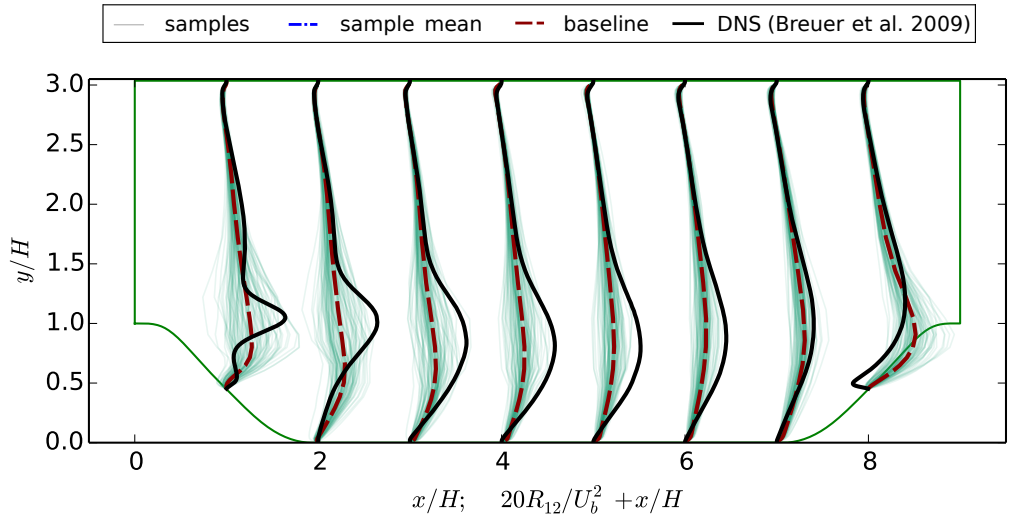

(a) Sample of R_{12} profiles, Case 3

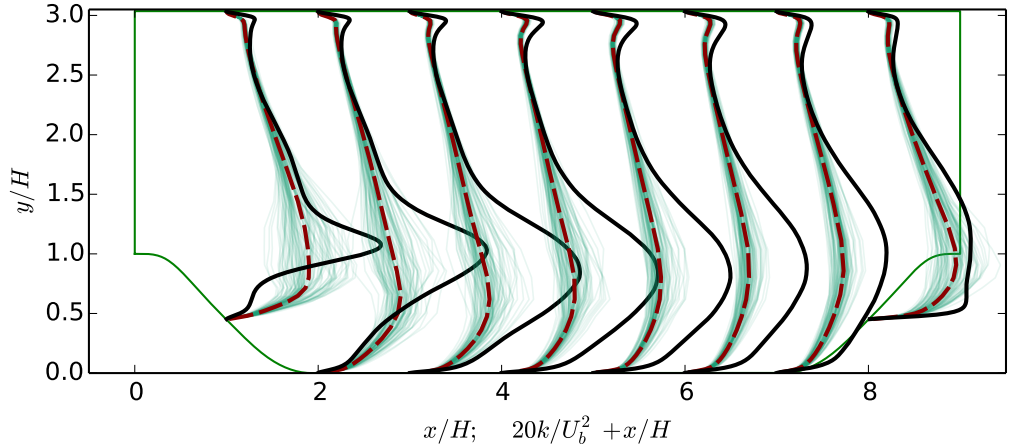

(b) Sample of k profiles, Case 3

Figure 4.9: The sampled turbulent shear stress R_{12} and turbulent kinetic energy k profiles for Case 3. The ensemble profiles are shown at eight streamwise locations $x/H = 1, \cdots, 8$, compared to the baseline results and the benchmark (DNS) results obtained by direct numerical simulations [39].

[**G**] can have large values near the wall, the Reynolds stress [R] reconstructed from Eq. (4.32) would still approach zero asymptotically towards the wall.

Ultimately it is the velocity fields and the associated auxiliary quantities (e.g., wall shear stress, reattachment point, and pressure drop across the channel) that are of interest in turbulent flow simulations. Therefore, the sampled Reynolds stress are propagated to velocities by using the RANS solver tauFoam [6], and the reattachment points are obtained by post-processing the velocity fields. The velocity profiles obtained for the three cases with different dispersion parameters are presented and compared in Fig. 5.12. Similar to the profiles of R_{12} and k, the velocity sample also show a small scattering in Case 1 ($\delta = 0.2$) and a larger scattering in Case 2 ($\delta = 0.6$). The advantage of using an informative $\delta(x)$ field can also be observed in this figure. Compared to the uniformly small scattering in Case 1 (panel a) and uniformly large scattering in Case 2 (panel c), the velocity scattering in Case 3 (panel c) is small in the upper channel and large in the free shear and recirculation regions, adequate to cover the benchmark (DNS) results in both regions. Finally, we note that in all three cases the velocity scattering in the lower part, particularly in the recirculation region, of the channel is larger, even though the Reynolds stress scattering is spatially uniform in Cases 1 and 2. This observation suggests that the velocity in the recirculation region is more sensitive to the Reynolds stresses, an important physical insight that is provided by the RANS solver. Similar analyses have been performed on other quantities of interest including the bottom wall shear stress and the reattachment point. Qualitatively similar observations are made as those presented above for the velocities, and thus the figures for the other QoIs are omitted here.

4.5 Discussions

4.5.1 Modeling Choices in Proposed Framework

A major motivation of using a random matrix approach with maximum entropy distribution is to minimize the amount of unwarranted information introduced into the prior. In the physics-based approach, the maximum entropy distributions can be defined on the physics-based components (magnitude, shape, and orientation) of the Reynolds stress tensor. In fact, this is exactly what was adopted in ref. [6] – they defined normal distributions (or log-normal for the magnitude) as priors for these physics-based variables. Normal distributions indeed have the maximum entropy with a given mean and variance [41]. However, a notable advantage of the current approach is that the maximum entropy distribution is defined for the *tensor*, and not for individual components. In the latter approach, it is not clear how large the variance of each component should be relative to each other. From this perspective, the current approach is more rigorous than the physics-based approach in that it introduces less unwarranted information.

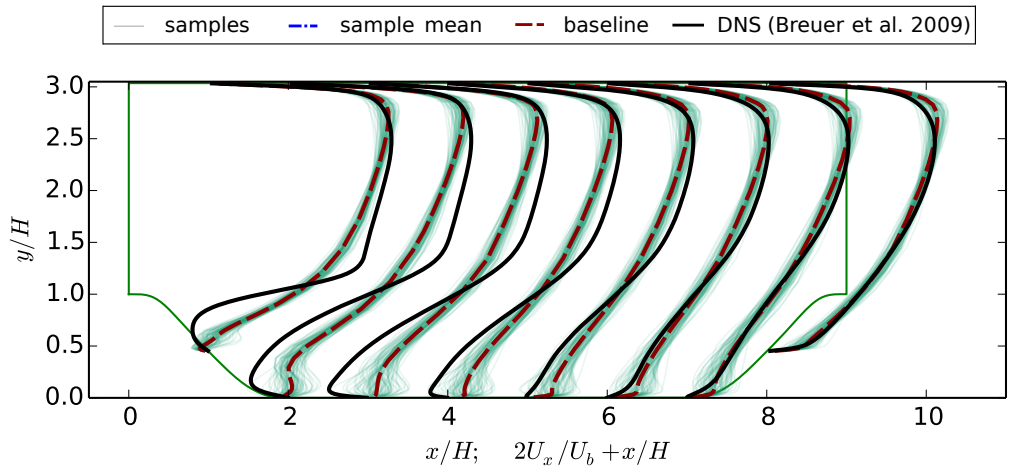

(a) Velocity samples, Case 1

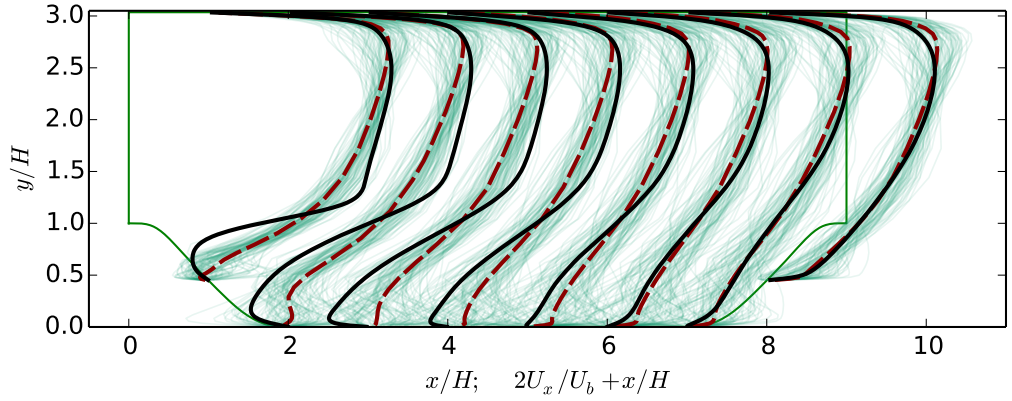

(b) Velocity samples, Case 2

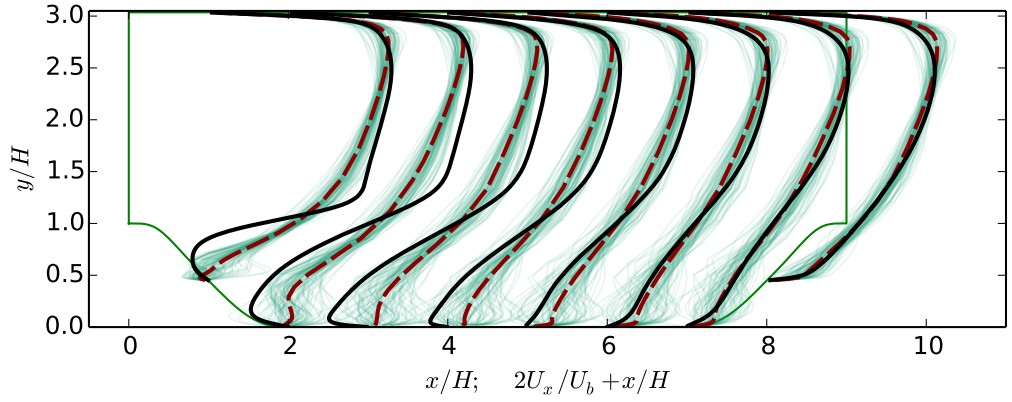

(c) Velocity samples, Case 3

Figure 4.10: Comparison of propagated velocity profile samples for Cases 1, 2, and 3. The profiles are shown at eight streamwise locations $x/H = 1, \cdots, 8$, compared to the baseline results and the benchmark (DNS) results obtained by direct numerical simulations [39].

Admittedly, the current approach only ensures maximum entropy for the Reynolds stresses at each point. It would be desirable to generalize our work to defining maximum entropy distribution for random tensor fields, but the authors are not aware of any such rigorous measures. Consequently, for the lack of better alternatives we used Gaussian processes with squared exponential kernels to construct the random tensor field. This is an *ad hoc* modeling choice made according to the state-of-the-art practice in the literature [18]. However, we emphasize that the implied smoothness of the random field by the chosen kernel, the specified correlation length scale of the kernel, and the nonstationary nature of the kernel may all introduce artificial information. The role played by the spatial correlation structure is particularly significant since it is the *divergence* of the Reynolds stress that appears in the RANS momentum equation. Therefore, it requires some physical understanding of the flow characteristics and prior knowledge of the RANS model performance.

4.5.2 Limitation of Uncertainty Space Exploration

Iaccarino et al. [4, 5] only computed three representative samples, each obtained by perturbing the baseline RANS predicted Reynolds stress toward the three limiting states and in a specified spatial pattern. They pointed out that the true Reynolds stresses are not necessarily convex combinations of the three limiting states, and thus the true uncertainty can fall outside the uncertainty range as indicated by the three perturbations. The same can be said of the velocities. As such, they referred to their approach as "uncertainty estimation" rather than "uncertainty quantification". In comparison, the current approach explores a much larger part of the uncertainty space by sampling from a functional space of spatial pattern as spanned by the specified modes ϕ_α. However, it is still not an exhaustive exploration of the uncertainty space of the Reynolds stresses, which can be very large and challenging to explore comprehensively, if possible at all. Moreover, note that no data are used to provide independent information on the model-form uncertainty of in the RANS simulation, and thus one should not expect the proposed framework alone can reduce model-form uncertainty.

In fact, even producing an uncertainty range to cover the truth is not the main objective of the current framework or that of Iaccarino et al. [4, 5]. If this was the objective, then one can simply perturb the Reynolds stress field as large as possible without even the need to account for any physical constraints. However, it would lead to overly large uncertainty ranges that are of little practical value. Rather, by perturbing the Reynolds stresses carefully respecting as many physical constraints as possible, the current approach aims to yield uncertainty estimates of the velocity field and other QoIs that show physical insights, e.g., on the sensitivity of velocities in the recirculation region to Reynolds stress perturbations as discussed in Section 4.2. On the other hand, hypothetically if a better turbulence model was used, which produces a baseline Reynolds stress field that is closer to the benchmark, then the same perturbation used here would have been able to cover the truth. However, this would be an issue outside the scope of the proposed algorithm, and one usually does not know the predictive skill of the turbulence model on the case of concern *a priori*.

4.5.3 Accessibility of Limiting States When Sampling Reynolds Stress

Whether the obtained maximum entropy distribution of Reynolds stress $[\mathbf{R}]$ should have zero measure on the two-component (and one-component) limiting states is an issue open for discussion. We explain below the implications based on the choices made in the proposed framework. Although practically we did not encounter this difficulty in this study, the discussion below adds to the theoretical completeness. The probability distribution for the normalized random matrix $[\mathbf{G}]$ as given in Eq. (4.13) has zero measure on the subset $\mathbb{M}_d^{+0} \setminus \mathbb{M}_d^+$ of singular positive semidefinite matrices, since $\det([G]) = 0$ in this set and thus $p_{[\mathbf{G}]}([G])|_{[G]\in\mathbb{M}_d^{+0}\setminus\mathbb{M}_d^+} = 0$. However, a valid distribution for semi-definite matrices could have non-zero measure in the set of singular matrices. One can draw an analogy to the exponential distribution, for instance, in the scalar case. If the specified mean $[\underline{R}]$ of $[\mathbf{R}]$ is singular, i.e., $\det([\underline{R}]) = 0$, then $\det([\underline{L}_R]) = 0$. Consequently, any realization $[R]$ constructed from Eq. (5.6), $[\mathbf{R}] = [\underline{L}_R]^T[\mathbf{G}][\underline{L}_R]$, is also singular since the distributive nature of determinants leads to $\det([R]) = 0$. The set $\mathbb{M}_d^{+0} \setminus \mathbb{M}_d^+$ of singular Reynolds stresses maps to the two-component limit edge ($C_3 = 0$) of the Barycentric triangle. This mapping can be explained by the fact that all matrices in this set have at least one eigenvalue that is zero (as they have zero determinants), which corresponds to two-component turbulence. This correspondence is indicated in Fig. 6.1a. The physical interpretation of the mathematical consequences above can be summarized as follows:

- When the specified Reynolds stress mean $[\underline{R}]$ corresponds to a turbulence state in a two-component limit, the samples of perturbed Reynolds stresses also have two-component states;
- When the specified mean corresponds to a generic three-component state, the samples can become infinitely close to a two-component limit but has zero probability of falling on the limit.

4.6 Conclusion

In this work we propose a random matrix approach to guarantee Reynolds stress realizability for quantifying model-form uncertainty in RANS simulation. In this approach, the Reynolds stress field is described with a probabilistic model of a random field of positive semidefinite matrices with specified mean and correlation structure. The marginal probability distribution of the Reynolds stress at any particular location satisfies the maximum entropy principle. By imposing maximum entropy on the distribution of the Reynolds stress tensors, the current framework aims to provide an objective approach for specifying priors (e.g., in the context of Bayesian inferences for uncertainty quantification). It can also be used for estimating uncertainties in RANS simulations in the absence of observation data. To

sample such a random matrix field, Gaussian random fields with specified covariance kernel are first generated and then are mapped to the field of positive semidefinite matrices based on polynomial chaos expansion and reconstruction. Numerical simulations have been performed with the proposed approach by sampling the Reynolds stress and propagating through the RANS solver to obtain velocities. The simulation results showed that generated Reynolds stress fields not only have the specified statistics, but also are physically reasonable. The mathematically rigorous approach based on random matrix and maximum entropy principle is a promising alternative to the previously proposed physics-based approach for quantifying model-form uncertainty in RANS simulations. Moreover, it can be used to gauge the entropy of the prior distributions specified in the physics-based approach and thus to measure the information introduced therein. Detailed comparison between the two approaches are presented in a separate work [21].

Acknowledgment

HX would like to thank Dr. Gianluca Iaccarino of Stanford University for his discussions on the materials presented in Section 4.5.2. The authors would like to acknowledge the four anonymous reviewers, whose comments helped improving the clarity and quality of the manuscript. We gratefully acknowledge partial funding of graduate research assistantship for JXW from the Institute for Critical Technology and Applied Science (ICTAS, Grant number 175258).

Bibliography

[1] T. Oliver, R. Moser, Uncertainty quantification for RANS turbulence model predictions, in: APS Division of Fluid Dynamics Meeting Abstracts, Vol. 1, 2009.

[2] L. Margheri, M. Meldi, M. Salvetti, P. Sagaut, Epistemic uncertainties in RANS model free coefficients, Computers & Fluids 102 (2014) 315–335.

[3] M. Emory, R. Pecnik, G. Iaccarino, Modeling structural uncertainties in Reynolds-averaged computations of shock/boundary layer interactions, AIAA paper 479 (2011) 1–16.

[4] M. Emory, J. Larsson, G. Iaccarino, Modeling of structural uncertainties in Reynolds-averaged Navier-Stokes closures, Physics of Fluids 25 (11) (2013) 110822.

[5] C. Gorlé, G. Iaccarino, A framework for epistemic uncertainty quantification of turbulent scalar flux models for Reynolds-averaged Navier-Stokes simulations, Physics of Fluids 25 (5) (2013) 055105.

[6] H. Xiao, J.-L. Wu, J.-X. Wang, R. Sun, C. J. Roy, Quantifying and reducing model-form uncertainties in Reynolds-Averaged Navier-Stokes simulations: An data-driven, physics-based, Bayesian approach, Journal of Computational Physics. 324 (2016) 115–136.

[7] J. L. Lumley, G. R. Newman, The return to isotropy of homogeneous turbulence, Journal of Fluid Mechanics 82 (01) (1977) 161–178.

[8] S. Banerjee, R. Krahl, F. Durst, C. Zenger, Presentation of anisotropy properties of turbulence, invariants versus eigenvalue approaches, Journal of Turbulence 8 (32) (2007) 1–27.

[9] J.-X. Wang, J.-L. Wu, H. Xiao, Incorporating prior knowledge for quantifying and reducing model-form uncertainty in RANS simulations, International Journal for Uncertainty Quantification. 6 (2) (2016) 109–126.

[10] J.-L. Wu, J.-X. Wang, H. Xiao, A Bayesian calibration-prediction method for reducing model-form uncertainties with application in RANS simulations, Flow, Turbulence and Combustion, 97 (3) (2016) 761–786.

[11] C. E. Shannon, A mathematical theory of communication, Bell System Technical Journal 27 (1948) 379–423, 623–659.

[12] E. T. Jaynes, Information theory and statistical mechanics, Physical Review 106 (1957) 620–630.

[13] R. R. Coifman, M. V. Wickerhauser, Entropy-based algorithms for best basis selection, Information Theory, IEEE Transactions on 38 (2) (1992) 713–718.

[14] S. C. Zhu, Y. Wu, D. Mumford, Filters, random fields and maximum entropy (FRAME): Towards a unified theory for texture modeling, International Journal of Computer Vision 27 (2) (1998) 107–126.

[15] C. Soize, A nonparametric model of random uncertainties for reduced matrix models in structural dynamics, Probabilistic engineering mechanics 15 (3) (2000) 277–294.

[16] C. Soize, Random matrix theory for modeling uncertainties in computational mechanics, Computer Methods in Applied Mechanics and Engineering 194 (12) (2005) 1333–1366.

[17] S. Das, R. Ghanem, A bounded random matrix approach for stochastic upscaling, Multiscale Modeling & Simulation 8 (1) (2009) 296–325.

[18] J. Guilleminot, C. Soize, R. G. Ghanem, Stochastic representation for anisotropic permeability tensor random fields, International Journal for Numerical and Analytical Methods in Geomechanics 36 (13) (2012) 1592–1608.

[19] M. Mignolet, C. Soize, Nonparametric stochastic modeling of linear systems with prescribed variance of several natural frequencies, Probabilistic Engineering Mechanics 23 (2) (2008) 267–278.

[20] C. Soize, Stochastic modeling of uncertainties in computational structural dynamics – recent theoretical advances, Journal of Sound and Vibration 332 (10) (2013) 2379–2395.

[21] J.-X. Wang, R. Sun, H. Xiao, Quantification of uncertainties in turbulence modeling: A comparison of physics-based and random matrix theoretic approaches, International Journal of Heat and Fluid Flows. In press, DOI: 10.1016/j.ijheatfluidflow.2016.07.005.

[22] S. B. Pope, Turbulent Flows, Cambridge University Press, Cambridge, 2000.

[23] U. Schumann, Realizability of Reynolds-stress turbulence models, Physics of Fluids (1958-1988) 20 (5) (1977) 721–725.

[24] J. L. Lumley, Computational modeling of turbulent flows, Advances in applied mechanics 18 (123) (1978) 213.

[25] S. Pope, PDF methods for turbulent reactive flows, Progress in Energy and Combustion Science 11 (2) (1985) 119–192.

[26] C. G. Speziale, R. Abid, P. A. Durbin, On the realizability of Reynolds stress turbulence closures, Journal of Scientific Computing 9 (4) (1994) 369–403.

[27] B. E. Launder, D. Spalding, The numerical computation of turbulent flows, Computer methods in applied mechanics and engineering 3 (2) (1974) 269–289.

[28] F. R. Menter, Two-equation eddy-viscosity turbulence models for engineering applications, AIAA journal 32 (8) (1994) 1598–1605.

[29] P. R. Spalart, S. R. Allmaras, A one-equation turbulence model for aerodynamic flows, Recherche Aerospatiale 1 (1994) 5–21.

[30] C. Gorlé, J. Larsson, M. Emory, G. Iaccarino, The deviation from parallel shear flow as an indicator of linear eddy-viscosity model inaccuracy, Physics of Fluids 26 (5) (2014) 051702.

[31] H. Goldstein, Classical Mechanics, 2nd Edition, Addison-Wesley, 1980, see "The Euler Angles and Euler Angles in Alternate Conventions" in Chapter 4.4.

[32] D. Stefanica, A Linear Algebra Primer for Financial Engineering, FE Press, 2014.

[33] N. J. Higham, Analysis of the Cholesky decomposition of a semi-definite matrix, in: M. G. Cox, S. J. Hammarling (Eds.), Reliable Numerical Computation, Oxford University Press, 1990, pp. 161–185.

[34] C. Soize, A comprehensive overview of a non-parametric probabilistic approach of model uncertainties for predictive models in structural dynamics, Journal of sound and vibration 288 (3) (2005) 623–652.

[35] S. Sakamoto, R. Ghanem, Polynomial chaos decomposition for the simulation of non-Gaussian nonstationary stochastic processes, Journal of engineering mechanics 128 (2) (2002) 190–201.

[36] O. P. Le Maître, O. M. Knio, Spectral methods for uncertainty quantification: with applications to computational fluid dynamics, Springer, 2010.

[37] E. Dow, Q. Wang, Optimal design and tolerancing of compressor blades subject to manufacturing variability, in: 16th AIAA Non-Deterministic Approaches Conference, American Institute of Aeronautics and Astronautics, 2014.

[38] D. Xiu, Numerical methods for stochastic computations: a spectral method approach, Princeton University Press, 2010.

[39] M. Breuer, N. Peller, C. Rapp, M. Manhart, Flow over periodic hills–numerical and experimental study in a wide range of reynolds numbers, Computers & Fluids 38 (2) (2009) 433–457.

[40] F. Billard, Development of a robust elliptic-blending turbulence model for near-wall, separated and buoyant flows, Ph.D. thesis, The University of Manchester, Manchester, UK (2012).

[41] S. Y. Park, A. K. Bera, Maximum entropy autoregressive conditional heteroskedasticity model, Journal of Econometrics 150 (2) (2009) 219–230.

[42] B. Debusschere, K. Sargsyan, C. Safta, UQTk User Manual, Sandia National Laboratories, Albuquerque, NM 87185 and Livermore, CA 94550, version 2.1 Edition (June 2014).

[43] J. C. Helton, F. J. Davis, Latin hypercube sampling and the propagation of uncertainty in analyses of complex systems, Reliability Engineering & System Safety 81 (1) (2003) 23–69.

Appendix

4.A Summary of the Algorithm of the Proposed Method

Given the mean Reynolds stress field $[\underline{R}](x)$ along with the correlation function structure of the random matrix field $[\mathbf{L}](x)$ as specified in Eq. (4.21), the following procedure is performed:

1. Expansion of given marginal distributions and covariances kernels:

   1.1. Perform the Cholesky factorization of the mean Reynolds stresses $[\underline{R}]$ at each cell according to Eq. (5.7), which yields field $\underline{L}_R(x)$ of upper triangular matrices.

   1.2. Perform KL expansion for the kernel function by solving the Fredholm equation (4.26) to obtain eigenmodes $\sqrt{\lambda_\alpha}\,\phi_\alpha(x)$.

   This is performed by first discretizing the integration with Gaussian quadrature and then solving the obtained discrete eigenvalue problem. This KL expansion procedure is implemented in many standard uncertainty quantification toolboxes. In the current work we adopted UQTk [42], which is developed at Sandia National Laboratories.

   1.3. For off-diagonal terms only, perform polynomial expansion of the marginal PDF as described in Eq. (4.20) at each cell. Coefficients U_β are obtained from Eq. (5.13), where $\beta = 1, \cdots, N_p$, and N_p is the number of polynomials retained in the expansion.

2. Sampling and reconstruction of random matrix fields for Reynolds stresses:

   2.1. For each element $\mathbf{L}_{ij}$ of the random matrix field $[\mathbf{L}]$, independently draw N_{KL} sample from the standard Gaussian distribution $\omega_{ij,\alpha}$ where $\alpha = 1, \cdots, N_{\mathrm{KL}}$, e.g., with random sampling or Latin hypercube sampling method [43].

   2.2. Synthesize realizations of the off-diagonal terms based on KL expansion:

$$\mathbf{w}_{ij}(x) = \sum_{\alpha=1}^{N_{\mathrm{KL}}} \sqrt{\lambda_\alpha}\,\phi_\alpha(x)\,\boldsymbol{\omega}_\alpha \quad \text{with} \quad i < j$$
$$\mathbf{L}_{ij}(x) = \sigma_d \mathbf{w}_{ij}(x)$$

   2.3. Synthesize the realizations of the diagonal terms based on KL and PCE expansions:

$$\mathbf{u}_i(x) = \sum_{\beta=0}^{N_p} U_\beta(x) \Psi_\beta(\mathbf{w}_{ii}(x))$$

   where the Gaussian random field sample $\mathbf{w}_{ii}(x)$ obtained in the previous step is used.

   2.4. Synthesize the diagonal terms of matrix $[\mathbf{L}]$ from $\mathbf{L}_{ii}(x) = \sigma_d \sqrt{\mathbf{u}_i}$, where $i = 1, 2, 3$.

2.5. Reconstruct $[\mathbf{G}]$ from $[\mathbf{G}] = [\mathbf{L}]^T[\mathbf{L}]$ and then reconstruct the random matrix $[\mathbf{R}]$ from $[\mathbf{R}] = [\underline{L}_R]^T[\mathbf{G}][\underline{L}_R]$.

3. Propagation the Reynolds stress field through the RANS solver to obtain velocities and other QoIs:

3.1 Use the obtained sampled Reynolds stress to velocity and other QoIs by solving the RANS equation.

3.2 Post-process the obtained velocity and QoI samples to obtain statistical moments.

Chapter 5

Quantification of Uncertainties in Turbulence Modeling: A Comparison of Physics-Based and Random Matrix Theoretic Approaches

(Published on *International Journal of Heat and Fluid Flow*, 62 (B): 577-592, 2016.)

J.-X. Wang, R. Sun, H. Xiao
Department of Aerospace and Ocean Engineering, Virgina Tech, Blacksburg, VA, 24061, USA

Abstract

Numerical models based on Reynolds-Averaged Navier-Stokes (RANS) equations are widely used in engineering turbulence modeling. However, the RANS predictions have large model-form uncertainties for many complex flows, e.g., those with non-parallel shear layers or strong mean flow curvature. Quantification of these large uncertainties originating from the modeled Reynolds stresses has attracted attention in the turbulence modeling community. Recently, a physics-based Bayesian framework for quantifying model-form uncertainties has been proposed with successful applications to several flows. Nonetheless, how to specify proper priors without introducing unwarranted, artificial information remains challenging to the current form of the physics-based approach. Another recently proposed method based on random matrix theory provides the prior distributions with maximum entropy, which is an alternative for model-form uncertainty quantification in RANS simulations. This method has better mathematical rigorousness and provides the most non-committal prior distributions without introducing artificial constraints. On the other hand, the physics-based approach has the advantages of being more flexible to incorporate available physical insights. In this

work, we compare and discuss the advantages and disadvantages of the two approaches on model-form uncertainty quantification. In addition, we utilize the random matrix theoretic approach to assess and possibly improve the specification of priors used in the physics-based approach. The comparison is conducted through a test case using a canonical flow, the flow past periodic hills. The numerical results show that, to achieve maximum entropy in the prior of Reynolds stresses, the perturbations of shape parameters in Barycentric coordinates are normally distributed. Moreover, the perturbations of the turbulence kinetic energy should conform to log-normal distributions. Finally, the result sheds light on how large the variance of each physical variable should be compared with each other to achieve the approximate maximum entropy prior. The conclusion can be used as a guidance for specifying proper priors in the physics-based, Bayesian uncertainty quantification framework.

5.1 Introduction

Despite the increasing availability of computational resources in the past decades, high-fidelity simulations (e.g., large eddy simulation, direct numerical simulation) are still not affordable for most practical problems. Numerical models based on Reynolds-Averaged Navier–Stokes (RANS) equations are still the dominant tools for the prediction of turbulent flows in industrial and natural processes. However, for many practical flows, e.g., those with strong adverse pressure gradient, non-parallel shear layers, or strong mean flow curvature, the predictions of RANS models have large uncertainties. The uncertainties are mostly attributed to the phenomenological closure models for the Reynolds stresses [1, 2]. Previous efforts in quantifying and reducing model-form uncertainties in RANS simulations have mostly followed parametric approaches, e.g., by perturbing, tuning, or inferring the parameters of the closure models of the Reynolds stress [3, 4, 5].

Recently, the turbulence modeling community has recognized the limitations of the parametric approaches and started investigating non-parametric approaches where uncertainties are directly injected into the Reynolds stresses [2, 6, 7, 8, 9, 10]. In their pioneering work, Iaccarino et al. [6, 8, 9] proposed a physics-based approach, where the Reynolds stress is projected onto six physically meaningful dimensions (its shape, magnitude, and orientation). They further perturbed the Reynolds stresses towards the limiting states in the physically realizable range, based on which the RANS prediction uncertainties are estimated. Building on the work of Iaccarino et al. [6, 8, 9], Xiao et al. [10] modeled the Reynolds stress discrepancy as a *zero-mean random field* and used a physical-based parameterization to systematically explore the uncertainty space. They further used Bayesian inferences to incorporate observation data to reduce the model-form uncertainty in RANS simulation. While the physics-based method has achieved significant successes, the method in its current form has two major limitations. First, uncertainties are only injected to the shape and magnitude of the Reynolds stresses but not to the orientations, and thus they do not fully explore the uncertainty space. Second, it is challenging to specify prior distributions over these physical

variables without introducing artificial constraints. The priors are critical for uncertainty propagation and Bayesian inference, particularly when the amount of data is limited [11]. Xiao et al. [10] specified Gaussian distribution for the perturbations of shape parameters in natural coordinates and log-normal distribution for the turbulence kinetic energy discrepancy. The perturbations in all physical parameters share the same variance field. However, it is not clear if or how much artificial constraints are introduced into the prior with this choice. Moreover, without sufficient physical insight, it is not clear how large the variance of perturbation for each physical variable should be relative to each other.

In information theory, Shannon entropy is an important measure of the information contained in each probability distribution. The distribution best representing the current state is the one with the largest information entropy, which is known as principle of maximum entropy [12]. This principle has been used as a guideline to specify prior distributions in Bayesian framework [13]. Although this theory has been extensively used in information processing problems such as communications and image processing, the application in conjunction with random matrix theory applied to physical systems is only a recent development, which was first proposed and developed by Soize et al. [14, 15]. Built on the theories developed by Soize et al., Xiao et al. [16] proposed a random matrix theoretic (RMT) approach with maximum entropy principle to quantify model-form uncertainties in RANS simulations. The RMT approach is an alternative to the physics-based approach in quantifying model-form uncertainties in RANS simulations. In this approach, the realizability of perturbed Reynolds stresses is guaranteed automatically in a mathematical way, since the uncertainties are directly injected within the set $\mathbb{M}_d^{+0}$ of positive semidefinite matrices. In addition, the RMT approach can provide objective priors for Bayesian inferences that satisfy the given constraints without introducing artificial information.

While the RMT approach has better mathematical rigorousness and provides a proper prior of the Reynolds stress tensors with maximum entropy, it has its own limitations. In particular, since the perturbations are directly introduced to the Reynolds stress itself, it is not straightforward to incorporate physical insights that are available for specific flows into the RMT approach. For example, for the flow in a channel with square cross section, the discrepancies of RANS-predicted Reynolds stress mainly come from the shape of the Reynolds stress tensor, while the predicted turbulence kinetic energy is rather accurate [17]. In this case, the perturbation variances of shape parameters should be specified much larger than that of the turbulence kinetic energy. Nonetheless, this piece of information is difficult to incorporate into the RMT approach. In comparison, the physics-based approach is more flexible and thus may be preferred in engineering applications for both uncertainty quantification and Bayesian inferences. The objective of this work is twofold. First, we compare the physics-based approach and RMT approach on model-form uncertainty quantification and propagation. The advantages and disadvantages of both approaches are discussed. Second, we use the results from the RMT approach to assess the artificial constraints introduced in the physics-based approach and possibly improve the specification of physics-based priors under the context of Bayesian inference. To this end, the Reynolds stress samples with

maximum entropy distribution obtained in the RMT approach are first projected onto the physically meaningful dimensions. Then, the distributions in the six physical dimensions are used to compare with the priors specified in the physics-based approach. The perturbed Reynolds stresses from both approaches are propagated to the quantities of interest (QoIs), e.g., velocity field and wall shear stress, and the differences of these propagated QoIs are investigated. The comparisons can provide useful insights on the model-from uncertainty quantification in RANS modeling. Moreover, they also sheds light on the specification of appropriate prior for each physical variable when no further physical knowledge is available.

This work is the first attempt to fully explore the uncertainty space in physics-based approach. The orientations of Reynolds stresses are perturbed, and their impacts on the propagated QoIs are investigated. Note that in this work we only focus on uncertainty propagation (i.e., prior). The assessment of posterior from Bayesian inference is not included. This is because the inversion schemes currently used for reducing RANS model-form uncertainties are approximate Bayesian approaches, e.g., iterative ensemble Kalman filtering in [10, 11], which are not sensitive to the prior and cannot provide a posterior uncertainty estimation with a comparable accuracy to that obtained from the exact Bayesian sampling scheme [18]. This compromise is under the consideration of high computational costs of RANS model evaluations, which make exact Bayesian approach (i.e., Markov Chain Monte Carlo (MCMC) sampling scheme) prohibitively expensive. Obtaining an accurate posterior is still an ongoing work, which can be possibly achieved by utilizing recently developed dimension reduction methods (e.g., active subspace methods [19]) and fast sampling scheme (e.g., parallel MCMC [20] and delayed rejection adaptive metropolis [21]).

The rest of the paper is organized as follows. Section 5.2 introduces the physics-based and RMT approaches for RANS model-form uncertainty quantification. Section 5.3 uses the flow over periodic hills as an example to perform the comparison between the two approaches. The results are then presented and discussed. Finally, Section 5.5 concludes the paper.

5.2 Comparison of Physics-Based Approach and RMT Approach

This work examines and compares two approaches, the physics-based approach and the random matrix theoretic approach, for quantifying RANS model-form uncertainties. We first briefly introduce the general background of RANS-based turbulence modeling and the common assumptions of the two approaches before presenting the technical details of the two approaches.

Reynolds-averaged Navier–Stokes equations describe the mean quantities (e.g., velocity and pressure) of the turbulent flows. They are obtained by performing time- or ensemble-averaging on the Navier–Stokes equations, which describes the instantaneous flow quantities. The averaging process leads to a covariance term of the instantaneous velocities, which is

referred to as Reynolds stresses and needs model closure in RANS simulations. It is the consensus of the turbulence modeling community that the modeling of the Reynolds stresses accounts for majority of the model-form uncertainty in RANS simulations [1]. In the physics based approach proposed by Iaccarino et al.[6, 8] and further extended by Xiao et al. [10, 11], perturbations are directly injected to the RANS-predicted Reynolds stresses. Specifically, the physically meaningful projections of the Reynolds stress, i.e., its shape, magnitude, and orientation are jointly perturbed around their respective mean values obtained in the RANS simulation, and the perturbations are then propagated through RANS solvers to the Quantities of Interests (QoI, e.g., velocities). The obtained ensemble is then used to assess the uncertainties in the RANS predictions. The specific form of perturbation for each variable is a modeling choice made by the user. The scheme ensures realizability (positive semi-definiteness) of the Reynolds stresses. Similar to the physics-based approach, zero-mean perturbations are also injected to the RANS-predicted Reynolds stresses in the RMT approach with realizability guaranteed. In contrast to the physics-based approach, however, in the RMT approach the true Reynolds stress is modeled as random matrices, for which a maximum entropy probabilistic distribution is constructed under the constraint that the mean is the RANS-predicted value. The maximum entropy distribution is then sampled to be obtain the perturbed Reynolds stress fields.

In summary, both the physics-based and the RMT approaches introduce zero-mean perturbations to the RANS predicted Reynolds stresses, which are then propagated to the QoIs to assess RANS prediction uncertainties. They differ in how the perturbations are introduced. The RMT approach introduces perturbations directly in the Reynolds stress tensor and the perturbations conform to a maximum entropy distribution, while the physics-based approach introduces perturbations to the physically meaningful projections of the Reynolds stresses. The details of the two schemes are presented below.

5.2.1 Physics-Based Approach

Here, we briefly summarize the physics-based model-form uncertainty quantification framework proposed by Xiao et al. [10] and its extension to account for uncertainties in tensor orientation. In the framework, the true Reynolds stress $[\mathbf{R}(x)]$ is modeled as a random tensorial field with the RANS-predicted Reynolds stress $[R(x)]^{rans}$ as prior mean, in which x denotes the spatial coordinate. To inject uncertainties into the physically meaningful projections of Reynolds stress tensor, the following eigen-decomposition is performed for its each realization at any given location x:

$$[R] = 2k\left(\frac{1}{3}[I] + [A]\right) = 2k\left(\frac{1}{3}[I] + [E][\Lambda][E]^T\right) \tag{5.1}$$

where k is the turbulent kinetic energy indicating the magnitude of $[R]$; $[I]$ is the second order identity tensor; $[A]$ is the anisotropy tensor; $[E] = [\vec{e}_1, \vec{e}_2, \vec{e}_3]$ and $[\Lambda] = \text{diag}[\tilde{\lambda}_1, \tilde{\lambda}_2, \tilde{\lambda}_3]$,where $\tilde{\lambda}_1 + \tilde{\lambda}_2 + \tilde{\lambda}_3 = 0$, are the orthonormal eigenvectors and the corresponding eigenvalues of $[A]$,

respectively, indicating the orientation and shape of $[R]$. In order to physically interpret the shape of the Reynolds stress and easily impose the realizability constraint, the eigenvalues $\tilde{\lambda}_1$, $\tilde{\lambda}_2$, and $\tilde{\lambda}_3$ are mapped to the Barycentric coordinates (C_1, C_2, C_3) with $C_1+C_2+C_3 = 1$. The Barycentric coordinates are defined as,

$$C_1 = \tilde{\lambda}_1 - \tilde{\lambda}_2 \tag{5.2a}$$

$$C_2 = 2(\tilde{\lambda}_2 - \tilde{\lambda}_3) \tag{5.2b}$$

$$C_3 = 3\tilde{\lambda}_3 + 1 \ . \tag{5.2c}$$

As shown in Fig. 6.1a, the Barycentric coordinates (C_1, C_2, C_3) of a point indicate the portion of areas of three sub-triangles formed by the point and with edge labeled as $C1$, $C2$, and $C3$, in the Barycentric triangle. For example, the ratio of areas of the sub-triangle labeled with $C3$ to the entire triangle is C_3. A point located on the top vertex corresponds to $C_3 = 1$ while a point located on the bottom edge has $C_3 = 0$. The Barycentric coordinates have clear

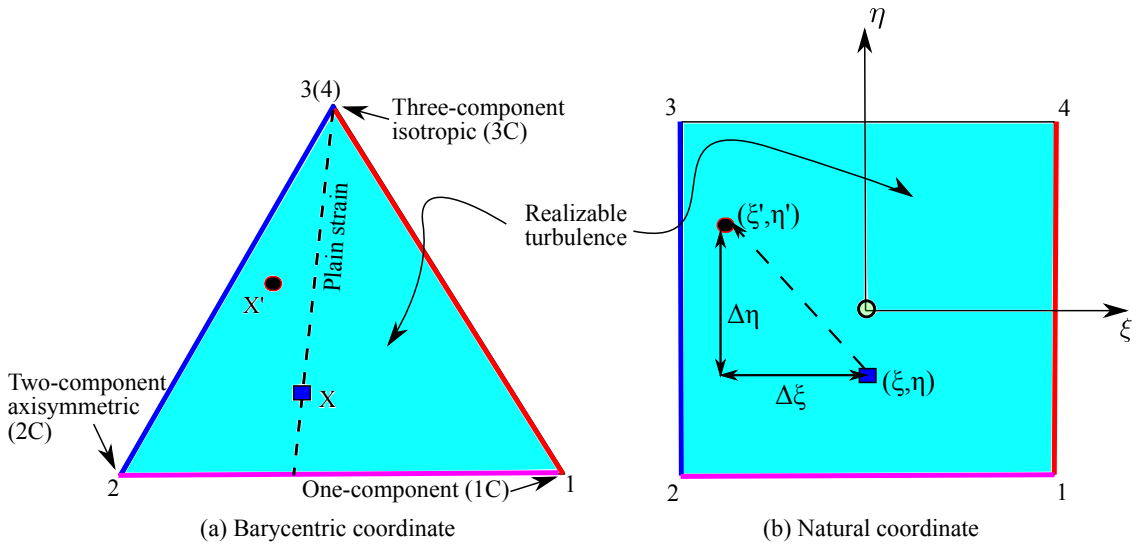

Figure 5.1: Mapping between the Barycentric coordinate to the natural coordinate, transforming the Barycentric triangle enclosing all physically realizable states [22, 8] to a square through standard finite element shape functions. Details of the mapping can be found in the appendix of ref. [10]. Corresponding edges in the two coordinates are indicated with matching colors.

physical interpretation, i.e., the dimensionality of the turbulence. All the edges and vertices indicate limiting states of turbulence, which are shown in Fig 6.1a. The projections of all Reynolds stresses should fall inside the Barycentric triangle to ensure the realizability. To facilitate parameterization, the Barycentric coordinates are further transformed to the natural coordinates (ξ, η) with the triangle mapped to the square, as shown in Fig. 6.1b. Details of the mapping can be found in ref. [10]. Although the tensor orientation ($[E] = [\vec{e}_1, \vec{e}_2, \vec{e}_3]$) has not been perturbed in ref. [10], it can be done with an appropriate parameterization

scheme, which is implemented in this work. The Euler angle with z-x'-z'' convention [23] is used to parameterize the orientation of the Reynolds stress tensor. That is, first, the local coordinate system x-y-z of eigenvectors of $[\mathbf{R}]$ initially aligned with the global coordinate system X-Y-Z rotates about the z axis by angle φ_1. Then, it rotates about the x axis by angle φ_2, and finally rotates about its new z axis by angle φ_3.

The Reynolds stress tensor field is transformed into six physically meaningful components denoted as $\xi, \eta, k, \varphi_1, \varphi_2$, and φ_3, which are all scalar fields. After the mapping, uncertainties are introduced to these quantities by adding discrepancy terms to the corresponding RANS predictions, i.e.,

$$\xi(x) = \tilde{\xi}^{rans}(x) + \Delta\xi(x) \tag{5.3a}$$

$$\eta(x) = \tilde{\eta}^{rans}(x) + \Delta\eta(x) \tag{5.3b}$$

$$\log k(x) = \log \tilde{k}^{rans}(x) + \Delta \log k(x) \tag{5.3c}$$

$$\varphi_i(x) = \tilde{\varphi_i}^{rans}(x) + \Delta\varphi_i(x), \quad i = 1, 2, 3 \tag{5.3d}$$

where $\Delta\xi(x)$ and $\Delta\eta(x)$ are discrepancies of the Reynolds stress shape parameters ξ and η, respectively; $\Delta \log k(x)$ is the log-discrepancy of the turbulent kinetic energy; $\Delta\varphi_i(x)$ $(i = 1, 2, 3)$ are the discrepancies of three Euler angles. To model the prior of these discrepancy fields with spatial smoothness, we assume that each discrepancy field is normally distributed at any location x and use a Gaussian kernel $K(x, x')$ to describe the correlation between any two different locations x and x'. That is,

$$K(x, x') = \sigma(x)\sigma(x') \exp\left(-\frac{|x - x'|^2}{l^2}\right) \quad \text{where } x, x' \in \Sigma, \tag{5.4}$$

where Σ is the spatial domain of the flow field. The variance $\sigma(x)$ is a spatially varying field representing the magnitude of injected uncertainties. The correlation length l also varies spatially based on the local length scale of the mean flow. It can be seen from Eq. 6.5 that the discrepancy fields for shape parameters (ξ, η) and Euler angles (φ_i) are Gaussian random fields, and the discrepancy field for magnitude parameter k is a log-normal random field. To reduce dimensions of the random fields, Karhunen–Loeve expansions of the random fields are adopted with chosen basis that are eigenfunctions of the kernel [24]. That is, the discrepancies can be represented as follows:

$$\Delta(x) = \sum_{j=1}^{\infty} \omega_\alpha \, \phi_\alpha(x), \tag{5.5}$$

where the coefficients ω_α (denoting ω_α^ξ, ω_α^η, ω_α^k, $\omega_\alpha^{\varphi_i}$ for discrepancy fields $\Delta\xi$, $\Delta\eta$, $\Delta \log k$ and $\Delta\varphi_i$, respectively) are independent standard Gaussian random variables. In practice, the infinite series are truncated to N_{kl} terms with N_{kl} depending on the smoothness of the kernel K. Therefore, the discrepancy fields in Reynolds stress are parameterized by the coefficients ω_α^ξ, ω_α^η, ω_α^k, $\omega_\alpha^{\varphi_i}$ with $\alpha = 1, 2, \cdots, N_{kl}$. These Reynolds stress discrepancies are then propagated to the QoI (e.g., velocity) as the model-form uncertainties.

In summary, the uncertainties are injected into the six physically meaningful dimensions of Reynolds stress separately in the physics-based approach. For each dimension, the uncertainties are represented by the Gaussian random fields to ensure the smoothness of the Reynolds stress perturbations (for incompressible flow). The perturbed Reynolds stresses are reconstructed with these six random fields, which are then propagated to the QoI as the quantified model-form uncertainties. Detailed algorithm of the physics-based approach is presented in 5.A.

5.2.2 Random Matrix Theoretic Approach with Maximum Entropy Principle

Since Reynolds stresses belong to the set $\mathbb{M}_d^{+0}$ of symmetric positive definite tensors, where $d = 3$, it is natural to describe them directly as random matrices in set $\mathbb{M}_d^{+0}$. In the following, we summarize the uncertainty quantification approach based on random matrix theory and maximum entropy principle proposed by Xiao et al. [16]. In this framework, a probabilistic model in matrix set is built to satisfy all the constraints in the context of turbulence modeling. Based on the principle of maximum entropy, the target probability measure $p_{[\mathbf{R}]} : \mathbb{M}_d^{+0} \mapsto \mathbb{R}^+$ is the most non-committal probability density function (PDF) satisfying all available constraints (e.g., realizability) but without introducing any other unwarranted constraints, where $\mathbb{R}^+$ is the set of positive real number.

A two-step approach is used to find such maximum entropy distribution for random Reynolds stress tensors. First, the PDF for a normalized, positive definite random matrix $[\mathbf{G}]$ is obtained, whose mean is the identity matrix, i.e., $\mathbb{E}\{[\mathbf{G}]\} = [I]$. The distribution of $[\mathbf{G}]$ should have the maximum entropy. Second, the distribution of Reynolds stress tensor $[\mathbf{R}]$ is obtained with its mean $[\underline{R}]$ and normalized random matrix $[\mathbf{G}]$ as follows:

$$[\mathbf{R}] = [\underline{L}_R]^T[\mathbf{G}][\underline{L}_R], \tag{5.6}$$

where $[\underline{L}_R]$ is an upper triangular matrix with non-negative diagonal entries obtained from the following factorization of the specified mean $[\underline{R}]$, i.e.,

$$[\underline{R}] = [\underline{L}_R]^T[\underline{L}_R]. \tag{5.7}$$

It is assumed that the RANS predicted Reynolds stress $[R]^{rans}$ is the best estimate of $[\underline{R}]$. Therefore, to determine the maximum entropy distribution of $[\mathbf{R}]$, one only needs to focus on the normalized random matrix $[\mathbf{G}]$. It is first represented by its Cholesky factorization:

$$[\mathbf{G}] = [\mathbf{L}]^T[\mathbf{L}], \tag{5.8}$$

where $[\mathbf{L}]$ are upper triangle matrices with six independent elements. To achieve the matrix entropy, the distributions for each element $\mathbf{L}_{ij}$ can be specified following the procedures in

Ref. [16]. Note that each of the six elements of [**L**] is a random scalar field independent of each other. The off-diagonal element fields $\mathbf{L}_{ij}(x)$ with $i < j$ are obtained from

$$\mathbf{L}_{ij}(x) = \sigma_d(x)\ \mathbf{w}_{ij}(x), \tag{5.9}$$

in which $\mathbf{w}_{ij}(x)$ (i.e., $\mathbf{w}_{12}(x)$, $\mathbf{w}_{13}(x)$, and $\mathbf{w}_{23}(x)$) represents an independent Gaussian random field with zero mean and unit variance. The uncertainty magnitude field $\sigma_d(x)$ is half of the dispersion parameter filed $\delta(x)$, which indicates the uncertainty of the random matrix and is defined as

$$\delta(x) = \left[\frac{1}{d}\mathbb{E}\{\|[G](x) - [I]\|_F^2\}\right]^{\frac{1}{2}}, \tag{5.10}$$

where $\|\cdot\|_F$ is Frobenius norm, e.g., $\|G\|_F = \sqrt{\mathrm{tr}([G]^T[G])}$. It can be seen that $\delta(x)$ is analogous to the variance field $\sigma(x)$ of a scalar random field shown in the physics-based approach. It has been shown in [14] that $0 < \delta(x) < \sqrt{2}/2$ for $d = 3$. For the three diagonal element fields, each one of them is generated as follows:

$$\mathbf{L}_{ii}(x) = \sigma_d(x)\sqrt{2\mathbf{u}_i(x)} \quad \text{with} \ \ i = 1, 2, 3, \tag{5.11}$$

where $\mathbf{u}_i(x)$ is a positive valued gamma random field. It is worth noting that due to the choice of positive diagonal elements of the Cholesky factor [**L**] of Reynolds stress [**R**], its realizability can be guaranteed in the RMT approach.

Since Reynolds stresses are correlated at different spatial locations, one needs to model the correlation structures in the six fields of elements. It is assumed here that both the off-diagonal and the square root of diagonal terms have the same spatial correlation structures with Gaussian kernel. The three independent Gaussian random fields for the off-diagonal terms can be generated by using Monte Carlo sampling. Similar to that in the physics-based approach, the Karhunen–Loeve expansions are used here for reducing the dimension. To express the non-Gaussian random fields used to obtain the diagonal terms (see Eq. 5.11), the Gamma random variable $\mathbf{u}_i$ at any spatial location x is expanded by polynomial chaos expansion with Gaussian random variables [25] (see 5.B).Finally, the constructed distribution of Reynolds stresses can be propagated by RANS equation to the QoI to quantify the model-form uncertainties.

In summary, the uncertainties are directly injected into the Reynolds stress tensors in the set $\mathbb{M}_d^{+0}$ of positive definite matrices in the RMT approach. The principle of maximum entropy is applied to avoid introducing artificial constraints. The perturbed Reynolds stresses are then propagated to the QoI as the quantified model-form uncertainties. Detailed algorithm of the RMT approach can be found in 5.B.

5.3 Numerical Results

5.3.1 Cases Setup

A canonical flow, the flow in a channel with periodic hills at $Re = 2800$, is studied to compare the prior distributions of Reynolds stresses perturbed by the physics-based approach and the random matrix theoretic (RMT) approach. The computational domain is shown in Fig. 5.2. Periodic boundary conditions are imposed in the streamwise (x-) direction and non-slip boundary conditions are applied at the walls.

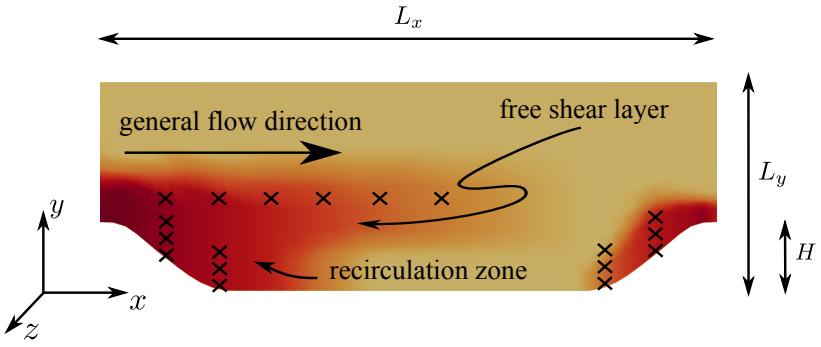

Figure 5.2: Domain shape for the flow in the channel with periodic hills. The x-, y- and z-coordinates are aligned with the streamwise, wall-normal, and spanwise directions, respectively. All dimensions are normalized by H with $L_x/H = 9$ and $L_y/H = 3.036$. Two typical locations A ($x/H = 2.0, y/H = 0.5$) and B ($x/H = 2.0, y/H = 0.01$) are marked in the figure.

In the physics-based approach the variance fields $\sigma(x)$ for generating random perturbation fields $\Delta\xi(x)$, $\Delta\eta(x)$, $\Delta \log k(x)$, and $\Delta\varphi_i(x)$ ($i = 1, 2, 3$) represent the magnitude of injected uncertainties. In the RMT approach the dispersion parameter $\delta(x)$ determines the variance of perturbations directly in the set $\mathbb{M}_3^+$ of positive definite matrices. To ensure that the distributions of perturbed Reynolds stresses from the two approaches are comparable, the amount of perturbation needs to be consistent with each other. Therefore, we estimate the dispersion parameter field $\delta(x)$ based on the samples of Reynolds stresses obtained in the physics-based approach with the given variance $\sigma(x)$. Although the physics-based approach is more flexible to specify different variances for the six discrepancy fields, it is difficult to determine how large the variance of each variable should be relative to each other. To be consistent with Xiao et al. [10], the Gaussian random fields for $\Delta\xi$, $\Delta\eta$, $\Delta \log k$, and $\Delta\varphi_i$ ($i = 1, 2, 3$) share the same variance field $\sigma(x)$. Since the aim of this work is to compare the two approaches, we choose a constant variance field to avoid the complexity caused by spatial variations of the perturbation variances. We investigate two groups of cases with different magnitudes of perturbation. For cases Phy1 and RM1, a relatively small constant variance field $\sigma = 0.2$ is used in the physics-based approach, and the corresponding dispersion parameter field $\delta(x)$ is estimated in the RMT approach. For cases Phy2 and RM2,

a larger constant variance field $\sigma = 0.6$ is applied. Note that the perturbation of TKE is in logarithmic scale, so it is a relative value of the baseline result. That is, the constant variances $\sigma = 0.2$ and $\sigma = 0.6$ indicate $e^{0.2}$ and $e^{0.6}$ times of the baseline TKE. For the perturbations on orientations, the variances $\sigma = 0.2$ and $\sigma = 0.6$ are in radian, which correspond to 12° and 34° in degree, respectively. For all cases, 30 modes are used in Karhunen–Loeve expansion to capture more than 90% of the variance of the Gaussian random field. To reflect the anisotropy of the flow, an anisotropic yet spatially uniform length scale ($l_x/H = 2$ and $l_y/H = 1$) is used in the correlation kernel. The value of the length scale is chosen according to the approximate length scale of the flow, which can be obtained either from physical understanding of the flow or from RANS model estimation. To adequately represent the prior distribution of Reynolds stresses, 10,000 samples are drawn. Among them, only 500 samples are randomly selected to propagate to the QoIs (e.g., velocity and wall shear stress) via the RANS solver, taking into consideration of the high computational cost of RANS model evaluation. The direct numerical simulation (DNS) results of this flow [26] are used as the benchmark reference for comparison only. The computational parameters are summarized in Table 5.1.

Table 5.1: Mesh and computational parameters used in the flow over periodic hills.

Parameters	**Phy 1**	**RM 1**	**Phy 2**	**RM 2**
variance/dispersion[(a)]	$\sigma = 0.2$	see note (a)	$\sigma = 0.6$	see note (a)
Karhunen–Loeve mesh	50×30			
RANS mesh	50×30			
number of modes N_{KL}	30			
correlation length scales[(b)]	$l_x/H = 2$, $l_y/H = 1$			
number of samples	10,000			
number of propagated samples	500			

(a) the dispersion parameter field $\delta(x)$ is estimated with the corresponding variance field $\sigma(x)$ of the companion physics-based case.
(b) see Eq. 5.4.

5.3.2 Numerical Results

Two groups of comparisons between the physics-based approach and the RMT approach are conducted with the samples drawn by the Monte Carlo method. In each case, the samples of Reynolds stress field $[\mathbf{R}(x)]$ are obtained by using both the physics-based algorithm described in Section 5.2.1 and the RMT approach in Section 5.2.2. To facilitate the comparison and gain physical insights, all the sampled Reynolds stresses are mapped to their physical dimensions, i.e., shape parameter (in Barycentric coordinates C_1, C_2, C_3 and natural coordinates ξ, η), magnitude k, and the Euler angles (φ_1, φ_2, and φ_3). Moreover, the decomposition into

physical components also allows visualization of the distribution of random tensor fields. The marginal distributions of all components are investigated at two typical points: (1) point A located at $x/H = 2.0$ and $y/H = 0.5$ and (2) point B located at $x/H = 2.0$ and $y/H = 0.01$, indicated in Fig. 5.2. Point A is a generic point in the recirculation region, and point B is a near-wall point with two-dimensional turbulence representing limiting states.

We first investigate the distributions of shape parameters of the Reynolds stress tensors in Barycentric coordinates, which have clear physical interpretations (see Fig. 6.1). The perturbed Reynolds stresses at the generic point A are sampled and projected onto the Barycentric triangle. The scatter plots of these samples for all cases are shown in Fig. 5.3. We can see that the baseline RANS-predicted Reynolds stress at this generic point is located in the interior of the triangle, while the benchmark result is located to the upper right of the baseline result. For all cases considered here, all samples fall inside the Barycentric triangle, demonstrating that the realizability is guaranteed in both approaches. The scatterings of samples in Figs. 5.3a and 5.3b are comparable, and this is also the case for Figs. 5.3c and 5.3d, indicating that the dispersion parameters δ estimated with the corresponding variances σ are acceptable. The samples are still scattered around the baseline state, especially when the perturbation variance is small ($\sigma = 0.2$). It shows that the sample mean overlaps with the baseline state in Fig. 5.3a. When the variance increases ($\sigma = 0.6$), the mean value slightly deviates from the baseline state (comparing Figs. 5.3a and 5.3c). This deviation is markedly amplified in the RMT approach (Fig. 5.3d), suggesting that although the mean of perturbed Reynolds stresses is assumed to be the baseline result in the RMT approach, the mean is not preserved during the projection to the Barycentric coordinates. As the perturbation becomes large, the constraint of realizability leads to this significant deviation. Another notable difference between the results of two approaches lies in the shape of sample scattering. The scattering in case Phy1 is more elliptical-like with a large amount of samples spreading along the plain strain line (Fig. 5.3a), while in case RM1 the samples are scattered more circularly (Fig. 5.3b). When the perturbation is large ($\sigma = 0.6$), we can see that in both cases Phy2 and RM2 the scatterings of samples show significant influence from the boundaries. In the results of the physics-based approach, a number of samples fall on the edges of the triangle, and a large number of samples are clustered near the top vertex (Fig. 5.3c). In contrast, in the RMT approach the samples are dispersed within the triangle without such clustering, and the frequency of occurrences decreases near the edges (Fig. 5.3d).

Detailed comparison can be conducted by examining the marginal distributions of shape parameters in Barycentric coordinates C_1, C_2, and C_3. In Fig. 5.4 we present the probability density function (PDF) of C_1 for cases Phy1 and RM1 and cases Phy2 and RM2. Since C_2 and C_3 are correlated and have the similar characteristics as C_1, thus are omited for brevity. When the variance σ is 0.2, the distributions obtained in both approaches are Gaussian, and the sample means are close to the baseline result. As the variance σ increases to 0.6, both distributions deviate from Gaussian. In the physics-based approach the mode of samples (at peak of PDF) moves towards $C_1 = 0$ and the sample mean increases slightly compared to the baseline results. This is caused by the scheme used to impose the realizability constraint

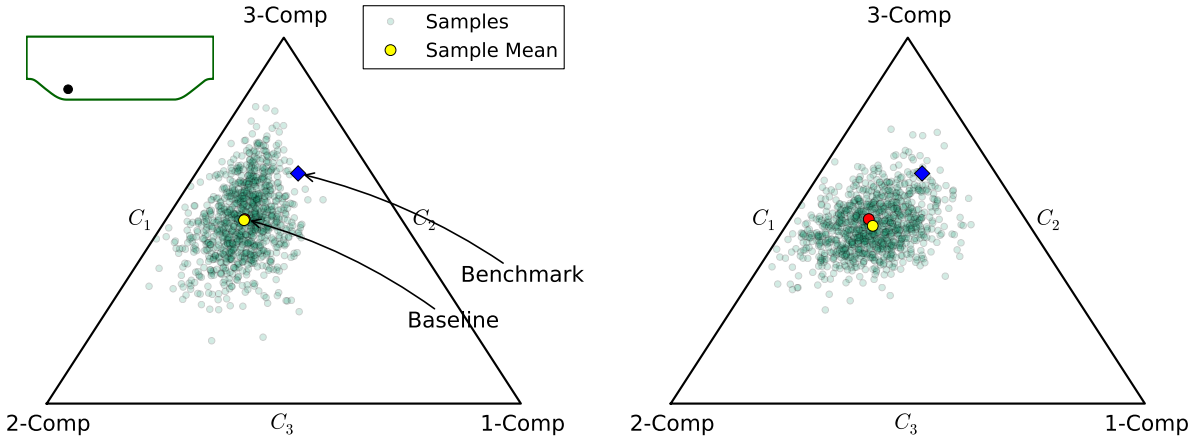

(a) Case Phy1, $\sigma = 0.2$

(b) Case RM1, $\sigma = 0.2$

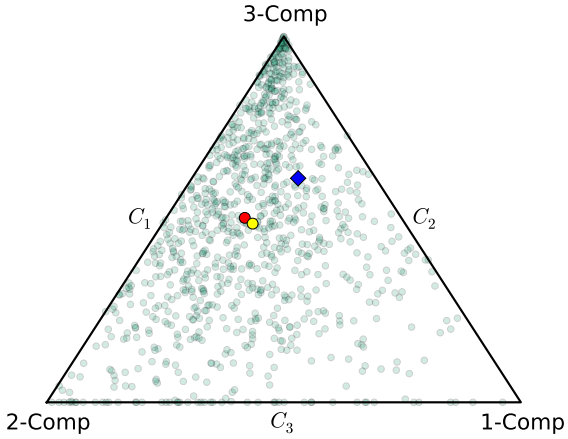

(c) Case Phy2, $\sigma = 0.6$

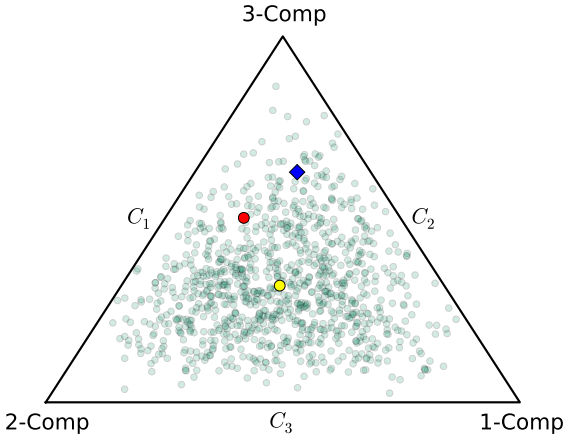

(d) Case RM2, $\sigma = 0.6$

Figure 5.3: Scatter plots of the Reynolds stress samples projected to the Barycentric coordinates for point A ($x/H = 2.0, y/H = 0.5$) located in the recirculation region. Panels (a) and (b) compare the two approaches with small perturbation ($\sigma = 0.2$), while panels (c) and (d) show the comparison with large perturbation ($\sigma = 0.6$). The baseline RANS result is plotted as a red dot. The benchmark state (DNS results from Breuer et al. [26]) is plotted as a blue square, which is located to the upper right of the baseline result.

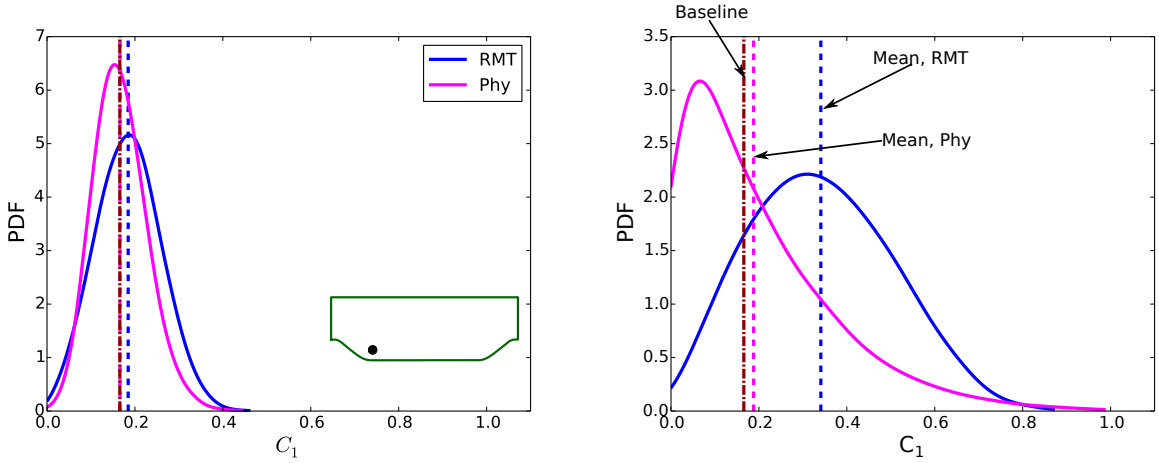

(a) cases Phy1 and RM1, $\sigma = 0.2$ (b) cases Phy2 and RM2, $\sigma = 0.6$

Figure 5.4: Probability distributions of the perturbed Barycentric coordinate C_1 for point A $(x/H = 2.0, y/H = 0.5)$ located in the recirculation region. The results from the physics-based approach and the RMT approach are compared in the same plot. Panels (a) and (b) show the comparison at perturbation variances of $\sigma = 0.2$ (cases Phy1 and RM1) and $\sigma = 0.6$ (cases Phy2 and RM2), respectively.

in the physics-based approach, where the samples falling outside the triangle are capped to the boundaries of natural coordinates (the four edges shown in Fig. 6.1b). Moreover, the samples spreading within the upper area of the natural coordinate square are squeezed in Barycentric triangle because of the mapping between the two coordinates. However, in the RMT approach the realizability of the Reynolds stress tensor $[\mathbf{R}]$ is guaranteed mathematically and no additional constraints are imposed due to the coordinates mapping. More precisely, the positive semi-definiteness of the normalized random matrix $[\mathbf{G}]$ is guaranteed by constructing from its Cholesky factor $[\mathbf{L}]$ (see Eq. 5.8). As a result, the distribution of C_1 is close to Gamma distribution with the sample mean increased compared to the baseline result. Based on the observations and discussions above, we find that some artificial constraints are introduced into the physics-based prior because of two issues of perturbing the shape parameters: (1) mapping between natural and Barycentric coordinates; (2) capping unrealizable samples. Therefore, it is better to specify Gaussian distributed perturbations of shape parameters in Barycentric coordinate to achieve maximum entropy for a generic location away from the wall.

It is also interesting to study the a point located close to the wall. Similarly, the comparisons of scatter plots of Reynolds stress samples at point B are presented in Fig. 5.5. It shows that the benchmark truth is located on the bottom edge of the triangle, indicating the two-component limiting state. This is because the velocity fluctuations in wall-normal direction are suppressed by the blocking of bottom wall of the channel. In contrast, RANS-predicted Reynolds stress is close to the three-component isotropic state, located near the top vertex

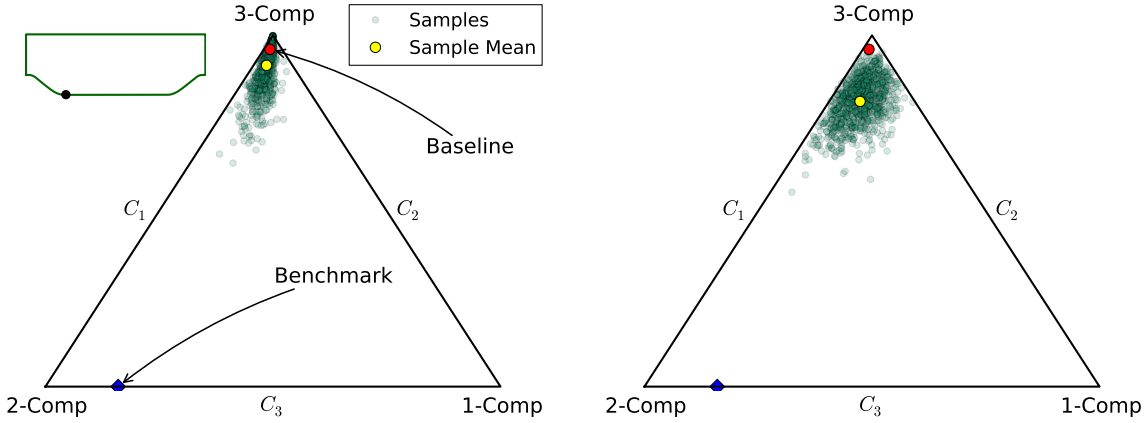

(a) Case Phy1, $\sigma = 0.2$

(b) Case RM1, $\sigma = 0.2$

(c) Case Phy2, $\sigma = 0.6$

(d) Case RM2, $\sigma = 0.6$

Figure 5.5: Scatter plots of the Reynolds stress samples projected to the Barycentric coordinates for point B ($x/H = 2.0, y/H = 0.01$) located in the recirculation region. Panels (a) and (b) compare the two approaches with small perturbation ($\sigma = 0.2$), while panels (c) and (d) show the comparison with large perturbation ($\sigma = 0.6$). The benchmark state (DNS results from Breuer et al. [26]) is plotted as a blue square, which is located on the bottom edge of the triangle, indicating two-component turbulence.

of the triangle. For the point B at the near wall location, the sample scatterings in all four cases are markedly affected by the boundaries of the triangle, and the sample means move downwards. This is due to the fact that the distances from the baseline state to the boundaries are relatively small compared to the perturbations, and thus the perturbed states are significantly affected by these constraints. However, the influences caused by the constraints imposed in the two approaches are different. In the case with a small variance $\sigma = 0.2$ (case Phy1, Fig. 5.5a), the samples are largely clustered near the top vertex and the scattering is squeezed artificially in the physics-based approach. Although enough samples are drawn, very few of them fall in the areas near the two side edges. In contrast, the samples in the RMT approach are dispersed within the entire upper area of the triangle and better explored the spanned uncertainty space (case RM1, Fig. 5.5b). When the variance is large ($\sigma = 0.6$, case Phy2, Fig. 5.5c), the capping scheme used to ensure realizability in the physics-based approach has a more pronounced effect on the obtained sample distribution. Specifically, about one half of the samples are capped to the edges or the vertices of the Barycentric triangle, leading to deteriorated sample effectiveness. It is worth noticing that the comparison is fair to both approaches, since the prior information is the same, i.e., all Reynolds stresses are realizable and the RANS predicted Reynolds stress is the best estimate of the mean. However, the ways of injecting uncertainties into Reynolds stresses are different between the two approaches, which lead to different sample scattering in the Barycentric coordinate.

The differences of perturbations in shape parameters between the two approaches are discussed above for two typical points A and B of the channel. In order to quantitatively explore the spatial variation of the difference between the two approaches, we calculate the Kullback-Leibler divergence of the distribution obtained by the physics-based approach from the distribution obtained by the RMT approach. The Kullback-Leibler divergence (also known as relative entropy) of q from p is a measure of the difference between two probability densities p and q, which is defined as [27]

$$D_{KL}(p||q) = \int_{\mathbb{I}} p(\vartheta) \log \frac{p(\vartheta)}{q(\vartheta)} d\vartheta, \tag{5.12}$$

where ϑ denotes the parameter, and $\mathbb{I}$ is the parameter space. The Kullback-Leibler divergence is analogous to a "distance" between two distributions, but it is not a distance measure since it does not preserve the symmetry in p and q. More intuitively, the Kullback-Leibler divergence of q from p can be interpreted as the measure of the information gained from the distribution p to distribution q. The Kullback-Leibler divergence is calculated to reflect the additional information introduced in the physics-based approach based on the maximum entropy distribution obtained with the RMT approach. Figure 5.6 shows the spatial profiles of Kullback-Leibler divergence for the shape parameter C_1. The profiles are shown at eight streamwise locations, $x/H = 1, \cdots, 8$, and the dashed black lines are plotted to indicate the axis of $D_{KL} = 0$. The geometry of the physical domain is also plotted to facilitate visualization. To clearly show the characteristics of the profiles, a larger scale factor

of 0.9 is used in Fig. 5.6a, while a smaller scale factor of 0.3 is used in Fig. 5.6b. When the variance is small ($\sigma = 0.2$), the Kullback-Leibler divergence is also small over the entire domain (Fig. 5.6a), suggesting that the distributions of shape parameters obtained from the physics-based approach are similar to those obtained from the RMT approach. When we increase the perturbation variance ($\sigma = 0.6$), the Kullback-Leibler divergence becomes larger over the entire domain (Fig. 5.6b), indicating that the additional, artificial constraints introduced in the physics-based approach are significant with large perturbation. Moreover, both Figs. 5.6a and 5.6b show that the Kullback-Leibler divergences for the locations near the wall are slightly larger than those at generic locations. As has been discussed above, the baseline RANS-predicted Reynolds stress near the wall is close to three-component isotropic limiting state. This results in the fact that the perturbation is large compared to the distance from baseline state to the boundary of the triangle, and thus more artificial information is introduced in the physics-based approach at the near-wall regions. It is noted that the D_{KL} is also large at $y/H = 2.5$, which is because the baseline state is closer to the top vertex of triangle at $y/H = 2.5$. All these observations are consistent with the discussion above for the two typical points A and B.

The analysis above suggests that imposing Gaussian perturbation directly in Barycentric coordinates (as oppose to the natural coordinates) leads to a distribution closer to maximum entropy. However, the perturbations were imposed in natural coordinates by Xiao et al. [10] due to practical considerations. Since the Barycentric coordinates C_1, C_2, and C_3 are correlated, and the triangle boundary edges pose difficulties on the capping scheme, the natural coordinates ξ and η are preferred for implementation purposes. In order to determine proper perturbations in ξ and η to obtain prior with maximum entropy in the physics-based approach, we also need to map the Barycentric coordinates to the natural coordinates in the RMT approach. With the samples of natural coordinates ξ and η, their joint density can be estimated with Gaussian kernels. Figures 5.7a and 5.7b show the comparison of joint PDF contours obtained by the two approaches with variances $\sigma = 0.2$ and $\sigma = 0.6$, respectively. Moreover, the comparisons of marginal distributions of ξ and η are also plotted in Fig. 5.8. When the perturbation is small ($\sigma = 0.2$), the contours in both cases Phy1 and RM1 are elliptical, indicating the joint distributions are approximately Gaussian (Fig. 5.8a). However, a notable difference between the results of the two approaches lies on the shapes of the contours. The elliptical contour in the RMT approach is anisotropic with larger variance for ξ but smaller for η. In the physics-based approach the contour is circular due to the artificial choice of the same perturbation variance for both ξ and η. Therefore, to achieve the prior with approximate maximum entropy, the perturbation in ξ should be larger than that in η for this flow of concern. More details can be found in their marginal distributions (Figs. 5.8a and 5.8c). For both approaches with small perturbation ($\sigma = 0.2$) in Reynolds stress, the marginal distributions for ξ and η are Gaussian. With the RMT approach, the perturbation variance of ξ is approximately twice as large as that with the physics-based approach, while the perturbation of η is slightly smaller than that with the physics-based approach. However, when the perturbation is large ($\sigma = 0.6$), the joint distribution of ξ and η obtained by both approaches are no longer Gaussian, and the density contours are influenced by the

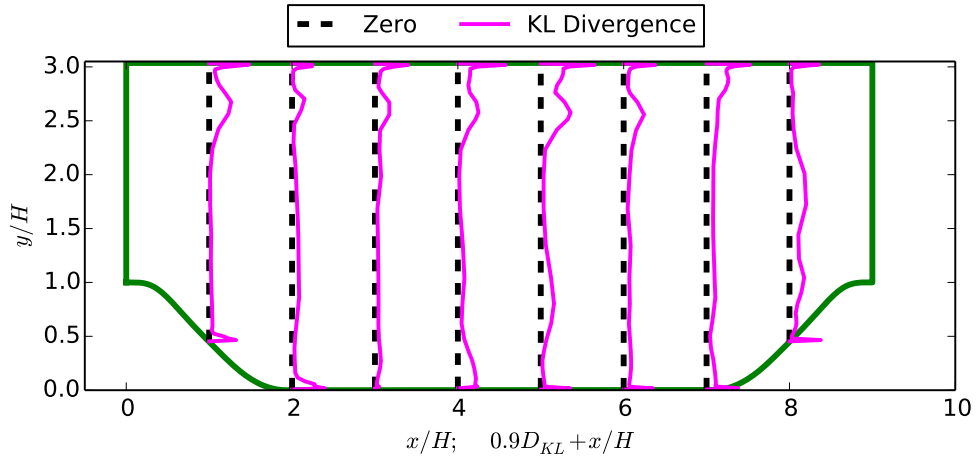

(a) $\sigma = 0.2$

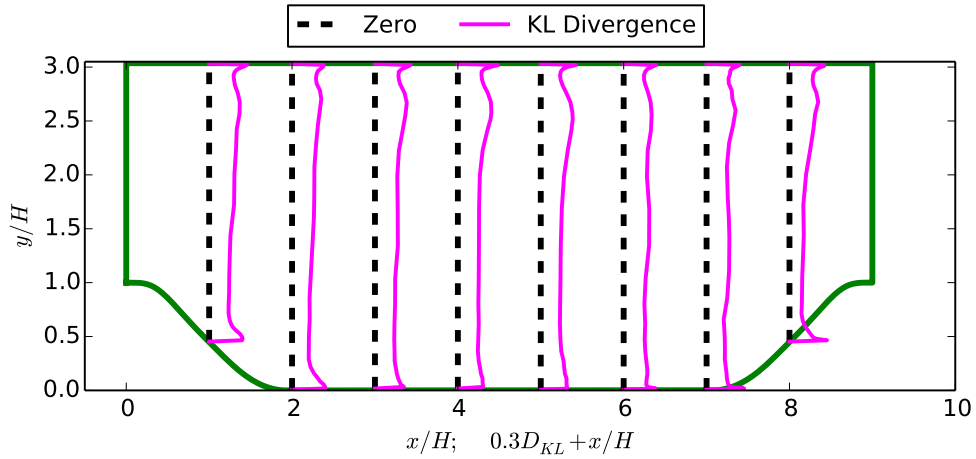

(b) $\sigma = 0.6$

Figure 5.6: Kullback-Leibler divergence profiles with (a) $\sigma = 0.2$ and (b) $\sigma = 0.6$. The profiles are shown at eight streamwise locations $x/H = 1, \cdots, 8$, and the reference lines, $D_{KL} = 0 + x/H$, are also plotted. Note that in panel (a), since the scale of D_{KL} is quite smaller than that of panel (b), a larger scale factor of 0.9 is used in (a), while a smaller scale factor of 0.3 is used in (b).

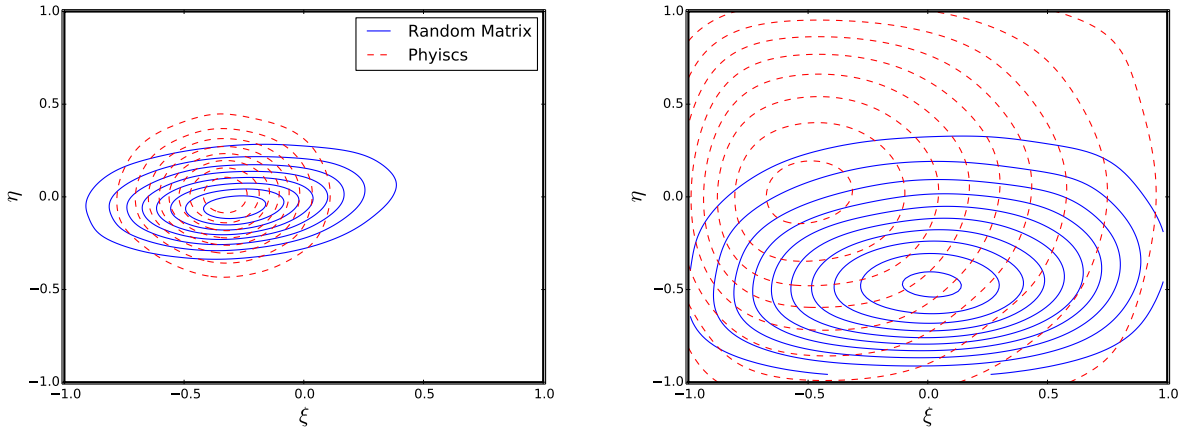

(a) Phy1 and RM1 ($\sigma = 0.2$) (b) Phy2 and RM2 ($\sigma = 0.6$)

Figure 5.7: Comparisons of probability density contours of natural coordinates (ξ and η) obtained from the physics-based approach and the RMT approach at point A ($x/H = 2.0, y/H = 0.01$. Panel (a) and (b) are with the perturbations $\sigma = 0.2$, and $\sigma = 0.6$, respectively.)

boundaries (Fig. 5.7b). Especially in case Phy2 the shape of the contour clearly follows the rectangular edges. Unlike the physics-based approach, the shape of the contour obtained with the RMT approach is less affected by the boundaries. Detailed comparisons are shown by the corresponding marginal distributions. All the distributions are distorted compared to the Gaussian PDF (Gaussian density with the sample mean and variance). The distortions in the physics-based approach are due to the fact that large number of unrealizable samples are capped onto the edges. However, in the RMT approach the sample means of ξ and η significantly deviate from the baseline results. The mean of ξ moves towards the middle point ($\xi = 0$) of ξ range, while the mean of η moves towards approximate one third ($\eta = -0.4$) of the η range $[-1, 1]$. This sample mean point ($\xi = 0.0$, $\eta = -0.4$) is close to the centroid of the triangle when mapped back to the Barycentric coordinates. Moreover, the distributions are approximately bounded Gaussian that satisfy the realizability constraint mathematically. The deviation of sample mean from the baseline when the perturbation is large can be interpreted intuitively. Since the large perturbation of Reynolds stress implies less confidence on the baseline prediction, it is reasonable to adjust the sample mean to the centroid of triangle to have a better sample scattering over the entire triangle. This means, under this circumstance, we can directly perform the perturbations based on the centroid of the triangle instead of the baseline state. The results shown in Figs. 5.7a, 5.8a, and 5.8c suggest that, for a generic point away from the wall, imposing small perturbations on ξ and η with Gaussian distributions lead to Reynolds stresses that are very close to the maximum entropy distribution. This observation lends partial support to the choice of prior distributions made in [10]. However, to achieve the maximum entropy prior, the perturbation

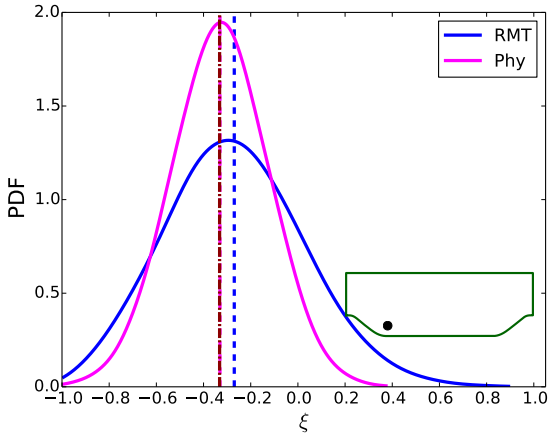

(a) PDF of ξ, $\sigma = 0.2$

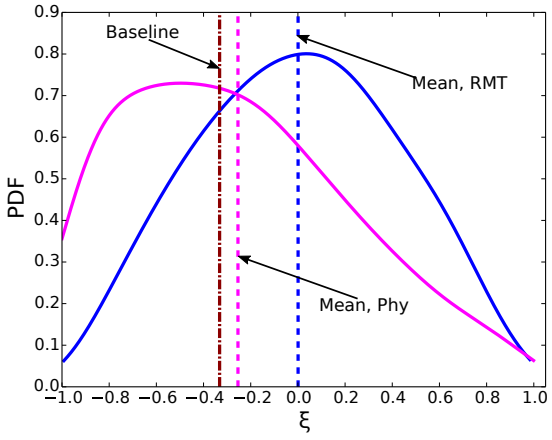

(b) PDF of ξ, $\sigma = 0.6$

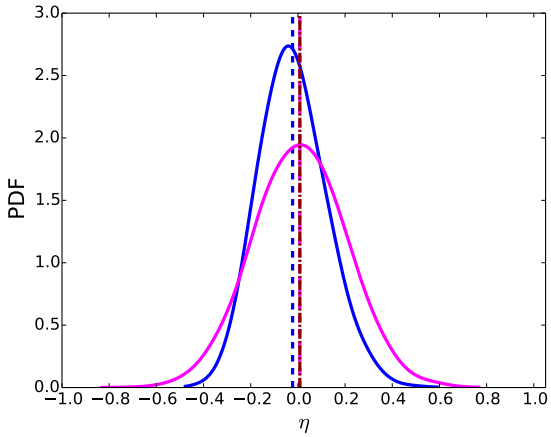

(c) PDF of η, $\sigma = 0.2$

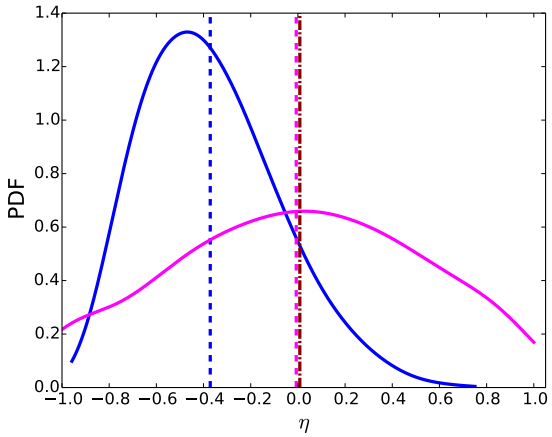

(d) PDF of η, $\sigma = 0.6$

Figure 5.8: Distributions of the perturbed natural coordinates ξ and η for point A $(x/H = 2.0, y/H = 0.5)$ located in recirculation region. The results from the physics-based approach and the RMT approach are compared in the same plot. Panels (a) and (b) show the comparison of ξ at perturbation variances of $\sigma = 0.2$ and $\sigma = 0.6$, respectively. Panels (c) and (d) show the comparison of η at perturbation variances of $\sigma = 0.2$ and $\sigma = 0.6$, respectively.

variance of ξ should be approximately twice as large as that of η. When the perturbation of Reynolds stress is large, to achieve maximum entropy we should first shift the baseline ξ and η to the centroid of the Barycentric triangle, and then perturb the shifted baseline results with bounded Gaussian distribution.

In addition to the shape of Reynolds stress, its magnitude i.e., the turbulence kinetic energy (TKE), is also difficult to predict in RANS models. In the physics-based approach, the perturbations in turbulence kinetic energy are specified to be log-normally distributed. To evaluate if this specification is justified, we compared the TKE perturbations in logarithmic scale $\Delta \log k$ obtained from the two approaches. The marginal distributions of $\Delta \log k$ with different perturbation levels ($\sigma = 0.2$ and $\sigma = 0.6$) at points A and B are presented in Fig. 5.9. In both the physics-based and RMT approaches, the perturbations in TKE obey the log-normal distribution, since all the PDFs of $\Delta \log k$ shown in Fig. 5.9 are close to the Gaussian distributions. This conclusion is also true for the cases with larger perturbations (cases Phy2 and RM2, $\sigma = 0.6$) as well. Therefore, introducing a log-normally distributed prior for TKE discrepancies leads to a distribution of Reynolds stresses that is close to the one with maximum entropy. This lends support to the choice of prior in the physics-based approach [10]. Another interesting observation in Fig. 5.9 is that the spreading of $\Delta \log k$ samples with the RMT approach is slightly smaller than that with physics-based approach. As mentioned above, in the physics-based approach the same variance field $\sigma(x)$ is shared by the perturbations of six variables (ξ, η, k, φ_1, φ_2, φ_3) due to the lack of prior knowledge. However, this assumption is another constraint imposed in the physics-based approach. Based on the comparisons in Fig. 5.9, we find that to achieve the maximum entropy, the perturbation variance for each parameter should be different. It suggests that a relatively smaller variance (approximate 50% of that for shape parameter) is proper for the perturbation of TKE in logarithmic scale for this flow of concern.

In order to fill the gap in the previous studies on physics-based approach [10, 8, 9] which did not fully explore the uncertainty space of Reynolds stress and make a fair comparison with the RMT approach, the orientations are perturbed with parameterization of Euler angles in this work. However, if or how large the orientation should be perturbed are model choices in the physics-based approach. Without further physical information, it is difficult to determine the variance of angle perturbations. To examine this issue, the marginal distributions of angle discrepancies obtained from both approaches are compared. Fig. 5.10 shows the comparison of PDF of $\Delta\varphi_1$ with different perturbation magnitudes at the points A and B. The perturbations in φ_2 and φ_3 have similar characteristics as that of φ_1, and thus they are omitted for brevity. We can see that to achieve the maximum entropy the orientation of the tensor should also be perturbed. Similarly to the perturbations in TKE, the sample mean of $\Delta\varphi_1$ is zero for all cases. This indicates that the sample means in tensor magnitude and orientation are the same as those of baseline RANS prediction, since there are no physical constraints on TKE and Euler angles (except for the range $[-\pi, \pi]$ specified in the definition). In the physics-based approach, the PDFs are Gaussian for all cases, since Gaussian random fields are employed to model the discrepancies in angles. For the generic

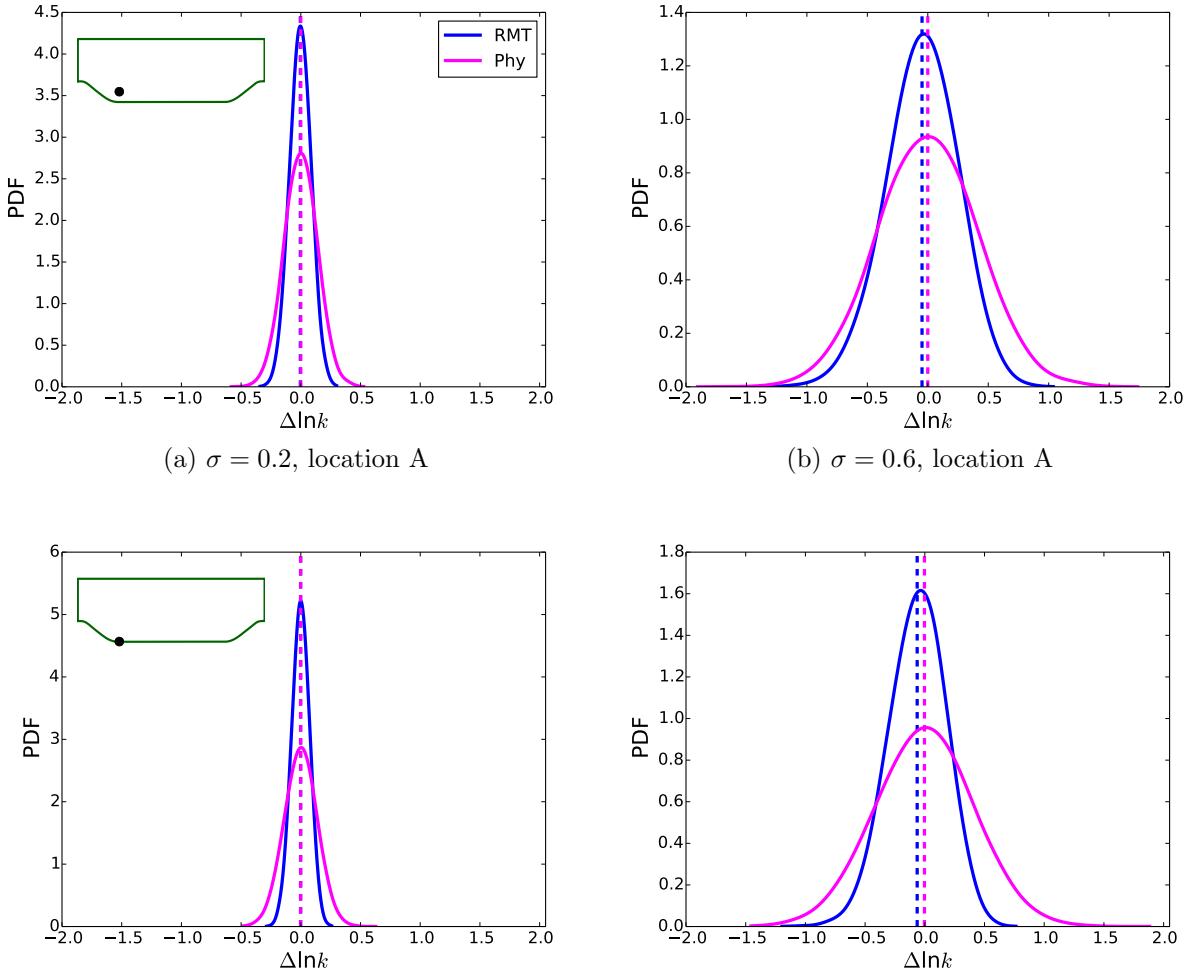

(a) $\sigma = 0.2$, location A

(b) $\sigma = 0.6$, location A

(c) $\sigma = 0.2$, location B

(d) $\sigma = 0.6$, location B

Figure 5.9: Distributions of the perturbations ($\Delta \log k$) in turbulence kinetic energy in logarithmical scale. The upper two panels show the results at point A ($x/H = 2.0, y/H = 0.5$), while the lower two panels show the results at point B ($x/H = 2.0, y/H = 0.01$). The results from physics-based approach and random matrix theoretic approach are compared in the same plot. The sample mean of the physics-based approach overlaps with that of the RMT approach (denoted as blue (dark) dashed line and pink (grey) dashed line, respectively)

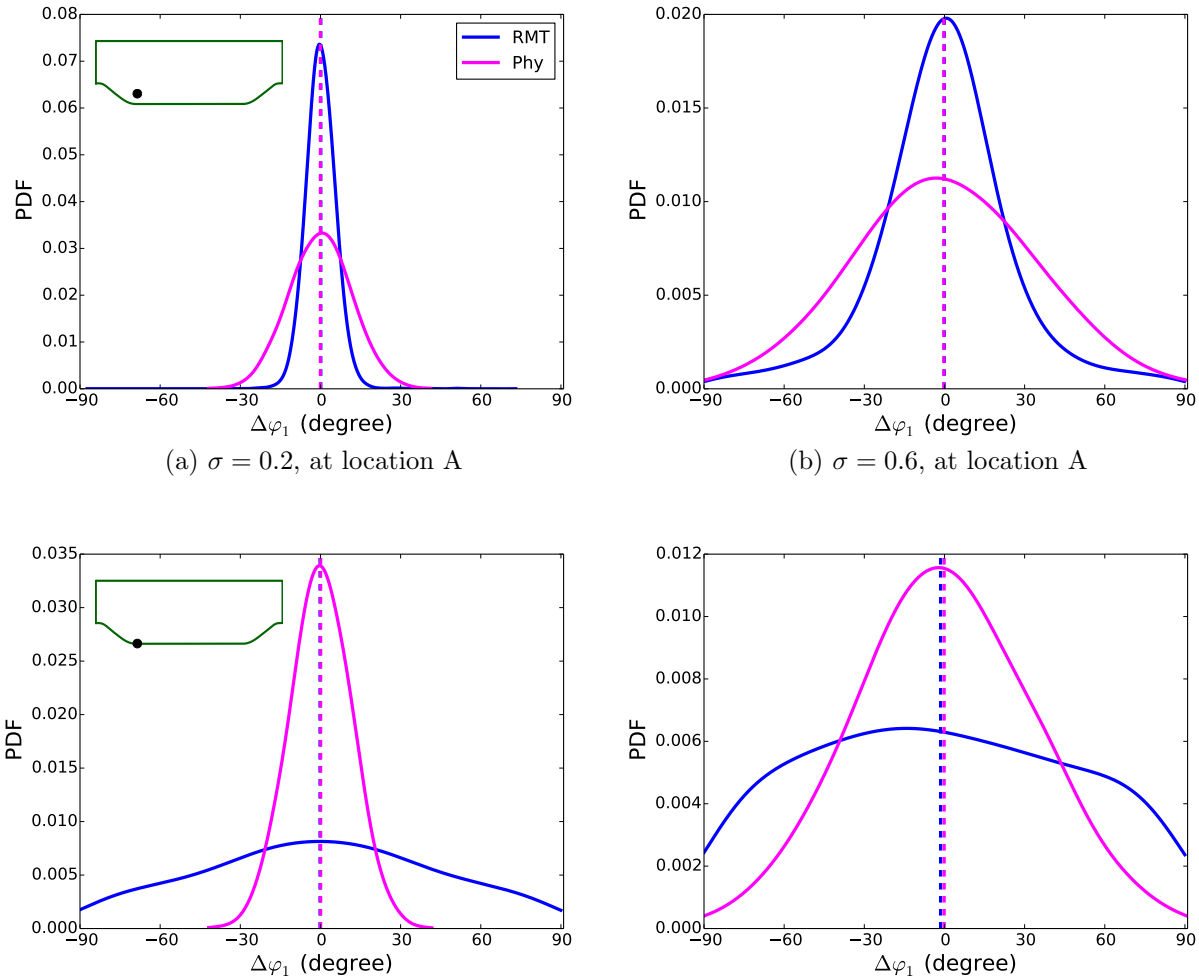

(a) $\sigma = 0.2$, at location A

(b) $\sigma = 0.6$, at location A

(c) $\sigma = 0.2$, at location B

(d) $\sigma = 0.6$, at location B

Figure 5.10: Distributions of the perturbations ($\Delta\varphi_1$) in orientation. The upper two panels show the results at point A ($x/H = 2.0, y/H = 0.5$), while the lower two panels show the results at point B ($x/H = 2.0, y/H = 0.01$). The results from Physics-based approach and random matrix theoretic approach are compared in the same plot. The sample mean of the physics-based approach overlaps with that of the RMT approach (denoted as blue (dark) dashed line and pink (grey) dashed line, respectively)

point A, the distribution of $\Delta\varphi_1$ obtained from the RMT approach is also close to Gaussian when the perturbation is small (Fig. 5.10a). However, the scattering of samples is smaller than what we specified in the physics-based approach, and most of the perturbations are within ± 20 degrees. As the perturbation magnitude is enlarged, the PDF obtained in the RMT approach is peaked compared to the Gaussian distribution (Fig. 5.10b). Consequently, most samples are with small perturbations (smaller than 30 degrees). However, for the point B located close to the wall, the variances of $\Delta\varphi_1$ in cases RM1 and RM2 are much larger, even though the perturbation of tensor is small (Fig. 5.10c). In the RMT approach the distribution of $\Delta\varphi_1$ is flatter than the corresponding Gaussian distribution, and most of the perturbations $\Delta\varphi_1$ are larger than 60 degrees. Especially when the dispersion parameter is large (i.e., $\delta(x)$ corresponding to $\sigma = 0.6$), the PDF of $\Delta\varphi_1$ significantly deviates from the Gaussian distribution (Fig. 5.10d). The observations above imply that, to obtain a maximum entropy prior, the perturbations variance in orientation should be spatially non-stationary. For this specific flow, smaller perturbations (with 30 degrees) should be used for a generic point away from the way, while larger perturbations are appropriate for the near wall locations. The above suggested perturbation variance for each physical variable is obtained under the two constraints: realizability of Reynolds stress and RANS predicted Reynolds stress as the mean. The first constraint is guaranteed mathematically in the RMT approach, which is independent on the flow case. However, the second constraint determines where the perturbation is from and the conclusion is therefore flow-dependent. The suggested relative magnitudes can be used to wall-bounded flows, but cautions should be exercised for other flows. It is worth noticing that when warranted physical knowledge of the flow are available, the relative magnitude should be adjusted to incorporate the physical information.

The results shown above focus on the comparisons for the six individual physical variables. It is also interesting to investigate the differences of perturbations on the tensor components between the two approaches. Among the six tensor components, turbulent shear stress R_{12} is the most relevant one to propagated velocities in the flow over periodic hills. Figure 5.11 presents the scatterings of R_{12} samples after perturbations specified in the physics-based and RMT approaches. Only the results with perturbation variance $\sigma = 0.6$ are shown, since those with $\sigma = 0.2$ are qualitatively similar. The sample scattering is indicated by the 2-σ credible interval, which is estimated from the samples. That is, at each point, 95.45% of the samples fall within the shaded region (red for the physics-based results and blue for the RMT results). The sample means from the physics-based (red dashed line) and RMT (blue dashed line) approaches are also plotted to compare with the benchmark results (black solid line) [26]. The baseline results overlap with the RMT sample mean profiles and are thus omitted to avoid clustering. Compared to the benchmark results, the baseline RANS predicted turbulent shear stresses are satisfactory in the upper region of the channel, but have large discrepancies in the lower region. Especially at the leeward of the hill and in the recirculation region, the RANS model under-predicts the shear component $|R_{12}|$. When the uncertainties are injected into the Reynolds stresses, the 2-σ shaded regions in both approaches cover the benchmark in most parts of the domain. However, a notable difference can be observed: the sample mean profiles in physics-based approach deviate from

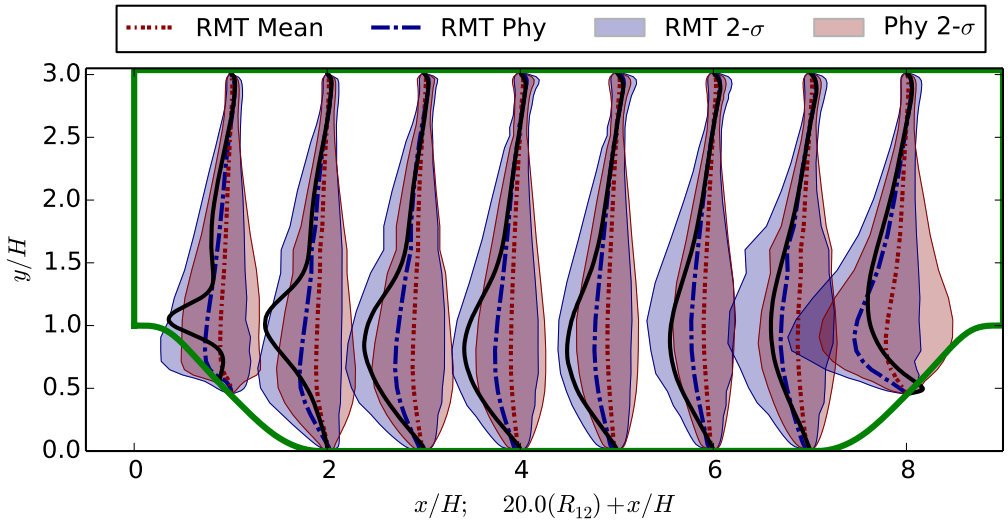

Figure 5.11: The 2-σ (95.45%) credible intervals of the perturbed turbulent shear stress R_{12} obtained from physics-based and RMT approaches. The profiles are shown at eight streamwise location $x/H = 1, \cdots, 8$. The sample means from Physics-based and RMT approach are plotted as red and blue dashed lines, respectively. The baseline results overlap with the RMT sample mean, which are omitted to avoid clustering. The benchmark results (black solid) obtained by direct numerical simulation [26] are also shown for comparison.

the baseline results, whereas in RMT approach they are well preserved. It can be seen that the mean of $|R_{12}|$ decreases in the physics-based approach, and the credible interval (shaded region) fails to cover the peaks of benchmark profiles in the free-shear region (at $y/H = 1.0$) from $x/H = 1.0$ to $x/H = 6.0$. In previous studies on physics-based approach [10, 11], it has been reported that prior means of perturbed Reynolds stresses and propagated velocities are very close to the baseline results. The "inconsistence" observed here results from the angle perturbation. Previous studies [10, 11, 8, 9], perturbed only the tensor's shape and magnitude. In this work, however, the tensor orientations are also perturbed simultaneously. Although in both physics-based and RMT approaches the perturbations are performed with the baseline RANS results being the mean, in physics-based approach they are conducted for physical components individually instead of directly perturbing the tensor as in the RMT approach. Since the shape parameters (eigenvalue) and Euler angles (eigenvector) are perturbed simultaneously yet independently, the mean of reconstructed tensor samples may not be the same as the baseline Reynolds stress, though the mean of each physical variable is still preserved.

Finally, the perturbed Reynolds stress samples are propagated to the velocity through the RANS equation tauFOAM [10], and the comparison of sample means of velocity profiles obtained in the two approaches is shown in Fig. 5.12. Similarly, the 2-σ credible intervals from both approaches are plotted. We can see that the shaded regions in both approaches basically cover the benchmark velocity profiles. The sample mean profiles in the RMT approach

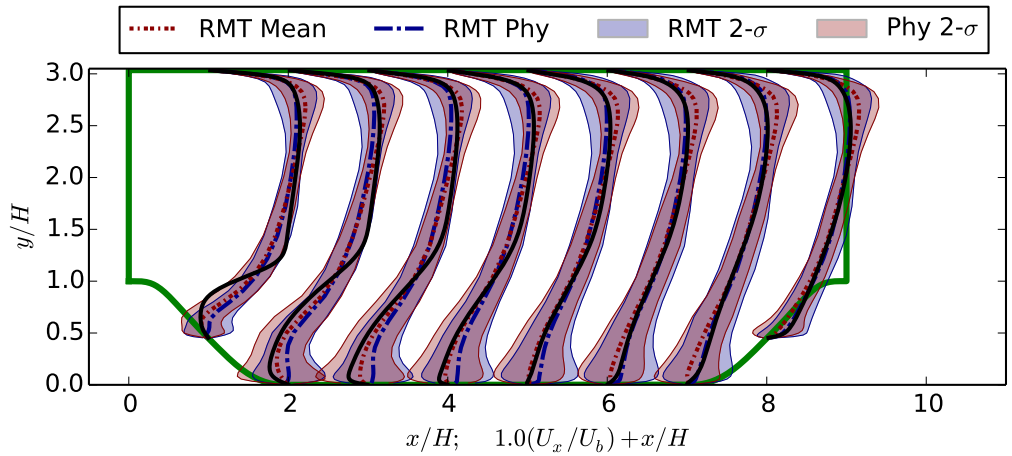

Figure 5.12: Comparison of propagated velocity profiles and corresponding 2-σ credible intervals for physics-based (blue shaded) and RMT (red shaded) approaches. The profiles are shown at eight streamwise locations at $x/H = 1, \cdots, 8$, compared to the benchmark results (black solid) obtained by direct numerical simulation [26]. The baseline results overlap with the RMT sample mean, which are omitted to avoid clustering.

overlap with the baseline results, indicating a linearity of the mapping from Reynolds stresses to the velocity. In the physics-based approach, the sample mean profiles deviate from the baseline results, and the credible interval region is also slightly shifted. It is interesting to see that the deviated sample mean in physics-based approach becomes closer to the benchmark results in the recirculation region, while it is worse than the baseline in the upper channel region. However, such "improvement" of recirculation prediction is a coincidence, since the information of benchmark results has not been incorporated.

5.4 Discussion

5.4.1 Effect of Relative Perturbation Variance of Each Physical Variable

A notable difference between the physics-based and RMT approaches lies on how to inject uncertainties into RANS modeled Reynolds stresses $[\mathbf{R}]^{rans}$. In the physics-based approach, the uncertainties are injected into each physically meaningful variable of $[\mathbf{R}]^{rans}$, while in the RMT approach the uncertainties are directly injected into Reynolds stresses as random matrices. Therefore, the relative perturbation variance of each of the six physical variables compared to each other is fixed beforehand in the RMT approach, while flexibility is still preserved in the physics-based approach. With the same perturbation variance of tensor, it is interesting to investigate whether different combinations of variances in physical variables

have markable impacts on the propagated QoI. Here we consider an extreme case: only the

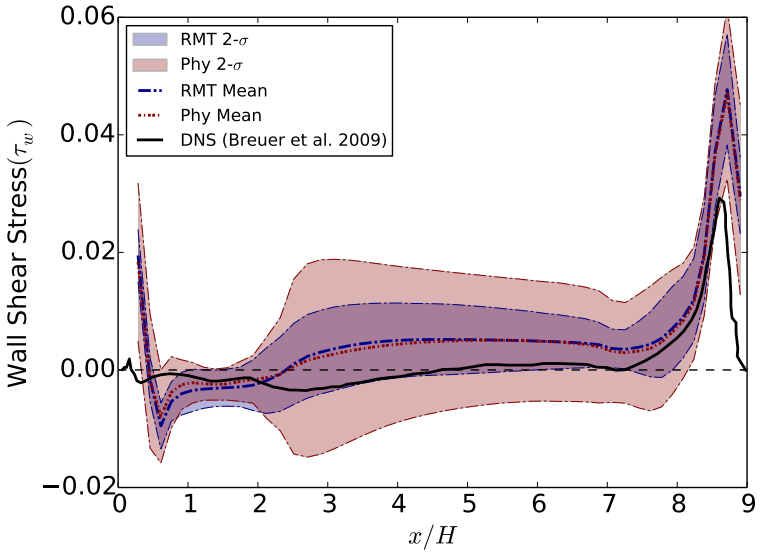

Figure 5.13: 2-σ credible intervals of propagated wall shear stress profiles from physics-based (red shaded) and RMT (blue shaded) approaches. the benchmark results obtained by direct numerical simulation [26] are plotted for comparison. The baseline results overlap with the both physic-based and RMT sample means, which are omitted to avoid clustering.

shape of anisotropy is perturbed in the physics-based approach with variance $\sigma(x) = 0.6$, while no perturbations are performed on other variables (magnitude and orientations). To achieve the same perturbation variance of tensor, the dispersion parameter $\delta(x)$ is estimated for the RMT approach. In this case, although the variances of the Reynolds stress tensors are similar, the scatterings of each tensor component are slightly different between the two approaches. For the turbulent normal stress component R_{11}, the scattering is slightly larger in the RMT approach. In contrast, for the turbulent shear stress component R_{12}, the scattering is larger in the physics-based approach where only the shape of anisotropy is perturbed. After propagation of these perturbed Reynolds stresses via RANS equations, the scatterings of QoI samples are markedly different. The bottom wall shear stresses, one of the propagated QoIs, obtained by post-processing the velocity fields are presented in Fig. 5.13. The 2-σ credible regions are also plotted for comparison. It can be clearly seen that even though the perturbation variances of tensors are similar, the 2-σ shaded region of bottom wall shear stresses by only perturbing the anisotropy is markedly larger than that using the RMT approach, and it better covers the benchmark results. This indicates that the wall shear stress is more sensitive to the shape of anisotropy than other variables for this specific flow. Qualitatively similar observations are obtained for the propagated velocities, the results of which are thus omitted. It is worth noticing that this observation is flow-dependent. Therefore, with more physical information and better understanding of the flows of interest, the physics-based approach is advantageous due to its flexibility on specifying different relative magnitude of variances for physical variables.

5.4.2 Modeling Choices in the Pysics-Based and RMT Approaches

The results shown in Section. 5.3 suggest that, when the RANS predictions are relatively reliable with small perturbations needed, using normally distributed perturbations for each of the six physical variables is a good choice to obtain the Reynolds stress prior that is close to the one with maximum entropy. This observation can be related to the case of a scalar random variable. With the constraints of a specified mean and variance, the maximum entropy distribution of a scalar random variable is a Gaussian distribution [28]. That is, by choosing Gaussian distributions for the discrepancies of Reynolds stresses in the physics-based approach, the maximum entropy distribution is achieved for each individual physical variable (magnitude, shape, orientation). The variance of each variable is, however, chosen by the user and is thus a modeling choice. In contrast, in the RMT approach the maximum entropy is achieved for the distribution of the Reynolds tensor. Consequently, the relative magnitude of the variance for each variable is implied based on the maximum entropy principle and is not a modeling choice of the user. However, it is worth pointing out that, although we use the results of the RMT approach as the golden standard to assess artificial constraints introduced in the physics-based approach, the correlation structure and the corresponding Karhunen-Loeve modes used to represent the random field are still modeling choices, which also may introduce artificial constraints. In summary, one can consider that in the RMT approach, maximum entropy is achieved for the pointwise distribution of the Reynolds stresses at each location x, but not necessarily for the random field $[\mathbf{R}(x)]$. In the physics-based approach, maximum entropy is achieved for the pointwise distribution for individual physical variables (k, ξ, η etc.) but not necessarily for the Reynolds stress tensor $[\mathbf{R}]$ or the field $[\mathbf{R}(x)]$.

It is also worth noting that the maximum entropy distribution in the RMT approach is obtained under two assumed constraints, i.e., (1) all Reynolds stresses are realizable and (2) the RANS predicted Reynolds stress is the best estimation of Reynolds stress mean. However, if other warranted physical information is incorporated, the current form of Reynolds stress distribution in the RMT approach may not have the maximum entropy. It is possible to adapt the maximum entropy distribution to the new constraints. For example, Ghanem et al. [15] have developed the maximum entropy distribution for the bounded random matrix. Nonetheless, to rigorously derive the maximum entropy distribution under the new constraints is nontrivial, and it is easier to incorporate the physical information in the physics-based approach. Since the physical knowledge is generally weak and vague in the context of quantifying model-form uncertainties in RANS modeling, the suggestions of prior specification given in Section 5.3 are still useful to achieve an approximate maximum entropy distribution even if some available physical information is incorporated. Moreover, if the artificial constraints in current form of the physics-based approach is predominantly large, the merits of incorporating physical information will be overwhelmed. Therefore, the comparison results shown in Section 5.3 can be used to "calibrate" the physics-based approach. However, caution still should be exercised to apply the current conclusion when strong physical constraints are incorporated.

5.5 Conclusion

Quantification of the uncertainties originating from the modeled Reynolds stresses is crucial when the RANS simulations are applied in the decision-making process. One of the challenges in current form of the physics-based model-form uncertainty quantification framework is to specify proper priors for the physical variables (shape, magnitude, and orientation). It is difficult to determine if or how much additional information is introduced into the priors specified in the physics-based approach. To evaluate the priors and gain insights on proper specification of the priors, the random matrix theoretic approach with the maximum entropy principle is used in this work. By comparing the distributions of shape, magnitude, and orientation variables obtained from the two approaches, we identified several factors which may introduce artificial constraints in the physic-based approach. Moreover, the comparisons also provide some useful guidelines of prior specification for these wall-bounded flows with separations. For the shape parameters, the Gaussian distributed perturbations in Barycentric coordinate is better to achieve maximum entropy. The mapping between the Barycentric coordinate to the natural coordinate may introduce some artificial constraints, especially when the RANS prediction is less reliable (large perturbation needed). For the turbulence kinetic energy, introducing log-normally distributed perturbations leads to a distribution of Reynolds stresses that is close to the one with the maximum entropy. This observation lends support to the choice of prior in [10]. For orientation, it suggests that the uncertainties should also be injected with a non-stationary variance field to achieve the maximum entropy distribution of tensors. For the specific flow in this study, the perturbations of Euler angles should be small for a generic location away from the wall, while large for the near wall locations. Simultaneously perturbing shape and orientation of anisotropy in the physics-based approach cannot preserve the mean of tensors as the baseline result. Finally, we discussed the relative magnitude of variance for each physical variable and its impact on the propagated quantities. Useful suggestions on specifying relative magnitudes of variances among the physical variables are provided. The observations and conclusion are meaningful to quantify the model-form uncertainties in RANS modeling and can be used as a guidance for the objective prior specification in the physics-based, Bayesian uncertainty reduction framework.

Bibliography

[1] S. B. Pope, Turbulent flows, Cambridge university press, 2000.

[2] T. Oliver, R. Moser, Uncertainty quantification for RANS turbulence model predictions, in: APS Division of Fluid Dynamics Meeting Abstracts, 2009.

[3] L. Margheri, M. Meldi, M. Salvetti, P. Sagaut, Epistemic uncertainties in RANS model free coefficients, Computers & Fluids 102 (2014) 315–335.

[4] W. Edeling, P. Cinnella, R. P. Dwight, H. Bijl, Bayesian estimates of parameter variability in the k–ε turbulence model, Journal of Computational Physics 258 (2014) 73–94.

[5] W. Edeling, P. Cinnella, R. P. Dwight, Predictive RANS simulations via Bayesian model-scenario averaging, Journal of Computational Physics 275 (2014) 65–91.

[6] M. Emory, R. Pecnik, G. Iaccarino, Modeling structural uncertainties in Reynolds-averaged computations of shock/boundary layer interactions, in: 49th AIAA Aerospace Sciences Meeting, 2011.

[7] E. Dow, Q. Wang, Quantification of structural uncertainties in the k–ω turbulence model, AIAA Paper 1762 (2011) 2011.

[8] M. Emory, J. Larsson, G. Iaccarino, Modeling of structural uncertainties in Reynolds-averaged Navier-Stokes closures, Physics of Fluids 25 (11) (2013) 110822.

[9] C. Gorlé, G. Iaccarino, A framework for epistemic uncertainty quantification of turbulent scalar flux models for Reynolds-averaged Navier-Stokes simulations, Physics of Fluids (1994-present) 25 (5) (2013) 055105.

[10] H. Xiao, J.-L. Wu, J.-X. Wang, R. Sun, C. J. Roy, Quantifying and reducing model-form uncertainties in Reynolds-Averaged Navier-Stokes simulations: An open-box, physics-based, bayesian approach, submitted. Available at http://arxiv.org/abs/1508.06315 (2015).

[11] J.-X. Wang, J.-L. Wu, H. Xiao, Incorporating prior knowledge for quantifying and reducing model-form uncertainty in RANS simulations, submitted. Available at http://arxiv.org/abs/1512.01750 (2015).

[12] S. Guiasu, A. Shenitzer, The principle of maximum entropy, The mathematical intelligencer 7 (1) (1985) 42–48.

[13] E. T. Jaynes, Information theory and statistical mechanics, Physical review 106 (4) (1957) 620.

[14] C. Soize, A nonparametric model of random uncertainties for reduced matrix models in structural dynamics, Probabilistic engineering mechanics 15 (3) (2000) 277–294.

[15] S. Das, R. Ghanem, A bounded random matrix approach for stochastic upscaling, Multiscale Modeling & Simulation 8 (1) (2009) 296–325.

[16] H. Xiao, J.-X. Wang, R. G. Ghanem, A random matrix approach for quantifying model-form uncertainties in turbulence modeling, to be submitted. Available at https://sites.google.com/a/vt.edu/hengxiao/papers (2016).

[17] J.-L. Wu, J.-X. Wang, H. Xiao, A Bayesian calibration-prediction method for reducing model-form uncertainties with application in RANS simulations, submitted. Available at http://arxiv.org/abs/1510.06040 (2015).

[18] K. J. Law, A. M. Stuart, Evaluating data assimilation algorithms, Monthly Weather Review.

[19] P. G. Constantine, C. Kent, T. Bui-Thanh, Accelerating MCMC with active subspaces, arXiv preprint arXiv:1510.00024.

[20] B. Calderhead, A general construction for parallelizing Metropolis- Hastings algorithms, Proceedings of the National Academy of Sciences 111 (49) (2014) 17408–17413.

[21] T. Cui, Y. M. Marzouk, K. E. Willcox, Scalable posterior approximations for large-scale Bayesian inverse problems via likelihood-informed parameter and state reduction, Journal of Computational Physics.

[22] S. Banerjee, R. Krahl, F. Durst, C. Zenger, Presentation of anisotropy properties of turbulence, invariants versus eigenvalue approaches, Journal of Turbulence 8 (32) (2007) 1–27.

[23] H. Goldstein, Classical Mechanics, 2nd Edition, Addison-Wesley, 1980, see "The Euler Angles and Euler Angles in Alternate Conventions" in Chapter 4.4.

[24] O. P. Le Maître, O. M. Knio, Spectral methods for uncertainty quantification: with applications to computational fluid dynamics, Springer, 2010.

[25] S. Sakamoto, R. Ghanem, Polynomial chaos decomposition for the simulation of non-Gaussian nonstationary stochastic processes, Journal of engineering mechanics 128 (2) (2002) 190–201.

[26] M. Breuer, N. Peller, C. Rapp, M. Manhart, Flow over periodic hills – numerical and experimental study in a wide range of Reynolds numbers, Computers & Fluids 38 (2) (2009) 433–457.

[27] S. Kullback, Information theory and statistics, Courier Corporation, 1968.

[28] S. Y. Park, A. K. Bera, Maximum entropy autoregressive conditional heteroskedasticity model, Journal of Econometrics 150 (2) (2009) 219–230.

Appendix

5.A Summary of Algorithms of The Physics-Based Approach

1. Decomposition to physically meaningful dimension and expansion of given marginal distributions

   1.1. Perform the baseline RANS simulation to obtain the baseline (mean) Reynolds stress $[\underline{R}]$.

   1.2. Perform the transformation $[\underline{R}] \mapsto (\tilde{\xi}^{rans}, \tilde{\eta}^{rans}, \tilde{k}^{rans}, \tilde{\varphi}_1^{rans}, \tilde{\varphi}_2^{rans}, \tilde{\varphi}_3^{rans})$.

   1.3. Compute Karhunen–Loeve expansion to obtain basis set $\{\phi_\alpha(x)\}_{\alpha=1}^{N_{kl}}$, where N_{kl} is the number of modes retained.

2. Sampling and reconstruction of physical variable fields for Reynolds stresses:

   2.1. Sample six independent coefficient vectors $\{\boldsymbol{\omega}_\beta\}_{\beta=1}^{N}$ for the six discrepancy fields (i.e., $\Delta\xi, \Delta\eta, \Delta\log k, \Delta\varphi_1, \Delta\varphi_2$, and $\Delta\varphi_3$), where N is the sample size.

   2.2. Reconstruct the six discrepancy fields with the six independent coefficient samples $\{\boldsymbol{\omega}_\beta\}_{\beta=1}^{N}$ and Karhunen–Loeve modes. Note that the variance field $\sigma(x)$ is the same for the six random fields.

   2.3. Obtained samples of Reynolds stress field $[\mathbf{R}]$ via mapping $(\xi,\ \eta,\ k,\ \varphi_1,\ \varphi_2,\ \varphi_3) \mapsto [R]$

3. Propagation the Reynolds stress to QoIs via RANS equations

   3.1 Use the obtained sampled Reynolds stress to velocity and other QoIs by solving the RANS equations.

   3.2 Post-process the obtained velocity and QoI samples to obtain statistical moments.

5.B Summary of Algorithms of The RMT Approach

Given the mean Reynolds stress field $[\underline{R}(x)]$ (e.g., from RANS-predicted results) along with the correlation function structure of the random upper triangle matrix field $[\mathbf{L}](x)$, the following procedure is performed:

1. Expansion of given marginal distributions and covariances kernels:

   1.1. Perform the Cholesky factorization of the mean Reynolds stresses $[\underline{R}]$ at each cell as $[\underline{R}] = [\underline{L}_R]^T[\underline{L}_R]$, which yields field $\underline{L}_R(x)$ of upper triangular matrices.

   1.2. Perform Karhunen–Loeve expansion for the kernel function by solving the Fredholm equation to obtain eigenmodes.

1.3. For diagonal terms of matrix [**L**], perform polynomial expansion (PCE) of the Gamma marginal PDF at each cell. PCE Coefficients U_β are obtained from

$$U_\beta = \frac{\langle \mathbf{u}\Psi_\beta \rangle}{\langle \Psi_\beta^2 \rangle} = \frac{1}{\langle \Psi_\beta^2 \rangle} \int_\Omega F_{\mathbf{u}}^{-1}[F_{\mathbf{w}}(w)]\ \Psi_\beta(w)\ p_{\mathbf{w}}(w) dw, \tag{5.13}$$

where $\langle \mathbf{\Psi}_\beta^2 \rangle$ is the variance of i^{th} order polynomial of standard Gaussian random variable $\mathbf{w}$; $F_w(\mathbf{w})$ and $p_{\mathbf{w}}$ are the cumulative distribution function (CDF) and PDF, respectively, of $\mathbf{w}$; Ω is the sample space of $\mathbf{w}$; $F_{\mathbf{u}}$ and $F_{\mathbf{u}}^{-1}$ are the CDF and its inverse, respectively, of random variable $\mathbf{u}$. The index β is from 1 to N_p, and N_p is the number of polynomials retained in the expansion.

2. Sampling and reconstruction of random matrix fields for Reynolds stresses:

2.1. For each element $\mathbf{L}_{ij}$ of the random matrix field [**L**], independently draw N_{kl} sample from the standard Gaussian distribution $\omega_{ij,\alpha}$ where $\alpha = 1, \cdots, N_{kl}$, e.g., with random sampling or Latin hypercube sampling method.

2.2. Synthesize realizations of the off-diagonal terms based on Karhunen–Loeve expansion:

$$\mathbf{w}_{ij}(x) = \sum_{\alpha=1}^{N_{\text{KL}}} \phi_\alpha(x)\ \boldsymbol{\omega}_\alpha \quad \text{with} \quad i < j$$
$$\mathbf{L}_{ij}(x) = \sigma_d \mathbf{w}_{ij}(x)$$

2.3. Synthesize the realizations of the diagonal terms based on Karhunen–Loeve and PCE expansions:

$$\mathbf{u}_i(x) = \sum_{\beta=0}^{N_p} U_\beta(x) \Psi_\beta(\mathbf{w}_{ii}(x))$$

where the Gaussian random field sample $\mathbf{w}_{ii}(x)$ obtained in the previous step is used.

2.4. Synthesize the diagonal terms of matrix [**L**] from $\mathbf{L}_{ii}(x) = \sigma_d \sqrt{2\mathbf{u}_i}$, where $i = 1, 2, 3$.

2.5. Reconstruct random normalized matrix [**G**] from $[\mathbf{G}] = [\mathbf{L}]^T[\mathbf{L}]$ and then reconstruct the Reynolds stress tensor [**R**] from $[\mathbf{R}] = [\underline{L}_R]^T[\mathbf{G}][\underline{L}_R]$.

3. Propagation the Reynolds stress field through the RANS solver to obtain velocities and other QoIs:

3.1 Use the obtained sampled Reynolds stress to velocity and other QoIs by solving the RANS equations.

3.2 Post-process the obtained velocity and QoI samples to obtain statistical moments.

Chapter 6

A Physics Informed Machine Learning Approach for Reconstructing Reynolds Stress Modeling Discrepancies Based on DNS Data

(Accepted by *Physical Review Fluids*, 2017)

J.-X. Wang, J.-L. Wu, H. Xiao
Department of Aerospace and Ocean Engineering, Virgina Tech, Blacksburg, VA, 24061, USA

Abstract

Turbulence modeling is a critical component in numerical simulations of industrial flows based on Reynolds-averaged Navier-Stokes (RANS) equations. However, after decades of efforts in the turbulence modeling community, universally applicable RANS models with predictive capabilities are still lacking. Large discrepancies in the RANS-modeled Reynolds stresses are the main source that limits the predictive accuracy of RANS models. Identifying these discrepancies is of significance to possibly improve the RANS modeling. In this work, we propose a data-driven, physics-informed machine learning approach for reconstructing discrepancies in RANS modeled Reynolds stresses. The discrepancies are formulated as functions of the mean flow features. By using a modern machine learning technique based on random forests, the discrepancy functions are trained by existing DNS databases and then used to predict Reynolds stress discrepancies in different flows where data are not available. The proposed method is evaluated by two classes of flows: (1) fully developed turbulent flows in a square duct at various Reynolds numbers and (2) flows with massive separations. In separated flows, two training flow scenarios of increasing difficulties are considered: (1) the

flow in the same periodic hills geometry yet at a lower Reynolds number, and (2) the flow in a different hill geometry with a similar recirculation zone. Excellent predictive performances were observed in both scenarios, demonstrating the merits of the proposed method.

6.1 Introduction

6.1.1 RANS Models as Workhorse Tool in Industrial CFD

Computational fluid dynamics (CFD) simulations have been widely used in aerospace, mechanical, and chemical industries to support engineering design, analysis, and optimization. Two decades ago when Large Eddy Simulations (LES) started gaining popularity with the increasing availability of computational resources, it was widely expected that LES would gradually displace and eventually replace Reynolds-Averaged Navier-Stokes (RANS) equations in industrial Computational Fluid Dynamics (CFD) work-flows for decades to come. In the past two decades, however, while LES-based methods (including resolved LES, wall-modeled LES, and hybrid LES/RANS methods) did gain widespread applications, and the earlier hope certainly did not diminish, the predicted time when these methods would replace RANS has been significantly delayed. This observation is particularly relevant in light of the recent discussions on the ending of the "Moore's Law era" with transistor sizes approaching their theoretical lower limit [1, 2]. RANS solvers, particularly those based on standard eddy viscosity models (e.g., k–ε [3], k–ω [4, 5], S–A [6], and k–ω–SST [7], are still and will remain the dominant tool for industrial CFD in the near future. This is likely to be true even in mission critical applications such as aircraft design. Interestingly, even the advanced RANS models such as Reynolds stress transport models [8] and Explicit Algebraic Reynolds stress models [9] have not seen much development in the past few decades. These advanced models are computationally more expensive and less robust compared to the standard eddy viscosity RANS models. As such, it is still practically important to further develop the standard RANS models for industrial CFD applications. However, improving the predictive capabilities of these models is critical yet technically challenging.

6.1.2 Progress and Challenges in Data-Driven Turbulence Modeling

While traditional development of turbulence models has focused on incorporating more physics to improve predictive capabilities, an alternative approach is to utilize data. In the past few years, a number of data-driven approaches have been proposed. Researchers have investigated the use of both offline data (i.e., existing DNS data for flows different from that to be predicted [10, 11, 12]) and online data (streamed monitoring data from the flow to be predicted [13, 14, 15]). Dow and Wang [10] used Direct Numerical Simulation (DNS)

data from a plane channel flow to infer the full-field discrepancy in the turbulent viscosity ν_t modeled by the k–ω model. To predict flows in channels with wavy boundaries, they modeled the (log-)discrepancies of ν_t in the new flows as Gaussian random fields, with the discrepancy field inferred above as mean. Duraisamy and co-workers [11, 16] introduced a full-field multiplicative discrepancy term β into the production term of the transport equations of turbulent quantities (e.g., $\tilde{\nu}_t$ in the SA model and ω in the k–ω models). They used DNS data to calibrate and infer uncertainties in the β term. It is expected that the inferred discrepancy field can provide valuable insights to the development of turbulence model and can be used to improve RANS predictions in similar flows. Xiao et al. [13] used sparse velocity measurements (online data) to infer the full-field discrepancies $\Delta\tau_\alpha$ in the RANS-predicted Reynolds stress tensors, or more precisely the physical projections thereof (turbulent kinetic energy, anisotropy, and orientations). Throughout this paper it is understood that τ_α indicates the physical projections and not the individual components of the Reynolds stress tensor. Good performance was demonstrated on several canonical flows including flow past periodic hills, flow in a square duct [13], and flow past a wing–body junction [17].

All three approaches [10, 11, 13] discussed above can be considered starting points toward the same destination: the capability of predictive turbulence modeling by using standard RANS models in conjunction with offline data. To this end, the respective discrepancies terms ($\Delta \log \nu_t$, β, and $\Delta\tau_\alpha$) are expected to be extrapolated to similar yet different flows. These contributions are all relatively recent and much of the research is still on-going. Duraisamy et al. [16, 18] performed *a priori* studies to show the potential universality of their discrepancy term β among a class of similar flows, but their performances in *a posteriori* tests, i.e., using the calibrated discrepancy in one flow to predict another flow, have yet to be demonstrated. Dow and Wang [10] extrapolated the logarithmic discrepancies $\Delta \log \nu_t$ calibrated in the plane channel flow to flows in channel with slightly wavy walls, where velocity predictions were made. Similarly, further pursuing the approach of Xiao et al. [13], Wu et al. [19] showed that the Reynolds stress discrepancy calibrated with sparse velocity data can be extrapolated to flows at Reynolds number more than an order of magnitude higher than that in the calibration case. The extrapolated discrepancy has lead to markedly improved predictions of velocities and other Quantities of Interest (QoIs), showing the potential of the approach in enabling data-driven predictive turbulence modeling. However, an intrinsic limitation in the approach of Wu et al. [19] is that they inferred the functions $f_\alpha^{(x)} : \mathbf{x} \mapsto \Delta\tau_\alpha$, or simply denoted as $\Delta\tau_\alpha(\mathbf{x})$, in the space of *physical coordinates* $\mathbf{x}$. Therefore, strictly speaking they only demonstrated that the discrepancy $\Delta\tau_\alpha$ can be extrapolated to flows in the same geometry at the same location. Consequently, their attempts of extrapolation to the flow in a different geometry (e.g., from a square duct to a rectangular duct) encountered less success. The approach of Dow and Wang [10] would share the same limitation since they built Gaussian random fields indexed by the physical coordinates $\mathbf{x}$.

6.1.3 Motivation of the Proposed Approach

A natural extension that overcomes the key limitation in the calibration–prediction approach of Wu et al. [19] is to build such functions in a space of well-chosen features $\mathbf{q}$ instead of physical coordinates $\mathbf{x}$. Despite its limitations, a key factor in the success of the original approach is that the Reynolds stress discrepancies are formulated on its projections such as the anisotropy parameters (ξ and η) and orientation (φ_i) of the Reynolds stresses and not directly on the individual components. These projections are normalized quantities [19]. We shall retain this merits in the current approach and thus use data to construct functions $\Delta\tau_\alpha(\mathbf{q})$ instead of $\Delta\tau_\alpha(\mathbf{x})$. This extension would allow the calibrated discrepancies to be extrapolated to a much wide range of flows. In other words, the discrepancies of the RANS-predicted Reynolds stresses can be quantitatively explained by the mean flow physics. Hence, these discrepancies are likely to be universal quantities that can be extrapolated from one flow to another, at least among different flows sharing the same characteristics (e.g., separation). As such, discrepancies in Reynolds stress projections are suitable targets to build functions for.

With the function targets identified, two challenges remain: (1) to identify a set of mean flow features based on which the discrepancies functions $\Delta\tau_\alpha(\mathbf{q})$ can be constructed and (2) to choose a suitable method for constructing such functions. Duraisamy and co-workers [18] identified several features and used neural network to construct functions for the multiplicative discrepancy term. Ling and Templeton [12] provided a richer and much more complete set of features in their pioneering work, and they evaluated several machine learning algorithms to predict point-based binary confidence indicators of RANS models [12]. Ling et al. [20] further used machine learning techniques to predict the Reynolds stress anisotropy in jet-in-cross flows. Based on the success demonstrated by Ling and co-workers [12, 20], we will use machine learning to construct the functions $\Delta\tau_\alpha(\mathbf{q})$ in the current work. Specifically, we will examine a class of supervised machine learning techniques, where the objective of the learning is to build a statistical model from data and to make predictions on a response based on one or more inputs [21]. This is in contrast to unsupervised learning, where no response is used in the training or prediction, and the objective is to understand the relationship and structure of the input data. Unsupervised learning will be explored as an alternative approach in future works.

6.1.4 Objective, Scope, and Vision of This Work

The objective of this contribution is to present an approach to predict Reynolds stress modeling discrepancies in new flows by utilizing data from flows with similar characteristics as the prediction flow. This is achieved by training regression functions of Reynolds stress discrepancies with the DNS database from the training flows.

In light of the consensus in the turbulence modeling community that the Reynolds stresses

are the main source of model-form uncertainty in RANS simulations [22, 5, 23], the current work aims to improve the RANS modeled Reynolds stresses. In multi-physics applications the QoIs might well be the Reynolds stresses and/or quantities that directly depend thereon. In these applications the current work is significant by itself in that it would enable the use of standard RANS models in conjunction with an offline database to provide accurate Reynolds stress predictions. Moreover, the improvement of Reynolds stresses enabled by the proposed method is an important step towards a data-driven turbulence modeling framework. However, the Reynolds stresses corrected by the constructed discrepancy function from DNS databases cannot necessarily guarantee to obtain improved mean flow fields. There are a number of challenges associated with propagating the improvement of Reynold stresses through RANS equation to the mean velocity field, which will be addressed in future works.

The rest of this paper is organized as follows. Section 2 introduces the components of the predictive framework, including the choice of regression inputs and responses as well as the machine learning technique used to build the regression function. Section 3 shows the numerical results to demonstrate the merits of the proposed method. Further interpretation of the feature importance and its implications to turbulence model development are discussed in Section 4. Finally, Section 5 concludes the paper.

6.2 Methodology

6.2.1 Problem Statement

The overarching goal of the current and companion works is a physics-informed machine learning (PIML) framework for predictive turbulence modeling. Here, "physics-informed" is to emphasize the attempt of accounting for the physical domain knowledge in every stage of machine learning. The problem targeted by the PIML framework can be formulated as follows: given high-fidelity data (e.g., Reynolds stresses from DNS or resolved LES) from a set $\{\mathcal{T}_i\}_{i=1}^N$ of N training flows, the framework shall allow for using standard RANS turbulence models to predict a new flow $\mathcal{P}$ for which data are not available. The flows $\mathcal{T}_i$ for which high-fidelity simulation data are available are referred to as *training flows*, and the flow $\mathcal{P}$ to be predicted is referred to as *test flow*. The lack of data in test flows is typical in industrial CFD simulations performed to support design and optimization. Furthermore, we assume that the training flows and the test flow have similar complexities and are dominated by the same characteristics such as separation or shock–boundary layer interaction. This scenario is common in the engineering design process, where the test flow is closely related to the training flows. Ultimately, the envisioned machine learning framework will be used in scenarios where the training flows consist of a wide range of elementary and complex flows with various characteristics and the test flow has a subset or all of them. However, the latter scenario is much more challenging and is outside the scope of the current study. Considering the proposed method is a completely new paradigm, we decide to take small steps by starting

from the closely related flows and to achieve the overarching goal gradually.

6.2.2 Summary of Proposed Approach

In the proposed approach we utilize training data to construct functions of the discrepancies (compared to the DNS data) in the RANS-predicted Reynolds stresses and use these functions to predict Reynolds stresses in new flows. The procedure is summarized as follows:

1. Perform baseline RANS simulations on both the training flows and the test flow.
2. Compute the feature vector field $\mathbf{q}(\mathbf{x})$, e.g., pressure gradient and streamline curvature, based on the RANS-predicted mean flow fields for all flows.
3. Compute the discrepancies field $\Delta\tau_\alpha(\mathbf{x})$ in the RANS modeled Reynolds stresses for the training flows based on the high-fidelity data.
4. Construct regression functions $f_\alpha : \mathbf{q} \mapsto \Delta\tau_\alpha$ for the discrepancies based on the training data prepared in Step 3.
5. Compute the Reynolds stress discrepancies for the test flow by querying the regression functions. The Reynolds stresses can subsequently be obtained by correcting the baseline RANS predictions with the evaluated discrepancies.

In machine learning terminology the discrepancies $\Delta\tau_\alpha$ here are referred to as *responses* or *targets*, the feature vector $\mathbf{q}$ as *input*, and the mappings $f_\alpha : \mathbf{q} \mapsto \Delta\tau_\alpha$ as *regression functions*. A regression function f_α maps the input feature vector $\mathbf{q}$ to the response $\Delta\tau_\alpha$, and the term "function" shall be interpreted in a broad sense here. That is, depending on the regression technique used, it can be either deterministic (e.g., for linear regression) or random (e.g., Gaussian process) [21, 25], and it may not even have an explicit form. In the case of random forests regression used in this work [26], the mapping does not have an explicit expression but is determined based on a number of decision trees.

In the procedure described above, after the baseline RANS simulations in Step 1, the input feature fields are computed in Step 2, the training data are prepared in Step 3, and the regression functions are constructed in Step 4. Finally, the regression functions are evaluated to make predictions in Step 5. It is worth noting that in each stage domain knowledge is incorporated, e.g., physical reasoning for identification of input features and consideration of realizability constraints of Reynolds stress in learning-prediction process. Each component is discussed in detail below. The choice of features and responses are presented in Sections 6.2.3 and 6.2.4, respectively, and the machine learning algorithm chosen to build the regression function is introduced in Section 6.2.5.

6.2.3 Choice of Mean Flow Features as Regression Input

As has been pointed out in Section 6.1, mean flow features are better suited as input of the regression function than physical coordinates as they allow the constructed functions to predict flows in different geometries. Ling and Templeton [12] proposed a rich set of twelve features based on clear physical reasoning. The set of features used in the present study mostly follow their work, except that we excluded the feature "vortex stretching" (input 8 in Table II of ref. [12]). This feature is present only in three-dimensional flows, but the test cases presented here are two-dimensional flow. We excluded two additional features related to linear and nonlinear eddy viscosities (features 6 and 12 in ref. [12]). These quantities were specifically chosen for evaluating qualitative confidence indicators of RANS predictions and, in our opinion, are not suitable input for regression functions of Reynolds discrepancies. Finally, experiences in the turbulence modeling communities suggest that mean streamline curvature has important influences on the predictive performance of RANS models [27]. Therefore, curvature is included as an additional feature. The complete list of the mean flow features chosen as regression inputs in this work is summarized in Table 6.1.

In choosing the mean flow features as regression inputs, we have observed a few principles in general. First, the input and thus the obtained regression functions should be Galilean-invariant. Quantities that satisfy this requirement include all scalars and the invariants (e.g., norms) of vectors and tensors. An interesting example is the pressure gradient along streamline (see feature q_4 in Table 6.1). While neither velocity U_k nor pressure gradient dP/dx_k (both being vectors) is Galilean-invariant by itself and thus is not a suitable input, their inner product $U_k \frac{dP}{dx_k}$ is. Second, since the truth of the mean flow fields in the test flows are not available, an input should solely utilize information of the mean flow field produced by the RANS simulations [12]. Therefore, all of the adopted features are based on RANS-predicted pressure P, velocity $\mathbf{U}$, turbulent kinetic energy k, and distance d to the nearest wall. Finally, to facilitate implementation and avoid ambiguity, only local quantities (i.e., cell- or point-based quantities in CFD solvers) of the flow field are used in the formulation of features, with the distance d to nearest wall being a notable exception. This principle is similar to that in choosing variables for developing turbulence models [27].

The interpretation of most feature variables are evident from the brief descriptions given in the table, but a few need further discussions. First, feature q_1 (Q-criterion) is based on the positive second invariant Q of the mean velocity gradient $\nabla\mathbf{U}$, which represents excess rotation rate relative to strain rate [28]. For incompressible flows, it can be computed as $Q = \frac{1}{2}(\|\mathbf{\Omega}\|^2 - \|\mathbf{S}\|^2)$, where $\mathbf{\Omega}$ and $\mathbf{S}$ are rotation rate and strain rate tensors, respectively; $\|\mathbf{\Omega}\| = \sqrt{\mathrm{tr}(\mathbf{\Omega}\mathbf{\Omega}^T)}$ and $\|\mathbf{S}\| = \sqrt{\mathrm{tr}(\mathbf{S}\mathbf{S}^T)}$, with superscript T indicating tensor transpose and tr indicating trace. The Q-criterion is widely used in CFD simulations as a post-processing tool to identify vortex structures for the visualization of flow structures [29]. Second, the wall distance based Reynolds number $Re_d = \sqrt{k}d/\nu$ in q_3 is an indicator to distinguish boundary layers from shear flows. This is an important feature because RANS models behave very

differently in the two types of flows. This quantity is frequently used in wall functions for turbulence models. Third, feature q_7 defines the deviation from orthogonality between the velocity and its gradient [30], which indicates the deviation of the flow from parallel shear flows (e.g., plane channel flows). Since most RANS models are calibrated to yield good performance on parallel shear flows, this deviation is usually correlated well with large discrepancies in RANS predictions. However, since it only accounts for misalignment angle and not the velocity magnitude, in regions with near-zero velocities this quantity becomes the angle formed by two zero-length vectors and is thus mostly noise. Finally, we remark that most of the features in Table 6.1 including the Q-criterion and wall-distance based Reynolds number are familiar to CFD practitioners.

Most of the features presented in Table 6.1 are formulated as ratios of two quantities of the same dimension, either explicitly (q_1, q_5, q_6, q_8, q_9) or implicitly (q_2 and q_3). Hence, they are non-dimensional by construction. Features q_4 and q_7 involve inner product of vectors or tensors, and thus they are normalized by the magnitude of the constituent vectors or tensors. Finally, feature q_{10} (streamline curvature) is normalized by $1/L_c$, where L_c is the characteristics length scale of the mean flow, chosen to be the hill height H (see Fig. 6.6) in the numerical examples.

We followed the procedure of Ling and Templeton [12] to normalize the features. Except for feature q_3, each element q_β in the input vector $\mathbf{q}$ is normalized as:

$$q_\beta = \frac{\hat{q}_\beta}{|\hat{q}_\beta| + |q^*_\beta|} \quad \text{where} \quad \beta = 1, 2, 4, \cdots, 10, \tag{6.1}$$

where the summation on repeated indices is not implied, $\hat{q}_\beta$ are raw values of the features, and q^*_β are the corresponding normalization factors. This normalization scheme limits the numerical range of the inputs within $[-1, 1]$ and thus facilitates the regression. The normalization is not needed for feature q_3 (wall distance based Reynolds number) since it is already in a non-dimensional form and in a limited range $[0, 2]$.

It can be seen that the choices of features and normalization factors heavily rely on physical understanding of the problem (turbulence modeling). That is, in the present data-driven modeling framework, the data are utilized only *after* physical reasoning from the modeler has been applied. This task can be a burden in certain applications. It is worth noting that the recent work of Ling et al. [31] aimed to relieve the modeler from such burdens by using a basis of invariants of tensors relevant in the specific application (e.g., strain rate $\mathbf{S}$ in turbulence modeling). Their work has the potential to systematically construct the input features based on raw physical variables and thus makes data-driven modeling even "smarter".

Table 6.1: Non-dimensional flow features used as input in the regression. The normalized feature q_β is obtained by normalizing the corresponding raw features value $\hat{q}_\beta$ with normalization factor q^*_β according to $q_\beta = \hat{q}_\beta/(|\hat{q}_\beta| + |q^*_\beta|)$ except for $\beta = 3$. Repeated indices imply summation for indices i, j, k, and l but not for β. Notations are as follows: U_i is mean velocity, k is turbulent kinetic energy (TKE), u'_i is fluctuation velocity, ρ is fluid density, ε is the turbulence dissipation rate, $\mathbf{S}$ is the strain rate tensor, $\mathbf{\Omega}$ is the rotation rate tensor, ν is fluid viscosity, d is distance to wall, $\mathbf{\Gamma}$ is unit tangential velocity vector, D denotes material derivative, and L_c is the characteristic length scale of the mean flow. $\|\cdot\|$ and $|\cdot|$ indicate matrix and vector norms, respectively.

feature (q_β)	description	raw feature ($\hat{q}_\beta$)	normalization factor (q^*_β)
q_1	ratio of excess rotation rate to strain rate (Q-criterion)	$\frac{1}{2}(\|\mathbf{\Omega}\|^2 - \|\mathbf{S}\|^2)$	$\|\mathbf{S}\|^2$
q_2	turbulence intensity	k	$\frac{1}{2}U_iU_i$
q_3	wall-distance based Reynolds number	$\min\left(\frac{\sqrt{k}d}{50\nu}, 2\right)$	not applicable[(a)]
q_4	pressure gradient along streamline	$U_k\frac{\partial P}{\partial x_k}$	$\sqrt{\frac{\partial P}{\partial x_j}\frac{\partial P}{\partial x_j}U_iU_i}$
q_5	ratio of turbulent time scale to mean strain time scale	$\frac{k}{\varepsilon}$	$\frac{1}{\|\mathbf{S}\|}$
q_6	ratio of pressure normal stresses to shear stresses	$\sqrt{\frac{\partial P}{\partial x_i}\frac{\partial P}{\partial x_i}}$	$\frac{1}{2}\rho\frac{\partial U_k^2}{\partial x_k}$
q_7	non-orthogonality between velocity and its gradient [30]	$\left\|U_iU_j\frac{\partial U_i}{\partial x_j}\right\|$	$\sqrt{U_lU_l\,U_i\frac{\partial U_i}{\partial x_j}U_k\frac{\partial U_k}{\partial x_j}}$
q_8	ratio of convection to production of TKE	$U_i\frac{dk}{dx_i}$	$\|\overline{u'_ju'_k}S_{jk}\|$
q_9	ratio of total to normal Reynolds stresses	$\|\overline{u'_iu'_j}\|$	k
q_{10}	streamline curvature	$\left\|\frac{D\mathbf{\Gamma}}{Ds}\right\|$ where $\mathbf{\Gamma} \equiv \mathbf{U}/\|\mathbf{U}\|$, $Ds = \|\mathbf{U}\|Dt$	$\frac{1}{L_c}$

Note: (a) Normalization is not necessary as the Reynolds number is non-dimensional.

6.2.4 Representation of Reynolds Stress Discrepancies as Responses

In Section 6.1.3 the Reynolds stress discrepancies $\Delta\tau$ have been identified as the responses for the regression functions. The response quantities should also be based on Galilean invariant quantities due to the same consideration as in the feature choice. As such, individual components of the Reynolds stresses or the discrepancies based thereon are not suitable, but those based on their eigenvalues or invariants are preferred. In turbulence modeling, the Lumley triangle has been widely used for the analysis of turbulence states related to realizability [32]. It is formulated based on the second and third invariants (II and III) of the anisotropy tensor. Recently, Banerjee et al. [33] proposed an improved formulation in which the eigenvalues of the anisotropy tensor are mapped to Barycentric coordinates as opposed to the variants II and III as in the Lumley triangle. An important advantage of their formulation is that the mapping to Barycentric coordinates is linear, which is in contrast to the nonlinear mapping to invariants II and III. Therefore, Barycentric coordinate provides a non-distorted visual representation of anisotropy and is easier to impose realizability constraints. The formulation of discrepancy starts with the eigen-decomposition of the Reynolds stress anisotropy tensor $\mathbf{A}$:

$$\boldsymbol{\tau} = 2k\left(\frac{1}{3}\mathbf{I} + \mathbf{A}\right) = 2k\left(\frac{1}{3}\mathbf{I} + \mathbf{V}\Lambda\mathbf{V}^T\right) \tag{6.2}$$

where k is the turbulent kinetic energy, which indicates the magnitude of $\boldsymbol{\tau}$; $\mathbf{I}$ is the second order identity tensor; $\mathbf{V} = [\mathbf{v}_1, \mathbf{v}_2, \mathbf{v}_3]$ and $\Lambda = \mathrm{diag}[\lambda_1, \lambda_2, \lambda_3]$ with $\lambda_1 + \lambda_2 + \lambda_3 = 0$ are the orthonormal eigenvectors and eigenvalues of $\mathbf{A}$, respectively, indicating its shape and orientation.

In the Barycentric triangle, the eigenvalues λ_1, λ_2, and λ_3 are mapped to the Barycentric coordinates (C_1, C_2, C_3) as follows:

$$C_1 = \lambda_1 - \lambda_2 \tag{6.3a}$$
$$C_2 = 2(\lambda_2 - \lambda_3) \tag{6.3b}$$
$$C_3 = 3\lambda_3 + 1 \tag{6.3c}$$

with $C_1 + C_2 + C_3 = 1$. As shown in Fig. 6.1, the Barycentric coordinates of a point indicate the portion of areas of three sub-triangles formed by the point and with edges of Barycentric triangle. For example, a point located on the top vertex corresponds to $C_3 = 1$ while a point located on the bottom edge has $C_3 = 0$. Similar to the Lumley triangle, all realizable turbulences are enclosed in the Barycentric triangle (or on its edges) and have positive Barycentric coordinates C_1, C_2, and C_3. The Barycentric triangle has been used by Emory et al. [34] as a mechanism to impose realizability of Reynolds stresses in estimating uncertainties in RANS simulations.

Placing the triangle in a Cartesian coordinate system $\boldsymbol{\xi} \equiv (\xi, \eta)$, the location of any point within the triangle is a convex combination of those of the three vertices, i.e.,

$$\boldsymbol{\xi} = \boldsymbol{\xi}_{1c}C_1 + \boldsymbol{\xi}_{2c}C_2 + \boldsymbol{\xi}_{3c}C_3 \tag{6.4}$$

where $\boldsymbol{\xi}_{1c}$, $\boldsymbol{\xi}_{2c}$, and $\boldsymbol{\xi}_{3c}$ denote coordinates of the three vertices of the triangle. An advantage of representing the anisotropy of Reynolds stress in the Barycentric coordinates is that it has a clear physical interpretation, i.e., the dimensionality of the turbulence state [35]. Typically, the standard-RANS-predicted Reynolds stress at a near wall location is located close to the isotropic, three-component state (vertex 3C-I) in the Barycentric triangle, while the truth is near the two-component limiting states (bottom edge). Moreover, the spatial variations from the near-wall region to the shear flow region are indicated as arrows in Fig. 6.1. It is clear that the trend of spatial variation predicted by a standard RANS model is opposite to that of the truth.

The three mutually orthogonal, unit-length eigenvectors $\mathbf{v}_1$, $\mathbf{v}_2$, and $\mathbf{v}_3$ indicate the orientation of the anisotropy tensor. They can be considered a rigid body and thus its orientation has three degrees of freedom, although they have nine elements in total. We use the Euler angle with the z–x'–z'' convention to parameterize the orientation following the convention in rigid body dynamics [36]. That is, if a local coordinate system x–y–z spanned by the three eigenvectors of $\mathbf{V}$ was initially aligned with the global coordinate system (X–Y–Z), the current configuration could be obtained by the following three consecutive intrinsic rotations about the axes of the local coordinate system: (1) a rotation about the z axis by angle φ_1, (2) a rotation about the x axis by φ_2, and (3) another rotation about its z axis by φ_3. The local coordinate axes usually change orientations after each rotation.

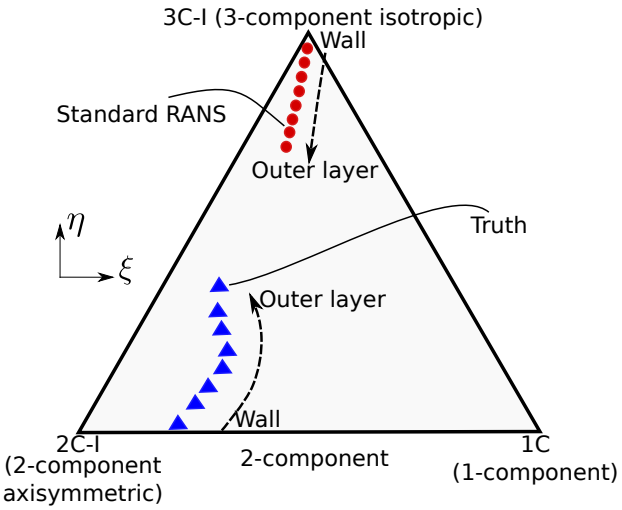

Figure 6.1: The Barycentric triangle that encloses all physically realizable states of Reynolds stress [33, 35]. The position within the Barycentric triangle represents the anisotropy state of the Reynolds stress. Typical mapped locations of near wall turbulence states are indicated with prediction from standard RANS models near the isotropic state (vertex 3C-I) and the turth near the bottom edge (2C-I). The typical RANS-predicted trends of spatial variation from the wall to shear flow and the corresponding truth are indicated with arrows.

In summary, the Reynolds stress tensor is projected to six physically interpretable, Galilean

invariant quantities representing the magnitude (k), shape (ξ, η), and orientation (φ_1, φ_2, φ_3). They are collectively denoted as τ_α. The truths of these quantities can be written as baseline RANS predictions corrected by the corresponding discrepancy terms, i.e.,

$$\log_2 k = \log_2 \tilde{k}^{rans} + \Delta \log_2 k \tag{6.5a}$$

$$\xi = \tilde{\xi}^{rans} + \Delta\xi \tag{6.5b}$$

$$\eta = \tilde{\eta}^{rans} + \Delta\eta \tag{6.5c}$$

$$\varphi_i = \tilde{\varphi_i}^{rans} + \Delta\varphi_i, \text{ for } i = 1, 2, 3. \tag{6.5d}$$

The discrepancies ($\Delta \log_2 k$, $\Delta\xi$, $\Delta\eta$, $\Delta\varphi_1$, $\Delta\varphi_2$, $\Delta\varphi_3$, denoted as $\Delta\tau_\alpha$ with $\alpha = 1, 2, \cdots, 6$) in the six projections of the Reynolds stress tensor are responses of the regression functions. We utilize data consisting of pairs of $(\mathbf{q}, \Delta\tau_\alpha)$ from training flow(s) to construct the functions $f_\alpha : \mathbf{q} \mapsto \Delta\tau_\alpha$. It is assumed that the discrepancies in six quantities $\Delta\tau_\alpha$ are independent, and thus separate functions are built for each of them. This simplification is along the same lines as that made in previous works [37].

6.2.5 Random Forests for Building Regression Functions

With the input (mean flow features $\mathbf{q}$) and responses (Reynolds stress discrepancies $\Delta\tau_\alpha$) identified above, a method is needed to construct regression functions from training data and to make predictions based on these functions. Supervised machine learning consists of a wide variety of such methods including K-nearest neighbors [38], linear regression and its variants (e.g., Lasso) [39], Gaussian processes [25], tree-based methods (decision trees, random forests, bagging) [26], neural networks [40], and support vector machine [41], among others. A major consideration in choosing the regression method is the high dimensionality of the feature space, which is typically ten or higher in our application. The curse of dimensionality makes such methods as K-nearest neighbors, linear regression, and Gaussian processes not suitable. Secondary considerations, which we believe are also important for turbulence modeling applications, are the capability to provide predictions with quantified uncertainties as well as physical insights (e.g., on the importance of each of the features and their interactions). After evaluating a number of existing machine learning techniques in light of these criteria, we identified *random forests* [26] as the optimal approach for our purposes, which is an ensemble learning technique based on decision trees.

In simple decision tree learning, a tree-like model is built to predict the response variable by learning simple if-then-else decision rules from the training data. Decision trees have the advantage of being easy to interpret (e.g., via visualization) and implement. They are also computationally cheap. However, they tend to overfit the data and lack robustness. That is, a small change in the training data can result in large changes in the built model and its predictions. Random forests learning is an ensemble learning technique proposed by Ho [42] and Briemann [43, 26] that overcomes these shortcomings of simple decision trees. Since

these techniques are generally not familiar to readers in the fluid dynamics community, here we use an illustrative example in the context of turbulence modeling to explain the algorithm.

A simple decision tree model is illustrated in Fig. 6.2. For clarity we consider an input with only two features: pressure gradient dp/ds (normalized and projected to the streamline tangential) and wall distance based Reynolds number $Re_d = C_\mu^{1/4} d\sqrt{k}/\nu$, as defined in Table 6.1. It can be also interpreted as wall distance in viscous unit. The response is the discrepancy $\Delta\eta$ of the vertical coordinate in the Barycentric triangle of the RANS-predicted Reynolds stress (see Fig. 6.1). During the training process, the feature space is *successively* divided into a number of boxes (leafs) based on the training data (shown as points in the dp/ds–Re_d plane in Fig. 6.2a). In the simplest decision tree model used for regression, the feature space is stratified with the objective of minimizing the total in-leaf variances of the responses at each step, a strategy that is referred to as greedy algorithm. After the stratification, a constant prediction model is built on each leaf. When predicting the response $\Delta\eta$ for a given feature vector $\mathbf{q}$, the constructed tree model in Fig. 6.2b is traversed to identify the leaf where $\mathbf{q}$ is located, and the mean response on the leaf is taken as the prediction $\Delta\eta(\mathbf{q})$.

The tree model has a clear physical interpretation in the context of turbulence modeling. For example, it is well known that a standard isotropic eddy viscosity model has the largest discrepancy when predicting anisotropy in the viscous sublayer ($Re_d \leq 5$). This is because the truth is located on the bottom, corresponding to a combination of one- or two-component turbulence, while a typical isotropic eddy viscosity model would predict an isotropic state located on the top vertex (see Fig. 6.1). In contrast, far away from the wall within the outer layer ($Re_d > 50$), the RANS-predicted anisotropy is rather satisfactory. Therefore, the first two branches divide the space to three regions based on the feature Re_d: outer layer (region 1) , viscous sublayer (region 2), and buffer layer (regions 3 and 4). In the buffer layer the pressure gradient plays a more important role than in the outer and viscous layers. Larger pressure gradients correspond to larger discrepancies, which can be explained by the fact that favorable pressure gradients (negative dp/ds values) tend to thicken the viscous sublayer [44], which leads to larger discrepancies in η. Therefore, a further division splits the buffer layer states to two regions in the feature space, i.e., those with strong (region 3) and mild (region 4) pressure gradients.

A simple regression tree model described above tends to overfit for high dimensional input space, i.e., yielding models that explain the training data very well but predict poorly for unseen data. In general the decision trees do not have the same level of predictive accuracy as other modern regression methods. However, by aggregating a large number of trees (ideally with minimum correlation), the predictive performance can be significantly improved and, the overfitting can be largely avoided. In random forests an ensemble of trees is built with bootstrap samples (i.e., sampling with replacement) drawn from the training data [21]. Moreover, when building each tree, it utilizes only a subset of $M \leq N_q$ randomly chosen features among the N_q features, which reduces the correlation among the trees in the ensemble

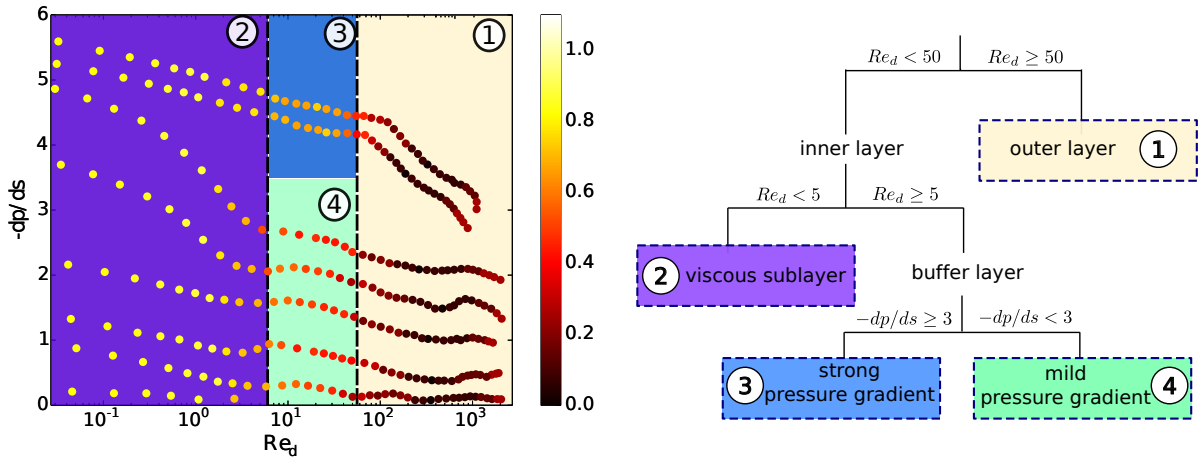

(a) feature space stratification (b) regression tree

Figure 6.2: Schematic of a simple regression tree in a two-dimensional feature space (pressure gradient along streamline dp/ds and wall-distance based Reynolds number Re_d), showing (a) the stratification of feature space and (b) the corresponding regression tree built from the training data. The response is the discrepancy $\Delta\eta$ in the Barycentric triangle of the RANS-predicted Reynolds stress. When predicting the discrepancy for a given feature vector $\tilde{\mathbf{q}}$, the tree model in (b) is traversed to identify the leaf, and the mean of the training data is taken as the prediction $\Delta\eta(\tilde{\mathbf{q}})$.

and thus decreases the bias of the ensemble prediction.

Random forest regression is a modern machine learning method with predictive performance comparable to other state-of-the-art techniques [39]. In decision tree models the maximum depth of trees must be limited (e.g., by pruning the branches far from the root) to ensure a sufficient number of training point (e.g., 5) on each node. In contrast, in random forests, one can build each tree to its maximum depth by successive splitting the nodes until only one training data point remains on each leaf. While each individual tree built in this manner may suffer from overfitting and has large prediction variances, the use of ensemble largely avoids both problems. Moreover, random forest regression is simple to use with only two free parameters, i.e., the number N_{rf} of trees in the ensemble and the number M of selected features. In this work we used an ensemble of $N_{rf} = 100$ trees and the a subset of features (i.e., $M = 6$) to build each tree. As a standard practice in statistical modeling, we performed cross-validations to optimize these parameters and performed sensitivity analysis to ensure that the predictions are not sensitive to the parameter choices.

6.3 Numerical Results

Almost all industrial flows involve some characteristics (e.g., strong pressure gradient, streamline curvature, and separation) that break the equilibrium assumption of RANS model. Therefore, we have these challenges in mind when developing the data-driven approach. In this study, we focus on the cases where training and test flows have similar characteristics. Specifically, we evaluate the proposed method on two classes of flows: (1) fully developed turbulent flows in a square duct at various Reynolds numbers and (2) flows with massive separations. The flow in a square duct at Reynolds number $Re = 3500$ and the flow in a channel with periodic hills at Reynolds number $Re = 10595$ are chosen as the prediction (test) flows for the respective flow classes. The square duct flow has an in-plane secondary flow pattern induced by the normal stress imbalance, while the periodic-hill flow features a recirculation bubble, non-parallel shear layer and mean flow curvature. All these characteristics are known to pose challenges for RANS based turbulence models, and thus large model-form discrepancies exist in the RANS-modeled Reynolds stresses. In the two test flows, the relative importance of Reynolds stress projections to the mean flow prediction are different. The Reynolds stress anisotropy plays an important role in obtaining the accurate secondary mean motion in the duct flow [45]. In contrast, the anisotropy is less important to predict the mean flow in the periodic-hill case, where the turbulent shear stress component is more essential to obtain an accurate mean velocity field [46]. Therefore, we use these two types of flows to highlight the improvements in the different Reynolds stress components that are important for the predictions of QoIs in the respective flow classes. In both cases, all RANS simulations are performed in an open-source CFD platform, OpenFOAM, using a built-in incompressible flow solver `simpleFoam` [47]. Mesh convergence studies have been performed.

6.3.1 Turbulent Flows In a Square Duct

Case Setup

The fully developed turbulent flow in a square duct is a challenging case for RANS-based turbulence models, since the secondary mean motion cannot be captured by linear eddy viscosity models (e.g., k–ε, k–ω), and even the Reynolds stress transport models (RSTM) cannot predict it well [46]. In this test, we aim to improve the RANS-modeled Reynolds stresses of the duct flow at Reynold number $Re = 3500$ by using the proposed PIML approach. The training data are obtained from DNS simulations [48] of the duct flows in the same geometry but at lower Reynolds numbers $Re = 2200, 2600$ and 2900. The DNS data of the prediction flow ($Re = 3500$) are reserved for comparison and are not used for training. The geometry of this flow case is shown in Fig. 6.3. The Reynolds number is based on the edge length D of the square duct and the bulk velocity U_b. All lengths presented below are normalized by $D/2$.

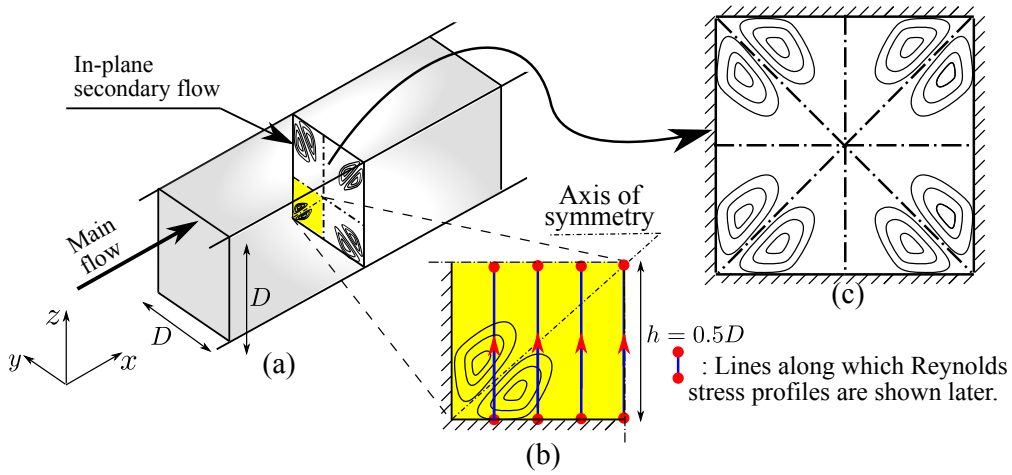

Figure 6.3: Domain shape for the flow in a square duct. The x coordinate represents the streamwise direction. Secondary flows induced by Reynolds stress imbalance exist in the y–z plane. Panel (b) shows that the computational domain covers a quarter of the cross-section of the physical domain. This is due to the symmetry of the mean flow in both y and z directions as shown in panel (c).

The baseline RANS simulations are performed for all training and test flows. The purpose is twofold: to obtain the mean flow feature fields $\mathbf{q}(\mathbf{x})$ as inputs and to obtain the discrepancies of Reynolds stress by comparing with the DNS data. To enable the comparison, the high-fidelity data are interpolated onto the mesh of RANS simulation. The Launder-Gibson RSTM [49] is adopted to perform the baseline simulations, since all the linear eddy viscosity models are not able to capture the mean flow features of the secondary motions. The y^+ of the first cell center is kept less than 1 and thus no wall model is applied. As indicated in Fig. 6.3, only one quadrant of the physical domain is simulated owing to the symmetry of the mean flow with respect to the centerlines along y- and z-axes. No-slip boundary condition is applied on the walls, and symmetry boundary condition is applied on the symmetry planes.

Prediction Results

We first investigate the prediction performance on the Reynolds stress anisotropy tensor, since its accuracy is important to capture the secondary flow. Figure 6.4 shows PIML-corrected anisotropy in Barycentric triangle compared with baseline and DNS results. The comparisons are performed on two representative lines at $y/H = 0.25$ and 0.75 on the in-plane cross section (Fig. 6.3b). The two lines are indicated in the insets on the upper left corner of each panel. The arrows denote the order of sample points plotted in the triangle, which is from the bottom wall to the outer layer. The general trends of spatial variations of the DNS Reynolds stress anisotropies are similar on both lines. That is, from the wall to the outer layer, the Reynolds stress starts from the two-component limiting states (bottom edge

of the triangle) toward three-component anisotropic states (middle area of the triangle). This trend is captured by the baseline RSTM to some extent, especially in the regions away from the wall. However, significant discrepancies still can be observed in the near-wall region. Very close to the wall, the DNS Reynolds stress is nearly the two-component limiting state. This is because the velocity fluctuations in the wall-normal direction are suppressed by the blocking of the bottom wall. Moreover, before approaching three-component anisotropic states, the DNS-predicted anisotropy first moves toward the one-component state (1C) as away from the wall. In contrast, the RANS-predicted anisotropy near the wall is closer to

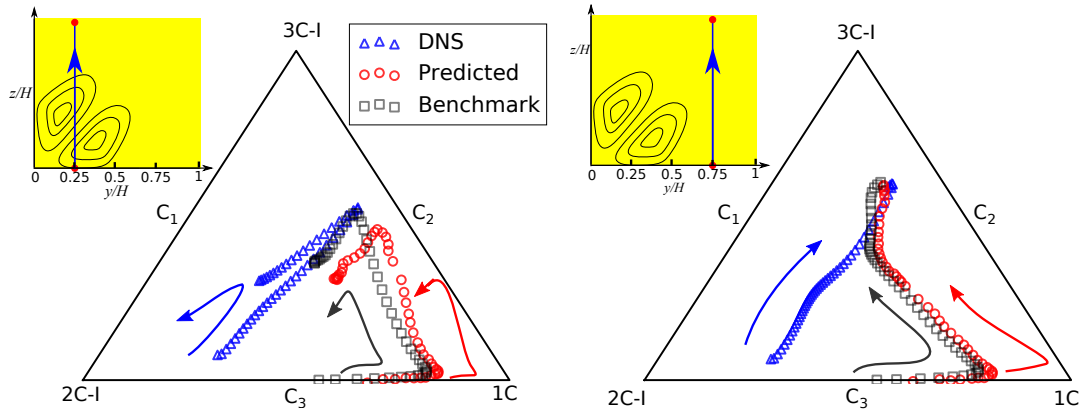

(a) $y/H = 0.25$ (b) $y/H = 0.75$

Figure 6.4: Barycentric map of the predicted Reynolds stress anisotropy for the test flow ($Re = 3500$), learned from the training flows ($Re = 2200, 2600$, and 2900) The prediction results on two streamwise locations at $y/H = 0.25$ and 0.75 are compared with the corresponding baseline (RSTM) and DNS results in panels (a) and (b), respectively.

the two-component isotropic state (2C-I), and it approaches toward the three-component anisotropic state directly. Therefore, in the near-wall region there are large discrepancies between the RANS predicted Reynolds stress anisotropy and the DNS result, particularly in the horizontal coordinate ξ. By correcting the baseline RSTM results with the trained discrepancy function, the predicted anisotropy of Reynolds stress is significantly improved. For both lines, the predicted anisotropy (circles) agrees well with the DNS results (squares). Especially on the line $y/H = 0.75$, the PIML-predicted anisotropy is almost identical to the DNS data.

Significant improvement of the PIML-predicted anisotropy can be seen from the Barycentric maps shown in Fig. 6.4. Similar improvements have also been demonstrated in the other physical projections (TKE and orientations) of the PIML-corrected Reynolds stresses. Therefore, it is expected that the Reynolds stress tensor components should be also improved over the RSTM baseline. In the six tensor components, two normal stress components τ_{yy} and τ_{zz} are among the most important ones to the mean velocity field since the normal stress imbalance $(\tau_{yy} - \tau_{zz})$ is the driving force of the secondary flow [45]. Figures 6.5a and 6.5b

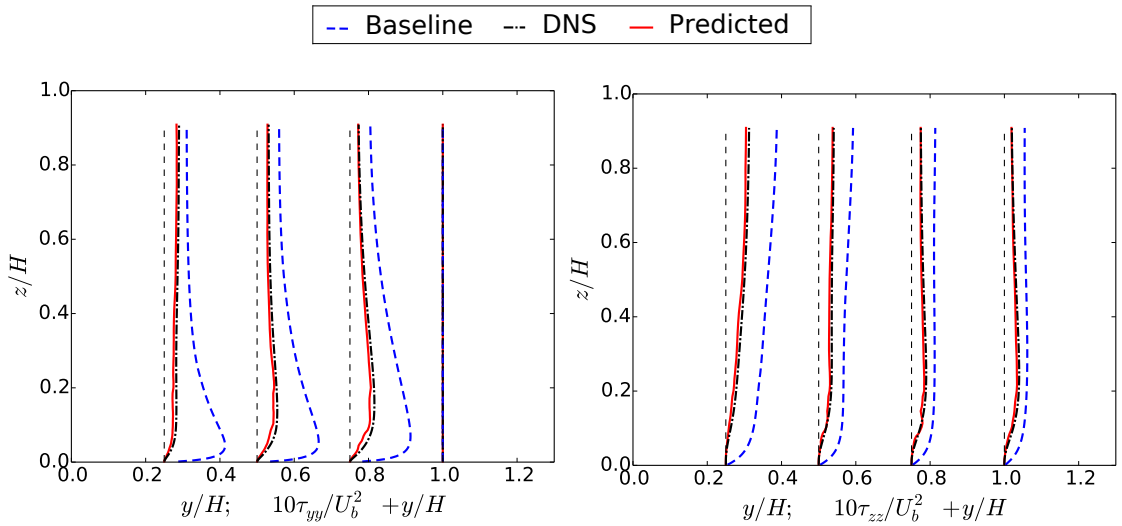

(a) τ_{yy} (b) τ_{zz}

Figure 6.5: Profiles of normal components (a) τ_{yy} and (b) τ_{zz} of corrected Reynolds stress with the discrepancy model. The profiles are shown at four streamwise locations $y/H = 0.25, 0.5, 0.75$, and 1. Corresponding DNS and baseline (RSTM) results are also plotted for comparison.

show the profiles of normal components τ_{yy} and τ_{zz} of the Reynolds stress reconstructed from the PIML-corrected physical projections. Corresponding baseline (RSTM) and DNS results are also plotted for comparison. Both τ_{yy} and τ_{zz} are overestimated by the RSTM over the entire domain. The discrepancy of the RSTM-predicted τ_{yy} is large near the wall and decreases when moving away from the wall. In contrast, τ_{zz} is significantly overestimated far from the wall but the discrepancy decreases toward the wall. As a results, the RSTM-predicted normal stress imbalance is pronouncedly inaccurate, which leads to unreliable secondary mean flow motion. As expected, the PIML predictions nearly overlap with the DNS results for both τ_{yy} and τ_{zz} and show considerable improvements over the RSTM baseline. In fact, the improvements are observed in all the tensor components, which are omitted here for brevity. The results shown above demonstrate excellent performance of the proposed PIML framework by using RSTM as the baseline.

6.3.2 Turbulent Flows With Massive Separations

Case Setup

The turbulent flow in a channel with periodic hills is another challenging case for RANS models due to the massive flow separations in leeward of the hill. Here, we examine two training scenarios with increasing difficulty levels. In the first scenario the training flows

have the same geometry as the test (prediction) flow but are different in Reynolds numbers. In the second scenario the training flows differ from the prediction case not only in Reynolds numbers but also in geometry.

Table 6.2: Database of training flows to predict flow past periodic hills at $Re = 10595$. The Reynolds numbers are defined based on the bulk velocity U_b at the narrowest cross-section in the flow and the crest/step height H.

Training flow scenario	Training flow & symbol	High fidelity data
Scenario I	Periodic hills, Re = 1400 (PH1400)	DNS by Breuer et al. [50]
	Periodic hills, Re = 5600 (PH5600)	DNS by Breuer et al. [50]
Scenario II	Wavy channel, Re = 360 (WC360)	DNS by Maaß et al. [51]
	Curved backward facing step, Re = 13200 (CS13200)	LES by Bentaleb et al. [52]

Four training flows with DNS/LES data to build random forest regressors are summarized in Table 6.2. In the first scenario two flows PH1400 and PH5600 are used for training, both of which are flows over periodic hills (same in geometry) at $Re = 1400$ and $Re = 5600$ (different in Reynolds numbers), respectively. For the second scenario, the training data are obtained from two different flows: one in a channel with a wavy bottom wall at $Re = 360$ and one over a curved backward facing step at $Re = 13200$, indicated as flows WC360 and CS13200, respectively.

A schematic of the flow geometry and RANS-predicted velocity contour for each case are presented in Fig. 6.6. The dimensions of each case are normalized with the respective hill heights H. Although the geometries of the training flows are different, all three flows share a similar characteristic as the test flow, i.e., separation on the leeward side of the hill or step. However, the separation bubbles are different in sizes and shapes. The flow over periodic hills has a stronger separation compared to the other two due to the steeper slope of the hill. Relatively mild separation can be observed in the flow over the wavy channel. For all cases, both high-fidelity data and RANS-predicted results are available. The high-fidelity data are obtained from DNS or resolved LES simulations, which have been reported in literature (see references in Table. 6.2). The DNS data for flows PH1400 and PH5600 are only available on vertical lines at eight streamwise locations $x/H = 1, 2, \cdots, 8$. On the other hand, full-field high-fidelity results are available for flows WC360 and CS13200, but only the lower part of the channel is adequately resolved. Since the separated flow is of interest in this study, only the data in the separation region (i.e., region below $y/H = 1.2$) are included.

In this test, the performance of the proposed PIML framework is evaluated on standard RANS models. Specifically, the baseline RANS predictions are obtained by using the two-

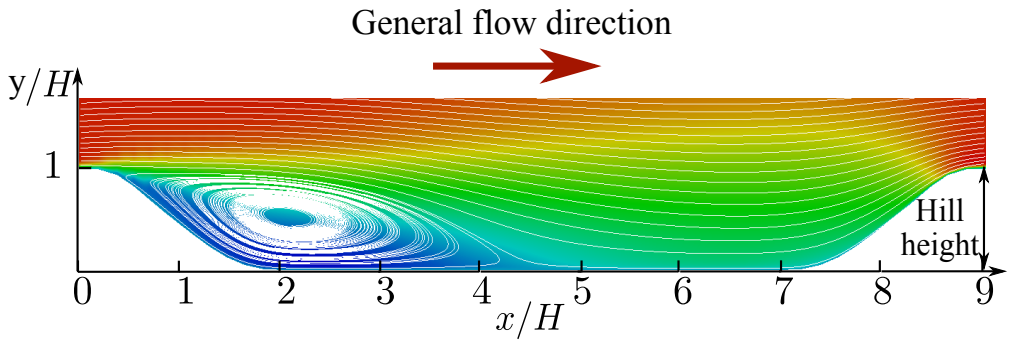

(a) Periodic hills (Re = 1400 and 5600, results from latter are shown)

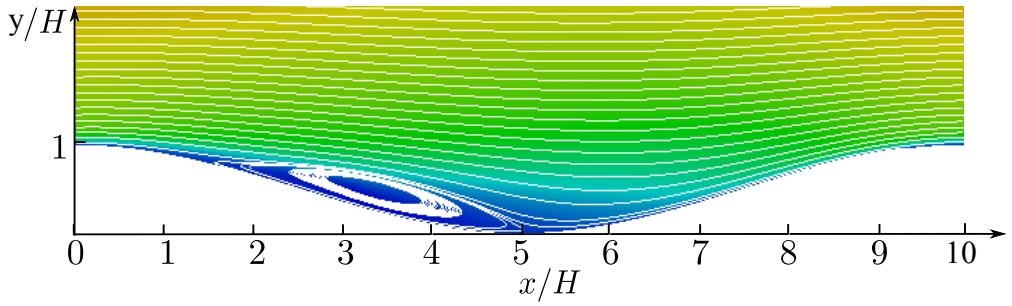

(b) Wavy channel (Re = 360)

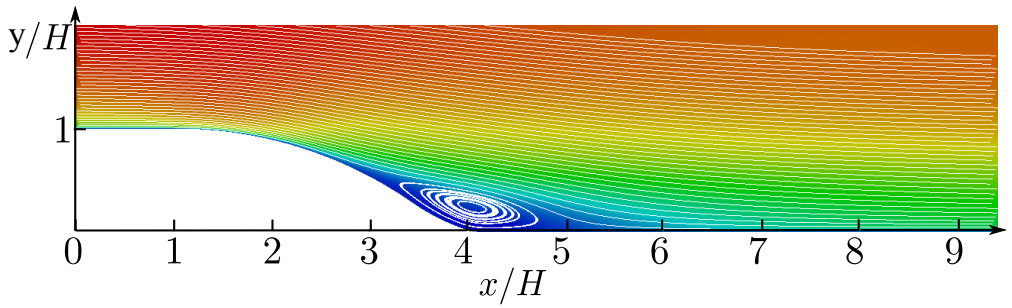

(c) Curved backward facing step (Re = 13200)

Figure 6.6: Computational domain and velocity field of each case in the training flow database. The velocity contours and streamlines are obtained from the baseline RANS simulations. The dimensions of each case are normalized with the respective hill heights H. Note that periodic boundary conditions are applied on the flows in panels (a) and (b) in steamwise direction, but not for the flow in panel (c).

equation Launder-Sharma k–ε model [3]. The reason for choosing standard turbulence models here is because of two considerations. First, the standard RANS models are the dominant tools for industrial CFD applications, while other sophisticated RANS models have been rarely used. Therefore, it is more significant to improve the widely used standard RANS models. Second, we understand that improvement of the Reynolds stresses starting from a standard RANS model is challenging. Nonetheless, this challenging scenario also can better explore the capability of machine learning approach.

Prediction Results

The functional forms of discrepancies in the six physical projections of Reynolds stress are learned from the training flows as mentioned in Section 6.3.2 and are used to correct the RANS-predicted Reynolds stress field of the test flow (PH10595). However, since the baseline RANS model used in this case is the standard eddy viscosity model, the Reynolds stress anisotropy cannot be accurately predicted. Therefore, the baseline RANS-predicted anisotropy is unphysical and is significantly different from the DNS result (see Fig. 6.1). Nonetheless, after the correction by using the discrepancy function learned from the training flows, the anisotropy of the test flow shows an excellent agreement with the DNS results [53]. The improvements are observed in the both training scenarios I and II, demonstrating that the discrepancy function even in the standard RANS-predicted anisotropy does exist and can be learned from the closely related flows based on the mean flow features $\mathbf{q}$. As mentioned above, in the periodic-hill flow, the correctness of Reynolds stress anisotropy is of little consequence to the prediction of the mean velocity, and the correct shear stress component and magnitude of the Reynolds stress are most important to obtain an accurate mean flow field. Therefore, the anisotropy prediction results are omitted here, and only the turbulence kinetic energy (TKE) and shear stress component of the PIML-corrected Reynolds stress are presented and discussed in detail.

The comparison of the TKE profiles of the baseline, DNS, and PIML-predicted results in the training scenario I are shown in Fig. 6.7. The TKE predicted by the baseline RANS model has notable discrepancies compared to the DNS result, particularly in the region with non-parallel free shear flow ($y/H = 0.8$ to 1.5). The poor performance of RANS model in such region is typical in these flows [13]. The RANS model underestimates the turbulence intensity along the free shear at $y/H = 1$, especially near the leeward side of the hill ($x/H = 1$ to 2). In the upper channel ($y/H = 1.5$ to 2.5), the DNS TKE is slightly smaller than the baseline RANS prediction. The profiles of TKE corrected by the PIML-predicted discrepancy $\Delta \log_2 k$ are significantly improved. The peaks along the streamwise free shear in the DNS profiles are well captured in the corrected results with the random forest prediction. It can be seen that the predicted TKE profiles (solid lines) nearly overlap with the DNS results (dashed lines). This clearly indicates that the TKE discrepancies can be learned from the data of the training flows.

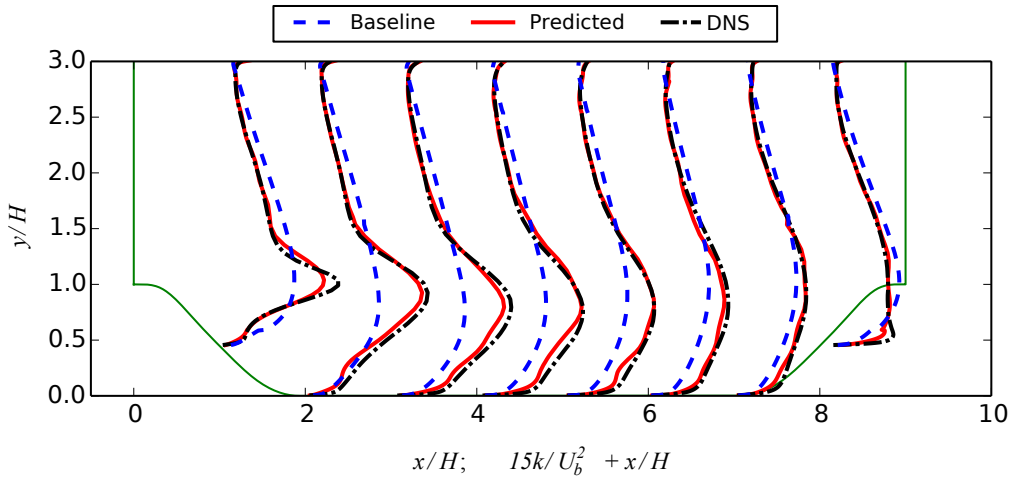

Figure 6.7: Magnitude (turbulence kinetic energy) of the corrected Reynolds stress for the test flow (PH10595) learned from cases with same geometry but at different Reynold numbers (PH1400 and PH5600). The profiles are shown at eight streamwise locations $x/H = 1, 2, \cdots, 8$. Corresponding baseline and DNS results are also plotted for comparison. The hill profile is vertically exaggerated by a factor of 1.3.

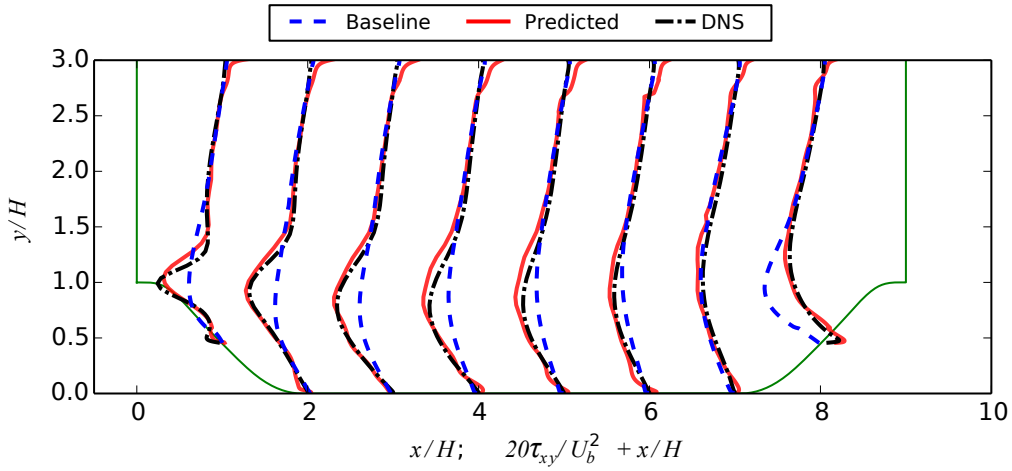

Figure 6.8: Predicted turbulence shear stress for the test flow (PH10595) learned from the flows with the same geometry but at different Reynold numbers (PH1400 and PH5600). The profiles are shown at eight streamwise locations $x/H = 1, 2, \cdots, 8$. Corresponding baseline and DNS results are also plotted for comparison. The hill profile is vertically exaggerated by a factor of 1.3.

It is also of interest to investigate the tensor components τ_{ij} of Reynolds stress, which are more relevant for predicting velocities and other QoIs of the flow fields. For the plane shear flows, the turbulent shear stress τ_{xy} is important to predict the velocity field. Figure 6.8 compares the turbulence shear component τ_{xy} of predicted Reynolds stress with the DNS. As expected, significant improvements are observed compared to the baseline results, which underestimate the peak of τ_{xy} on the leeward hill side but overestimate it on the windward hill side. As shown in Fig. 6.8, the profiles of predicted τ_{xy} agree well with the DNS results.

The results above demonstrate that the discrepancy function of Reynolds stress in its physical projections (i.e., magnitude, shape, and orientation) trained from the flows at Re = 2800 and 5600 can be used to predict the Reynolds stress field of the flow at Re = 10595. Significant improvements are observed in the predicted Reynolds stress compared to the baseline RANS results. Although in this scenario the training and test flows are quite similar (with the same geometry), and the success of extrapolation has been demonstrated in physical space by Wu et al. [19], it should not be taken for granted that the accurate prediction is also guaranteed in feature space. Since the regressions are performed in the ten-dimensional feature space and there is no direct reference to the physical coordinate, the success is not trivially expected *a priori*.

We investigate a more challenging scenario where the training flows have different geometries from the prediction case. This scenario is also more realistic in the context of using RANS simulation to support engineering design and analysis. Specifically, the data are more likely to be available for a few flows with specific Reynolds numbers and geometries, but predictions are needed for the similar flows yet at different Reynolds numbers and with modified geometries.

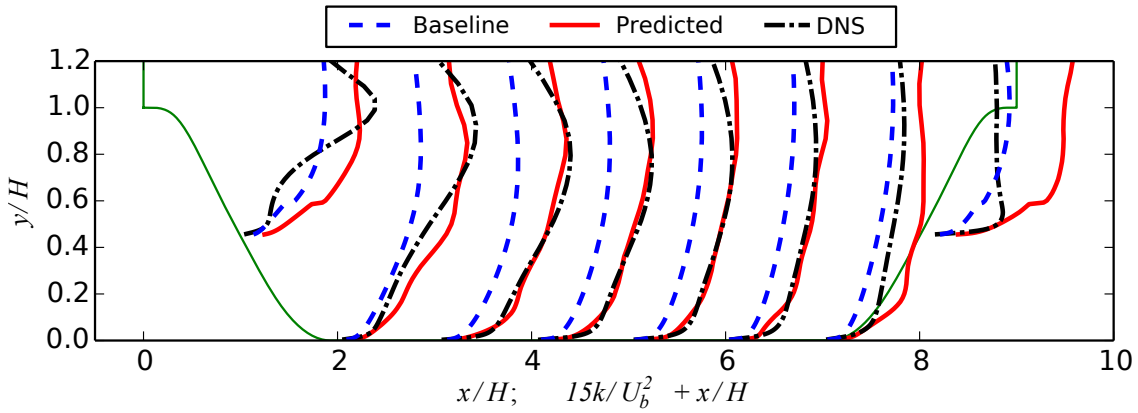

Figure 6.9: Magnitude (turbulence kinetic energy) of the corrected Reynolds stress for the test flow (PH10595) learned from cases with different geometries and at different Reynold numbers (WC360 and CS13200). The profiles are shown at eight streamwise locations $x/H = 1, 2, \cdots, 8$. Corresponding baseline and DNS results are also plotted for comparison. The hill profile is vertically exaggerated by a factor of 2.4.

The comparison of the TKE profiles on eight lines is shown in Fig. 6.9. Note that only the domain below $y/H = 1.2$ is investigated due to the lack of reliable high-fidelity training data in the upper channel region. This inadequacy of data quality can be exacerbated when the Reynolds stress is decomposed to its physical projections. Moreover, the flow separation is the phenomenon of concern in this study, and thus we only focus on the recirculation region. In Fig. 6.9, the random forest predicted TKE (solid lines) is significantly improved over the baseline results (dotted lines) and better agrees with the DNS profiles (dash-dotted lines). The agreement is particularly good in the region from the center of recirculation bubble ($x/H = 2$) to the beginning of flow contraction ($x/H = 6$). Nonetheless, the PIML-predicted TKE does not show any improvement and even deteriorates compared to the baseline results near the windward side of the hill ($x/H > 7$), where the flow starts to be contracted. As shown in Fig. 6.9, the predicted TKE is markedly overestimated at $x/H = 8$. This is because the flow features in the contraction region ($x/H > 7$) are not supported in the training set, since the contracted flow does not exist in the training flow CS13200 (Fig. 6.6c) and is much weaker in the training flow WC360 (Fig. 6.6b) due to the mild slope of wavy bottom in this geometry.

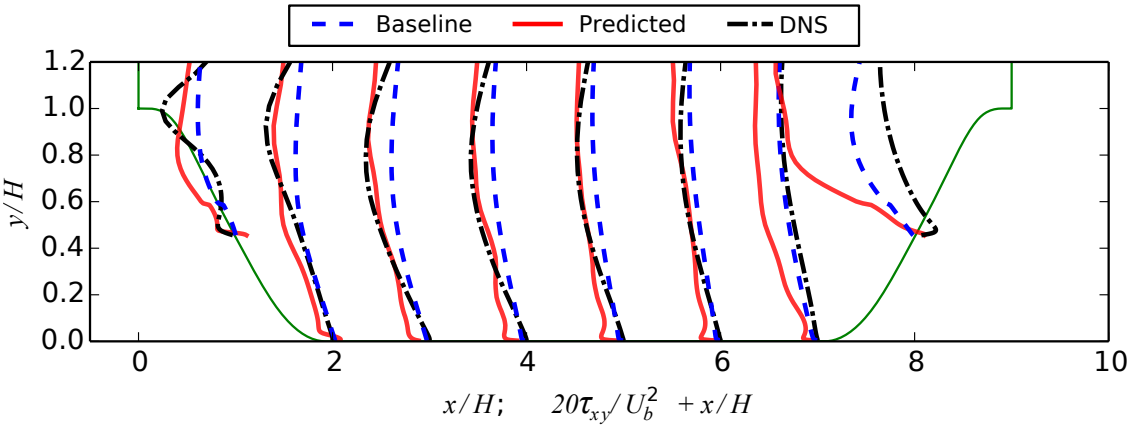

Figure 6.10: Predicted turbulence shear stress for the test flow (PH10595) learned from the flows with different geometries and at different Reynold numbers (WC360 and CS13200). The profiles are shown at eight streamwise locations $x/H = 1, 2, \cdots, 8$. Corresponding baseline and DNS results are also plotted for comparison. The hill profile is vertically exaggerated by a factor of 2.4.

Finally, we compare the predicted turbulent shear stress τ_{xy} with the DNS profiles in Fig. 6.10. Similar to the results of TKE, the PIML-predicted turbulent shear stress τ_{xy} shows notable improvements in the recirculation region. However, deterioration occurs in the flow contraction region. At $x/H = 7$ and 8, the magnitudes of turbulent shear stresses are overestimated with the correction based on the predicted discrepancies. This is consistent with the results observed in physical projections of Reynolds stress. Such a small region with abnormal Reynolds stress corrections (artificial peaks or bumps) can introduce large errors to the velocity predictions.

In general, the physical projections (i.e., magnitude, shape, and orientation) of Reynolds stress corrected by random forest predicted discrepancies are still significantly improved with the training flows in different geometries (WC360 and CS13200). The Reynolds stress is markedly improved in the separated flow region, but not in the contracted flow region. This is because the features in training flows cannot well support the predicted flow, and thus more extrapolations are expected. Although the improvement is less significant compared to that in the scenario I, the random forest predictions in this more realistic scenario are still satisfactory, demonstrating the merits of the proposed PIML framework.

6.4 Discussion

6.4.1 Feature Importance and Insight for Turbulence Modeling

In addition to the predictive capability of the regression model, it is also important to interpret the functional relation between the mean flow features and the discrepancies of the RANS modeled Reynolds stresses. For example, it is useful to find the most important features to the Reynolds stress discrepancy in each of its physical projection (i.e., magnitude k, shape ξ, η, and orientation φ_i), and how each of these features impacts the regression response. Identification of such correlation or causal relationship enables modelers to im-

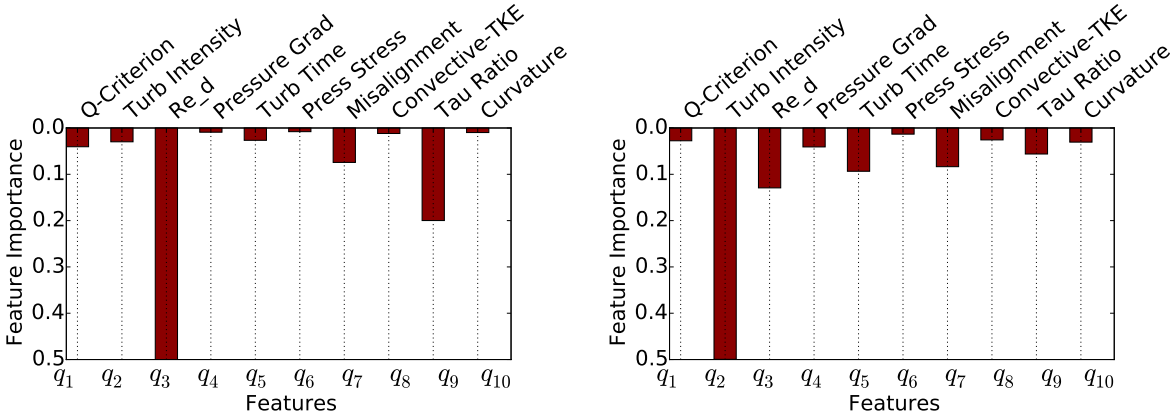

(a) $\Delta\eta$ (b) $\Delta \log_2 k$

Figure 6.11: Feature importance of random forests regressors (a) for $\Delta\eta$ and (b) for $\Delta \log_2 k$ for scenario I (i.e., training flows in the same geometry, see Table. 6.2). The features q_i ($i = 1$ to 10) are denoted by their respective abbreviations. Turb Intensity denotes the turbulence intensity (feature q_2), and Re_d is the wall distance based Reynolds number (feature q_3). For the full name list of features, see Table 6.1.

prove the RANS turbulence models. The random forest regressor used in the proposed PIML framework can also shed light on this issue by calculating the feature importance,

which is a measure to evaluate the relative importance of a feature variable for predicting response variables [26]. The bar plots of the importances of feature vector $\mathbf{q}$ with respect to the discrepancies $\Delta\eta$ and $\Delta \log_2 k$ are shown in Figs. 6.11a and 6.11b, respectively. For discrepancy $\Delta\eta$ in the anisotropy, feature q_3 (i.e., wall-distance based Reynolds number Re_d) is the most important one. As discussed in Section 6.2.3, Re_d is the wall distance normalized by the approximate viscous unit. Therefore, the result of feature importance is consistent with the PIML prediction, which have shown that the discrepancy $\Delta\eta$ is notably dependent on the distance away from the wall [53]. Figure 6.11b shows that the most important feature for predicting discrepancy $\Delta \log_2 k$ of turbulence kinetic energy is feature q_2, turbulence intensity.

It is demonstrated that random forest used in the proposed framework can interpret the relationship between the features and the response to a certain extent, although the feature importance has its limitation due to bias introduced under certain conditions [54, 55]. In the machine learning community, improving interpretability of random forest is an active research topic, e.g., several improvements of the importance measure have been proposed [55, 56, 57]. Moreover, in addition to calculating the feature importance, it is also helpful to examine the interactions among features, which have important implications for the interpretation of the regression models. As the base learner in random forest is a decision tree, which can capture the feature interactions, it is possible to further investigate the interacting relationship among mean flow variables. Breiman et al. have studied feature interaction in random forest method [26], but more research is still ongoing. A better understanding of the physics behind the regression model for Reynolds stress discrepancies has a profound implication to RANS turbulence modeling. Therefore, to explore the correlation or causal relationship between the mean flow features and the discrepancies of RANS modeled Reynolds stress is an important and promising extension of the proposed framework.

6.4.2 Success and Limitation of The Current Framework

The objective of the proposed framework is to improve the baseline RANS-predicted Reynolds stresses of a flow where high-fidelity (e.g., DNS, LES, experimental) data are not available. The main novelty lies in using machine learning techniques to find the functional forms of Reynolds stress discrepancies with respect to mean flow features by learning from the existing offline database of the closely related flows. Numerical simulation results have demonstrated the feasibility and merits of the framework. Moreover, the excellent performance of the PIML predicted Reynolds stress in not only the anisotropy but also in the TKE and turbulent shear stress shows the fact that Reynolds stress discrepancies can be extrapolated even to complex flows sharing similar characteristics. This finding is noteworthy by itself.

The improvement of the RANS-predicted Reynolds stress is considered a viable and promising path toward obtaining better predictions of velocities and other quantities of interest. However, due to a few limitations of the current framework, the improvement of the prop-

agated velocities from the corrected Reynolds stress field can not be guaranteed. A small region with abnormal Reynolds stress corrections (e.g., non-smoothness or artificial peaks) can introduce large errors to the velocity predictions. For example, the small wave-number variations in Reynolds stresses are visible in Fig. 6.10. These fluctuations, despite being small in amplitude, can lead to abnormal behaviors in the divergence term and thus in the predicted velocities. These abnormal predictions of Reynolds stress corrections can be caused by several factors. First, the features in certain regions of the prediction flow may not be well supported in the training flows, e.g. the contraction region of periodic-hill flow mentioned in Sec. 6.3.2. Second, the random forest regression used here only provides pointwise estimations but cannot consider the spatial information of the Reynolds stress field. Therefore, the smoothness of the prediction cannot be guaranteed. Finally, although the input feature space is constructed based on physical reasoning, it is possible that the input features are not rich enough, and thus the randomness in the ensemble of the trained decision trees is significant.

6.5 Conclusion

In this work, we proposed a physics-informed machine learning approach to reconstruct Reynolds stresses modeling discrepancies by utilizing DNS databases of training flows sharing similar characteristics as the flow to be predicted. For this purpose, we formulated discrepancy of Reynolds stresses (or more precisely its magnitude and the shape and orientation of the anisotropy) as target functions of mean flow features and used modern machine learning techniques based on random forest regression to learn the functions. The obtained functions are then used to predict Reynolds stress discrepancies in new flows. To evaluate the performance of the proposed approach, the method is tested by two classes of flows: (1) fully developed turbulent flows in a square duct at various Reynolds numbers and (2) flows with massive separations. In the separated flows, two training flow scenarios of increasing difficulties are considered: In the less challenging scenario, data from two flows in the same periodic hill geometry at lower Reynolds numbers ($Re = 2800$ and 5600) are used for training. In a more challenging scenario, the training data come from separated flows in different geometries (wavy channel and curved backward facing step). In all test cases the corrected Reynolds stresses are significantly improved compared to the baseline RANS predictions, demonstrating the merits of the proposed approach. In the scenario, where the training flows and the prediction flow have different geometries, the improvement is not as drastic as in the the scenario with the same geometry. This is expected since the prediction involves more extrapolations in the feature space for this more challenging scenario. In other words, compared to the first scenario where the training and prediction flows have identical geometry, the prediction flow is less "similar" to the training flows in this scenario. The extent to which the training and prediction flows are "similar" to each other can be assessed *a priori* based on their respective RANS predicted mean flow field, and methods for such assessment are presented in companion publications [24, 58].

As the inaccuracy in modeled Reynolds stresses is the dominant source of model-form uncertainty in RANS simulations, the proposed method for improving RANS-predicted Reynolds stresses is an important step towards the goal of enabling predictive capabilities of RANS models. Moreover, the random forests regression technique adopted in this work can provide physical insights regarding the relative importance of mean flow features that contributed to the discrepancies in the RANS predicted Reynolds stresses. This information can be used to assist future model development in that developers can devise models that are aware of and correctly respond to these flow features. However, a number of challenges need to be tackled before the improved Reynolds stresses can be used to predict more accurate quantities of interests that are needed in engineering design (e.g., draft and lift coefficients). This topic will be investigated in future research.

Acknowledgment

We thank Dr. Julia Ling of Sandia National Laboratories and Dr. Eric G. Paterson of Virginia Tech for helpful discussions during this work. We also thank the anonymous reviewers for their comments, which helped improving the quality and clarity of the manuscript.

Bibliography

[1] M. M. Waldrop, The chips are down for moores law, Nature News 530 (7589) (2016) 144.

[2] S. Kumar, Fundamental limits to Moore's law, arXiv preprint arXiv:1511.05956 (2015).

[3] B. Launder, B. Sharma, Application of the energy-dissipation model of turbulence to the calculation of flow near a spinning disc, Letters in heat and mass transfer 1 (2) (1974) 131–137.

[4] D. C. Wilcox, Reassessment of the scale-determining equation for advanced turbulence models, AIAA journal 26 (11) (1988) 1299–1310.

[5] D. C. Wilcox, et al., Turbulence modeling for CFD, 3rd edition, Vol. 2, DCW industries La Canada, CA, 2006.

[6] P. R. Spalart, S. R. Allmaras, A one equation turbulence model for aerodynamic flows., AIAA journal 94 (1992) 1–22.

[7] F. R. Menter, Two-equation eddy-viscosity turbulence models for engineering applications, AIAA journal 32 (8) (1994) 1598–1605.

[8] B. Launder, G. J. Reece, W. Rodi, Progress in the development of a Reynolds-stress turbulence closure, Journal of fluid mechanics 68 (03) (1975) 537–566.

[9] S. Wallin, A. V. Johansson, An explicit algebraic Reynolds stress model for incompressible and compressible turbulent flows, Journal of Fluid Mechanics 403 (2000) 89–132.

[10] E. Dow, Q. Wang, Quantification of structural uncertainties in the k–ω turbulence model, in: 52nd AIAA/ASME/ASCE/AHS/ASC Structures, Structural Dynamics and Materials Conference, AIAA, Denver, Colorado, 2011, AIAA Paper, 2011-1762.

[11] E. J. Parish, K. Duraisamy, A paradigm for data-driven predictive modeling using field inversion and machine learning, Journal of Computational Physics 305 (2016) 758–774.

[12] J. Ling, J. Templeton, Evaluation of machine learning algorithms for prediction of regions of high Reynolds averaged Navier Stokes uncertainty, Physics of Fluids (1994-present) 27 (8) (2015) 085103.

[13] H. Xiao, J.-L. Wu, J.-X. Wang, R. Sun, C. Roy, Quantifying and reducing model-form uncertainties in Reynolds-averaged Navier–Stokes simulations: A data-driven, physics-informed bayesian approach, Journal of Computational Physics 324 (2016) 115–136.

[14] J.-X. Wang, H. Xiao, Data-driven CFD modeling of turbulent flows through complex structures, International Journal of Heat and Fluid Flow 62 (B) (2016) 138–149.

[15] G. Iungo, F. Viola, U. Ciri, M. Rotea, S. Leonardi, Data-driven RANS for simulations of large wind farms, in: Journal of Physics: Conference Series, Vol. 625, IOP Publishing, 2015, p. 012025.

[16] A. P. Singh, K. Duraisamy, Using field inversion to quantify functional errors in turbulence closures, Physics of Fluids 28 (2016) 045110.

[17] J.-L. Wu, J.-X. Wang, H. Xiao, Quantifying model form uncertainty in RANS simulation of wing–body junction flow, submitted, Available at: arXiv:1605.05962 (2016).

[18] K. Duraisamy, Z. J. Zhang, A. P. Singh, New approaches in turbulence and transition modeling using data-driven techniques, in: AIAA SciTech, Kissimmee, Florida, Vol. 1284, 2015, p. 2015.

[19] J.-L. Wu, J.-X. Wang, H. Xiao, A Bayesian calibration-prediction method for reducing model-form uncertainties with application in RANS simulations, Flow, Turbulence and Combustion 97 (2016) 761–786.

[20] J. Ling, A. Ruiz, G. Lacaze, J. Oefelein, Uncertainty analysis and data-driven model advances for a jet-in-crossflow, Journal of Turbomachinery 139 (2) (2017) 021008.

[21] J. Friedman, T. Hastie, R. Tibshirani, The elements of statistical learning, Springer, Berlin, 2001.

[22] T. Oliver, R. Moser, Uncertainty quantification for RANS turbulence model predictions, in: APS Division of Fluid Dynamics Meeting Abstracts, Vol. 1, 2009.

[23] S. Pope, Turbulent Flows, Cambridge University Press, 2000.

[24] J.-L. Wu, J.-X. Wang, J. Ling, H. Xiao, Physics-informed machine learning for predictive turbulence modeling: A priori assessment of prediction confidence, submitted, Arxiv preprint (2016).

[25] C. E. Rasmussen, Gaussian processes for machine learning, MIT Press, 2006.

[26] L. Breiman, Random forests, Machine learning 45 (1) (2001) 5–32.

[27] P. R. Spalart, Strategies for turbulence modelling and simulations, International Journal of Heat and Fluid Flow 21 (3) (2000) 252–263.

[28] J. C. Hunt, A. A. Wray, P. Moin, Eddies, streams, and convergence zones in turbulent flows, Tech. Rep. 19890015184, Center of Turbulence Research, Stanford University (Dec. 1988).

[29] P. Chakraborty, S. Balachandar, R. J. Adrian, On the relationships between local vortex identification schemes, Journal of Fluid Mechanics 535 (2005) 189–214.

[30] C. Gorle, M. Emory, G. Iaccarino, RANS modeling of turbulent mixing for a jet in supersonic cross flow: model evaluation and uncertainty quantification, in: ICHMT DIGITAL LIBRARY ONLINE, Begel House Inc., 2012.

[31] J. Ling, R. Jones, J. Templeton, Machine learning strategies for systems with invariance properties, Journal of Computational Physics 318 (2016) 22–35.

[32] J. L. Lumley, G. R. Newman, The return to isotropy of homogeneous turbulence, Journal of Fluid Mechanics 82 (01) (1977) 161–178.

[33] S. Banerjee, R. Krahl, F. Durst, C. Zenger, Presentation of anisotropy properties of turbulence, invariants versus eigenvalue approaches, Journal of Turbulence (8) (2007) N32.

[34] M. Emory, R. Pecnik, G. Iaccarino, Modeling structural uncertainties in Reynolds-averaged computations of shock/boundary layer interactions, AIAA paper 479 (2011) 1–16.

[35] M. Emory, G. Iaccarino, Componentality-based wall-blocking for rans models, in: Proceedings of the CTR Summer Program, 2014, pp. 193–208.

[36] H. Goldstein, The Euler angles, Classical Mechanics, (1980) 143–148.

[37] B. Tracey, K. Duraisamy, J. Alonso, Application of supervised learning to quantify uncertainties in turbulence and combustion modeling, AIAA Paper 259 (2013) 2013.

[38] N. S. Altman, An introduction to kernel and nearest-neighbor nonparametric regression, The American Statistician 46 (3) (1992) 175–185.

[39] G. James, D. Witten, T. Hastie, R. Tibshirani, An introduction to statistical learning, Vol. 112, Springer, 2013.

[40] J. A. Anderson, An introduction to neural networks, MIT press, 1995.

[41] N. Cristianini, J. Shawe-Taylor, An introduction to support vector machines and other kernel-based learning methods, Cambridge university press, 2000.

[42] T. K. Ho, The random subspace method for constructing decision forests, Pattern Analysis and Machine Intelligence, IEEE Transactions on 20 (8) (1998) 832–844.

[43] L. Breiman, J. Friedman, C. J. Stone, R. A. Olshen, Classification and regression trees, CRC press, 1984.

[44] W. Jones, B. Launder, The prediction of laminarization with a two-equation model of turbulence, International journal of heat and mass transfer 15 (2) (1972) 301–314.

[45] P. Bradshaw, Turbulent secondary flows, Annual review of fluid mechanics 19 (1) (1987) 53–74.

[46] F. Billard, Development of a robust elliptic-blending turbulence model for near-wall, separated and buoyant flows., Ph.D. thesis, School of Mechanical Aerospace and Civil Engineering, The University of Manchester., Manchester, UK (2011).

[47] H. G. Weller, G. Tabor, H. Jasak, C. Fureby, A tensorial approach to computational continuum mechanics using object-oriented techniques, Computers in physics 12 (6) (1998) 620–631.

[48] A. Pinelli, M. Uhlmann, A. Sekimoto, G. Kawahara, Reynolds number dependence of mean flow structure in square duct turbulence, Journal of fluid mechanics 644 (2010) 107–122.

[49] M. Gibson, B. Launder, Ground effects on pressure fluctuations in the atmospheric boundary layer, Journal of Fluid Mechanics 86 (03) (1978) 491–511.

[50] M. Breuer, N. Peller, C. Rapp, M. Manhart, Flow over periodic hills–numerical and experimental study in a wide range of Reynolds numbers, Computers & Fluids 38 (2) (2009) 433–457.

[51] C. Maaß, U. Schumann, Direct numerical simulation of separated turbulent flow over a wavy boundary, in: Flow Simulation with High-Performance Computers II, Springer, 1996, pp. 227–241.

[52] Y. Bentaleb, S. Lardeau, M. A. Leschziner, Large-eddy simulation of turbulent boundary layer separation from a rounded step, Journal of Turbulence (13) (2012) N4.

[53] H. Xiao, J.-L. Wu, J.-X. Wang, E. G. Paterson, Physics-informed machine learning for predictive turbulence modeling: Progress and perspectives, in Proceedings of the 2017 AIAA SciTech, In press (2017).

[54] A. Dobra, J. Gehrke, Bias correction in classification tree construction, in: Proceedings of the Eighteenth International Conference on Machine Learning, Morgan Kaufmann Publishers Inc., 2001, pp. 90–97.

[55] C. Strobl, A.-L. Boulesteix, A. Zeileis, T. Hothorn, Bias in random forest variable importance measures: Illustrations, sources and a solution, BMC bioinformatics 8 (1) (2007) 1.

[56] M. Sandri, P. Zuccolotto, A bias correction algorithm for the Gini variable importance measure in classification trees, Journal of Computational and Graphical Statistics 17 (3) 611–628.

[57] A. Altmann, L. Toloşi, O. Sander, T. Lengauer, Permutation importance: a corrected feature importance measure, Bioinformatics 26 (10) (2010) 1340–1347.

[58] J.-L. Wu, J.-X. Wang, H. Xiao, J. Ling, Visualization of high dimensional turbulence simulation data using t-sne, in Proceedings of the 2017 AIAA SciTech, In press (2017).

Chapter 7

Conclusion and Future Work

Quantification and reduction of uncertainties originating from the Reynolds stress closures in RANS simulations are of critical importance to obtaining risk-informed predictions for mission-critical applications. In this work, two frameworks for estimating model-form uncertainties in RANS simulations are proposed. One is the physics-based approach, where uncertainties are injected onto physical projections of Reynolds stress tensor accounting for empirical prior knowledge and physical constraints (e.g., realizability of Reynolds stress, smoothness, and symmetry). This approach is a development based on the seminal framework of Iaccarino and co-workers [1, 2] but with a full exploration of the uncertainty space of Reynolds stresses. Instead of only considering the eigenvalue perturbation towards three limiting states in [1], this work employed Gaussian random fields with compact parameterization by Karhunen-Loéve expansions to represent uncertainties in all six physically meaningful components of the Reynolds stress tensor (i.e., its shape, magnitude, and orientations). On the other hand, a random matrix theoretic (RMT) approach is proposed, where the Reynolds stress filed is described with a probabilistic model of a random field of positive semidefinite matrices with a specified mean and correlation structure. The marginal probability distribution of the Reynolds stress at a particular location satisfies the maximum entropy principle. Moreover, the realizability constraint of the perturbed Reynolds stresses is guaranteed mathematically by the construction from the Cholesky factorization of the normalized Reynolds stress tensor. By imposing maximum entropy on the distribution of the Reynolds stress tensors, the RMT framework aims to provide an approach for specifying objective priors (e.g., in the context of Bayesian inferences for uncertainty reduction). To sample such a random matrix field, Gaussian random fields with specified covariance kernel are first generated and then mapped to the field of positive semidefinite matrices based on polynomial chaos expansion and reconstruction. For both physics-based and RMT approaches, numerical simulations have been performed by sampling the perturbed Reynolds stresses and propagating them through the RANS equations. A canonical flow, the flow past periodic hills, is tested. The simulation results show that perturbed Reynolds stress fields not only have the specified statistics, but also are physically reasonable. To

evaluate the priors and gain insights on proper specification of the priors, a comparison analysis between the physics-based approach and RMT approach has been conducted. By comparing the distributions of shape, magnitude, and orientation variables obtained from the two approaches, we identify several factors which may introduce artificial constraints in the physic-based approach. Moreover, the comparisons also provide some useful guidelines of the prior specification for wall-bounded flows with separations. For eigenvalues of Reynolds stress anisotropy, the Gaussian distributed perturbations in Barycentric coordinate are better at achieving maximum entropy. For the turbulence kinetic energy, introducing log-normally distributed perturbations leads to a distribution of Reynolds stresses that is close to the one with the maximum entropy. This observation lends support to the choice of prior in [3]. For orientation, it suggests that the uncertainties should also be injected with a non-stationary variance field to achieve the maximum entropy distribution. Simultaneously perturbing shape and orientation of anisotropy in the physics-based approach cannot preserve the mean of tensors as the baseline result. Useful suggestions on specifying relative magnitudes of variances among the physical variables are provided. The observations and conclusion are meaningful to quantify the model-form uncertainties in RANS modeling and can be used as a guidance for the objective prior specification in the physics-based, Bayesian uncertainty reduction framework.

In this dissertation, the use of available on-line and off-line data has also been leveraged to reduce the model-form uncertainties and to calibrate model discrepancies in RANS simulations. A physics-based, Bayesian framework is proposed for reducing model uncertainties and improving the prediction accuracy based on sparse velocity measurement data. An iterative ensemble Kalman method is used to incorporate the prior knowledge with available observation data in a Bayesian framework and to propagate the uncertainties to posterior distributions of Reynolds stresses and other QoIs. Two test cases, the flow over periodic hills and the flow in a square duct, have been used to demonstrate its feasibility and to evaluate the calibration performance. Simulation results suggest that even with sparse data, the obtained posterior mean velocities and other QoIs significantly better agree with the DNS results. Moreover, the merits of incorporating various prior knowledge into the proposed Bayesian framework have been discussed. The role of physical prior knowledge, including smoothness, realizability, overall understanding of the coherent structures, and the empirical assessments of the RANS prediction accuracy are examined. The simulation results demonstrate that incorporating prior information enables a more efficient use of limited amount of observation data. The proposed Bayesian methodology provides a general framework for combining information from physical prior knowledge, on-line observation data, and low-fidelity numerical models that are frequently used in engineering practice. In the scenario with no on-line observation data, the Bayesian data assimilation framework is not applicable. In this case, off-line data (data of cases with similar configurations) are usually available. To leverage the off-line database, a physics-informed, machine learning (PIML) framework is developed to learn the functional form of model discrepancy in RANS simulations from the database of related flows. The trained discrepancy function can be used to improve predictions of the flow where data are not available. For this purpose, the discrepancies of

Reynolds stresses are formulated as target functions of mean flow features and random forests are used to learn these functions. To evaluate the prediction performance, two scenarios of training flows at different Reynolds numbers and with changed geometries are considered. The Reynolds stresses in both training scenarios are significantly improved over the baseline RANS predictions. Since the inaccuracy in RANS-modeled Reynolds stresses is the dominant source of model-form uncertainties in RANS simulations, the proposed framework for improving RANS-simulated Reynolds stresses is an important step towards the predictive RANS turbulence modeling.

Finally, the computational costs for the proposed frameworks by using on-line data assimilation and off-line machine learning are summarized. By assimilating on-line data, the iterative ensemble Kalman method is used. Normally, 10^2 samples are used and 10 iterations are needed to achieve statistical convergence. Therefore, it involves 10^3 evaluations of the forward RANS model. Since each forward simulation is only 10% as expensive as a baseline RANS simulation, and the total cost is 10^2 times as that of the baseline. If the propagation of all samples can be done in parallel with 100 CPU cores, the wall time of off-line data assimilation is approximately the same as that of the baseline simulation. In the off-line machine learning approach, the computational costs associated with the machine learning process (e.g., feature generation, random forest regression, data processing) can be neglected compared to that of the forward RANS simulations. That is, using off-line data to improve the Reynolds stresses will not increase the total computational cost.

Model-form uncertainty estimation in RANS simulations and data-driven predictive RANS modeling are still in the infancy stages. Much future works are still needed. In the following, a few research directions are listed for future investigation:

1. In the proposed physic-based, data-driven Bayesian framework for estimating and reducing model-form uncertainties in RANS simulations (presented in Chapter 2), there are two limitations. One limitation is that the full Reynolds stress field inferred, i.e., mean of the posterior of the Reynolds stress fields, is not accurate. This is attributed to many factors, e.g., the high dimension of the Reynolds stress uncertainty space, the sparseness of the data, and the nonlinear or even non-unique mapping between Reynolds stresses and velocities as described in RANS equations. Although the inferred Reynolds stress field is not accurate, it can provide the improved quantities of interests (QoI) such as the velocity field after propagation. However, when the Reynolds stress field itself is the QoI, more investigations are needed to improve the inversion scheme. Proper regularization methods might be useful to overcome issues of the nonlinearity or non-uniqueness by constraining the inversion to be performed in a low manifold. Another limitation of this framework lies in the iterative ensemble Kalman methods for uncertainty quantification. Although the ensemble Kalman method is less computational costly compared to the exact Bayesian sampling, its computed uncertainties are inaccurate and often underestimated. This is because the ensemble Kalman method is an approximate Bayesian approach, which is developed by

using the maximum likelihood estimation. The impact of the approximate Bayesian inference method will be investigated by comparing it with the exact Bayesian approach based on Markov Chain Monte-Carlo (MCMC) sampling in the future study.

2. The proposed random matrix theoretic approach for estimating model-form uncertainties in RANS simulations can provide maximum entropy distribution of Reynolds stress at each point without introducing artificial constraints. Nonetheless, the specifications of the spatial structure and the magnitude field of perturbations are still the modeling choices, which highly rely on prior physical knowledge and subjective judgment. These modeling choices might introduce artificial information. It would be desirable to generalize the current work to defining maximum entropy distribution for random tensor fields for future investigation. Moreover, the role of the spatial correlation structure is particularly crucial since it is the divergence of the Reynolds stress that appears in the RANS momentum equation. Therefore, how to properly incorporate physical constraints on spatial correlations is another future research direction. Finally, it is important to investigate methods for determining the magnitude of perturbations, which indicates the confidence level on RANS predictions. One possible method is to learn from available flow databases by using machine learning techniques.

3. Although it has been demonstrated that the proposed physics-informed, machine learning (PIML) framework is a promising way to improve RANS modeling by using the off-line database, there are a few challenges associated with the propagation, data, and parameterization of learning targets, which need to be investigated in the future work. First, to propagate the success in the corrected Reynolds stresses (shown in Chapter 6) to the QoIs is still a challenge. This is because the improvement of the Reynolds stress is achieved at each point, but the non-smoothness of the Reynolds stress field might exist, for the fact that random forest regressor provides point-wise estimations. As discussed above, physical constraints on the spatial structures of Reynolds stress field should be encoded into the learning process. For example, besides the Reynolds stress tensor, the divergence of Reynolds stresses can also be augmented as the learning target. Second, the limited amount of DNS data could be another limitation of the current framework, because the high-fidelity simulations (e.g., DNS) are ultimately limited to flows in relatively low Reynolds numbers and with simple geometric configurations. How to conduct the effective learning with a limited amount of data ought to be explored in the future study. Third, to obtain the confidence of the prediction performance based on the analysis of training databases is very important. More effective qualitative and quantitative metrics and approaches should be developed to determine how accurate the prediction will be with the given extrapolation range. Finally, since the ultimate goal of offline machine learning framework is to improve the turbulence models, more rigorous feature importance analysis is required to gain insight to improve the current models or to develop new turbulence models.

[1] M. Emory, J. Larsson, G. Iaccarino, Modeling of structural uncertainties in Reynolds-averaged Navier-Stokes closures, Physics of Fluids 25 (11) (2013) 110822.

[2] C. Gorlé, G. Iaccarino, A framework for epistemic uncertainty quantification of turbulent scalar flux models for Reynolds-averaged Navier-Stokes simulations, Physics of Fluids 25 (5) (2013) 055105.

[3] H. Xiao, J.-L. Wu, J.-X. Wang, R. Sun, C. Roy, Quantifying and reducing model-form uncertainties in Reynolds-averaged Navier–Stokes simulations: A data-driven, physics-informed bayesian approach, Journal of Computational Physics 324 (2016) 115–136.